

Trinity College Dublin
Coláiste na Tríonóide, Baile Átha Cliath
The University of Dublin

School of Physics

# Morphological & Electrical Characterisation of Nanosheet Networks

Luke Doolan

Supervisor: Prof. Jonathan N. Coleman

March 12, 2025

A dissertation submitted in partial fulfilment
of the requirements for the degree of
PhD in Physics

# Declaration

I hereby declare that this dissertation is entirely my own work and that it has not been submitted as an exercise for a degree at this or any other university.

I have read and I understand the plagiarism provisions in the General Regulations of the University Calendar for the current year, found at `http://www.tcd.ie/calendar`.

I have completed the Online Tutorial on avoiding plagiarism 'Ready Steady Write', located at `http://tcd-ie.libguides.com/plagiarism/ready-steady-write`.

I consent to the examiner retaining a copy of the thesis beyond the examining period, should they so wish (EU GDPR May 2018).

I agree that this thesis will not be publicly available, but will be available to TCD staff and students in the University's open access institutional repository on the Trinity domain only, subject to Irish Copyright Legislation and Trinity College Library conditions of use and acknowledgement.

Signed: _____ Date: _____

# Morphological & Electrical Characterisation of Nanosheet Networks

## Abstract

Since the discovery of the stability and excellent electrical properties of the graphene monolayer, there has been a great deal of excitement about the superlative electrical, mechanical and thermal properties of 2D materials. While individual nanosheets show excellent electrical properties, this promise has not translated to networks composed of nanosheets, which regularly show properties that are considerably inferior to their constituent nanosheets. A number of reasons have been proposed to explain these inferior electrical properties, including the network morphology and the resistance of the junctions between the nanosheets. The aim of this thesis is to develop methods to characterise the morphology of nanosheet networks and the electrical properties of the junctions between the nanosheets so that the properties of nanosheet networks can be better understood and optimised.

The morphology of a nanosheet network affects its performance in a range of applications, from energy storage to sensing to printed electronics. While it is known that the network morphology is important, techniques to investigate it have remained limited. Focused ion beam-scanning electron microscope nanotomography (FIB-SEM nt) is presented as a technique which can be used determine an array of network morphological parameters. Using size-selected graphene networks as a case study, the ability of this technique to characterise network morphology was investigated. A variety of properties, including network porosity, nanosheet alignment, nanosheet aggregation, and nanosheet and pore tortuosity factors were calculated. It was found that each of these parameters varies with the size of the nanosheets in the network. This technique was then extended to investigate the morphology of size-selected networks of tungsten disulphide ($WS_2$) and silver nanosheets (AgNSs). The morphology of the networks is found to vary with the constituent nanosheets, as well as the nanosheet size. The technique was then extended to heterostack devices. The interface between 2 size-selected graphene networks and a silver nanoparticle (AgNP) network, which is printed on top of the graphene networks, was investigated. It was found that the penetration of the AgNPs into the network depends on the size of the graphene nanosheets in the network. The technique was also applied to an out-of-plane $WS_2$ device with an indium tin oxide (ITO) bottom electrode and a gold top electrode, finding that shorting between the top and bottom electrode was caused by the high surface roughness of the $WS_2$ network.

The electrical properties of nanosheet networks are limited by the high resistance of the junctions between the nanosheets, as well as the morphology of the network. A model which relates network conductivity to the resistance of these junctions, the network morphology and the electrical properties of the constituent nanosheets was derived. This model suggests that the network conductivity depends on the size of the nanosheets in the network, with

the nature of this dependence being controlled by the nanosheet carrier concentration. To investigate this size-selected graphene and $WS_2$ networks were produced. The graphene network conductivity increases with decreasing nanosheet length, in line with the predictions of the model. Using the model the nanosheet conductivity was calculated as $32 \pm 2$ kS.m$^{-1}$ and a value of $1.4 \pm 0.1$ kΩ was calculated for the junction resistance. The size-selected $WS_2$ network conductivity exhibited the opposite behaviour with nanosheet length, peaking at larger nanosheet lengths and sharply decreasing as the length decreased. This behaviour is also in line with the predictions of the model. Using the model the $WS_2$ nanosheet conductivity was calculated as $0.6 \pm 0.1$ S.m$^{-1}$ and the junction resistance was calculated as $17 \pm 3$ GΩ. These results demonstrate the importance of optimising nanosheet length for nanosheet network devices.

While solution-processed nanosheet networks show promise for electronic devices, producing these devices is energy and time consuming. Recently, a technique which allows for the mass-production of nanosheets by mechanical exfoliation has been demonstrated. This technique was used to produce mechanically exfoliated nanosheets, yielding large area, thick, high aspect ratio nanosheets. These nanosheets were then stacked to form a network. To understand the morphology of these networks FIB-SEM nt was used to image these networks, finding that the networks are composed of well-aligned nanosheets, with a low porosity and surface roughness. These morphological properties suggest that the network should show excellent electrical properties. The electrical properties of the networks were investigated by ionic liquid gated transistor measurements. It was found that the mobility of the networks depended on the starting material, with nanosheets exfoliated from crystal $MoS_2$ showing mobility of $2.2 \pm 0.3$ cm$^2$.V$^{-1}$.s$^{-1}$, while networks of nanosheets exfoliated from $MoS_2$ powder had a mobility of $0.025 \pm 0.002$ cm$^2$.V$^{-1}$.s$^{-1}$. These mobilities are below what has been obtained from electrochemically exfoliated $MoS_2$ nanosheet networks. To understand the low mobilities of the networks exfoliated from crystal, the nanosheet and junction resistance were calculated. This was achieved by combining the model derived for network conductivity with electrical impedance spectroscopy (EIS). The junction resistance was calculated as $890 \pm 130$ kΩ and the nanosheet conductivity was calculated as $110 \pm 20$ S.m$^{-1}$, suggesting that the low network mobility was caused by the low mobility of the $MoS_2$ nanosheets. To further understand charge transport in these networks temperature dependent EIS was carried out, revealing that the nanosheet conductivity is limited by phonon scattering of charge carriers while the junctions transition from Miller-Abrahams hopping (MAH) at room temperature to 3D-variable range hoping (3D-VRH) at low temperatures. The MAH has an associated activation energy of 64 meV, while from the 3D-VRH regime a localisation length of 0.4 nm was calculated for the charge carriers in the $MoS_2$ nanosheet.

# Publications

1. Liu, S., Ding, E., Kelly, A.G., Doolan, L., Gabbett, C., Kaur, H., Munuera, J., Carey, T., Garcia J. and Coleman, J. N. (2022), Solution processed, vertically stacked heterostructured diodes based on liquid-exfoliated $WS_2$ nanosheets: from electrode-limited to bulk-limited behaviour. *Nanoscale*, 14, 15679-15690.

2. Kelly, A. G., Sheil, S., Douglas-Henry, D. A., Caffrey, E., Gabbett, C., Doolan, L., Nicolosi, V., and Coleman, J. N., (2023) Transparent Conductors Printed from Grids of Highly Conductive Silver Nanosheets. *ACS Applied Materials & Interfaces*, 15(33), 39864-39871.

3. Liu, S., Carey, T., Munuera, J., Synnatschke, K., Kaur, H., Coleman, E., Doolan, L., Coleman, J. N. (2023) Solution-Processed Heterojunction Photodiodes Based on $WSe_2$ Nanosheet Networks. *Small*, 2304735

4. Gabbett, C., Doolan, L., Synnatschke, K., Gambini, L., Coleman, E., Kelly, A. G., Liu, S., Caffrey, E., Munuera, J. M., Murphy, C., Sanvito, S., Jones L. and Coleman, J. N. (2024) Quantitative analysis of printed nanostructured networks using high-resolution 3D FIB-SEM nanotomography. *Nature Communications*, 15(1), 278
**Basis of chapter 5**

5. Sinnott, A. D., Kelly, A. G., Gabbett, C., Munuera, J., Doolan, L., Möbius, M., Ippolito, S., Samorì, P., Coleman, J. N. and Cross, G. L. W., (2024), Mechanical Properties of Conducting Printed Nanosheet Network Thin Films Under Uniaxial Compression. *Advanced Materials*, 2306954.

6. Garcia, J., Caffrey, E., Doolan, L., Horvath, D.V., Carey, T., Gabbett, C. and Coleman, J.N. (2024), Near Room Temperature Production of Segregated Network Composites of Carbon Nanotubes and Regolith as Multifunctional, Extra-Terrestrial Building Materials. *Small*, 2310954.

7. Carey, T., Maughan, J., Doolan, L., Caffrey, E., Garcia, J., Liu, S., Kaur, H., Ilhan, C., Seyedin, S. and Coleman J.N., (2024), Knot Architecture for Biocompatible and Semiconducting 2D Electronic Fiber Transistors. *Small methods*, 2301654.

8. Gabbett, C., Kelly, A. G., Coleman, E., Doolan, L., Carey, T., Synnatschke, K., Liu, S., Dawson, A., O'Suilleabhain, D., Munuera, J., Caffrey, E., Boland, J. B., Sofer, Z., Ghosh, G., Kinge, S., Siebbeles, L. D. A., Yadav, N., Vij, J. K., Awais Aslam, M., Matkovic, A. and Coleman, J. N. (2024) Understanding how junction resistances impact the conduction mechanism in nano-networks. *Nature Communications*, 15(1), 4517.
**Basis of chapter 6**

9. Gambini, L., Gabbett, C., Doolan, L., Jones, L., Coleman, J. N., Gilligan, P., and Sanvito S. (2024) Video frame interpolation neural network for 3D tomography across different length scales. *Nature Communications*, 15, 7962.

10. Caffrey, E., Carey, T., Doolan, L., Dawson, A., Colemam, E., Sofer, Z., Cassidy, O., Gabbett, C., Coleman, J. N. (2025) Using electrical impedance spectroscopy to separately quantify the effect of strain on nanosheet and junction resistance in printed nanosheet networks. *Small*, 21, 5, 2406864.

11. Cassidy, O., Synnatschke, K., Munuera, J. M., Gabbett, C., Carey, T., Doolan, L.,

Caffrey, E., Coleman, J. N. (2025) Layer-by-layer assembly yields thin graphene films with near theoretical conductivity. *npj 2D Materials and Applications,* 9, 2.

12. Coleman, E., Kelly, A. G., Gabbett, C., Doolan, L., Liu, S., Yadav, N., Vij, J. K., Coleman, J. N., (2025) Extracting the temperature dependence of both nanowire resistivity and junction resistance from electrical measurements on printed silver nanowire networks. *ACS Applied Electronic Materials*, 7, 2, 806–815.

# Acknowledgements

I would like to start by thanking Johnny for giving me the opportunity to work with such an amazing group. I started during the height of COVID and so the legend of the group night out, often planned but never realised, loomed large over my first year. When we finally made it to Merrion square and everyone had to suffer through our 3 song long first year karaoke, I was certain that the next 3 years would be filled with endless fun. Your advice and enthusiasm, in the face of my almost endless pessimism was always reassuring and gave me the hope to go forward and fail again and again.

To the Coleman group, it has been an incredible 4 years and I would like to thank you all for the endless list of good times, both in and out of the lab. To Cian, who taught me everything I know about both microscopy and electronics, in other words everything in this thesis, I owe an incalculable debt, for which I have done a Johnny style back of the envelope calculation and decided it is at least 1000 pints. Without all your hard work, endless optimism and guidance, the last 4 years would never have been the meagre scientific success that they can claim to be. Once I get on the postdoc money I shall buy you the 1000 pints. To Adam and Kev, the bad boys of physics, I would like to thank you for all your scientific guidance, but far more importantly for showing me that a lot of the most important research can be done in the pub. To the rest of the Coleman group, past and present, Tian, Jose, Erxiong, Rebekah, Joe, Shixin, Dan, Bathrathi, Yash, Domhnall, Alina, James, Mark, Dominic, Jack, Emmet, Oran C. & B., Anthony, and Lalia, thank you for all the help, support and good memories.

To Eoin, who has remained friends with me for the past 4 years despite my endless nattering about science, thank you. I have no idea how, or why, you put up with working and living with me for 3 years, but I imagine all the races around campus and evenings idled away in the pub helped. Without having you as a sounding board to talk at endlessly, I think I would still be baffled by the most basic of electronic concepts. You are a good friend even if you annoy me to no end and you should have never been allowed in the premium upstairs office space. To Andrew, who put up with living with the two of us for 2 years, all I can say is that if I ever grow up and get a real job maybe I can pay for a therapist to help heal the scars that sort of thing must leave on your psyche. To the rest of my friends thank you for giving me the chance to get out of my head.

To Andres and everyone in the 2D-Foundry group, I would like to thank you for welcoming me into your group and keeping me entertained while I was in Madrid.

I would also like to thank Aaron, for indulging me whenever I was looking for help squishing something.

I would like to thank Ryan, for putting up with me for the past 4 years and supporting me while I mess about doing science instead of getting a real job. Thank you for never letting me take myself too seriously and reminding me that there is more to life than work. To my family, without whose endless support I would never have had the opportunity to waste the last 8 years chasing my passion, thank you so very much. I could not have done this without you all!

Finally, I would like to thank all the dogs that have helped me along the way, especially Sandie, Henry Rufus, Madeline Joy, Milo, and Elliot Beau, without whom I would have lost my mind long before I managed to finish this PhD.

# Contents


**1 Introduction** **1**

**2 2D materials: properties and synthesis** **4**

2.1 2D materials . . . 4

2.1.1 Graphene . . . 5

2.1.2 Transition Metal Dichacolgenides (TMD) . . . 7

2.2 Synthesis of 2D materials . . . 10

2.2.1 Mechanical exfoliation . . . 10

2.2.2 Chemical vapour deposition (CVD) . . . 11

2.2.3 Solution-based-synthesis . . . 12

2.3 Nanosheet Stabilisation . . . 17

2.3.1 Solvent Stabilisation . . . 17

2.3.2 Surfactant Stabilisation . . . 19

2.4 Control of material size . . . 20

**3 Nanosheet networks: deposition, and electrical & morphological characteristics** **23**

3.1 Depositing nanosheets . . . 23

3.1.1 Spray-coating . . . 24

3.1.2 Aerosol Jet Printing (AJP) . . . 25

3.2 Electrical devices & their characterisation . . . 26

3.2.1 Electrical conductivity & device resistance . . . 26

3.2.2 Transistors . . . 28

3.2.3 Alternating currents & electrical impedance spectroscopy (EIS) . . . 31

3.3 Nanosheet networks . . . 32

3.3.1 Percolation effects . . . 33

3.3.2 Conduction in nanosheet networks . . . 35

3.3.3 The morphology of nanosheet networks . . . 39

**4 Nanosheet and network characterisation techniques** **42**

4.1 Nanosheet characterisation . . . 42

4.1.1 Atomic force microscopy (AFM) . . . 42

4.1.2 Ultraviolet-visible (UV-vis) spectroscopy . . . 44

4.1.3 Raman spectroscopy . . . 45

4.2 Morphological characterisation . . . 46

4.2.1 Scanning electron microscopy (SEM) . . . 47

4.2.2 Focused ion beam (FIB) microscopy . . . 49

4.2.3 Focused ion beam-scanning electron microscope nanotomography (FIB-SEM nt) . . . 51
4.2.4 Image processing techniques . . . 54

**5 The effect of nanosheet dimensions on network morphology 58**
5.1 Materials & Methods . . . 59
5.2 Results & Discussion . . . 61
5.2.1 Characterisation of size-selected inks . . . 61
5.2.2 Microscopy of printed networks . . . 63
5.2.3 Morphological characterisation of printed graphene networks . . . 65
5.2.4 The effect of nanosheet length on graphene network morphology . . . 71
5.2.5 Morphology of networks of nanomaterials beyond graphene . . . 75
5.2.6 3D imaging of devices . . . 80

**6 The relationship between nanosheet dimension & network conductivity 85**
6.1 Experimental procedure . . . 86
6.2 Results & discussion . . . 88
6.2.1 Model development . . . 88
6.2.2 Electrical properties of size-selected graphene networks . . . 93
6.2.3 Electrical properties of size-selected $WS_2$ networks . . . 97

**7 The morphological & electrical properties of mechanically exfoliated nanosheet networks 103**
7.1 Experimental procedure . . . 104
7.2 Results & discussion . . . 106
7.2.1 Material characterisation . . . 106
7.2.2 The morphology of mechanically exfoliated networks . . . 107
7.2.3 Network electrical properties . . . 110
7.2.4 Temperature dependence of electrical properties . . . 120

**8 Conclusions & Future Work 127**
8.1 Conclusions . . . 127
8.2 Future work . . . 129
8.2.1 Mechanically exfoliated $MoS_2$ networks . . . 129
8.2.2 Factors affecting junction resistance . . . 129
8.2.3 Compression of spray-coated networks . . . 130

**A Appendix 134**

# List of Figures


2.1 Graphene . . . 5
2.2 Transition metal dichacogenides . . . 8
2.3 Layer-dependent band structure . . . 9
2.4 Mechanical exfoliation . . . 11
2.5 Liquid phase exfoliation . . . 14
2.6 Electrochemical exfoliation . . . 16
2.7 Solvent stabilisation . . . 18
2.8 Surfactant stabilisation . . . 20
2.9 Liquid cascade centrifugation . . . 21

3.1 Spray-coater . . . 24
3.2 Aerosol jet printing . . . 26
3.3 Transistors . . . 28
3.4 Ionic liquid gated transistors . . . 30
3.5 Electrical impedance spectroscopy . . . 31
3.6 Nanosheet networks . . . 33
3.7 Percolation theory . . . 34
3.8 Conduction in nanosheet networks . . . 36
3.9 Morphology of nanosheet networks . . . 39

4.1 Atomic force microscopy . . . 43
4.2 Ultraviolet visible spectroscopy . . . 44
4.3 Raman Spectroscopy . . . 45
4.4 Scanning electron microscope . . . 47
4.5 Interaction volume and electron detection . . . 49
4.6 Focused ion beam microscope . . . 50
4.7 Focused ion beam-scanning electron microscope nanotomography sample preparation . . . 52
4.8 Focused ion beam-scanning electron microscope nanotomography slicing procedure . . . 53
4.9 Image segmentation . . . 55
4.10 Image stack alignment . . . 56

5.1 Size-selected graphene ink characterisation . . . 62
5.2 Surface morphology of size-selected graphene networks . . . 63
5.3 Cross-sections and 3D images of size-selected graphene networks . . . 64
5.4 Measuring network porosity . . . 66
5.5 Calculating tortuosity, nanosheet aggregation and alignment . . . 69
5.6 Effect of nanosheet length on the pore volume . . . 72

5.7 Relationship between nanosheet length and network tortuosity, nanosheet aggregation, and alignment . . . 74
5.8 3D imaging materials beyond graphene . . . 76
5.9 Network pore volume of different materials . . . 77
5.10 Tortuosity factors of different materials . . . 78
5.11 $WS_2$ nanosheet aggregation and alignment . . . 79
5.12 Graphene-silver nanoparticle heterostack . . . 81
5.13 Graphene-silver nanoparticle interface . . . 82
5.14 Shorting in a $WS_2$ hetrostack . . . 83

6.1 Modelling charge transport . . . 89
6.2 Factors impacting network conductivity . . . 92
6.3 Electrical characterisation of size-selected graphene networks . . . 93
6.4 Nanosheet length dependent conductivity of graphene networks . . . 94
6.5 Size-selected $WS_2$ inks . . . 98
6.6 Spray-coated $WS_2$ networks . . . 99
6.7 Size-selected tungsten disulphide network conductivity . . . 100
6.8 Material conductivity and junction resistance . . . 101

7.1 Mechanical exfoliation of $MoS_2$ nanosheets . . . 106
7.2 Networks of mechanical exfoliated $MoS_2$ . . . 108
7.3 Tomography of a mechanical exfoliated $MoS_2$ network . . . 109
7.4 D.C. characterisation of mechanical exfoliated $MoS_2$ networks . . . 112
7.5 Electrical impedance spectroscopy of mechanical exfoliated $MoS_2$ networks 115
7.6 Converting from network to nanosheet-junction impedance . . . 117
7.7 Nanosheet and junction properties . . . 118
7.8 Nanosheet conductivity and junction resistance . . . 120
7.9 Network doping . . . 121
7.10 Temperature dependent impedance . . . 123
7.11 Temperature dependence of nanosheet and junctions . . . 124

8.1 Morphology of compressed network . . . 131
8.2 Electronics of compressed network . . . 132

*For my family and Ryan, without whom none of this would be possible*

*"Don't believe in yourself, don't deceive with belief*
*Knowledge comes with death's release"*
*-Quicksand*

*David Bowie*

*"They (Odin, Vili and Ve) took Ymir and bore into him the middle of the yawning void, and made of him the earth: of his blood the sea and the water; the land was made of his flesh, and the crags of his bones; gravel and stones they fashioned from his teeth and his grinders and those bones that were broken"*

Snorri Sturluson

# 1

# Introduction

Control over material properties is of great interest to humanity. The nature of the material world has long fascinated humanity. The quotes given at the start of each chapter in this work are various mythological descriptions of how the physical world was formed, showing the wonder with which people have always interpreted their surroundings. Research into the properties of materials began in earnest with alchemy, which was widely practised in medieval Europe, as people struggled to gain insight into the fundamental nature of materials, such that they could control them. Since the industrial revolution there has been an explosion in the mass production of materials for an ever-expanding range of applications. Recent progress means that we can now design materials with such precision that transistors just 3 nm in size can be produced. This incredible control over material properties has revolutionised the modern world, enabling everything from re-usable rockets for space travel to cheap 3D printers, allowing the individual to design and produce devices to aid in their everyday life.

In recent decades, there has been an explosion in interest the field of nanoscience. While nanomaterials have been used since ancient times, the discovery of their unique properties, and the invention of microscopes capable of imaging them, has led to an rapid increase in research into these materials. While all types of nanomaterials show unique and interesting properties, the class of nanomaterials called 2D materials is the focus of this work. These materials show superb electrical properties and they can be mass produced by a variety of techniques to form cheap electronic devices.

Interest in the field of printed electronics has grown exponentially in recent years due to the expansion of the Internet of Things, which describes devices embedded with sensors, which exchange information with each other. Printed electronics allows for the formation of cheap electronic devices on a variety of substrates from flexible plastics to fabrics, for a range of applications, such as energy storage, mobile healthcare, and diagnostics.[1] These devices can

be produced cheaply, making them ideal for applications which require low cost, disposable electronic devices. However, the performance of current printed electronic devices is limited, and improvements are required for these devices to fulfil their potential.

The use of 2D materials should offer a solution to the poor performance of printed electronic devices, 2D materials show superlative electronic properties and encompass the whole range of possible electronic structures. They can be deposit by standard printing techniques on a range of substrates to form an array of different devices. The large basal planes of these materials allows for them to overlap, forming well aligned nanosheets, which should allow them to offer superior performance to networks of nanoparticles and nanowires.[2] However, despite the hype around these materials they have failed to live up to their potential, which brings us to the central question of this thesis "What limits the performance of nanosheet networks?" While there has been a large amount of speculation about this question with the morphology of the networks as well as the junctions between the individual nanosheets often receiving the blame, techniques to measure these properties and their effects on a networks electrical properties have been limited.

One property which is often blamed for the poor performance of nanosheet networks in a range of applications is the morphology of the network. This catch all term describes everything from the porosity of the network to the alignment of the nanosheets to the interface between 2 materials in a heterostack devices. Despite the importance of the network morphology investigations into its effect are sparse. One of the main reasons for this is the lack of techniques to investigate it, while individual techniques allow for the characterisation of specific components of the morphology, no technique capable of characterising a large amount of morphological information at once has been demonstrated. 3D imaging using focused ion beam-scanning electron microscope nantomography (FIB-SEM nt) is presented as a solution to this problem in Chapter 5. Using this method a range of morphological parameters, including network porosity, nanosheet alignment, nanosheet aggregation, and nanosheet and pore tortuosity factors, are calculated. This technique is demonstrated on size-selected graphene networks, finding that the morphological parameters scale with nanosheet size. It is then extended to size-selected networks of tungsten disulphide ($WS_2$, a semiconductor) and silver nanosheets (AgNSs, a metal), demonstrating its ability to characterise a range of materials. It is also applied to a printed heterostack devices allowing for the interrogation of the interface between printed layers.

Before the discovery that individual layers of 2D materials could be removed from a bulk crystal, it has been suggested that the junctions between nanomaterials in a network limits the electrical properties of networks.[3,4] Despite this, simple models which relate network conductivity to the resistance of the junction, have been limited. In Chapter 6 a simple model relating the network conductivity to the network morphology, the electrical properties of the nanosheets and the junction resistance is derived. This model suggests that the electrical properties of nanosheet networks should depend strongly on the size of the con-

stituent nanosheets, with the nature of dependence being related to the the carrier denisty of the nanosheets. To investigate if these predictions are accurate, the electrical properties of size-selected graphene and $WS_2$ networks were investigated, finding that the network conductivity shows opposite length dependent trends. The graphene network conductivity increases as nanosheet length is decreased, while in the $WS_2$ networks the conductivity peaks at large nanosheet lengths and decreases rapidly for smaller nanosheets. Using the derived model the resistance of the junctions between the nanosheets and the conductivity of the nanosheets are calculated.

While solution-processed nanosheet networks are being investigated for a range of applications, the production of these devices is time and energy consuming. Recently a new cheap and scalable method for the production of nanosheet networks has been proposed. This technique mass produces nanosheets by mechanical exfoliation, and allows for these nanosheets to be deposited on a range of substrates to form devices.[5] While the performance of individual mechanically exfoliated nanosheets are promising, indeed it was mechanical exfoliation that lead to the discovery of the stability of a single layer of graphene and the subsequent excitement about 2D materials, the performance of networks of mechanically exfoliated nanosheets is inferior to their solution processed counterparts. To investigate the reasons for this subpar performance, FIB-SEM nt is used to understand the morphology of mechanically exfoliated networks of molybdenum disulphide ($MoS_2$) in Chapter 7. The model describing the charge transport in nanosheet networks, presented in Chapter 6, is combined with an electrical characterisation technique called electrical impedance spectroscopy (EIS) to calculate the properties of the material and junctions in the network. The temperature dependent electrical properties of both the nanosheets and the junctions in the networks are investigated using this technique. The results obtained are used to suggest possible methods for device optimisation.

Finally, Chapter 8 concludes the main findings of this thesis and provides some suggestions for future research. In particular the techniques presented are combined to demonstrate how they can be used to understand the relationship between the morphological and electrical properties of nanosheet networks. It is hoped that the techniques and results presented in this thesis can be used by future researchers, to optimise the performance of nanosheet networks so that they can fulfil their potential.

*"In truth at first Chaos came to be, but next wide-bosomed Gaia, the ever-sure foundation of all the deathless ones who hold the peaks of snowy Olympus, and dim Tartarus in the depth of the wide-pathed Earth, and Eros, fairest among the deathless gods... And Gaia first bore starry Uranus, equal to herself, to cover her on every side, and to be an ever-sure abiding-place for the blessed gods. And she brought forth long hills, graceful haunts of the goddess Nymphs who dwell amongst the glens of the hills. She bore also the fruitless deep with his raging swell, Pontus, without sweet union of love."*

Hesoid

# 2

# 2D materials: properties and synthesis

The field of nanoscience stretches far back into the past, before the scientific method allowed for understanding of the cause of the unique properties of nanomaterials. Metallic nanoparticles were in use as early as the 14th century B.C. in Egypt and Mesopotamia, to create coloured glass. The use of metallic nanoparticles to colour glass continued through to the medieval ages in Europe.[6] Research into the field of nanoscience began in earnest with the discovery of the Buckminsterfullerene in 1984, a particle made of just 60 carbon atoms, arranged into a ball.[7] This was followed quickly by the discovery of carbon nanotubes (CNT) in 1991,[8] a tube of carbon atoms which can have a diameter as small as 0.3 nm.[9] In 2004, the family of carbon based nanomaterials was completed with the discovery of graphene,[10] a sheet of carbon which is a single layer of atoms thick. The unique properties of this material led to a sudden explosion of interest into the family of materials known as 2D materials.

## 2.1 2D materials

Graphene belongs to a family of materials known as 2D materials. These materials can be formed by the exfoliation of layered materials. Layered materials differ from standard materials due to the large bonding anisotropy in their crystal. Layered materials are held together by strong interatomic bonds in one plane but by far weaker bonds, called van der Waals bonds, perpendicular to this plane. The difference in bonding strength varies from material to material but can reach as high as a factor of 30 in the case of graphene.[11] This large difference in bonding strength means that individual sheets, which can be as thin as a single atom thick, can be isolated from the layered material. When a thin sheet has been

removed from its parent crystal, it is called a 2D material. In this work, a single layer of material is referred to as a monolayer (ML), while exfoliated material that is thicker than a ML is referred to as a nanosheet. ML and nanosheets are interesting to physicists as their 2D nature confines the electrons within the material to a single plane. This confinement leads to a variety of interesting properties.

It has been suggested that over 5000 layered materials could be synthesisable.[12] These materials span the breadth of possible electrical, optical, thermal, and, mechanical properties, meaning the possible applications of 2D materials are almost endless. This chapter briefly introduces the 2D materials used in this work and describes some of the wide variety of different ways in which they can be produced, with a focus on liquid-based synthesis methods.

### 2.1.1 Graphene

Graphite, a layered material, has been used for an array of applications since its first use in the pencil in 1564, ranging from control rods in nuclear reactors to the anode in lithium ion batteries.[13–15] The assortment of uses of graphite has led to a great deal of research into its properties. Investigations into the crystal structure of graphite began shortly after the invention of X-ray crystallography; J.D. Bernal suggested that graphite was composed of layers of carbon atoms, with a hexagonal arrangement of atoms in the plane and AB stacking between the planes in 1924.[16] The electronic properties of graphite was also an area of interest, with P.R. Wallace correctly predicted that a graphene ML would be a semi-metal, with a linear dispersion relation in 1947.[17]

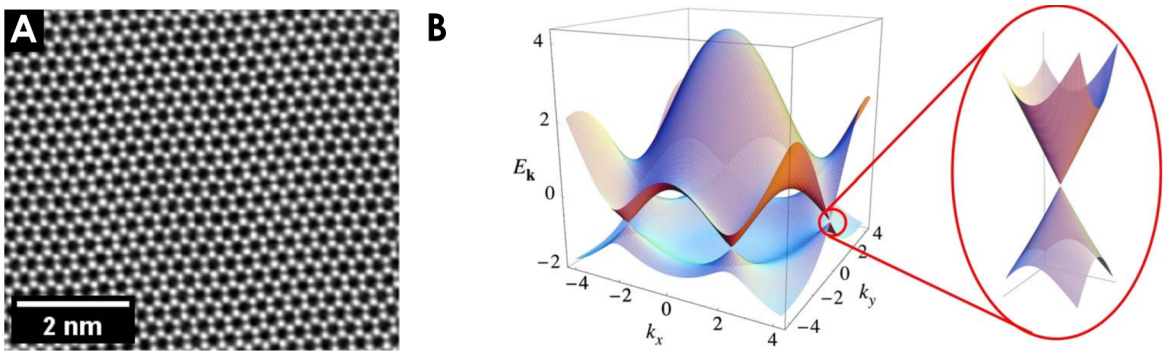



Figure 2.1: **Graphene: A)** Scanning Tunnelling Electron Microscope image of a graphene ML showing the honeycomb arrangement of the carbon atoms. Adapted from ref.[18] **B)** Electronic dispersion of a graphene ML, with the magnified region showing one point at which the band structure shows a linear dispersion relation, the point at which the linear dispersion meets is called the dirac point. Reproduced from ref.[13]

However, before the Nobel prize-winning discovery and electrical characterisation of graphene in 2004,[10] it was believed that an isolated ML of a material would be unstable. It was theorised that a ML could not exist as thermal vibrations would induce large atomic displacements which would cause the disintegration of the material.[19] After the dis-

covery of graphene, it was theorised that the presence of a substrate prevented these large thermal vibrations from tearing the material apart. However, it was shown in 2007 that suspended graphene sheets are, in fact, not perfectly flat but have a corrugated structure, which prevents large atomic displacements and ensures material stability.[20]

The discovery of the graphene ML sparked a great deal of excitement, both because it demonstrated that single layers of material could be removed from a bulk crystal and because of the unique electrical, mechanical, and, chemical properties of graphene MLs. Research into graphene exploded in the years following its discovery, with an assortment of different methods of synthesising graphene MLs and nanosheets developed, and their unique properties extensively characterised.

The atoms within a graphene sheet are arranged in a hexagonal honeycomb lattice, with each carbon atom being bonded to 3 adjacent carbon atoms, a scanning transmission electron microscope image showing the atomic arrangement in a graphene ML can be seen in Fig. 2.1A. Within a graphene ML, the carbon atoms have an $sp^2$ electron arrangement, the 3 $sp^2$ hybridised orbitals form $\sigma$ bonds with adjacent carbon atoms. The remaining p orbital, which is perpendicular to the hybridised orbitals, forms a delocalised $\pi$ bond,[21] this bond gives graphene its unique electrical properties. The $\sigma$ bonds within graphene are very strong (6.1 eV), leading to a very low defect density.[11,22] The in-plane bond length in graphene is 1.42 Å. When combined with the low defect density of graphene, this leads to a graphene ML having a very high impermeability.[23] The high bond strength and low defect density of graphene also leads to it having the highest reported tensile strength and Young's modulus of any material.[24]

The electronic properties of a graphene sheet are dependent on the number of layers present.[23] A graphene ML is a semi-metal, which has a linear dispersion relation at specific wave-vectors. The dispersion relation for graphene can be seen in Fig. 2.1B. The linear dispersion relation means that the charge carriers in a graphene ML are massless fermions. These massless fermions experience ballistic transport under an applied field, meaning that charge carriers travel very quickly through a graphene sheet even when a small potential is applied, this leads to the graphene ML having a very high charge carrier mobility.[13] The mobility in graphene MLs is limited by scattering at defects, edges, and, by interactions between the graphene nanosheet and the substrate, limiting these factors leads to a mobility of over 200,000 $cm^2.V^{-1}.s^{-1}$.[25] However, the linear dispersion limits the number of electrons which can be excited into the conduction band of graphene, meaning that graphene transistors have very low on/off ratios, which limits their applicability.[10]

Graphene nanosheets show layer-dependent electronic properties until they are ~10 layers thick.[26] While a graphene ML is a semi-metal, bulk graphite is a semiconductor with a small band gap (~40 meV).[27] The reported conductivities of graphite are direction dependent, the reported in-plane values vary between 50,000-170,000 $S.m^{-1}$, while the out-of-plane values are considerably lower, with reported values varying between 300-2500 $S.m^{-1}$.[28]

Due to its 2D nature and the low atomic mass of carbon, the graphene ML has a very large gravimetric specific surface area (SSA) of 2630 $m^2.g^{-1}$.[29] The large SSA of the graphene ML makes it an ideal material for applications in sensing, due to the area available for material adsorption. In particular, graphene shows promise in the sensing of gases such as ammonia and hydrogen,[30,31] biological molecules such as glucose[32] and environmental contaminants such as heavy metals.[33]

Since its discovery in 2004, the superlative properties of graphene have led to a great deal of research, with a large variety of interesting physical properties of the material having been discovered. The excellent electrical properties of graphene have made it of interest for printing electronic devices. Chapter 5 and 6 focus on the morphological and electrical properties of devices printed from graphene, respectively.

### 2.1.2 Transition Metal Dichacolgenides (TMD)

While the discovery of graphene by mechanical exfoliation in 2004 sparked a great deal of excitement, a class of materials known as transition metal dichalcogenides (TMDs) had been exfoliated down to a thickness of 2 layers, by the same method, as early as 1963.[34] TMDs are a family of materials with the structure $MX_2$, where M is a transition metal and X is a chalcogen (S, Se or Te). Depending on the combination of metal atom and chalcogen, TMDs can exist as both layered and non-layered materials,[35] the TMDs which show a layered crystal structure are shown in Fig. 2.2A.

TMDs are composed of a hexagonal layer of the transition metal, with an off-set hexangonal lattice of the chalcogen atoms above and below it, forming a ML, which for molybdenum disulphide ($MoS_2$), the most prominent of the TMDs, is 0.65 nm thick,[36] almost twice as thick as a graphene ML which is 0.35 nm.[37] TMDs can exist in several different polytypes, the 1T (trigonal), 2H (hexagonal) and 3R (rhombohedral) phase, here, the number denotes the number of layers in the unit cell and the letter denotes its the crystal structure.[38] In the 1T phase, the ML shows ABC stacking, with the chalcogen atoms shifted relative to each other as well as the metal atom, giving the metal an octahedral coordination as is shown in Fig. 2.2B. In contrast, the layers in the 2H and 3R polytypes show ABA stacking, with the chalcogen atoms stacked directly above each other, leading to trigonal prismatic co-ordination of the metal atom. The stacking of the individual layers to form the unit cell of the crystal structures is shown in Fig. 2.2C. Depending on the constituent atoms, any phase can be the thermodynamically favourable at room temperature and pressure, with the other phases often being metastable.[38] The polytype of a TMD has a large effect on its physical properties: for example, $MoS_2$ is a semiconductor in the 2H phase but transforms to a metal in the 1T phase, leading to a 7 order of magnitude increase in conductivity.[39]

TMDs encompass all possible electronic structures, with insulating ($HfS_2$), semiconducting ($MoS_2$, $WS_2$), semi-metallic ($WTe_2$), and, metallic ($NbS_2$) materials.[42] This wide variety

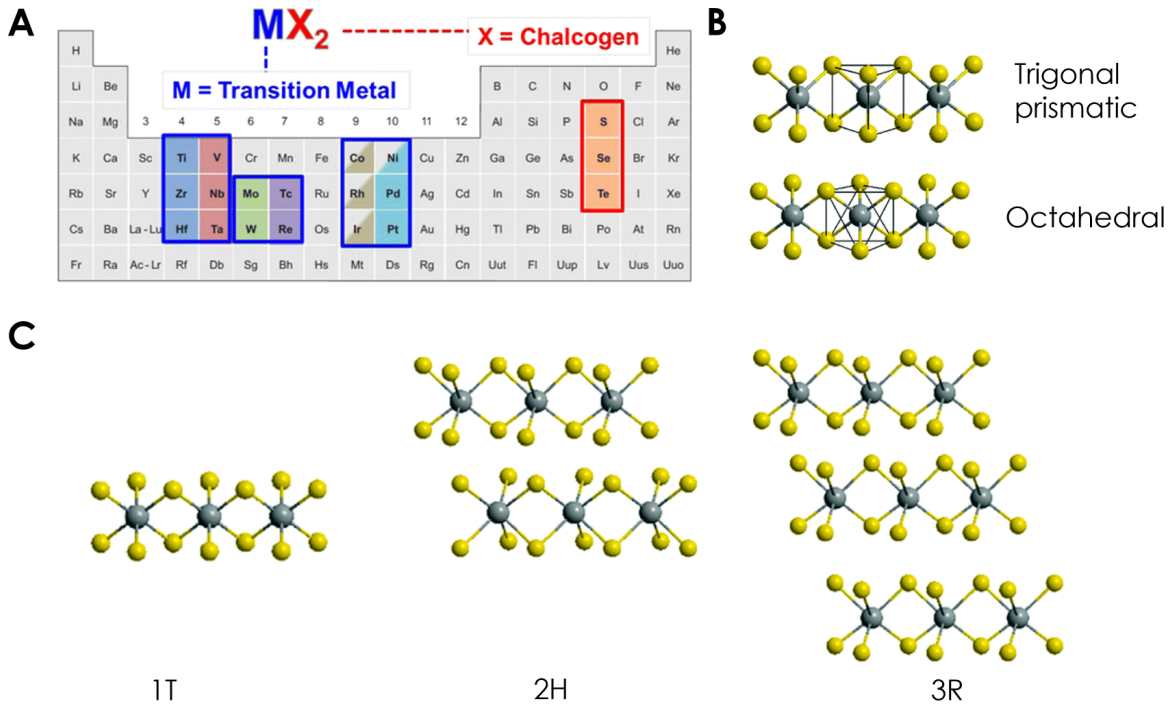



Figure 2.2: **Transition metal dichacogenides: A)** Periodic table with the elements which form layered TMD highlighted. The partially highlighted metal elements form layered TMDs with some chalcogenide elements but not with others. Image reproduced from ref.[40] **B)** Image showing the octahedral and trigonal prismatic co-ordination of a metal atom in a TMD. **C)** Image showing the 3 stacking structures of a TMD. Here the number refers to the number of layers in the unit cell and the letter describes the crystal structure of the unit cell. B and C are adapted from ref.[41]

of electronic properties occurs due to the increasing number of d electrons contributed by the metal atom as you move from left to right across the periodic table. Within a TMD, the transition metal and chalcogen are held together by a strong $\sigma$ bond between the metal's s orbitals and the chalcogen's p orbitals. This creates deep $\sigma$ and $\sigma^*$ bands. The d orbitals of the metal then bond to form bands, the energy of which is between the $\sigma$ and $\sigma^*$ bands. If these bands are partially filled then the TMD is a metal, while if the bands are completely filled it is a semi-metal, a semiconductor or an insulator.[42] As well as the number of d electrons, the energy of the electrons also affects the band structure, for example, tungsten has higher energy d electrons than molybdenum and this leads to a higher energy band structure.[43] The chalcogen atom present also affects the electronic structure, with increasing chalcogen atomic number leading to a decrease in the band gap, for example, the bulk band gap decrease from 1.3 eV to 1.0 eV moving from $MoS_2$ to $MoTe_2$.[44]

The electronic properties of a TMD sheet is also dependent on its layer number. Taking $MoS_2$ as an example, the change in band structure as the layer number decreases can be seen in Fig. 2.3. Calculations suggest the band gap of $MoS_2$ should change from 0.88 eV to 1.71 eV as you go from a bulk crystal to a ML, while experimental values suggest that the ML band gap may be as high as 2.16 eV.[38] The band gap is layer dependent as the out-

of-plane $p_z^*$ orbitals of the sulphur atoms interact with the d-orbitals of the molybdenum atoms, as the thickness of the flake decreases the degree of this interaction reduces.[45] Simultaneously, there is an increase in quantum confinement effects as the layer number decreases.[46] Both of these effects lead to the large change in band gap and a transition from an indirect to direct band gap for the ML.[47]

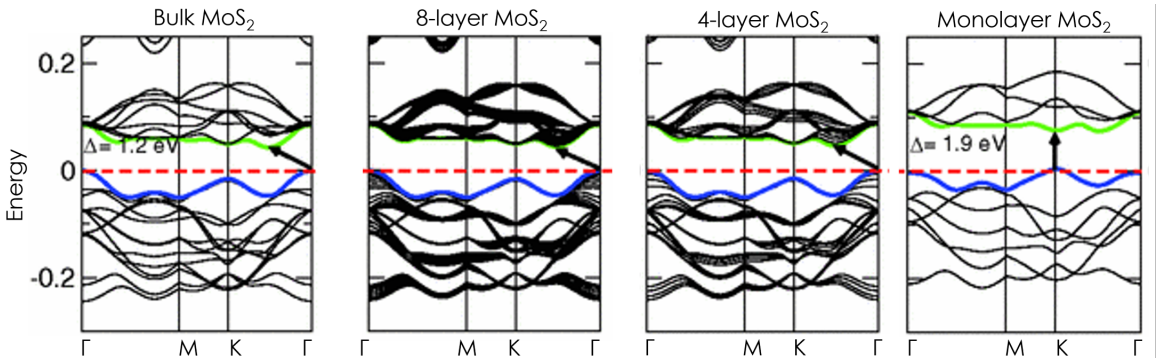



Figure 2.3: **Layer-dependent band structure:** Figure showing the band structure of a bulk, 8-layer, 4-layer and ML $MoS_2$ calculated by DFT. As the thickness of the $MoS_2$ nanosheet is decreased the bandgap of the flake increases. The band gap changes from indirect to direct for ML $MoS_2$. Image adapted from ref.[46]

Defect type and density strongly affect the electronic properties of TMDs. While computational studies suggest that $MoS_2$ should be an ambipolar material, it is generally found experimentally to be an n-type material; this discrepancy is attributed to defects.[48] Within TMDs the most common defects are chalcogen vacancies,[48] anti-site substitution defects (the replacement of an X atom with an M atom),[48] and substitutional defects.[49] In the literature, a wide variety of different defects have been suggested as the cause of the n-type behaviour of $MoS_2$, with the behaviour having recently been ascribed to carbon interstitial defects.[50] Another study suggests that impurities such as ruthenium, which is often found in natural $MoS_2$ crystals, could cause the n-type behaviour.[51] As well as a high defect density, the wide range of metal atoms which form layered TMDs means that substitutional doping can be utilised to control the carrier density and dominant carrier type of TMD flakes.[52,53]

TMDs have a considerably reduced charge carrier mobility compared to graphene, as they do not have a linear dispersion. The mobility of a $MoS_2$ flake varies with nanosheet thickness, for example, a study shows $MoS_2$ nanosheets exhibit a maximum mobility of 70 $cm^2.V^{-1}.s^{-1}$ at ~5 layers, while bulk $MoS_2$ has a mobility of ~20 $cm^2.V^{-1}.s^{-1}$.[54] Due to the effect of nanosheet thickness, the presence of a wide variety of defects and the array of methods for $MoS_2$ production, the reported mobility of $MoS_2$ varies widely in the literature, with the mobility of transistors produced from $MoS_2$ often limited by contact effects.[55] As with graphene the mobility of $MoS_2$ is limited by scattering of charge carriers, measurements of the mobility of $MoS_2$ nanosheets at low temperature have reached values as high as 34,000 $cm^2.V^{-1}.s^{-1}$, but the mobility of the device decreased to 100 $cm^2.V^{-1}.s^{-1}$ at room temperature.[56]

## 2.2 Synthesis of 2D materials

Given the promise of 2D materials for a wide variety of applications, a great deal of research has been done to develop different methods to produce them. In general the synthesis of nanomaterials can be divided into two categories, top-down and bottom-up synthesis. Top-down synthesis involves the breaking apart of a bulk material into a nanomaterial, while bottom-up synthesis involves the growth of the nanomaterial from individual atoms.[57] Both of these techniques have advantages and disadvantages, with the best method for producing a material being context dependent.

The quality of a synthesis method for a 2D material depends on a number of factors. Both the nanosheet area and thickness are important parameters, which affect the electrical properties of the synthesised nanosheet.[23,54] The defect density is another important parameter, as defects affect the electrical properties of the synthesised material. Finally, for the mass production of material a high throughput and yield are required to make the method economically viable. This section will review some of the most prominent methods for nanosheet production, discussing their advantages and disadvantages.

### 2.2.1 Mechanical exfoliation

The simplest method for the exfoliation of a layered material is mechanical exfoliation. This technique has been widely used since it was discovered that it could be used to exfoliate a graphene ML, but was used to create thin nanosheets before this.[10,34] In this method adhesive tape is attached to a crystal of a layered material and then peeled off. This creates tape covered with nanosheets with a wide variety of thicknesses and lengths. If the peeling procedure is repeated several times then the thickness of the nanosheets adhered to the tape will continually decrease, until the tape is covered predominantly in MLs and thin nanosheets. An optical microscope can then be used to identify flakes of interest on the tape and these flakes can then be transferred to a substrate.[58] This procedure is shown in Fig. 2.4A. This method can be used to produce thin, large-area nanosheets, with the electrical quality of the nanosheets being dependent on the quality of the starting material. The main disadvantage of this technique is its low throughput, as it requires finding individual well-exfoliated nanosheets and cannot produce a large area covered by nanosheets, limiting its applicability. However, it is still widely used in research to investigate the physical properties of 2D materials.[59]

Recently Sozen *et al.* have proposed a high throughput method for the mechanical exfoliation of nanosheets, which they dubbed massive parallel mechanical exfoliation (MPME).[5] In this method, powder or crystal of a layered material is adhered to a section of adhesive tape and a roller is used to press the material against another piece of tape, as shown in Fig. 2.4B. This procedure produces tape covered in exfoliated nanosheets which can then be transferred to a substrate by placing the tape on the substrate and annealing it at

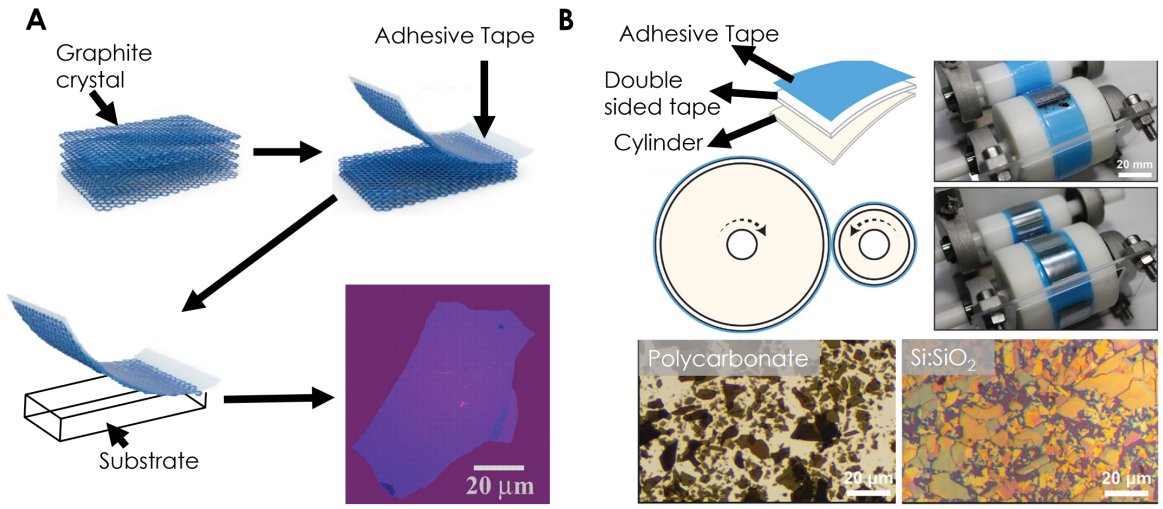



Figure 2.4: **Mechanical Exfoliation: A)** Schematic showing the method of mechanically exfoliating graphene. Adhesive tape is attached to and then removed from a graphite crystal. The adhesive tape is then placed on a substrate leaving graphene nanosheets on the substrate. The final image is an AFM of a mechanically exfoliated graphene nanosheet. Adapted from ref.[10,60] **B)** Image showing the procedure of massive parallel mechanical exfoliation. A roller is used to transfer layered material from one piece of adhesive tape to another. The material can then be transferred to a variety of substrates covering the area with a high density of nanosheets. Adapted from ref.[5]

110°C, this low temperature means this procedure is compatible with flexible substrates. This method produces nanosheets with a large variety of thicknesses and lengths; for $MoS_2$ exfoliated by this method the majority of the nanosheets have thicknesses and lengths between 10-60 nm and 2-8 $\mu$m, respectively. The electrical properties of the devices made by this method require further optimisation, with the mobility of $MoS_2$ transistors produced by this technique generally having values below 1 $cm^2.V^{-1}.s^{-1}$. An investigation into the morphological and electrical properties of $MoS_2$ networks produced by this technique forms the basis for Chapter 7. The MPME samples used in this work were produced by Yigit Sozen from Prof. Andres Castellanos-Gomez group in the Instituto de Ciencia de Materiales de Madrid.

### 2.2.2 Chemical vapour deposition (CVD)

Chemical vapour deposition (CVD) is a method used in a variety of industries for the production of thin films, it can be used to grow a variety of 2D materials. CVD is a bottom-up synthesis method, which allows for a large amount of control over the atomic composition of the synthesised material. There are several different types of CVD but they all share a similar operating principle: a material adsorbs onto a substrate and then decomposes or reacts with another adsorbed species, or the substrate itself, to form a thin layer of the desired material. This process requires the use of high temperatures to produce high quality single crystal nanosheets.[61] CVD is widely used in the semiconductor industry and research into CVD of 2D materials is focused on the production of large area thin films

so the superlative electronic properties of 2D materials can be used in the next generation of computer chips.[62]

A wide variety of 2D materials have been grown by CVD, with a large amount of research being focused on the growth of highly crystalline graphene, hexagonal boron nitride (hBN, an insulator), and $MoS_2$.[61] The first growth of $MoS_2$ by CVD was achieved by the sulphurisation of a thin Mo layer, which yielded a polycrystalline film with grain sizes of less than 30 nm, leading to a low mobility of 0.04 $cm^2.V^{-1}.s^{-1}$.[63] Further research into the field since then has led to the production of highly crystalline, large-area ML films with grain sizes of 10 $\mu$m and mobilities of 30 $cm^2.V^{-1}.s^{-1}$.[64] The growth mechanism of CVD allows for the addition of substitutional dopants into the synthesised material. $MoS_2$ doped with a wide variety of atoms including carbon,[65] ruthenium,[66] and erbium,[67] have been synthesised. This allows for an additional degree of control over the electronic properties of the nanosheets, with the production of p-type 2D material being required for electronic devices.[68]

### 2.2.3 Solution-based-synthesis

Nanosheet formation in a liquid is an ideal method for the scalable production of nanosheets for mass consumer products; it allows for the deposition of the nanosheets by an array of methods to produce a broad range of devices. Solution-based-synthesis can be achieved by both bottom-up and top-down methods. This section focuses on solution-based-synthesis methods relevant to this work.

One solution-based-synthesis method which will not be discussed in detail but should be touched upon is top-down chemical synthesis. In this method nanosheets are produced in a liquid by chemicals reacting with either a layered or non-layered material. Graphene oxide (GO) and a class of materials called MXenes are the most common 2D materials synthesised by this technique. GO is a highly oxidised form of graphene, it is formed by oxidation of graphene by strong acids and oxidisers. Due to its high oxygen content it is stable in water. GO is insulating but can be converted back to a conductive material by reduction to form reduced graphene oxide (rGO).[69] MXenes are a class of 2D materials formed by the etching of ternary carbides, followed by mild sonication, this yields 2D materials with formula $M_{n+1}X_n$, where M is a transition metal, X is carbon or nitrogen and n=1-3. MXenes tend to be highly conductive materials.[70] Both of these materials can be used to form conductive nanosheets networks and will be discussed in Chapter 3.

#### Bottom-up solution-based-synthesis

One method for the production of nanosheets in a liquid is bottom-up solution-based-synthesis, which involves synthesis of the material in a liquid by chemical reactions. Bottom-up synthesis of nanosheets can be divided into 2 categories, the synthesis of naturally layered

materials and the synthesis of non-layered materials with a nanosheet geometry. This section will briefly discuss both of these methods for nanosheet production.

Bottom-up solution-based-synthesis of naturally layered materials has focused primarily on the formation of TMDs, with a wide variety of different methods such as hydrothermal/solvothermal synthesis, hot-injection and calcination having been used.[41] Investigation into the solvothermal synthesis of TMDs began before the discovery of the graphene; however, it yielded small nanosheets with lengths of approximately 100 nm.[71] Hot-injection methods have shown more promise, with nanosheets with aspect ratios (nanosheet length divided by thickness) approaching 75, having been synthesised; however, the nanosheet size is still below 100 nm.[72] Networks produced by spin-coating nanosheets made by this method yield conductivities of ~$1 \times 10^{-6}$ S.m$^{-1}$.[73] While the chemical synthesis of TMDs has been achieved by a wide variety of methods, bottom-up chemical synthesis of other layered materials has proven more difficult with no reports for bottom-up chemical synthesis of a wide range of layered materials including graphene.

One advantage of bottom-up solution-based-synthesis is that it allows for the synthesis of non-layered materials with a nanosheet geometry. Nanosheets of a wide range of metal and metal alloys have been synthesised by this method.[74] The synthesis of metal nanomaterials can be carried out by a variety of methods leading to an array of different geometries from nanoparticles to nanowires to nanosheets.[75] The synthesis of metal nanosheets can be achieved by surfactant/polymer mediated synthesis, template-assisted synthesis, and seed growth, to name just a few.[76] The simplest method is surfactant mediated synthesis, which uses a reducing agent to reduce metal ions and a surfactants to control the direction of the growth of the material and define the 2D geometry of the resulting material. The roles of reducing agent and stabilising agent can often be combined, for example, starch can be used to reduce silver nitrate, control the growth of the reduced silver into nanosheets and stabilise the silver nanosheets (AgNSs) in water.[77] Silver nanomaterials have excellent antimicrobial properties and AgNSs are being investigated for a wide variety of biomedical applications, including in the treatment of burn victims.[78] Additionally, they can also printed into highly conductive traces.[79,80] The morphology of networks printed from silver nanosheets will be explored in Chapter 5.

### Liquid-phase exfoliation (LPE)

The simplest top-down method for the production of nanosheets is liquid-phase exfoliation (LPE). LPE describes a range of different techniques which utilise the agitation of a liquid containing powder of a layered material, to exfoliate it. LPE is a cost effective and scalable method for the production of nanosheets, which produces a dispersion of nanosheets with a range of lengths and thicknesses.[81] In Chapter 5 and 6 the morphological and electrical properties of size selected networks of graphene and $WS_2$ nanosheets, produced by LPE are discussed. This section discusses the mechanism of the production of nanosheets by LPE

and their properties.

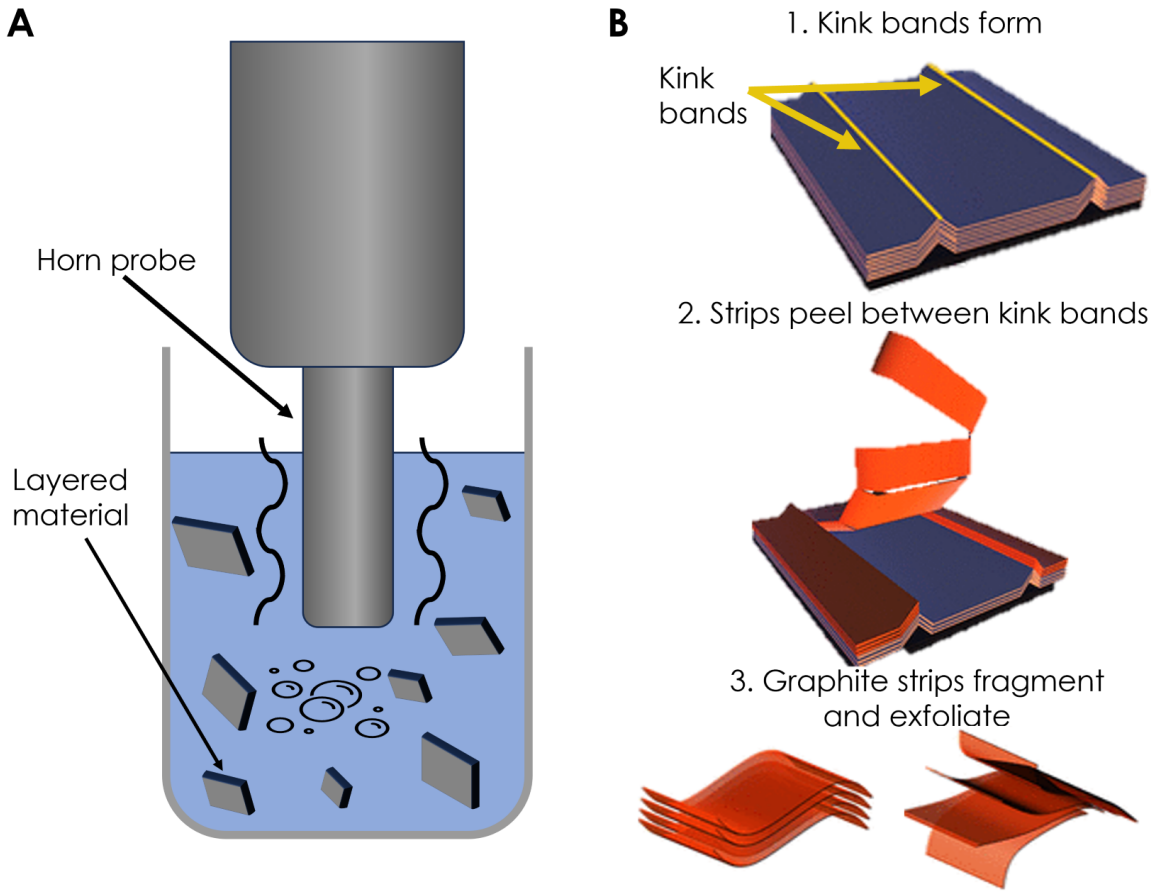



Figure 2.5: **Liquid phase exfoliation: A)** Schematic of the exfoliation of a layered material by horn probe sonication. Adapted from ref.[82] **B)** Schematic showing the mechanism of the exfoliation of graphene by LPE. Adapted from ref.[83]

LPE exfoliates a layered material by exposing it to large amounts of energy within a liquid. There is an array of different methods by which this energy can be created, the most commonly used is sonic energy. The process of using sonic energy to drive changes within a liquid is called ultrasonication. Sonic energy can be introduced into a liquid using a variety of techniques, this work utilises horn probe sonication, in which a probe vibrating in the liquid produces the sonic energy, this method allows large amounts of energy to be introduced.[84] The process of using a horn probe for LPE is shown in Fig. 2.5A.

Layered materials are exfoliated by ultrasonication due to the bursting of cavitation bubbles near the material. These bubbles burst near the powder of the layered material, causing large localised pressures of ~20 MPa and local temperatures of up to 5000 K, this pressure causes in-plane compression of the material, which leads to its exfoliation.[85] Li *et al.* suggest that the exfoliation of graphene by ultrasonication can be broken down into three stages, shown in Fig. 2.5B. In the first stage, large pieces of graphite crystal are fragmented along the zigzag direction. This occurs as the sonic waves travelling through the crystal cause local twinning to occur, which leads to kink band formation within the crystal, breaking it apart. The formation of the kink bands is a highly energetic process, causing the oxygenation of

the graphite crystal along the kink bands. In the second step strips of graphite are then peeled from the graphite crystal between kink bands, this leads to oxygen being present on the edge of graphene nanosheets exfoliated by LPE. In the final step the size of the exfoliated nanosheets is further reduced by fragmentation and exfoliation of the graphite strips into graphene nanosheets.[83]

In the final step of the exfoliation process the nanosheets undergo both fragmentation and peeling. The ratio of peeling to fragmentation that occurs determines the aspect ratio of the resulting nanosheets. It has been demonstrated that the aspect ratio of the nanosheets ($k_{NS}$) produced by LPE is given by the equation:

$$k_{NS} \approx 2a\frac{Y_{In-plane}}{Y_{Out-of-plane}}\langle N\rangle^{b-1} \tag{2.1}$$

where $Y_{In-plane}$ and $Y_{Out-of-plane}$ are the in-plane and out-of-plane Young's modulus of the material being exfoliated, respectively, $a$ is constant which describes if peeling or fragmentation is more likely, $\langle N\rangle$ is the average nanosheet layer number and $b$ is a constant which is close to 1, a derivation of this equation can be found in appendix A.1.1. Fits to experimental data yields a $\approx 1$, meaning that the energy that a nanosheet experiences during ultrasonication is equally distributed between peeling and fragmentation.[86] As the elastic moduli are material constants, the possible aspect ratio of nanosheets produced from a material by LPE are limited. The aspect ratio given by Eqn. 2.1 is the maximum that can be achieved for a given material, in non-ideal conditions aspect ratios below this value are achieved.[86] The maximum aspect ratio for a material such as graphene is ~100, well below the value obtained by most other methods for the production of 2D materials.[86] The constant aspect ratio of LPE nanosheets limits there applicability as for printed electronic devices high aspect ratio nanosheets are preferable.[82]

Ultrasonication is a very versatile technique that can be used to produce nanosheets from all naturally layered materials and, if carried out in inert conditions, it can be used to produce nanosheets which are prone to oxidation.[87] As well as the production of nanosheets from layered materials LPE can also be used to produce nanosheets from non-layered materials. The large amount of sonic energy that materials experience during ultrasonication causes their fragmentation, if this occurs for a material with stronger bonds in 2 directions than in a third it leads to the formation of nanosheets.[88] Here, the aspect ratio of the nanosheets is quite low as the presence of covalent bonds in all directions leads to low values for $Y_{In-plane}/Y_{Out-of-plane}$. Interestingly, there are reports of sonication leading to nanosheets for materials with isotropic bonds,[89] with some materials such as boron showing high aspect ratios,[90] the mechanism by which this occurs has recently been uncovered but is beyond the scope of this work.[91] The ability to exfoliate non-layered materials means the range of materials that can be produced as nanosheets by LPE is incredibly vast.

LPE can be carried out by a variety of easily scaled methods such as shear mixing,[92] high

pressure homogenisation[93] and ball milling.[94] Furthermore, methods such as shear mixing can be adapted to make them cyclable, meaning that a yield of 100% exfoliated material can be achieved.[95] The excellent scability and yield of LPE makes it ideal for the production of nanaosheets for cheap consumer devices.

### Electrochemical exfoliation (EE)

Electrochemical exfoliation (EE) is a top-down method for the production of nanosheets within a liquid. It has been gaining prominence in recent years due to its ability to produce nanosheets with higher aspect ratios than LPE. EE may be the first method used for the production of a ML of a layered material, with reports of a $MoS_2$ ML having been exfoliated by EE as early as 1986.[96] However, investigation into EE nanosheets did not gain prominence until the discovery of the graphene ML and the explosion of interest into 2D materials. EE uses the intercalation of ions into a layered material to reduce its out-of-plane bonding strength, allowing for the exfoliation of high aspect ratio nanosheets.[82]

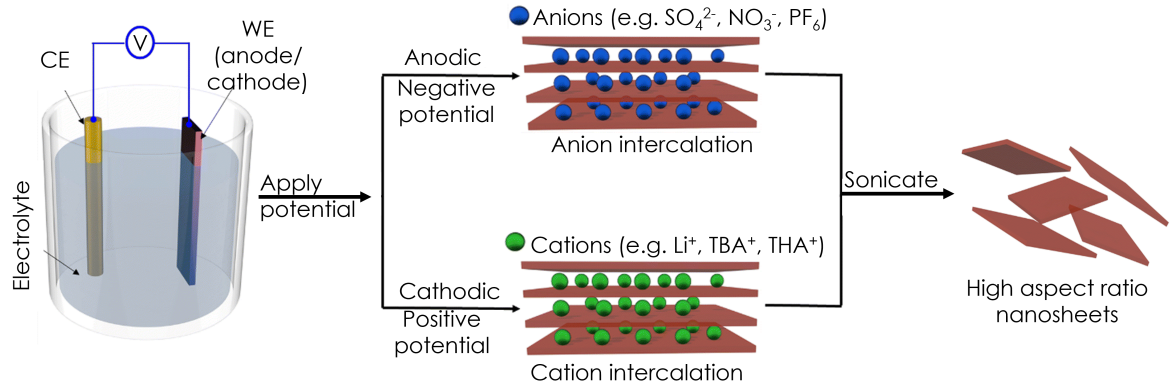



Figure 2.6: **Electrochemical exfoliation:** Schematic explaining the process of EE. First a layered material is placed in a solution of electrolyte. A potential is applied between the layered material and a counter electrode, causing ions to intercalate into the material. The layered material is then sonicated to produce high aspect ratio nanosheets. Image adapted from ref.[97]

The process of EE is shown in Fig. 2.6, it is a more complex process than LPE. First, ions are intercalated between the layers of a material by applying a bias to a crystal or foil of a layered material in an ionic solution. Here the layered material can be the anode, the cathode or both depending on the ion used for the intercalation.[98] The choice of ion can affect the electrical properties of the resulting nanosheets, for example, the intercalation of lithium ions into $MoS_2$ induces a phase change from the 2H to the 1T phase,[99] changing the material from semiconducting to metallic. However, intercalating bulky organic ions such as tetrabutylammonium does not induce a phase change in $MoS_2$ nanosheets.[100] The intercalation of ions into a layered material causes it to expand and break apart. The expanded material is then collected and sonicated. A lower sonic energy is required than for LPE as the expansion of the material weakens the out-of-plane van der Waals bonds meaning less energy is required to exfoliate the nanosheets.

EE has a number of disadvantages when compared to LPE, firstly, it requires a conductive crystal to allow the intercalation of ions, which limits this method of exfoliation to conductive and semiconductive materials.[101] For crystals of semiconducting materials to be conductive they generally require large crystal sizes, which means that to use powder of layered materials high temperature annealing steps (1100°C for $MoS_2$) are generally required to increase the crystallite size.[102] This leads to the starting materials of EE being more expensive the LPE. Recent improvements in electrode design have demonstrated that EE can be carried out on TMD powders, however, the aspect ratio of the nanosheets obtained from this method are lower than EE of crystalline material.[103] Furthermore, the intercalation of ions into layered materials can induce damage. EE of graphene causes the raman D to G peak ratio, a measure of the number of defects, to increase from 0.1 for the starting material, to 0.21 for the exfoliated nanosheets.[104] Despite these limitations there has been a large increase in the number of devices produced from EE nanosheets in recent years, as the large aspect ratio of the nanosheets allows for the formation of electronic devices with superior performance to devices produced from LPE nanosheets.[82,100,101,105–110]

## 2.3 Nanosheet Stabilisation

When synthesising nanosheets in a liquid, it is important to ensure that the nanosheets are stable in the liquid. Nanosheets will naturally tend to aggregate as having exposed surfaces is energetically unfavourable. Stabilisation is particularly important for nanosheets produced by LPE, where solvent-nanosheets interactions reduce the energy required for exfoliation and thus increase yield.[57] Nanosheets can be stabilised in a liquid by several methods, a suitable solvent can be used; alternatively, a surfactant or a polymer which interacts with both the nanosheet and the solvent can be chosen. This section discusses the stabilisation of nanosheets in a liquid by both solvents and surfactants.

### 2.3.1 Solvent Stabilisation

The simplest method for stabilising nanosheets in a liquid is to choose a solvent which minimises nanosheet reaggreagation. This can be achieved by having the interaction between the nanosheets and the solvent be similar to the interaction between the exfoliated nanosheets, thus reducing the energy gain of nanosheet reaggregation.[111] The simplest way to understand what solvents achieve this is to assume that the surface tension of the solvent should be similar to the surface energy of the material ($\approx$ 40 mJ.m$^{-2}$ for graphite).[81] The relationship between graphene concentration in a solvent, after exfoliation by LPE and the solvent's surface tension is shown in Fig. 2.7A. While this model describes the dispersal of graphene in high boiling point organic solvents it fails to explain the relative stability of graphene in other solvents with high surface tensions.[111]

A more complete description of the dispersability of graphene in different solvents was

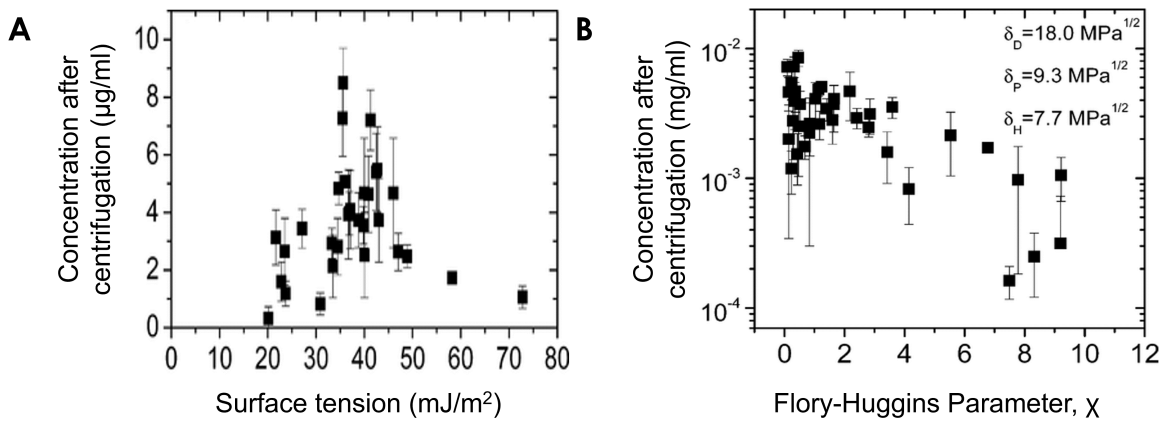



Figure 2.7: **Solvent stabilisation: A** Concentration after centrifugation of graphene exfoliated, by LPE, in different solvents, plotted as a function of solvent surface tension. **B** Concentration after centrifugation of graphene exfoliated, by LPE, in different solvents, plotted as a function of the solvents Flory-Huggins parameter. Adapted from ref.[111]

suggested by Hernandez *et al.*, they model the dispersability of nanosheets in a solvent by considering the cohesive energy density ($E_{C,T}/V$ ), which describes the amount of energy required to completely remove molecules from a material.[111] The square root of the cohesive energy density is called the Hildebrand solubility parameter ($\delta_T$) and is given by

$$\delta_T^2 = \delta_D^2 + \delta_P^2 + \delta_H^2 \tag{2.2}$$

where the subscript D, P, and H correspond to the dispersive, polar and hydrogen inter-molecular forces, respectively. The dispersability of polymers in a solvent has been described using Flory-Huggins theory, which suggests that the Flory-Huggins parameter ($\chi$) can be used to model the dispersability of a polymer.

$$\chi = \frac{v_0}{k_B T}\left[(\delta_{D,A} - \delta_{D,B})^2 + (\delta_{P,A} - \delta_{P,B})^2 + (\delta_{H,A} - \delta_{H,B})^2\right] \tag{2.3}$$

Where the subscript A and B correspond to the solvent and the polymer, respectively, $v_0$ is the solvent molecular volume, $k_B$ is Boltzman's constant and $T$ is temperature. Here a low value of $\chi$ suggests that the energetics of the interaction have been minimised and the polymer will be well dispersed in the solvent. This model can also be applied to the dispersion of 2D materials in a solvent,[111] graphene concentration as a function of $\chi$ in a variety of solvents is shown in Fig. 2.7B, demonstrating that minimising $\chi$ allows for the formation of more stable graphene dispersions.

Notably, the solvents which show high graphene dispersability tend to be high boiling point and toxic solvents such as N-methyl-2-pyrrolidone (NMP) and dimethylformamide (DMF).[112] For the mass production of solution processed nanosheets a more environmentally friendly solvent would be preferable. One solvent which has been suggested as an alternative to NMP and DMF is cyrene, which is a non-toxic, biobased solvent.[113] Cyrene is a good solvent for the exfoliation of graphene, with dispersions stable at concentrations of 10

mg.ml$^{-1}$.[112] Cyrene has also been demonstrated as a suitable solvent for the exfoliation of TMDs.[114] Cyrene, however, is a high boiling point solvent which makes it unsuitable for nanosheet deposition by a variety of techniques, meaning that exchanging the material into a low boiling point solvent is required before material deposition.[115]

The use of environmentally friendly low boiling point solvents for the exfoliation of graphene nanosheets has been investigated, although no single solvent has proven promising. To solve this problem, investigations have focused on co-solvent blends with water:ethanol mixtures being the most promising. Graphene has been found to be most stable in a 70:30 ethanol:water mixture, although the stability is still considerably reduced when compared with NMP, DMF and cyrene.[116] Irish whiskey, a water:ethanol mixture containing a range of additional organic molecules has been shown to be superior to water:ethanol mixtures, yielding a two-order of magnitude increase in graphene stability when compared to a standard water:ethanol mixture.[117] This demonstrates the wide range of solvents which can be used to create stable dispersions of nanosheets and that the presence of additional organic molecules can improve nanosheet stability.

While no single low boiling point, environmentally friendly solvent has been reported for the stabilisation of graphene, it has been reported that TMDs can be exfoliated in isopropanol (IPA), a low boiling point organic solvent. IPA has been used in the exfoliation of $WS_2$ nanosheets by LPE, and while using this solvent leads to a reduction in the aspect ratio of the nanosheets obtained, it removes the requirement for processing the exfoliated material before deposition.[118] In Chapter 5 and 6 the morphological and electrical properties of networks of $WS_2$ nanosheets exfoliated in IPA are investigated.

### 2.3.2 Surfactant Stabilisation

While few low boiling points solvents are suitable to produce high aspect ratio nanosheets on their own, nanosheets can be stabilised in environmentally friendly solvents through the addition of surfactants. This method allows for the stabilisation of nanosheets in water and is therefore, an environmentally friendly method for nanosheet stabilisation. A surfactant is an amphiphilic organic molecule, which can be anionic, cationic, zwitterionic or non-ionic; they have a hydrophobic tail and a hydrophilic head.[119] The hydrophobic tail of the molecule can adsorb to the surface of a nanosheet by van der Waals forces, while the hydrophilic head stabilises the nanosheets in water.[57] Nanosheet aggregation is then prevented by either steric or electrostatic repulsion of adjacent nanosheets.

In this work ionic surfactants are used. These surfactants stabilise the nanosheets by the formation of an electric double layer (EDL) at the nanosheet surface. The adsorption of an ionic surfactant onto the surface of a nanosheet is shown in Fig. 2.8A. The hydrophobic tail adsorbs onto the nanosheet, while the charged hydrophilic head interacts with the solvent. The arrangement of charged head groups around the nanosheet leads to an apparent charge

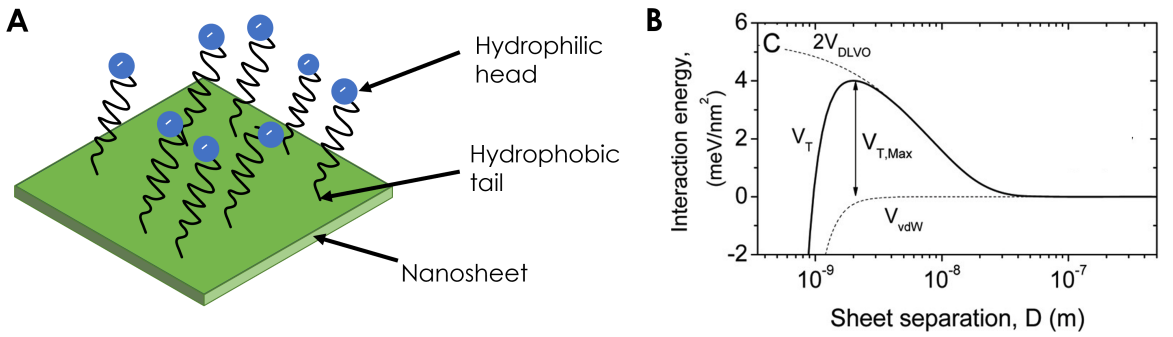



Figure 2.8: **Surfactant stabilisation: A)** Image showing the adsorption of an anionic surfactant onto the surface of a nanosheet. The hydrophobic tail bonds with the nanosheet while the charged hydrophobic head stabilises the nanosheet in the solvent. **B)** Graph of the interaction energy of 2 nanosheets stabilised by surfactant as a function of nanosheet separation. Reproduced from ref.[120]

on the nanosheet at close range. When two nanosheets approach each other, the apparent charges on the nanosheets leads to them repelling each other. The forces involved in this interaction are described by DLVO theory, named after the 4 physicists who did the pioneering work in this field, Boris Derjaguin, Lev Landau, Evert Verwey and Theodoor Overbeek.[121,122] Using DLVO theory to model the repulsive forces between the nanosheets, and Hamaker theory to model the attractive forces the potential energy of the interaction between 2 nanosheets can be expressed as

$$V \approx 4A_{NS}\epsilon\kappa\zeta^2 e^{-kx} - \frac{A_{NS}\pi\rho^2 C}{2x^4} \tag{2.4}$$

where $A_{NS}$ is the nanosheet area, $\zeta$ is the zeta potential, $\epsilon$ is the permittivity of the solvent, $\kappa^{-1}$ is the Debye screening length, which is related to the thickness of the EDL, $\rho$ is the number of atoms per unit area, $C$ is a constant relating the interatomic van der Waals forces to the interatomic separation and $x$ is the distance between the interacting nanosheets.[120] Fig. 2.8B shows the interaction energy as a function of nanosheet separation. The zeta potential is key for forming stable dispersions. For nanosheet dispersions it has been shown that increasing the zeta potential leads to an increase in stability.[123] The concentration of surfactant is also important for the stability of nanosheet dispersions, with the stability as a function of concentration showing a peak at a value of ~2 mg.ml$^{-1}$.[124] In Chapter 5 and 6 graphene nanosheets are produced by sonication of graphite powder in water, with sodium cholate, an ionic surfactant, to stabilise the resulting dispersion.

## 2.4 Control of material size

Solution-based-synthesis methods produce dispersions of nanosheets which are polydisperse with respect to nanosheet length and thickness.These parameters affect the performance of nanosheet devices for a wide variety of applications from catalysts[125] to conductive traces,[126] therefore, control over nanosheet dimensions is important for optimising device performance.

A number of techniques have been developed to size-selected nanosheets in a dispersion. This section discusses some common methods for nanosheet size-selection.

Density gradient ultracentrifugation (DGU) is a commonly used method for separating different size of nanomaterials. DGU uses differences in the buoyancy of materials to separate them in a medium which has an internal density gradient. Here, centrifuging a mixture of two miscible solvents causes the solvents to separate creating a density gradient; the dispersed material will then move to it's isopycnic point, which is the point where its buoyant density is the same as the surrounding media.[127] This method has been successfully used to separate CNTs, whose buoyant density is related to the nanotube's (NT) diameter.[128] The application of this technique to nanosheets comes with complications, a nanosheets buoyant density is independent of its dimensions. However, larger nanosheets have more surface area, this means they can adsorb more polymer or surfactant, which induces a difference in buoyant density.[129] This mechanism limits DGU to nanosheets stabilised by polymers or surfactants,[57] therefore, a technique which can be size-select nanosheets without additives is required.

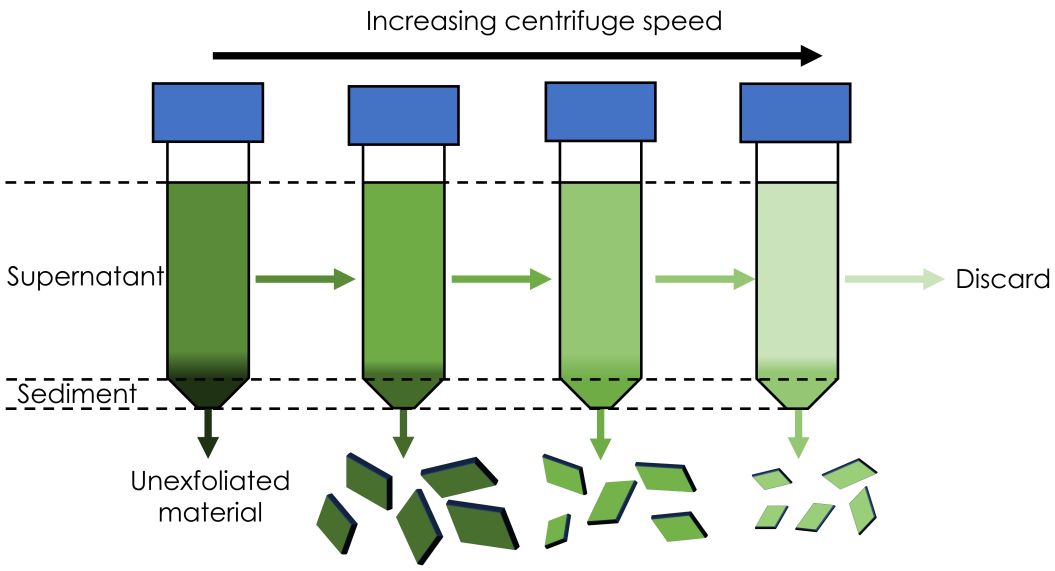



Figure 2.9: **Liquid cascade centrifugation (LCC):** Schematic showing the procedure of LCC, an exfoliated 2D material is centrifuged at a low speed, the sediment is discarded and the supernatant is centrifuged at higher speed. The supernatant is then removed and the sediment is redispersed in a given solvent This process can be repeated several times to produce nanosheets with decreasing length as the centrifuge speed is increased. The final supernatant of the process can then be discarded as it contains very small particles.

Liquid cascade centrifugation (LCC) is a method for size-selecting nanosheets which uses a series of centrifugation steps to sediment different size nanosheets, this process is called sedimentation-based separation.[57] The process of LCC is shown in Fig. 2.9. A polydiserse dispersion of nanosheets is taken and centrifuged at a low speed, this causes large nanosheets to sediment and can be used to remove unexfoliated material from a dispersion. The supernatant is removed and centrifuged at a higher speed, which leads smaller nanosheets to sediment, while the supernatant contains even smaller nanosheets. This process can be

repeated a number of times to produce sediments composed of nanosheets with decreasing size.[130] The sediments can then be redispersed in a solvent. The relationship between the size of nanosheets produced by LCC and the applied relative centrifugal force (RCF) has been derived by Ogilvie *et al.*[131] they demonstrate that the average volume of the nanosheets, $V_{NS}$, is given by

$$V_{NS} = \left( \frac{\pi \eta h}{10(\rho_{2D} - \rho_l) R g t} \right)^{\frac{3}{2}} \tag{2.5}$$

where $\eta$ is the solvent viscosity, $h$ is the height of the liquid in the centrifuge tube, $\rho_{2D}$ and $\rho_l$ are the density of the 2D material and the liquid respectively, $t$ is the time the dispersion is centrifuged for, $g$ is acceleration due to gravity, and $R$ is the RCF.[131] $V_{NS}$ can be calculated by AFM, which is discussed in detail in Chapter 4.1.1. The value of $V_{NS}$ is still polydisperse after the size selection process; however, the width of the distribution is reduced.[132] The derivation of this equation models nanosheets as spheres; however, it appears to describe experimental data well and can be used to approximate the volume of a nanosheet produced by LCC.[131]

LCC has numerous advantages when compared with DGU. The first is ease of use, as this technique involves the sedimentation of material it is easier to separate the different sizes. Secondly, as the volume of nanosheets produced by LCC depends on the time and relative $g$ force it can be used with all nanosheet stabilisation methods. Furthermore, as LCC involves the sedimentation of nanosheets it allows for the redispersal of the nanosheets in a different solvent from the one they were exfoliated in, which is important for the deposition of nanosheets which have been exfoliated in high boiling point solvents. It can also be used to remove stabilisers from exfoliated nanosheets, which is important for the production of electronic devices from nanosheets.[82,133] In Chapter 5 and 6 LCC is used to control the size of the nanosheets produced.

The main disadvantage of LCC is that it is a labour and energy intensive process. For commercial applications of solution-processed nanosheets a more energy-efficient method would be preferable. More scalable and energy efficient size-selection methods such as cross flow filtration have been suggested for size-selecting nanosheets; however, this method has not demonstrated the ability to separate nanosheets of an arbitrary size or the ability to size-select EE nanosheets.[134]

*" The world began as a watery chaos called Nun, from which the sun-god Atum emerged on a mound. By his own power he engendered the twin deities Shu (air) and Tefnut (moisture), who in turn bore Geb (earth) and Nut (sky). Geb and Nut finally produced Osiris, Isis, Seth and Nephthys."*

Jeff Hays

# 3

# Nanosheet networks: deposition, and electrical & morphological characteristics

The formation of devices from solution-processed nanosheets requires depositing the material onto a substrate to form a network, with many devices requiring different materials to be stacked on top of each other. The deposition of nanosheets can be achieved by a wide variety of techniques to form an array of devices including sensors, thermoelectrics, batteries, catalysts, and electronic devices, which are the focus of this work.[135–138] This chapter discusses methods for the deposition of nanomaterials, the electronic properties of materials and then reviews the literature on the electrical and morphological properties of nanosheet networks.

## 3.1 Depositing nanosheets

Once dispersed in a liquid, a nanosheet can be deposited using a plethora of techniques to form a wide range of electronic devices including transistors, capacitors, and memristors.[138–140] When comparing deposition techniques, there are several important parameters which have to be considered: the resolution, deposition rate, and scalability of the technique are all key parameters for the applicability of the technique to produce mass consumer products. This section discusses the deposition techniques used in this work, focusing on their advantages and disadvantages for the production of electronic devices.

### 3.1.1 Spray-coating

One simple and scalable method for the deposition of nanosheets is spray-coating, it was developed as a technique late in the 19th century.[141] It uses the flow of a gas to produce droplets of a liquid and carry them to the desired location. This technique is widely used in industry and in everyday life, for the deposition of a variety of materials, from cosmetics and paint to polymers. One of the main advantages of spray-coating is its versatility, it can be used to deposit a wide range of materials dispersed in a variety of solvents, without the limitations on the ink properties required by other deposition techniques such as inkjet printing (IJP).[142] It is also not limited to printing on planar substrates, but is capable of printing on 3D objects.[143] For these reasons spray-coating has been used to produce devices from a wide variety of different nanomaterials including nanoparticles, CNTs, silver nanowires (AgNW), and a variety of nanosheets.[57,144–146]

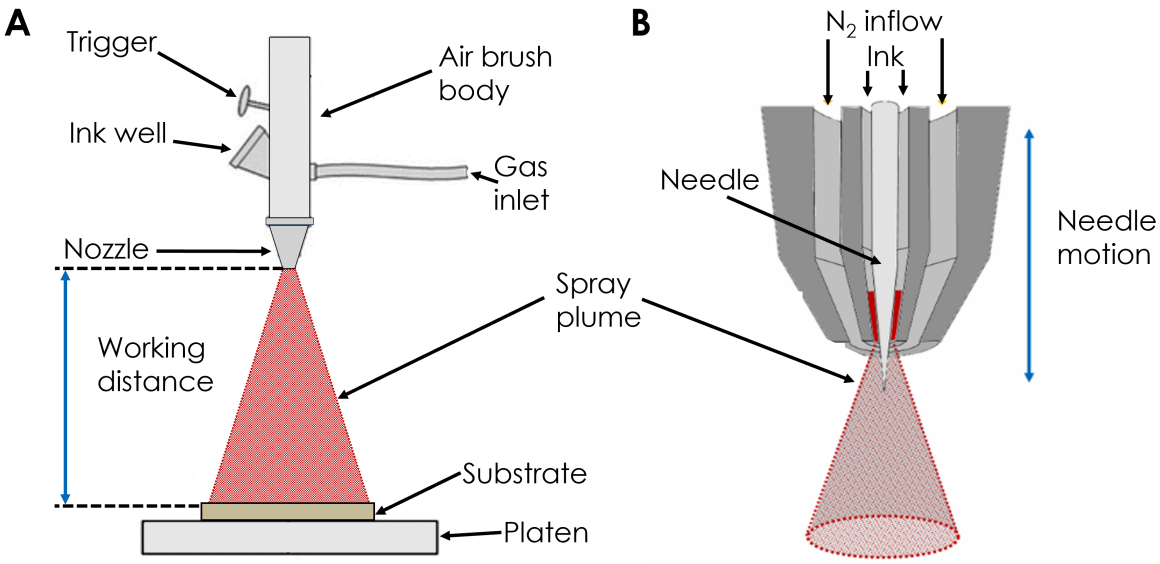



Figure 3.1: **Spray-coater: A)** Schematic showing the operation of a spray-coater. Adapted from ref.[147] **B)** Magnified schematic showing the operation of the nozzle of a spray-coater. Adapted from ref.[148]

The operating principle of a spray-coater is shown in Fig. 3.1. Spray-coating is carried out with an airbrush, the airbrush body is composed of two chambers, one chamber contains the ink and the other contains compressed nitrogen. The constant flow of ink and nitrogen from the nozzle is prevented by a needle, when the trigger is pressed it causes the needle to rise, this allows the nitrogen to flow, which shears the ink into droplets and carries the droplets towards the substrate. The shearing of the ink by the nitrogen produces droplets which are tens of microns in size.[149] The ink flow rate is controlled by the amount the needle is lifted. The substrate is generally heated to encourage rapid droplet evaporation. A movable gantry can be used to move the spray-coater over an area, however, spray-coating is not a high resolution technique and the use of shadow masks is required to define the shape of deposited features.

Despite the relatively simple operating principle of this technique there is a rich parameter space for optimisation. The working distance (distance of the nozzle from the substrate), scan speed (how quickly the spray-coater moves over the area it is depositing on), ink flow rate, substrate temperature, and nitrogen pressure, all affect the quality of the deposit produced. The ink flow rate and substrate temperature are important parameters to prevent droplet coalescence, which can lead to coffee ring effects, causing non-uniform deposits.[150] The working distance controls the area over which the device is deposited and so affects the thickness of the deposit and the material wastage. The nitrogen pressure has been found to be the most important parameter for the performance of spray-coated AgNW transparent conductors.[146] The pressure of a gas used to shear a liquid controls the size and uniformity of droplets produced, with higher pressures producing smaller, more uniform droplets, preventing droplet coalescence, leading to a more uniform deposit.[146,149]

While spray-coating is a very versatile technique for depositing materials, which boasts the advantages of low cost and excellent scalability, it has disadvantages for depositing electronic devices. Its main disadvantage is that it cannot deposit high resolution features without the use of a shadow mask. Furthermore, the use of shadow masks to deposit high-resolution features leads to a large amount of material wastage, which increases the cost of produced devices. Therefore, a technique which is capable of printing high resolution features, with low material wastage is important for the formation of complex devices.[151]

### 3.1.2 Aerosol Jet Printing (AJP)

Aerosol Jet Printing (AJP) is a technique that has been growing in prominence in recent years due to its ability to print high-resolution traces.[152] AJP uses sonic energy to create droplets from an ink, which are then focused onto a substrate by a gas flow. By this method, feature sizes as low as 10 $\mu$m can be produced.[153] AJP is capable of printing both on planar and non-planar objects and it can be used to print both 2D and 3D structures.[154] AJP offers advantages in ink design over other high resolution printing techniques such as IJP which requires inks with viscosity in a narrow range of 10-40 cP, while AJP can print with ink viscosities in the range 1-1000 cP.[155] These advantages have led to fully AJP transistors.[156]

A schematic of an aerosol jet printer is shown in Fig. 3.2. To generate the aerosolised ink, the ink is sonicated with MHz frequency, this sonication generates capillary waves on the surface of the ink, at the peaks of the waves droplets are sheared from the liquid. These droplets are generally between 2-5 $\mu$m in size.[157] The droplets are then carried away from the ink and towards the printing head by the carrier gas. At the deposition head the aerosol is focused through the use of a sheath gas. It is then deposited on a substrate, which is generally heated to encourage ink evaporation.

The quality of the deposit produced by AJP is dependent on several parameters, including

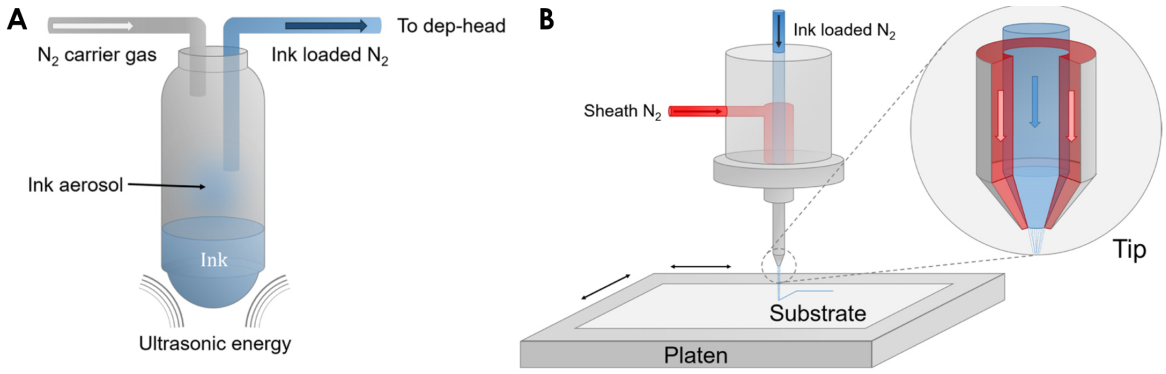



Figure 3.2: **Aerosol jet printing: A)** Schematic of the ink vial showing the formation of of the aerosol in an aerosol jet printer. **B)** Schematic showing the printer head, in an aerosol jet printer, with a magnified image of the deposition head, showing the focusing of the aerosol by the sheath gas. Image reproduced from ref.[155]

the carrier gas pressure, sheath gas pressure, and substrate temperature. The carrier gas pressure controls the amount of material carried to the substrate, while the sheath gas pressure affects the deposited line width. As with spray-coating, the substrate temperature is important for preventing droplet coalescence. The most important parameter affecting the resolution of the printed trace is the focusing ratio, which is the ratio of the carrier gas pressure to the sheath gas pressure, with an optimum value of 2.[158] Research into AJP is still in its early stages, with more research likely to yield further improvements in printed trace quality. In this work, AJP is used to deposit silver nanoparticles (AgNP) onto the surface of graphene networks. The AJP devices presented in this work were printed by Dr. Cian Gabbett.

## 3.2 Electrical devices & their characterisation

Understanding the electrical properties of materials is of vital importance for developing efficient and effective electronic devices. For nanosheet networks to become components of printed electronic devices, the electrical properties of the individual nanosheets and the network they create needs to be understood. This section serves as an introduction to the electrical properties of materials, with a focus on the properties important for printed devices and the techniques used to characterise these properties in this work.

### 3.2.1 Electrical conductivity & device resistance

Electrical conductivity is an important material parameter, which describes the ease with which current can flow through a material. Traditional materials can be divided into 3 categories, materials with high conductivities are called conductors, this includes metals and semi-metals such as graphene. These materials can be used as wires in electronic devices as they allow for the transmission of current with minimal power loss. For printed devices networks with conductivities greater than $10^4$ S.m$^{-1}$ are required.[138] Materials

with very low conductivities are called insulators, insulators are not the focus of this work, but will be discussed where relevant. Finally, materials which have conductivities between conductors and insulators are called semiconductors, these materials can be used for a wide variety of applications from photodetectors to transistors.

Conductivity ($\sigma$) is an intrinsic material property which can be expressed as

$$\sigma = n\mu e \tag{3.1}$$

where $n$ is the number of charge carriers, these can be electrons, holes, or both, $\mu$ is the mobility of the charge carriers, and $e$ is the charge of an electron.[159] Both $n$ and $\mu$ are intrinsic material properties. The conductivity of a material can also be expressed in terms of its resistance in a specific geometry as

$$\sigma = \frac{L}{RA} \tag{3.2}$$

where L is the electrode separation, which is the distance the current travels, A is the cross-sectional area through which the current flows and R is the resistance.[160] This equation allows for the calculation of the conductivity of a material.

To measure the conductivity of a device, the resistance first has to be measured. The resistance of a device is related to the current ($I$) which flows when a voltage ($V$) is applied, by Ohm's law, $V = IR$.[160] This law can be used to determine the resistance of a device by sweeping the voltage applied to a material and measuring the current, the slope of the resulting curve, in the linear region, is the device's resistance. The resistance of the device is given by $R_{device} = R_m + 2R_c + 2R_e$, where $R_m$ is the material resistance, $R_c$ is the contact resistance, which is the resistance between the material and the electrodes, and $R_e$ is the resistance of the electrodes and the external circuit. Here, $R_e$ can be minimised through the use of highly conductive materials, meaning it can be ignored. For conductive materials the contribution of $R_c$ can be significant and so it must be calculated before $R_m$ can be calculated. There are several methods to measure $R_c$ for a sample, the method used in this work is the transmission line method (TLM). This technique uses an array of electrodes at different distances from each other, the resistance between the electrodes is measured, the contribution of $R_c$ to each measurement is constant, while the contribution of $R_m$ depends on the electrode separation. The resistance of the device as a function of the electrode separation will be linear, with the slope giving the resistance per unit length of the material and the intercept giving $2R_c$.[161] This method is used to calculate $R_c$ in Chapters 6 and 7.

Contact resistance is an important parameter when designing electrical devices as it can strongly affect the performance of the device.[138] Changing from IJP silver to graphene contacts on an $MoS_2$ transistor led to a reduction in the device mobility from 5.5 $cm^2.V^{-1}.s^{-1}$ to 0.8 $cm^2.V^{-1}.s^{-1}$, demonstrating the effect of contact resistance on device performance.[162]

Contact resistance effects arise due to differences between the work function of the 2 materials in contact. If the work function of the two materials are similar, the materials will have an ohmic contact, that is a contact that obeys Ohms law. Ohmic contacts lead to contact resistances which are much smaller than the material resistance, and are the ideal contact for a range of applications.[163] However, if the work function of the electrode is quite different from the material they can form a Schottky contact. For a Schottky contact the difference in the work function between the electrode and the material causes charge carriers to flow from the material to the electrodes, or vice versa, this creates a region depleted of charge carriers between the material and electrode and leads to a barrier that must be overcome for charge carriers to flow in the material.[163] This effect occurs at the interface between 2D materials and bulk materials as well as at 2D/2D interfaces.[164] As the effect of contact resistance is important for device applications, the ability to calculate the contact resistance for printed devices is important for device optimisation.

### 3.2.2 Transistors

Transistors have changed the world drastically since their invention in 1947. The digital revolution of the last several decades has been driven by an incredible increase in computational power, which in turn has been driven by a rapid increase in the density of transistors within devices. The size of the transistor has decreased rapidly since the first fist-sized transistor was produced almost 80 years ago, with 3 nm transistors on wafers with approximately $1\times10^8$ transistors.mm$^{-2}$ being produced currently. This incredible decrease in transistor size and increase in transistor density was predicted by Gordon Moore, one of the co-founders of Intel, in 1965, he suggested that transistor density would double every two years. Modern devices are based predominantly on the metal/oxide/semiconductor field-effect transistor (MOSFET), which are discussed here, before moving to ionically gated transistors which are used in this work.

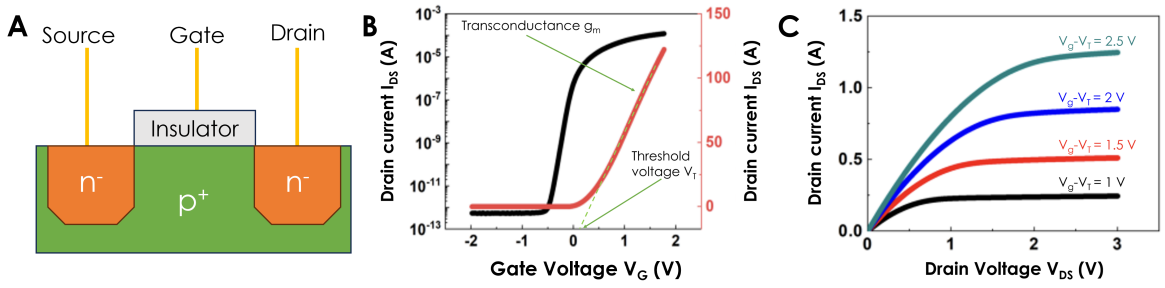



Figure 3.3: **Transistors: A)** Image showing a cross-section of a typical MOSFET. It is composed of a source and drain electrode which are attached to a highly doped n-type region of a semiconductor and a gate electrode separated from the p-type channel by an insulating layer. **B)** Transfer curve for a n-type transistor on a linear scale (red) and a log scale (black). The threshold voltage and linear region of the curve, the slope of which is called the transconductance, are shown. **C)** Output curve, which shows the drain current as a function of the drain voltage at different gate voltages, the current is linear for low voltages and saturates at higher voltages. B and C are adapted from ref.[165]

Fig. 3.3A shows a cross-sectional view of a typical MOSFET. A MOSFET is composed of 3 electrodes, the source and drain electrodes, which are in a planar geometry and are separated by a semiconducting channel, and the gate electrode, which is separated from the semiconducting channel by an insulating layer. To ensure ohmic contacts the source and drain electrodes are attached to highly doped regions.[166] The conductivity of the semiconducting channel is modulated by applying a voltage to the gate, called the gate voltage ($V_G$). When a gate voltage is applied the insulator acts as a capacitor causing charges to build up in the semiconducting material at its interface with the insulator. This layer with increased charge concentration is called the inversion layer. Due to the increase in charge concentration in the inversion layer the conductivity of the device increases.[163] The increase in the conductivity of the channel causes an increase in the current that flows between the source and drain electrodes when a voltage ($V_{DS}$) is applied, as can be seen in Fig. 3.3B. The current flowing between the source and drain ($I_{DS}$), in the linear regime, is given by

$$I_{DS} = \frac{w\mu C}{L}(V_G - V_T)V_{DS} \tag{3.3}$$

where $w$ and $L$ are the length and the width of the device, $\mu$ is the semiconductor's mobility, $C$ is the capacitance of the insulating layer and $V_T$ is the threshold voltage, the voltage at which the device switches on.[163] The transistor, therefore, acts as a switch, when no gate voltage is applied the channel is very resistive and very little current flows between the source and drain electrodes, while when a gate voltage above the threshold is applied the device switches on, and a large current flows between the source and drain. The ratio of the current when the device is off ($I_{off}$) to the current when the device is on ($I_{on}$) is called the on/off ratio and is an important parameter for the device performance.[167]

The mobility of a material can be calculated by measuring it in a transistor configuration. The rate at which a transistor switches on, called the transconductance ($g_m$), is given by

$$g_m = \frac{\delta I_{DS}}{\delta V_G} = \frac{w\mu C}{L}V_{DS} \tag{3.4}$$

all the parameters in this equation are measurable allowing for the calculation of the materials mobility.

Fig. 3.3C shows the dependence of $I_{DS}$ on $V_{DS}$, which is called the output characteristic of the transistor. When a small $V_{DS}$ is applied to the channel it behaves as a standard resistor and the voltage varies linearly with the applied voltage. However, as $V_{DS}$ increases the current saturates, this occurs when the source-drain potential becomes larger than the gate potential, causing the shape of the inversion layer to change, and no longer connect the source and drain electrodes.[163]

### Ionically gated transistors

The previous discussion describes the behaviour of electrostatically gated transistors, that is transistors which are gated by the application of an electric field to a capacitor. The depth of the material gated is relatively limited, with the electric field only penetrating ~40 nm.[168] When testing a variety of materials, including nanosheet networks, electrostatic gating may not always be effective, due to the thickness of the network. One method which can be used to overcome this problem is to gate the material with ions, either through the use of an ionic dielectric or an ionic liquid (IL).[156,169] This section focuses on the use of IL to gate transistors.

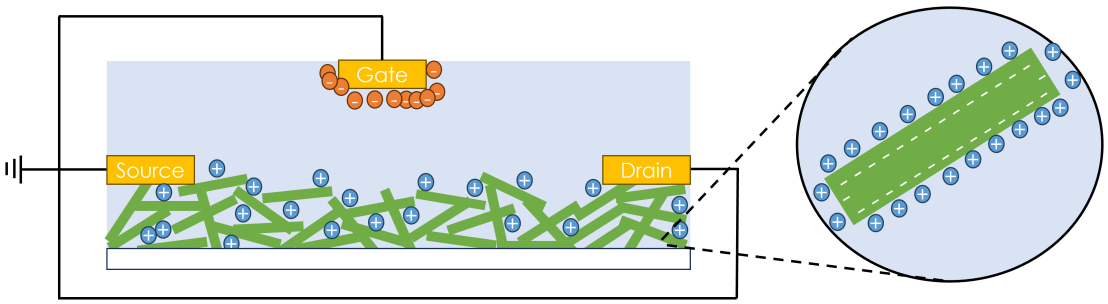



Figure 3.4: **Ionic liquid (IL) gated transistors:** Figure showing the operating principle of an ionically gated transistor. When a positive potential is applied to the gate electrode it causes anions to flow to the gate, cations then flow to the channel and adsorb onto the surface of the material creating an EDL at the interface, increasing the number of electrons in the material.

In an IL gated transistor, a liquid containing ions is dropped on top of the material, the liquid can be an aqueous solution of a salt or a liquid called an IL, which is an ionic material which is liquid at room temperature. In this work 1-ethyl-3-methylimidazolium bis(trifluoromethylsulfonyl)imide (EMIM-TFSI) is used as the IL. The operating principle of an IL gated transistor is shown in Fig. 3.4. The gate electrode is in contact with the IL, and on the application of a positive potential to the gate anions flow to the gate, the cations in the IL are then attracted to the material in the channel, these ions adsorb onto the surface of the material creating an EDL on the surface, inducing a buildup of electrons in the material, increasing its conductivity.[169]

Ionically gated transistors tend to have very high capacitances. In the case of a porous open material, ions can absorb onto the large available surface area, this means the entire volume of the transistor is gated by the IL. In this case Eqn. 3.3 can be rewritten as

$$I_{DS} = \frac{w\mu C_v t}{L}(V_G - V_T)V_{DS} \tag{3.5}$$

where $C_V$ is the volumetric capacitance of the device and $t$ is the thickness of the device.[170] The volumetric capacitance of a nanosheet network has been shown to be related to the nanosheet thickness.[125] The tunability of the network thickness allows for the production of devices with high transconductance.[170] The applicability of IL gated transistor is limited

to sensors due to their slow switching speed, which is caused by slow ion transport in the liquid.[138,169,170] Another limitation of IL gated transistors is that the IL is conductive, which leads to an alternative current path through the IL instead of through the device. If the IL is more conductive than the device then the majority of the current will flow through the IL, not the device, preventing measurement of the device properties. This limits the use of IL gated transistors to materials which are more conductive than the IL.[171] Despite these limitations, ionically gated transistors are useful for calculating the mobility of devices that are too thick to be gated electrostatically.

### 3.2.3 Alternating currents & electrical impedance spectroscopy (EIS)

The discussion of electronics in this chapter thus far has focused on the properties of materials when a direct current (DC) is applied, the behaviour of materials change when an alternating current (AC) is applied, with the electrical properties becoming dependent on the frequency of the current.[172] These changes in resistance can be used to characterise the electrical properties of a material by a technique called electrical impedance spectroscopy (EIS).

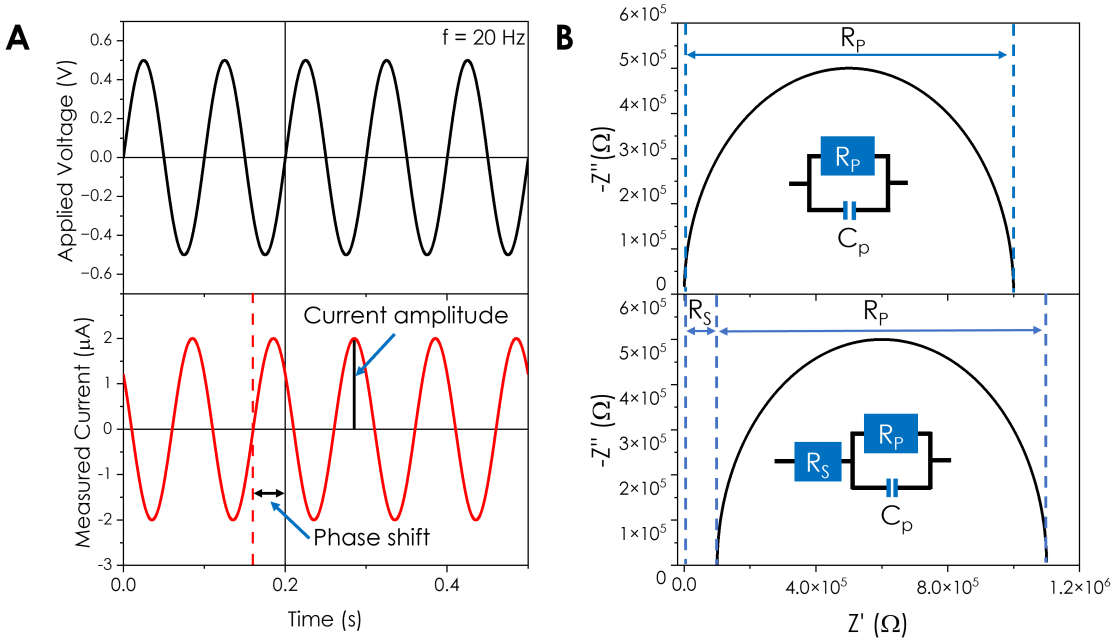



Figure 3.5: **Electrical impedance spectroscopy: A)** Graph showing the principle of an EIS measurement. An alternating voltage is applied to a material and the phase shift and amplitude of the current generated is measured. **B)** Nyquist plots for a resistor ($R_P$) in parallel with a capacitor ($C_P$) and for a resistor in series ($R_S$) with a parallel resistor and capacitor. The circuit diagram for each curve is shown as an inset.

EIS operates by applying a sinusoidally alternating voltage to a material and measuring the magnitude of the produced current and the phase shift between the voltage and the current. The measured quantities are shown in Fig. 3.5A. For AC measurements the resistance is

referred to as impedance ($Z$) and is given by

$$Z(\omega) = \frac{V(t)}{I(t)} = \frac{V_0 e^{i\omega t}}{I_0 e^{i\omega(t-\theta(\omega))}} = \frac{V_0 e^{i\theta(\omega)}}{I_0} = |Z| e^{i\theta(\omega)} \tag{3.6}$$

where $\omega$ is the angular frequency of the applied voltage, $\theta$ is the phase shift, $t$ is time, and $V_0$ and $I_0$ are the amplitude of the voltage and current respectively. The impedance can be split into real and imaginary components

$$Z = |Z|\cos\theta + i|Z|\sin\theta = Z' + iZ'' \tag{3.7}$$

The impedance of a device depends on the components it is composed of; it can be described by a circuit composed of the three core circuit elements in series and/or in parallel with each other. The three core circuit elements are the resistor, capacitor, and inductor. Fig. 3.5B shows a Nyquist plot, which is a plot of the imaginary versus the real impedance, for both a resistor in parallel with a capacitor and a resistor in series with the parallel resistor-capacitor pair. These two circuits show different impedance spectra.

To understand charge transport in a material, the EIS spectra can be compared to a circuit model composed of the core circuit elements, where the circuit elements correspond to different charge transfer processes.[172] EIS has been used to measure the resistance of grains within metals,[173] as well as the resistance of the junctions between CNT bundles.[174] AC can be used to make sensitive and selective sensors,[175] with a resistor in series with a resistor-capacitor pair having been used to model the change in resistance in a printed $MoS_2$ network when gas is adsorbed,[176] the Nyquist plot of this circuit is shown in Fig. 3.5B. The use of EIS to understand charge transport in nanosheet networks will be explored in Chapter 7.

## 3.3 Nanosheet networks

When nanosheets are deposited onto a substrate to form a device they sit on the substrate and on each other forming a nanosheet network. The electrical properties of the network depend on the properties of the nanosheets, the resistance of the junctions between the nanosheets (hereafter referred to as the junction resistance), and the morphology of the network.[82] Fig. 3.6A shows a schematic of nanosheets in a network, showing several of the parameters that affect the network properties, including morphological parameters such as porosity and factors believed to effect the junction resistance, including nanosheet overlap area and the presence of residues between nanosheets.[82] To optimise the electrical properties of nanosheet networks, techniques to measure these properties are required.

Kelly *et al.* have suggested that the morphology of nanosheet networks can be divided into 3 classes: obliquely aligned nanosheets, which show point like junctions between adjacent nanosheets; edge aligned nanosheets, which are nanosheets aligned on a substrate which

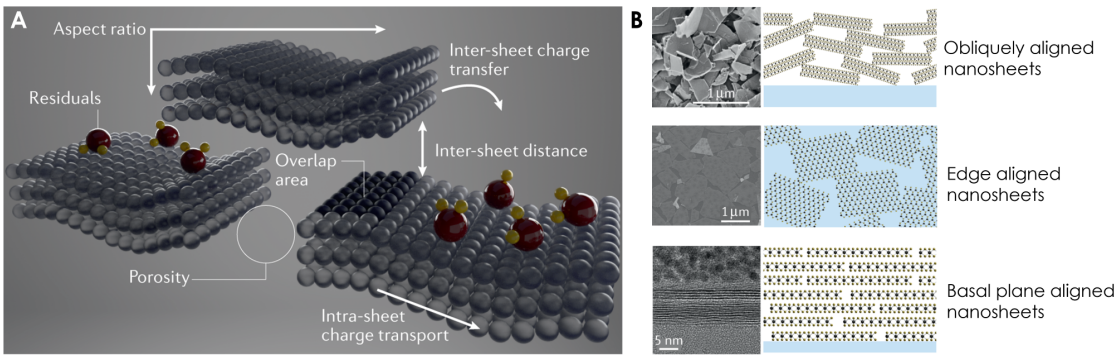



Figure 3.6: **Nanosheet networks: A)** Image showing a network , highlighting the factors which are believed to effect network properties. **B)** Image showing the different classifications of nanosheet network morphology suggested by Kelly *et al.* Images are adapted from[82]

touch through edges; and basal plane aligned nanosheets, which have a large amount of overlap between adjacent nanosheets.[82] Each of these network morphologies is shown in Fig. 3.6B. The ideal network morphology is application dependent. While knowledge of network morphology is important for optimising nanosheet based devices, techniques to interrogate network morphology have been limited.

This section discusses the literature on electrical conduction in nanosheet networks, first, considering the effect of a network's thickness on its electrical properties and then examining the literature on the electrical properties of nanosheet networks. The morphological characterisation of nanosheet networks is then discussed.

### 3.3.1 Percolation effects

In section 3.2.1 the conductivity of materials is discussed, as conductivity is an intrinsic property, it is thickness independent in standard materials. However, this is not the case for nanosheet networks below some critical thickness, called the bulk conductivity thickness ($t_B$). Below $t_B$ the connection between the two electrodes is limited, and the conductivity of the network is strongly dependent on the network's thickness, this thickness dependence is described by percolation theory.[177,178]

Percolation theory was developed to describe gelation in polymer systems, but has since been expanded to describe a wide variety of physical phenomena.[179,180] In nanosheet networks, percolation theory describes the increase in electrical connectivity as the thickness increases.[117,177] Fig. 3.7A shows how the connectivity increases as the network thickness increases. Below a critical thickness, called the percolation threshold ($t_C$) there is no electrical connection between the electrodes and the network is insulating. Above $t_C$ but below $t_B$ there is electrical contact between the electrodes and the network conducts; however, the conductivity is limited by the small number of highly tortuous paths. Above $t_B$, the network has a thickness independent conductivity as there is a large number of paths connecting both electrodes. Percolation theory suggests that the thickness dependent

conductivity ($\sigma(t)$) is given by

$$\sigma(t) = \sigma_B \left( \frac{t - t_C}{t_B - t_C} \right)^n \tag{3.8}$$

where $\sigma_B$ is the bulk conductivity, $t$ is the network thickness and n is the percolation threshold, which is related to the geometry of the material in the network.[177] A distribution in the resistance in the network leads to an increase in the value of $n$.[181] A graph showing the evolution in conductivity of an IJP graphene as network thickness increases is shown in Fig. 3.7B.

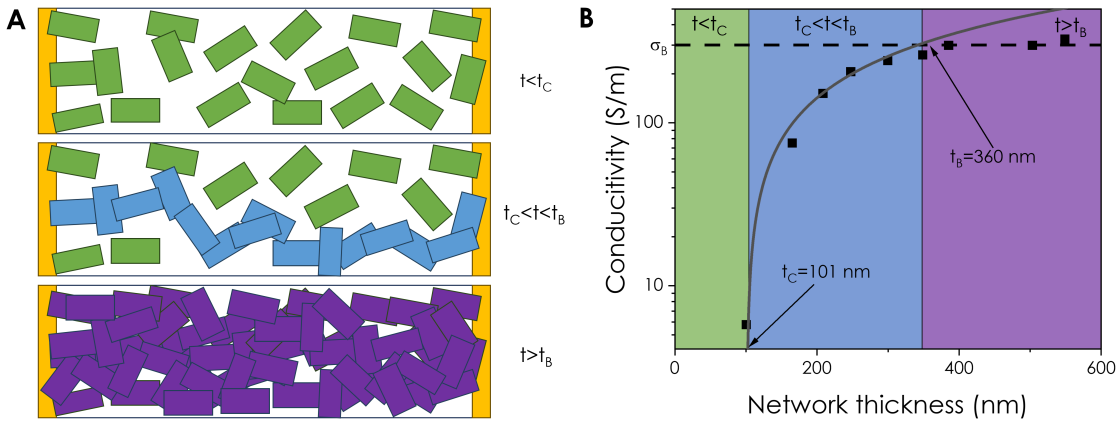



Figure 3.7: **Percolation theory: A)** Schematic showing electrical contact in a nanosheet network with thickness, below the percolation threshold, between the percolation threshold and the bulk conductivity threshold and above the bulk conductivity threshold. **B)** Conductivity as a function of thickness for an IJP graphene network. Data reproduced from.[117]

Percolation theory models the increase in connection between electrodes by considering the increase in the number of connective paths between 2 sets of electrodes. While percolation theory is generally used to describe the increase in conductivity with network thickness, it has also been demonstrated that for CNT networks, it can be used to describe the super-linear increase in resistance with channel length and width.[182,183] It has been suggested that the decrease in conductivity with increasing channel length can be modelled as

$$\sigma \propto L^{-\gamma} \tag{3.9}$$

where $L$ is the channel length, and $\gamma$ is a the channel length percolation exponent (CLPE), which is related to the NT density between the electrodes.[178] The NT density is analogous to film thickness in nanosheet networks. This effect occurs when the network thickness is below the bulk thickness as the number of connected paths decreases as the channel length increases.[180] This relationship can be used to modulate the on/off ratio in networks of CNT.[178,183] This effect has also been observed for LPE $MoS_2$ networks.[184] Percolation like scaling of conductivity with channel length in $MoS_2$ networks is discussed in Chapter 7.

### 3.3.2 Conduction in nanosheet networks

Nanosheet networks are being investigated for use in printed electronic devices. Understanding the conduction mechanism in these networks is important to optimise their performance. It has been known for over 20 years that the junction resistance limits the electrical properties of nanomaterial networks,[182] however, measurements of the junction resistance have been limited. This section discusses models which describe the conduction in nanosheet networks, measurement of the junction resistance, and the temperature dependent conductivity in nanosheet networks. Where relevant conduction in CNT networks is also discussed.

The electrical properties of nanosheet networks are generally considerably inferior to the nanosheets they are composed of. The mobility of TMD nanosheet networks produced by IJP LPE inks have mobilities that are over 1,000 times lower than the nanosheets they are composed of.[170] This reduction in the electrical performance of printed devices can be attributed to high junction resistance. In a recent review, Kelly *et al.* have proposed models to describe the relationship between nanosheet properties, junction resistance, and network conductivity.[82] They show that there is no clear relationship in the literature between graphene nanosheet length and network conductivity, shown in Fig. 3.8A. This demonstrates that improving network conductivity is not as simple as reducing the number of junctions. They suggest conduction in nanosheet networks can be divided into categories depending on the ratio of junction to nanosheet resistance.[82] In the case where the junction resistance is far higher than the nanosheet resistance, dubbed a junction-limited network, they suggest that the network conductivity ($\sigma_{Net}$) is given by

$$\sigma_{Net} \approx \frac{1 - P_{Net}}{t_{NS} R_J} \tag{3.10}$$

where $P_{Net}$ is the network porosity, $R_J$ is the junction resistance, and, $t_{NS}$ is the nanosheet thickness. This suggests that the conductivity of junction limited networks is strongly dependent on the nanosheet thickness. Fig. 3.8B shows data from Yakimchuk *et al.*, showing graphene network mobility as a function of nanosheet thickness, demonstrating network mobility decreases as nanosheet thickness increases.[185] Fitting this data with Eqn. 3.10 suggests $R_J \approx 1$ MΩ, this high junction resistance may be in part caused by the presence of surfactants on the nanosheets.[185]

When the junction and nanosheet resistance are similar, dubbed material- and junction-limited networks, Kelly *et al.* suggested that the network conductivity is given by

$$\sigma_{Net} \approx \frac{(1 - P_{Net}) n_{NS} t_{NS}^2}{R_J} \tag{3.11}$$

where $n_{NS}$ is the nanosheet carrier concentration.[82] This equation conflicts with a recent publication from Clifford *et al.,* showing highly conductive size-selected graphene networks with increasing network conductivity as the nanosheet thickness decreases. Their networks

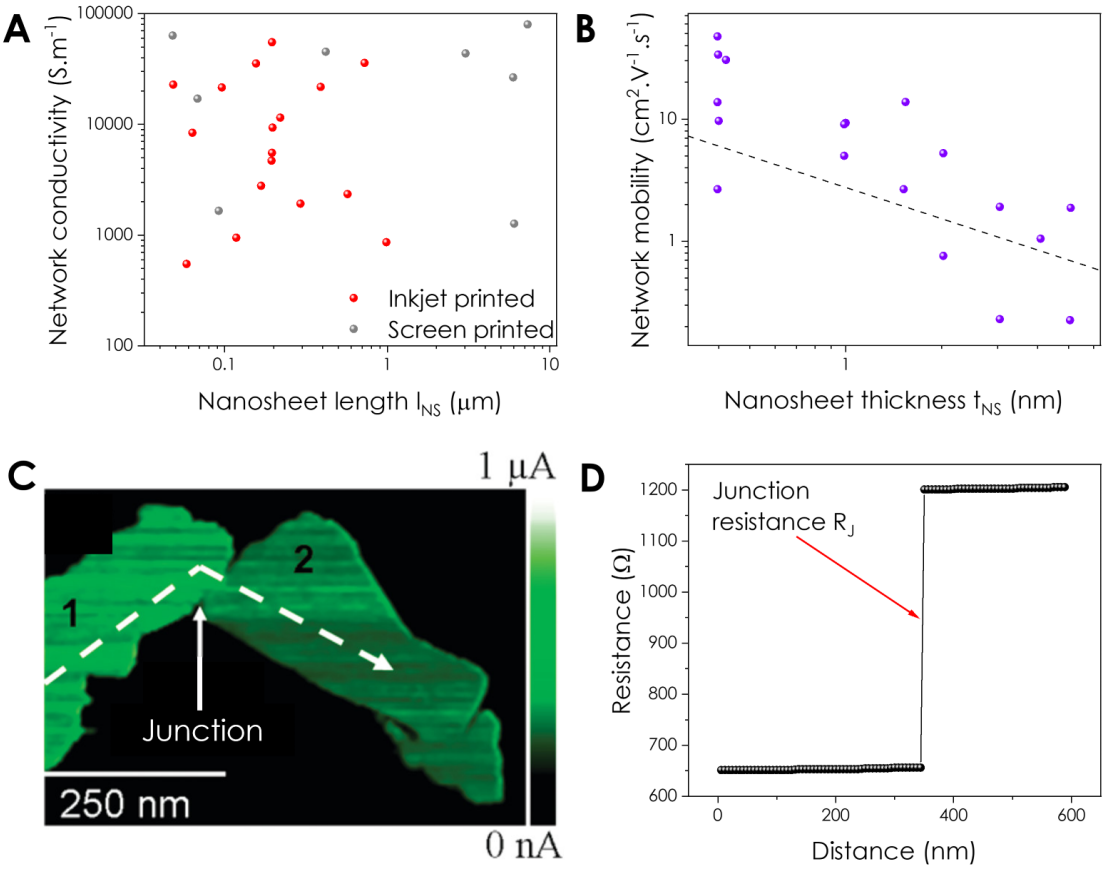



Figure 3.8: **Conduction in nanosheet networks: A)** Graphene network conductivity as a function of nanosheet length for IJP and screen-printed networks. Adapted from ref.[82] **B)** Network mobility as a function of graphene thickness. Fit to equation 3.10 is shown, yielding $R_J \approx 1$ MΩ. Data is adapted from ref.[185] and fit is from ref.[82] **C)** Conductive AFM image of two graphene nanosheets labelled 1 and 2. Sheet 1 is connected to an electrode and there is a junction between 1 and 2, which is marked. **D)** Resistance as a function of distance along the white line shown in C. C and D are adapted from ref.[26]

show $\sigma_{Net} \approx 1 \times 10^5$ S.m$^{-1}$, too high to be junction-limited, yet they show behaviour suggested by Kelly *et al.* for junction limited networks.[82,126] Clifford *et al.* explain this discrepancy by suggesting that the junction resistance may decrease as nanosheet size is decreased, which implies a 2 order of decrease in $R_J$ for an order of magnitude decrease in $t_{NS}$.[126] In Chapter 6 an alternative equation describing conduction in nanosheet networks is presented.

As the performance of nanosheet networks is strongly affected by the junction resistance a number of methods to reduce it have been suggested. These techniques allow for an insight into the factors which affect the junction resistance. One method, which has been used to improve the mobility of printed $MoS_2$ transistors, is to use organic molecules to cross-link the nanosheets improving connectivity between the nanosheets. This led to an order of magnitude increase in the mobility of the device, with minimal increase in nanosheet conductivity.[184,186] An alternative method is high temperature annealing, which removes residual stabilisers and solvents from the exfoliation and printing process,[126] this can be combined with device compression to improve the contact between adjacent nanosheets,[93]

this process increased the conductivity of a screen-printed graphene networks by a factor of 34.[187] Optimised deposition methods can also reduce the junction resistance, the conductivity of $PtSe_2$ networks has been shown to increase by a factor of 7 when deposited by Langmuir-Schaefer (LS), a method which produces well-aligned nanosheets, when compared to spray-coating.[188] Finally, the use of high aspect ratio nanosheets, which can form networks of basal plane aligned nanosheets, instead of obliquely aligned nanosheets, reduces the junction resistance.[82] High aspect ratio nanosheets can be produced by EE, networks of EE $MoS_2$ show much higher mobilities than LPE networks, with mobilities as high as 80 $cm^2.V^{-1}.s^{-1}$ having been reported.[108] These results show a variety of methods can be used to optimise the conductivity of nanosheet networks. However, to fully optimise device performance an understanding of the factors affecting the junction resistance is required, to achieve this techniques to measure junction resistance are needed.

The simplest method to interrogate junction resistances is to measure the resistance of an individual junction directly. This can be achieved by conductive AFM (C-AFM), which measures resistance as a function of distance from an electrode, a C-AFM image and line-scan along 2 graphene nanosheets is shown in Fig. 3.8C,D, showing the sudden change in resistance at the junction between the nanosheets. Reports of C-AFM on nanosheet networks are limited, one report on graphene grown by CVD shows the junction resistance scales with the thickness of the top flake, with the junction resistance increasing from 500 Ω to 10 kΩ as the top flake thickness increases from 1 nm to 7.5 nm.[26] C-AFM measurements can also be used to measure the junction resistance in CNT networks. It has been shown that the acid treatment of the NTs decreases the junction resistance by a factor of 3 with minimal change in the nanosheet conductivity,[189] while annealing the networks in an argon environment leads to a factor of 3 decrease in the NT conductivity and a factor of 5 increase in the junction resistance. This suggests that the junction resistance is related to material conductivity.[190]

An alternative method to investigate junction resistance is to form devices with a single junction and compare their properties to that of the constituent materials'. For single junction devices composed of metallic-metallic CNT junctions and semiconducting-semiconducting CNT junctions it was found that the junction resistance is similar in both cases and can be related to the probability that an electron can tunnel between the two NTs. However, the junction resistance of a metallic-semiconducting CNT junction was found to be considerably higher due to the formation of a depletion region at the junction.[3] Single junction transistors of $MoS_2$ have been combined with C-AFM to gain a quantitative understanding of the junction resistance and its effect on device mobility. For a device composed of two 8L nanosheets, the device mobility was minimally reduced by the junction, with the average mobility of the constituent nanosheets being 48 $cm^2.V^{-1}.s^{-1}$, while the device had a mobility of 46 $cm^2.V^{-1}.s^{-1}$, this minimal decrease in mobility is likely due to the large junction area. However, C-AFM measurements suggest the device resistance is driven by the junction, which has a resistance 10 times larger than the nanosheets. The C-AFM

showed that the resistance increased at the edge of one of the nanosheets, which suggests the junction resistance is driven by scattering at the nanosheet edge.[191] However, this explanation cannot explain variations in film conductivity that have been achieved by different deposition methods or by network compression,[93,187,188] demonstrating the complexity of junction resistance effects.

Beyond measurements of individual junctions a measurement technique that calculates the average material and junction resistance in a network would be useful. EIS has been used to extract the ratio of NT bundle to junction resistance in CNT networks, showing that the junction resistance was a factor of 3 higher than the bundle resistance.[174] The use of EIS to calculate nanosheet and junction resistances is explored in Chapter 7.

Further information about the conduction mechanism in nanosheet networks can be obtained by carrying out temperature dependent electrical measurements. It has been found that the temperature dependent electrical properties of nanosheet networks can be divided into different regimes.[184] At very low temperatures, the conduction is dominated by tunnelling between nanosheets, which is a temperature independent phenomenon.[184] In the temperature dependent regime, a number of different temperature dependent conduction mechanisms are observed. The temperature dependent conductivity can be expressed as

$$\sigma(T) = \sigma_0 \exp\left[-\left(\frac{T_0}{T}\right)^{\alpha}\right] \tag{3.12}$$

where T is the temperature, $\sigma_0$ and $T_0$ are constants the physical meaning of which depends on the conduction mechanism and $\alpha$ tells you which type of conduction mechanism present. For $\alpha$=1 the conduction is described by Miller-Abrahams hopping (MAH), where there is an activation energy associated with hopping across junctions. If $\alpha$<1 then the conduction is described by variable-range-hopping (VRH). VRH describes the hopping of charge carriers between the 2 most energetically favourable sites, with larger hops then occur in MAH being possible. VRH hopping can be further divided: Mott-VRH (M-VRH) is described by $\alpha = 1/(1+d)$ where d is the dimensionality of the system, while Efros–Shklovskii VRH (ES-VRH) occurs when $\alpha = 1/2$ and describes the opening of a Coulomb gap at the Fermi level.[184] MAH, 2D-VRH, 3D-VRH and ES-VRH have been observed in nanosheet networks.[101,184,192–194] The conduction mechanism can be combined with the value of $T_0$ to better understand components of the conduction mechanism such as the average hop distance.[193]

Nanosheets, like networks have shown an array of different temperature dependent conduction mechanisms, from decreasing conductivity with increasing temperature due to charge carrier scattering limited transport, to increasing conductivity with increasing temperature due to hopping between defects in the nanosheet.[195,196] This can lead to difficulties in determining the conduction mechanism in material and junction limited networks. Piatti *et al.* find that the average hop distance of a charge carrier in their IJP EE $MoS_2$ networks is less than the nanosheet separation, suggesting that the temperature dependent electrical

properties of the network are governed by the nanosheets, despite the network conductivity being governed by the junction resistance.[192] A method to examine both the temperature dependence of both the nanosheet and junction resistance is presented in Chapter 7.

### 3.3.3 The morphology of nanosheet networks

The morphology of nanosheet networks effects its performance in a range of applications, including batteries,[197] supercapacitors[198] and sensors.[177] In printed electronics morphology is particularly important, morphological factors can affect the electrical properties by 2 mechanisms, firstly, high porosity and tortuosity reduce network conductivity, secondly, the nanosheet alignment is related to junction resistance.[82] In printed heterostacks morphology is also important, as a well defined interface between layers is important to prevent device shorting.[118] Despite the importance of the morphology in the performance of printed devices investigations into device morphology remain limited. This section reviews the literature on the morphology of nanosheet networks with a focus on techniques which have been used to characterise network morphology.

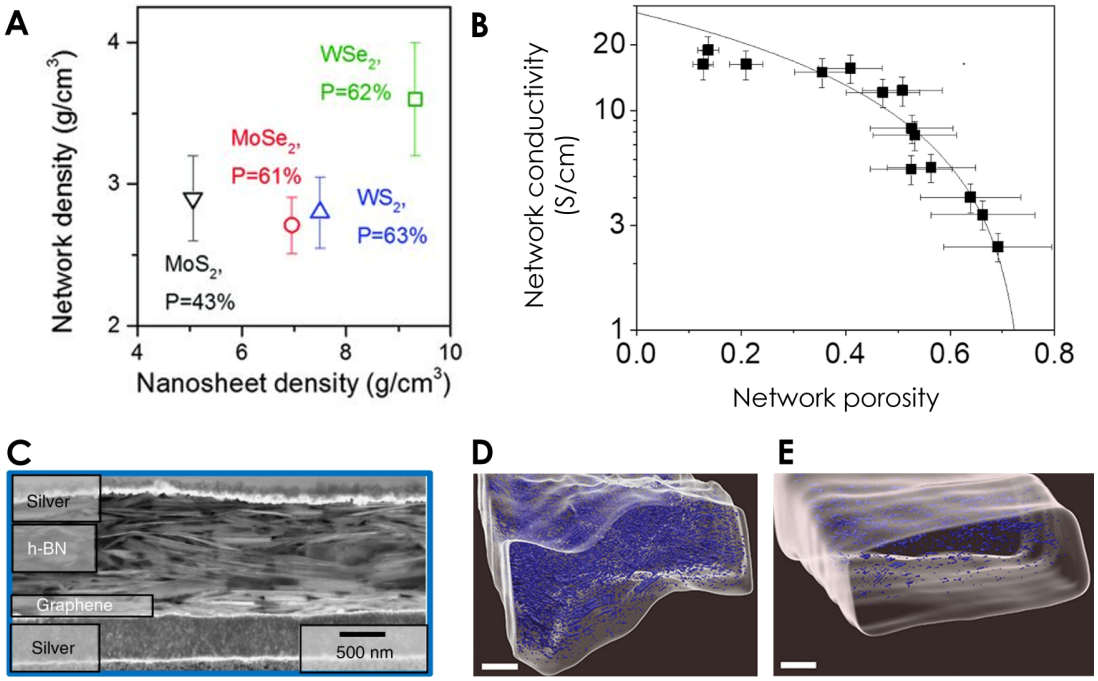



Figure 3.9: **Morphology of nanosheet networks: A)** Network density as a function of nanosheet density for spray-coated LPE TMD networks. Reproduced from ref.[170] **B)** Network conductivity as a function of porosity for vacuum filtered LPE graphene networks. The line shows a fit to percolation theory. Adapted from ref.[199] **C)** Cross-sectional TEM image of a printed graphene transistor with a hBN capacitor and silver contacts. Reproduced from ref.[200] **D-E)** 3D Focused ion beam-scanning electron microscope nanotomography (FIB-SEM nt) images of vacuum filtered MXene networks before and after a chemical treatment to cross-link the nanosheets. The blue shows the pores within the networks. Scale bars are 2 $\mu$m. Image reproduced from ref.[201]

The morphology of a nanosheet network is described by an array of parameters including

nanosheet alignment, surface area, and nanosheet and pore tortuosity. The most commonly discussed morphological parameter is the network porosity. Porosity describes the empty space contained within a network, it negatively affects conduction in networks by reducing the material available for current to flow through.[202] The porosity of nanosheet networks can be calculated by measuring the network density and comparing it to the density of the nanosheets. The porosity of spray-coated TMD networks was calculated using this method, finding porosities of ~60%,[170] network density as a function of nanosheet density for these networks is shown in Fig. 3.9A. Clifford *et al.* measured the porosity of size selected spray-coated graphene networks using the same method, finding that the porosity decreased from ~70% to ~40% as the nanosheet size decreased from ~2.5 $\mu m$ to ~250 nm.[126] Barwich *et al.* measured the porosity of vacuum filtered film in the same manner. Using compression they were able to systematically vary the porosity and measure the networks conductivity. They show that the conductivity scales non-linearly with network porosity and suggest that this can be described by a percolation like scaling, with the networks showing a constant junction resistance, which they estimate as 10 $k\Omega$,[199] network conductivity as a function of porosity is shown in Fig. 3.9B. Measuring porosity by calculating network density leads to large uncertainties due to the difficulty in accurately measuring network density.

As well as conductivity, Barwich *et al.* measured pore diameter, nanosheet alignment and surface area as a function of compression. They measure surface area and pore diameter using both nitrogen adsorption/desorption isotherms and mercury intrusion porosimetry (MIP), these techniques suggest that there is a wide distribution of pore diameters from 10-1000 nm, with a decrease in pore diameter as the network is compressed. The surface area of the networks varies between 30-50 $m^2.g^{-1}$, well below the value for a graphene ML due to thickness of the nanosheets and the aggregation of the nanosheets during the film formation process.[199] While nitrogen adsorption/desorption isotherms and MIP are ideal techniques for measuring pore diameter and SSA in some materials, they require thick networks so their application to nanosheet networks has been limited[199] .

The alignment of the nanosheets in a network has been measured as a function of compression using fracture cross-sections images and image analysis techniques, finding the full width half maximum (FWHM) of the distribution of nanosheet angle decreases with compression.[93,199] There are a number of limitations to this measurement method, firstly, fracture cross-section do not create perfect cross-sections and secondly, the resolution of the images used is too low to identify individual nanosheets. An alternative method is to use AFM to image the surface of a network, this has been used to calculate the distribution of nanosheet angles for MXene, EE $MoS_2$ and LPE graphene networks, finding that the MXene and $MoS_2$ networks show a high degree of in-plane alignment with FWHM of 5.2°and 8.67°respectively, while the LPE graphene shows a worse in-plane alignment with a FWHM of 20.8°.[192] Well aligned nanosheets will form a junction with larger overlap area and are likely to produce more conductive networks. It has been shown that the formation of conformal junctions requires high aspect ratio nanosheets such as MXenes and EE

$MoS_2$, which may explain the difference in alignment. While AFM can measure nanosheet alignment at the network surface, it cannot see internal variations in morphology.

Cross-sectional microscopy allows for the investigation of the interface within printed heterostacks which is important to understand when designing out-of-plane devices. Carey *et al.* show cross-sectional transmission electron microscopy (TEM) and scanning electron microscopy (SEM) images of IJP transistors with a graphene channel, silver electrodes and a hBN capacitor, allowing for visualisation of the interface between the materials, which is important to understand interlayer shorting.[200] A cross-section TEM image of a printed hetrostack is shown in Fig. 3.9C. Interlayer shorting like all morphological parameters is a 3D problem which cannot be characterised fully from 2D cross-sections, therefore, the use of 3D imaging to understand the structure of nanomaterial networks would be ideal.

While 3D imaging has been used widely to research the morphology of devices such as batteries and fuel cells reports of 3D imaging of nanomaterials networks have been limited.[203] Forro *et al.* report 3D imaging of a AgNW polymer composite by nano-X-ray computed tomography (CT), although they do not use the images for morphological characterisation but instead for simulating the strain response of the composite.[204] Tagliaferri *et al.* report 3D imaging of 3D printed graphene supercapacitors by nano-X-ray CT, from the image they extract the nanosheet alignment and pore diameter.[205] Wan *et al.* use 3D imaging by focused ion beam-scanning electron microscope nanotomography (FIB-SEM nt), to measure the decrease in porosity and the change in pore volume of MXene networks after a cross-linking treatment.[201] A 3D image of a MXene network before and after cross-linking is shown in Fig. 3.9D. While these reports demonstrate the ability of 3D imaging to characterise nanomaterial networks, the number of morphological parameters calculated has remained limited. Chapter 5 discusses the use of FIB-SEM nt, to characterise the morphology of printed networks and heterostacks.

*"Hereupon all the Heavenly Deities commanded the two Deities His Augustness the Izana-gi-no-kami and Her Augustness the Izana-mi-no-kami, ordering them to "make, consolidate, and give birth to this drifting land." Granting to them an heavenly jewelled spear, they thus deigned to charge them. So the two Deities, standing upon the Floating Bridge of Heaven, pushed down the jewelled spear and stirred with it, whereupon, when they had stiffed the brine till it went curdle-curdle, and drew the spear up, the brine that dripped down from the end of the spear was piled up and became an island."*

Basil Hall Chamberlain

# 4

# Nanosheet and network characterisation techniques

Nanosheet networks show great promise for a range of applications in printed electronic devices; however, to reach their potential, their properties require optimisation. The electrical properties of nanosheet networks are dependent on the electrical properties of the constituent nanosheets, the size of the nanosheets, and the morphology of the network. Techniques to measure these quantities are required so that the performance of nanosheet networks can be optimised. This chapter focuses on the techniques used in this work to characterise both nanosheets and their networks.

## 4.1 Nanosheet characterisation

An array of techniques have been developed to characterise the properties of exfoliated nanosheets. While the focus of this work is to develop new techniques for the characterisation of nanosheet networks, an understanding of the properties of the constituent nanosheets is required to understand the relationship between the nanosheets and the network they produce. This section discusses the methods used in this work to interrogate nanosheet properties.

### 4.1.1 Atomic force microscopy (AFM)

Solution-processing of nanosheets began in 2008, since then a great deal of research has been carried out on the effect of size on the properties of these nanosheets.[81,130,206–209] Both nanosheet length and thickness affect the performance of nanosheet networks.[82,125] One method that can calculate both nanosheet length and thickness is AFM. In this technique

a tip moves along the surface of a material to measure its height. Scanning the tip over a large area can be used to generate images of a material's surface topography. As discussed in Chapter 3.3.3, this technique can be used to measure the alignment of nanosheets on the surface of a network.[192] If it is instead used to measure a substrate coated with very few nanosheets, it can be used to identify individual nanosheets and measure their length and thickness.[86]

The operating principle of AFM is relatively simple, a sharp tip is attached to a cantilever, the tip is moved along the surface of a material, and the deflection of the cantilever as it scans across the surface is measured. AFM can be divided into different categories depending on the type of contact the tip has with the sample. If the tip is in constant contact with the sample, the AFM is carried out in contact-mode. If the tip does not contact the sample, but oscillates with a small amplitude above the sample, it is carried out in non-contact mode. Finally, AFM can be carried out in tapping mode, here the tip oscillates with a large amplitude, tapping against the sample with each oscillation. Tapping mode eliminates friction between the sample and the tip and allows the tip to pass through solvent layers on the surface.[210] In this work, the AFM was carried out in tapping mode.

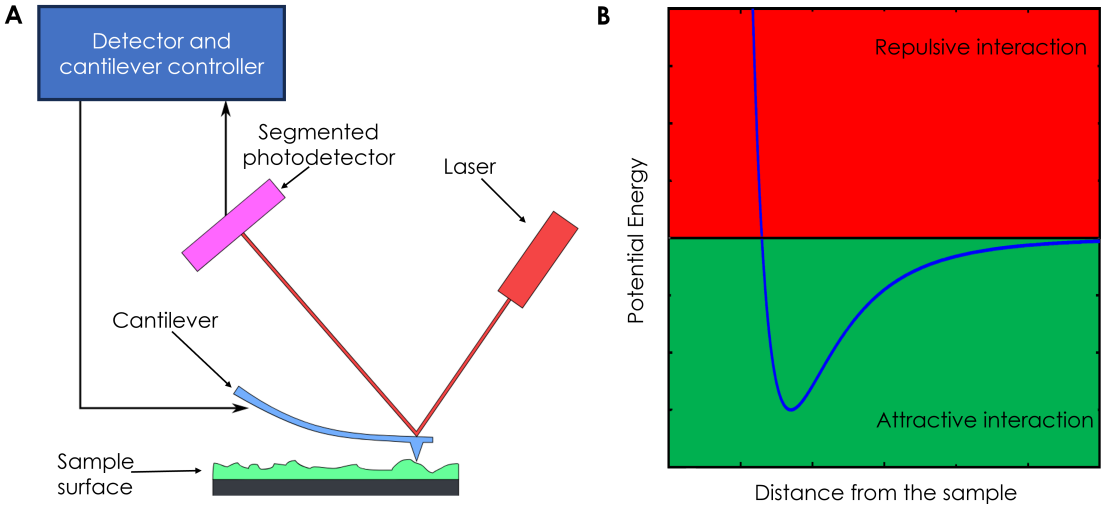



Figure 4.1: **Atomic force microscopy: A)** Schematic of an atomic force microscope. **B)** Lennard-Jones potential, which is used to model the interaction between an AFM tip and the sample.

A schematic of an atomic force microscope is shown in Fig. 4.1A. In tapping mode, a piezoelectric crystal is used to ensure that the cantilever tip is close to the sample, the tip is then oscillated with an amplitude between 1-100 nm.[210] A laser, which is reflected off the cantilever and onto a segmented photodetector, is used to determine the position of the cantilever. As the AFM tip oscillates it interacts with the sample, this interaction is generally modelled by a Lennard-Jones potential,[211] shown in Fig. 4.1B. As the tip oscillates above the sample it experiences both attractive and repulsive forces, these forces affect the amplitude of the oscillations and can be used to determine the height of the sample at each point.[210]

To calculate the average nanosheet length and thickness for a nanosheet ink, a dilute drop of the ink is dropcast onto a heated $Si/SiO_2$ substrate. The solvent then evaporates leaving a substrate which is partially coated in nanosheets. AFM scans of the substrate allow for the thickness of each of the nanosheets to be measured. The length (longest dimension of the nanosheet) and width (dimension perpendicular to the length) of the nanosheets can also be calculated by measuring the start and end point of the nanosheet. In Chapters 5, 6 and 7 the reported nanosheet length is calculated as (length+width)/2. The AFM presented in this work was carried out by Dr. Kevin Synnatschke and Anthony Dawson.

### 4.1.2 Ultraviolet-visible (UV-vis) spectroscopy

When producing nanosheet inks, knowledge of the ink concentration is important to prevent reaggreagation.[212] While ink concentration can be calculated by filtration and subsequent weighing of a known volume of ink, this method is wasteful. An alternative method for the measurement of ink concentration is ultraviolet-visible (UV-vis) spectroscopy. This technique measures the concentration of a solution based on the amount of light it absorbs.

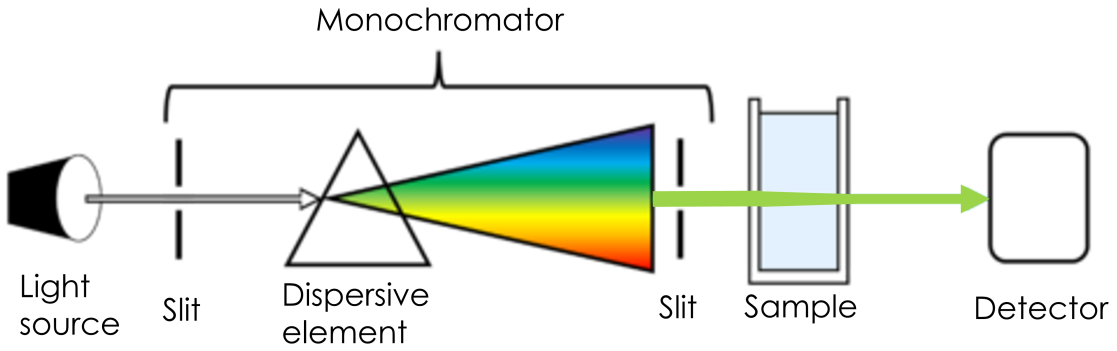



Figure 4.2: **Ultraviolet visible spectroscopy:** Schematic of an UV-vis spectrometer. Adapted from ref.[213]

Fig. 4.2 shows a schematic of a UV-vis spectrometer. Here, white light is split into its constituent components by a monochromator and then passed through a quartz cuvette containing the sample before reaching a photodetector. The intensity of light that passes through the sample ($I$) relative to a reference sample ($I_0$) is calculated, this can be related to the sample extinction ($Ext$) by

$$Ext = \ln\frac{I}{I_0} = -\ln T \tag{4.1}$$

where $T$ is the transmittance. The sample extinction can be related to the material concentration by the Beer-Lambert law:

$$Ext(\lambda) = \epsilon(\lambda)cl \tag{4.2}$$

where $\epsilon$ is the extinction coefficient of the material, $c$ is the concentration of the solution,

and $l$ is the path length of the beam.[214] There are distinctions between UV-vis spectroscopy of soluble materials and nanomaterials. In soluble materials, $\epsilon$ is related to the amount of light absorbed by the material, while for nanomaterials $\epsilon$ describes both light absorbed and scattered by the material. Furthermore, for nanosheets, both the absorption and scattering are dependent on nanosheet size.[207,209,215] The absorption component of the extinction spectra can be measured using an integrating sphere, which reflects all scattered light so it can be measured.[216] While the extinction of nanosheet dispersions is nanosheet size-dependent, some nanosheets such as graphene and $WS_2$ show a nanosheet-length independent value, where the extinction depends only on the dispersion concentration, the extinction at this wavelength can be used to calculate the ink concentration.[130,209]

### 4.1.3 Raman spectroscopy

The use of light to characterise materials extends far beyond UV-vis spectroscopy, another technique that can be used to characterise a material based on its interaction with light is Raman spectroscopy. Raman spectroscopy uses a high power monochromatic light source to measure the change in energy of light scattered by a material.

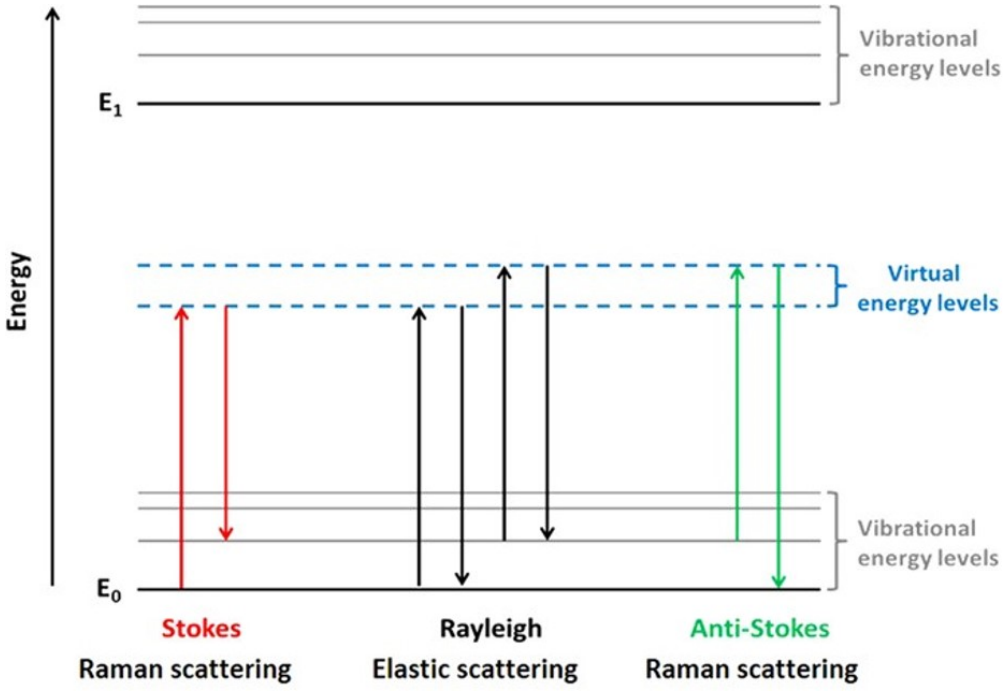



Figure 4.3: **Raman Spectroscopy:** Image showing the different scattering mechanisms for light interacting with a material. Image reproduced from ref.[217]

The scattering processes that can occur in a material are shown in Fig. 4.3. The most common is Rayleigh scattering, in which a photon excites an electron to a virtual excited state, the electron decays from this virtual excited state, emitting a photon with the same energy as the absorbed photon. For approximately 1 in 100 million photons Stokes or anti-Stokes scattering occurs.[217] For Stokes scattering, the absorbed photon drives atomic vibrations in the material, these atomic vibrations generate a phonon, when the electron decays from

the virtual excited state it releases a photon with lower energy than the absorbed photon. The energy of the emitted photon is reduced due to the energy lost to the generation of the phonon. Anti-Stokes scattering is a similar process in which the photon is absorbed by the material already in an excited state, when the electron decays from the virtual energy level, it decays to the ground state, emitting an photon that is higher in energy than the absorbed photon.[214] Both these processes cause a change in the frequency of the scattered light, which is given by

$$\nu = \frac{1}{\lambda_i} - \frac{1}{\lambda_s} \tag{4.3}$$

where $\lambda_i$ and $\lambda_s$ are the wavelength of the incident and scattered light respectively and $\nu$ is the frequency change. The intensity distribution of $\nu$ can be used to determine a wide variety of material properties, from the phase of the material to its defect density.[218] The Raman spectroscopy presented in this work was carried out by Dr. Tian Carey.

## 4.2 Morphological characterisation

Knowledge of the morphology of a network is important to understand its properties and allows for optimisation for the desired application. The morphology of nanosheet networks can be interrogated by both microscopy techniques and physical measurements, as discussed in Chapter 3.3.3. The simplest method to interrogate a network's morphology is to examine its surface using a microscope. This can be carried out with an array of microscopes, allowing for the morphology to be understood at different length scales. However, the amount of information that can be gained from surface images is limited. To understand the internal morphology of a material, tomography is required. Tomography refers to a technique that allows for the generation of a 3D image of the internal structure of an object. Tomography is widely used in medicine, with computed tomography (CT) and magnetic resonance imaging (MRI) scans both being types of tomography. In recent years, there has been an increase in the use of tomography in the field of material science, imaging the internal structure of a wide variety of materials from shale rock,[219] to high-entropy alloys,[220] and devices from fuel cells,[221] to batteries.[222] As with surface microscopy, a wide variety of tomographic techniques have been developed, allowing for everything from the visualisation of the position of each atom in a small volume of a material to viewing the structure of a material over several centimetres with a resolution of microns.[223,224]

The choice of imaging technique for interrogating both the surface and the internal structure of a network is important, with different techniques having different contrast mechanisms, resolutions and field-of-views (FOVs). When imaging nanosheet networks, an imaging technique with sufficiently resolution to image the individual nanosheets within the network and sufficient FOV to capture hundreds if not thousands of nanosheets is required. This section discusses SEM as a technique for imaging the surface of a material, focused ion beam (FIB) microscopy as a technique to image, deposit material, and remove material from

a sample. The combination of both techniques into a tomographic technique, FIB-SEM nt, is then be discussed. Finally, the use of image processing techniques for the extraction of quantitative information from images is described.

### 4.2.1 Scanning electron microscopy (SEM)

SEM is a microscopy technique that scans an electron beam over a material to image its surface. It is a versatile technique, used in an array of fields from biology to physics, to image a range of materials. It offers several different contrast mechanisms, allowing for a variety of different morphologies to be observed. The only requirement for imaging a material in the SEM is that the surface is conductive and grounded.

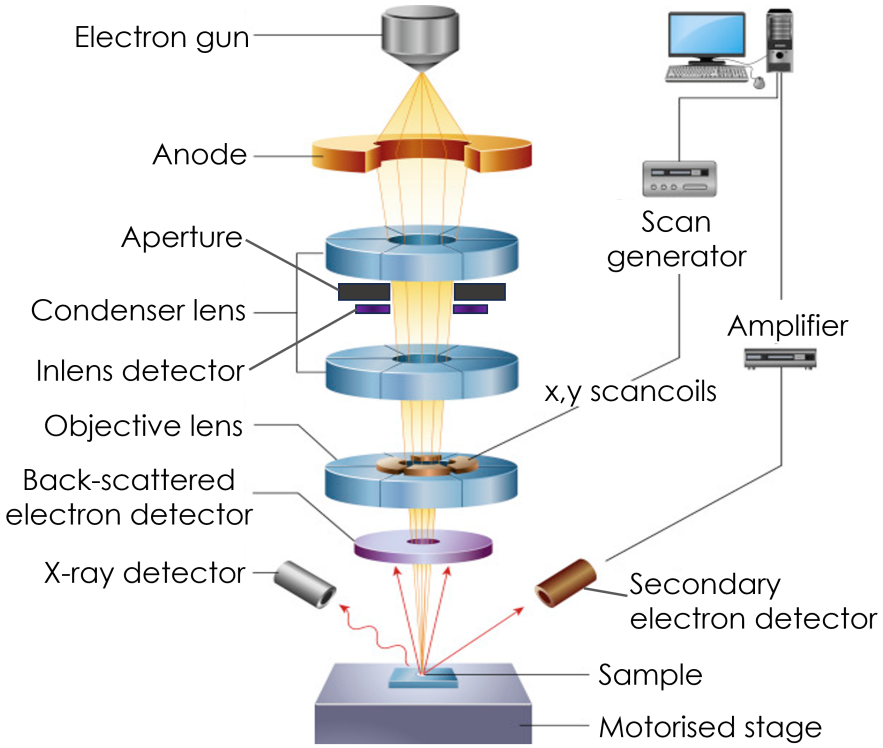



Figure 4.4: **Scanning electron microscope:** Schematic showing the components of a SEM similar to the one used in this work. Adapted from ref.[225]

The SEM uses the interaction of a focused electron beam with the surface of a material to generate an image of its surface. A schematic showing the key components of an SEM can be seen in Fig. 4.4. The electron beam is generated by field emission from a tungsten tip, the tungsten tip is sharp, approximately 100 nm in diameter, it is negatively charged and is close to a positively charged anode, which causes electrons to be emitted from the tip. The beam path and shape are controlled by electromagnetic lenses, which make use of the interaction of electrons with a magnetic field. The condenser lens reduces the beam width before the beam is passed through an aperture, which controls the beam current by physically blocking some of the beam.[226] An objective lens is used to focus the beam onto a small area, the area of the beam controls the maximum possible resolution of the SEM. Beam diameters as low as 0.7 nm have been achieved. The objective lens also defines the

energy of the electron beam, this affects the depth that signals are emitted from the sample and the resolution of the image.[227] XY scan coils are used to raster the SEM beam over the surface of the material. At each point that the SEM beam passes over, it interacts with the sample, causing the emission of a wide variety of signals.

Fig. 4.5A shows the different signals that are emitted from a sample as it interacts with the SEM beam. The signals that are most commonly measured are secondary electrons (SEs), backscattered electrons (BSEs), and X-rays. Both BSEs and X-rays can be used for compositional analysis. BSEs are electrons that have undergone Rutherford scattering, having been reflected back in the direction of the incident beam. The likelihood of a charged particle being backscattered by a nucleus scales with its atomic number. Therefore, BSEs offer the ability to differentiate between regions with different average atomic number.[228] This technique does not, however, identify the elements present. Analysis of X-rays emitted from a sample during the imaging process allows for the determination of the chemical composition of the sample. When an electron beam interacts with the sample, it generates X-rays which can be divided into 2 categories: Bremsstrahlung and characteristic X-rays. Bremsstrahlung are X-rays emitted from a sample due to electrons undergoing a sudden change in direction, these X-rays can take a wide range of energies and don't offer information on the composition of the sample.[229] Characteristic X-rays are emitted when the electron beam causes the emission of a core electron from an atom in the sample, a higher energy electron then decays from an outer shell into the vacated level, as it does so, it emits an X-ray, the energy of this X-ray can be used to identify the element for which it occurred.[230] The use of characteristic X-rays to identify the elements in a material is called energy-dispersive X-ray spectroscopy (EDS).

Surface images in the SEM are obtained from SEs, a SE is defined as an electron that has an energy of less than 50 eV. SEs are electrons that are emitted from close to the surface of the material due to inelastic scattering of the electron beam within the sample, knocking electrons from their position, a portion of these electrons are then emitted from the sample surface.[233] SEs can be divided into several categories, the first, called SE1 are electrons emitted from near the surface, these electrons tend to have higher energy and are collected by the Inlens detector, which is located inside the pole piece of the SEM, shown in Fig. 4.4.[234] The electrons are attracted to this detector by the magnetic field outside the pole piece and are then detected by an annular semiconductor detector.[235] The second type of SEs collected are called SE2, these are electrons that undergo multiple scattering events before exiting the sample, these electrons tend to have lower energy than the SE1 and are collected by an Everhart–Thornley (ET) detector.[234] An additional signal, detected by the ET detector, which introduces noise into the image are the SE3, which are electrons produced by the interaction of electrons or X-rays with internal components of the microscope. The ET detector uses a positively charged grid to attract electrons, which are then incident on a scintillator tube which produces photons, the photons then travel down a light guide to a photocathode, that converts them back to electrons which travels

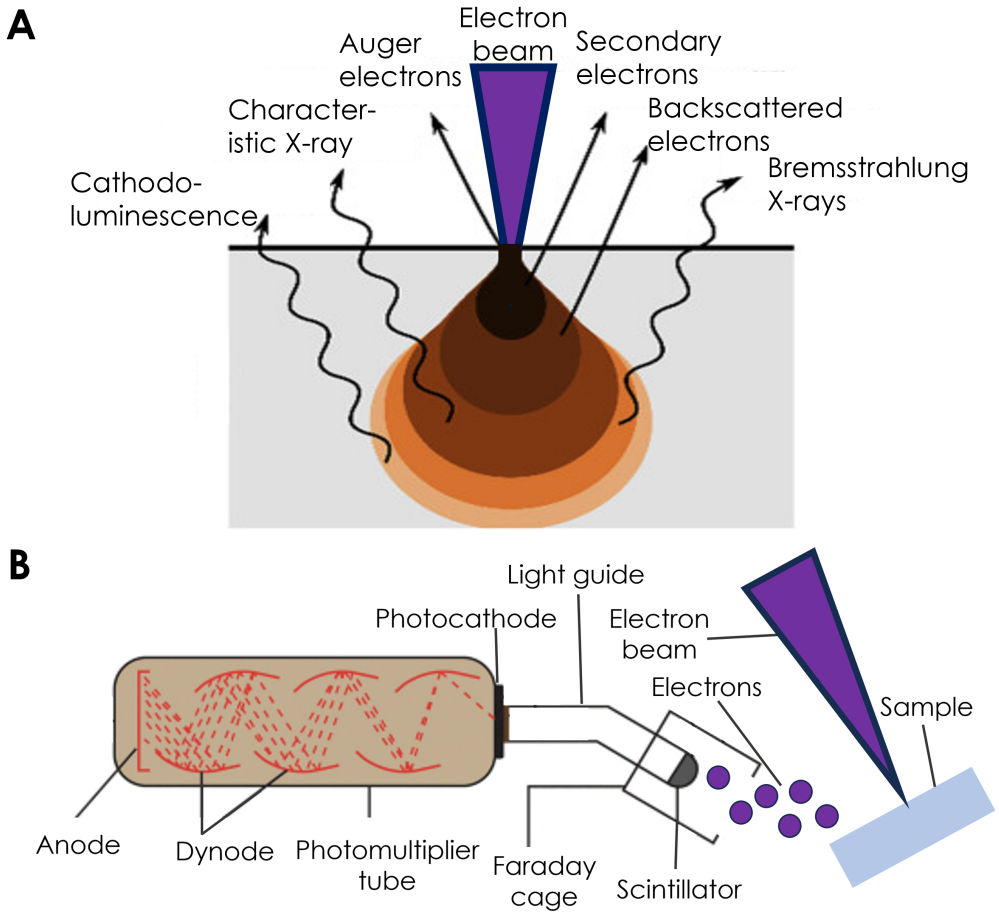



Figure 4.5: **Interaction volume and electron detection: A)** Image showing the interaction of an electron beam with a sample, showing the depth from which signals are emitted. Adapted from ref.[231] **B)** Schematic showing the detection mechanism of an Everhart-Thornley detector. Adapted from ref.[232]

down a photomultiplier tube, increasing the signal intensity before the signal is collected.[236] A schematic of an ET detector can be seen in Fig. 4.5B.

The region of the sample that interacts with the electron beam, from which the signals are released, is called the interaction volume. The size of the interaction volume depends on the energy of the incident beam, with increasing energy leading to far larger interaction volumes, decreasing the resolution of the images obtained. The increase in the depth of the interaction volume at higher energy causes the information obtained to be less surface sensitive, as electrons from deeper within the sample have enough energy to escape.[237] However, the spot size of the electron beam on the sample is energy dependent, with higher energies allowing for a smaller spot size on the sample surface. Therefore, to maximise the resolution of SEM images there is an ideal value for the accelerating voltage.[238]

### 4.2.2 Focused ion beam (FIB) microscopy

A FIB microscope offers a range of functionalities, allowing for the removal and deposition of material, as well as the imaging of a sample. A FIB microscope has a similar operating

principle to a SEM; the main difference is that it uses a focused beam of ions, instead of electrons. A wide variety of ions can be used for a FIB, with gallium, and xenon being the most common, this section will focus on the gallium FIB, which is used in this work.

A gallium ion beam is produced by heating gallium so that it wets a tungsten tip that is 2-5 $\mu$m in diameter. An electric field is then used to ionise Ga atoms to form $Ga^+$, the combination of the electrostatic and surface tension causes the liquid $Ga^+$ to be drawn into a thin cone, which is ~5 nm in diameter, this is called the Taylor cone. When the electric field experienced by the $Ga^+$ ions exceeds a critical value, a beam of $Ga^+$ is then emitted and accelerated down the FIB column.[239] This process is shown in Fig. 4.6A. The focusing of an ion beam requires a different process than an electron beam. The strength of electromagnetic lenses used to focus the electron beam in the SEM are related to the charge to mass ratio of the particles, due to the large mass of the ions electromagnetic lenses are ineffective, so electrostatic lenses are used instead.[240] Controlling the beam current is particularly important as it impacts the rate of both material removal and deposition, as in the SEM, an aperture is used to control the beam current.[241]

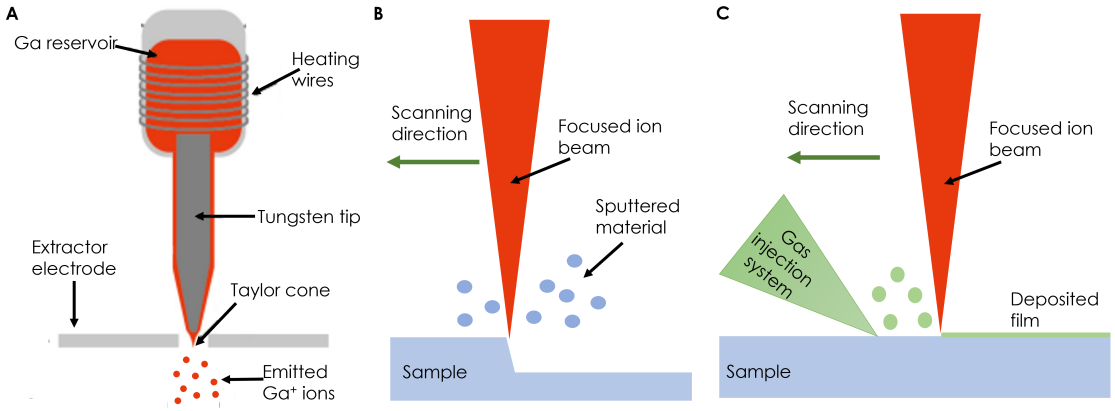



Figure 4.6: **Focused ion beam microscope: A)** Image showing a gallium liquid metal ion source. Adapted from ref.[239] **B)** Image showing a FIB removing material from the surface of a sample. **C)** Image showing a FIB being used to deposit a film on the surface of a sample.

The interaction of a FIB with a sample is quite different from an electron beam due to the mass of the ions. The ions can interact with the electrons within the sample and undergo inelastic scattering events, which leads to the emission of the same signals that are obtained in the SEM. These signals can be used to image the surface of the sample. The ions can also undergo elastic interactions with the nuclei in the material, which due to the high energy of the incident beam, can cause the removal of material from the surface, this is called sputtering. Here, the ion collides with an atom in the sample, if the energy transferred exceeds a critical value (~20 eV) the atom is removed from its site and a vacancy is created, if this vacancy is created near the surface of the material the atom can be emitted from the sample. If the sputtered atom has sufficient energy, it can repeat the process, meaning that a single ion can lead to the removal of as many as 20 atoms from the sample.[240] The rate at which sputtering occurs, called the milling rate, is still not fully understood, but it is known

that it depends on a number of factors, including the ion beam current and energy, and the average atomic number of the sample.[241] For crystalline materials, ion channelling can occur, channelling is a process where ions can travel preferentially through certain directions of a crystal, which reduces the milling rate in that direction.[240] While sputtering limits the resolution of the FIB, it can be utilised for a number of applications, from the cutting of viewing trenches to image the internal structure of a material, to the cutting of a thin slice from a material so that it can be imaged in a higher resolution microscopes, such as the TEM.[241]

As well as imaging and removing material, the FIB can be used to deposit both metallic and insulating materials on the surface of a sample, the process by which this is achieved is called ion beam induced deposition (IBID). In this process, a needle called the gas injection system (GIS) is used to inject a gas near the surface of the sample. In the case of metal deposition, an organometallic precursor gas is used and for insulating deposits, a silane based gas is used.[242,243] The gas is absorbed onto the surface of the sample, and when the ion beam is incident on it, it decomposes, with the metallic or insulating material forming a film on the surface of the sample. The rate of this process is controlled by the beam current and energy, with higher currents leading to faster deposition rates.[244] This process can be used to pattern electronic devices on the surface of a material.[245] A metal layer on the sample's surface can also be used to prevent damage to a region-of-interest (ROI) during milling.[241]

Due to the resolution limitations of FIB microscopes, they are generally produced as dual beam instruments, with both an electron and ion beam, called a dual beam focused ion beam-scanning electron microscope (FIB-SEM). This setup allows for the use of the FIB to sputter and deposit material and the electron beam to image the sample. These instruments have the electron beam and FIB beam at an angle of ~50° so that sputtering by the FIB and imaging by the electron beam can be carried out concurrently. This angle also allows for imaging of the internal structure of the sample with the electron beam after a viewing trench has been created by the FIB. This instrument has been extended to allow 3D imaging of a sample by FIB-SEM nt.

### 4.2.3 Focused ion beam-scanning electron microscope nanotomography (FIB-SEM nt)

FIB-SEM nt is a destructive tomography technique that uses the FIB to remove material from a cross-section face and the SEM to image the exposed cross-section, this process is repeated hundreds of times. The technique is very versatile and can be used to image a wide variety of materials and devices.[221,222,224,246] FIB-SEM nt can be combined with EDS to characterise the distribution of elements in a material.[247]

FIB-SEM nt can be carried out in by a variety of methods, with each company that makes

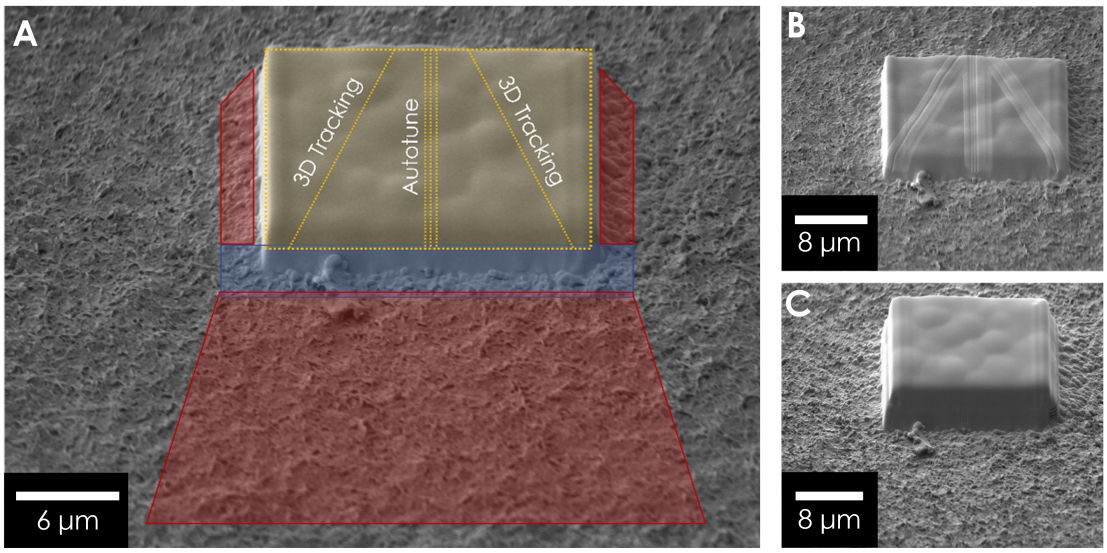



Figure 4.7: **Focused ion beam-scanning electron microscope nanotomography sample preparation: A)** SEM image showing a platinum pad (highlighted in yellow) on the surface of a spray-coated graphene network. The position that the 3D tracking and autotune lines will be etched into the pad are shown. The regions shown in red are milled with a high beam current and the region shown in blue is milled with a lower beam current. The regions marked in red and blue in front of the platinum pad are the viewing trench used to view into the sample, the region marked in red on each side of the platinum pad is the side trench used to prevent redepositon. **B)** Image of the same network as in A with the 3D track marks and the autotune marks etched into the platinum pad and filled with tungsten. **C)** Image showing the same network as in A,B with platinum deposited on top of the 3D tracking and autotune marks.

FIB-SEMs having their own method. This section discusses the version used in this work, which was carried out using the Zeiss Atlas 5 software. The setup for this method is outlined in Fig. 4.7. First, a pad of metal is deposited on the ROI, this prevents damage during milling. Next, lines are etched into the metal pad. The lines are then filled with another metal, which shows contrast in the SEM with the metal the pad is composed of. In this work, the metals used are platinum and tungsten. Which metal is used for which component is sample dependent, the metal used for the protective pad was chosen to maximise contrast between the sample and pad. The lines can be divided into two categories, the first are the 3D tracking lines, these two lines start at the edge of the metal pad and move back towards its centre at a known angle, as can be seen in Fig. 4.7A,B. The movement of these lines from the edge to the centre of the platinum pad can be used to measure the thickness of each slice removed from the cross-section face. The three central lines, called the autotune lines in Fig. 4.7A, are used to periodically ensure that the SEM beam is in focus during the imaging procedure.[248] An additional layer of the metal that the pad is composed of is deposited on the lines, this protects the lines during the milling procedure and improves their contrast, shown in Fig. 4.7C.

To view the sample's internal structure with the SEM, a viewing trench is milled into the sample, the geometry of the viewing trench is shown in red in Fig. 4.7A. The size of the

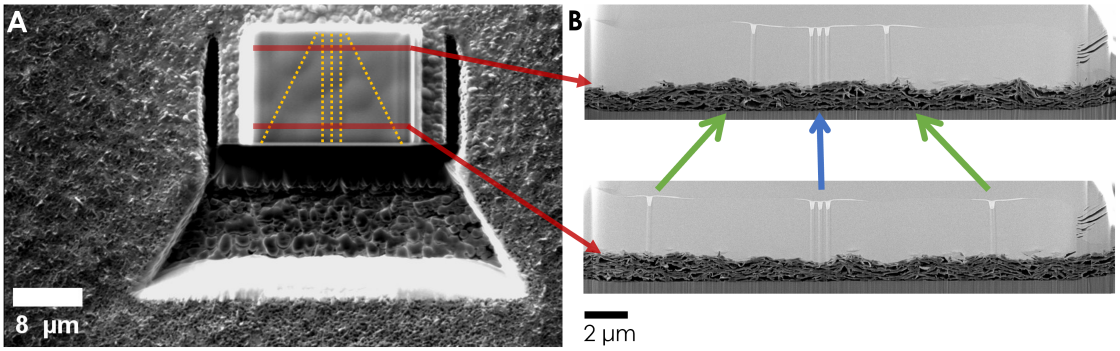



Figure 4.8: **Focused ion beam-scanning electron microscope nanotomography slicing procedure: A)** FIB image showing the network in Fig. 4.7 with the viewing and side trenches milled from the sample. **B)** Cross-sectional SEM images from the start and end of a FIB-SEM nt run showing the movement of the 3D tracking marks from the edge to the centre of the platinum pad. The autotune lines do not move during the imaging process.

trench controls the depth into the sample that can be viewed. Trenches are also milled on either side of the ROI. The area directly in front of the ROI is then milled with a lower beam current to prevent sample damage, this area is shown in blue in Fig. 4.7A. Fig. 4.8A shows the sample surface after the milling procedure has been carried out. After the milling has been completed, the cross-section can be viewed in the SEM. The FIB beam current is then reduced to the current to be used for the slicing procedure, the choice of beam current here is important: low currents cannot mill as deeply into the sample, while large currents can cause curtaining.[249] The beam then removes slices from the face of the cross-section; the 3D tracking lines are used to measure the thickness of each slice removed. The movement of the tracking marks as viewed by the SEM is shown in Fig. 4.8B, the software uses this information to ensure that a consistent slice thickness is maintained during the imaging procedure. Imaging occurs at the same time as slicing to ensure rapid imaging.

There are a number of artefacts which affect the quality of images obtained from FIB-SEM nt. Firstly, sample charging can be an issue, during the setup procedure the SEM and FIB beams are not incident on the sample at the sample time, but during the imaging procedure they are, the increase in current during the imaging procedure can cause sample charging to become a problem.[249] Furthermore, in the case of printed electronic devices, like the ones imaged in this work, the substrate is non-conductive, imaging these devices requires imaging of the substrate, which can cause charging. Therefore, when carrying out FIB-SEM nt, it is particularly important to ensure that the sample is well grounded to minimise charging. Fager *et al.* have demonstrated that non-conductive materials can be imaged by FIB-SEM nt by using the GIS to inject carbon gas near the cross-section face after each milling step to remove charge build up, however, this slows the rate of imaging considerably.[246]

Another artefact that can be encountered during FIB-SEM nt is curtaining. The rate at which a material is milled by a FIB is dependent on its density. Local variations in density can cause variations in the rate at which a sample is milled, this can prevent the cross-

sections from being flat, which reduces the accuracy of values calculated from the images. The metal pad used to protect the sample reduces curtaining as it makes the density of the sample more similar throughout the ROI.[250] Curtaining can also be reduced by using a low beam current.[246]

Two artefacts that can affect the quality of images obtained from porous materials by FIB-SEM nt are redeposition and the shine-through effect. Both of these effects reduce the measured porosity and related parameters. Redeposition describes the process by which sputtered material can diffuse into the pore volume and deposit there. The side trenches milled on either side of the ROI in Fig. 4.8A are designed to reduce the effect of redeposition.[251] Redeposition is also affected by the beam current, with large currents causing an increase.[252]

The shine-through effect describes the phenomenon of signals escaping from inside pores during the FIB-SEM nt imaging procedure. The simplest method to avoid the shine-through effect is to fill the pores with resin, so that all the signals come from the cross-section face, however, this can change the structure of the sample.[253] Alternatively, this effect can be minimised through the use of a low energy electron beam, which reduces the number of electrons which have sufficient energy to escape from inside the pores.[254] The choice of detector can also affect the shine-through effect, the electrons collected by the SE2 detector are lower energy than the electrons collected by the Inlens or BSE detector, which leads to a reduction in shine-through for images from this detector.[255]

### 4.2.4 Image processing techniques

Images without any processing allow for qualitative observation of a variety of phenomena, from differences between two samples to the structure of the interface between two materials. However, to extract quantitative information from an image, image processing techniques are required. This section discusses image processing, with a focus on the techniques required to analyse FIB-SEM nt images.

An image is a matrix with each entry describing the intensity of the pixel at that point. For a greyscale image, that is an image which does not contain any colour, each value in the matrix describes the intensity of the pixel at that point. For an 8-bit image values of 0 and 255 correspond to black and white respectively, with all the values in-between corresponding to varying intensities of grey. For a colour image, the image can be described by 3 matrices, which contain values for the intensity of red, green, and blue light at each pixel, the combination of these 3 colours allows for any colour to be generated.[256] This section focuses on image processing techniques for greyscale images.

The first step in an image processing pipeline is usually to segment an image into its components, for two phase segmentation this involves converting an image from a greyscale image to a binarised image, that is an image where the intensity at a given point tells you the

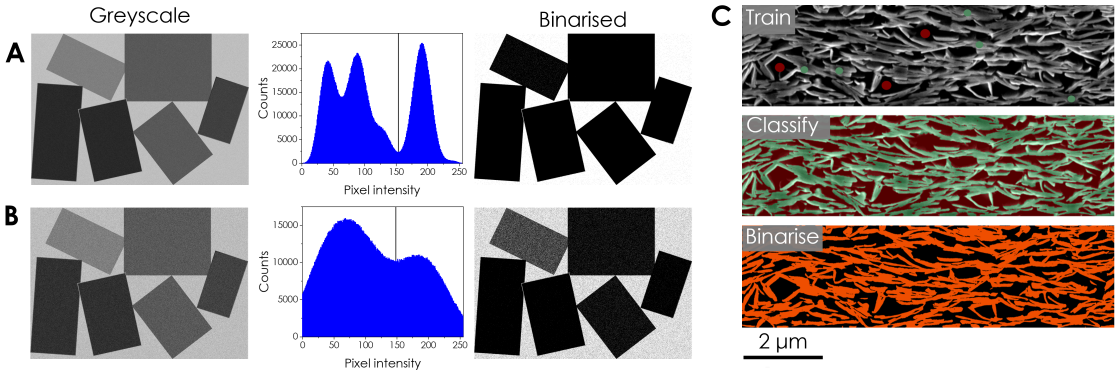



Figure 4.9: **Image segmentation: A)** Schematic explaining the mechanism of thresholding for image segmentation. An image can be thresholded by finding the minimum point between the background and material peak in the intensity histogram, called the threshold, pixels above and below the threshold are defined as 2 distinct phases. This yields a binarised image with well defined features. **B)** Schematic showing the failure of thresholding for an image due to the noise present. In images with a large amount of noise, thresholding leads to noise in the binarised image. **C)** Image explaining the procedure of trainable WEKA segmentation on a spray-coated graphene network. First the algorithm is trained by marking material in the phases to be segmented, in this image nanosheet and pore. The algorithm then classifies the image into the nanosheet and pore components, the training can then be repeated until the classification is satisfactory. A binarised image is then produced.

phase of material. For an image with two well defined phases, segmentation can be achieved by thresholding, here the minimum point between the peaks in the intensity histograms is found, this value is called the threshold; values below the threshold are assigned to one phase and values above the threshold are assigned to the other phase.[257] The process of thresholding is shown in Fig. 4.9A. Thresholding can also be used to separate multiple phases in an image through the use of multiple threshold values.[258]

Thresholding is an effective method of separating two phases that show different intensities, however, in the majority of cases there will be some overlap in the intensity of the phases, due to the limitations of the imaging technique used. An image with a large amount of noise, for which thresholding is not suitable, is shown in Fig. 4.9B. In this cases, a more complex segmentation algorithm is required. A large number of algorithms have been designed for image segmentation.[256] The algorithm used in this work is trainable Waikato environment for knowledge analysis (WEKA) segmentation (TWS), which is a trainable machine learning based algorithm for image segmentation. TWS is based on the WEKA software, which is a free software that can be used for data visualisation and analysis. It uses a random forest classification algorithm, which has been shown to be effective for segmenting FIB-SEM nt images.[249] TWS is available in the open-source image processing platform FIJI.[259] This segmentation algorithm is capable of segmenting an image into any number of different phases. TWS has been used to classify data from an array of microscopy techniques for a range of applications.

The process of training the TWS algorithm to segment two phases is shown in Fig. 4.9C.

First, areas belonging to the different phases are manually marked in the image. The segmentation algorithm then applies a variety of filters chosen by the user to the image, each filter generates a new image. The filters are designed to distinguish a number of features in the image: Gaussian blur based filters remove noise, the mean, median, and mode filters detect textural features, the bilateral and Kuwahara filters detect edges, and the Lipschitz filter removes background.[259] The algorithm then segments the image using a random forest classifier with 200 decision trees. Each decision tree is trained on a different set of the training data, with the data assigned randomly, to prevent correlation between the trees. The decision tree uses the training data combined with the pixel intensity after filters have been applied to generate a model capable of determining the phase of each pixel. The ability of each decision tree to correctly determine the phase of a material is assessed and the quality of each decision trees are ranked. Each decision tree then votes on what phase each pixel in the image belongs to, and the votes are combined to calculate the probability that a given pixel belongs to a given phase.[260] The algorithm then overlays the outcome of the segmentation procedure on the original image so the result can be seen, training can be repeated until the segmentation algorithm is sufficiently precise. The algorithm can output a binarised image or a probability map; in the probability map the intensity of each pixel corresponds to the calculated probability that the pixel belongs to a given phase.

The segmentation algorithm also tests its results against the training data, the algorithm uses two-thirds of the input data for training and keeps the remainder to test the classification accuracy. The algorithm compares the results of the classification model to the input data for the data not used to generate the classification model. It uses this to calculate the out-of-bag error (OOB), which can be used to determine the quality of the image segmentation.[260] The OOB error can be used as a measure of the quality of the segmentation and can be used to determine the uncertainty in values calculates from the binarised images.

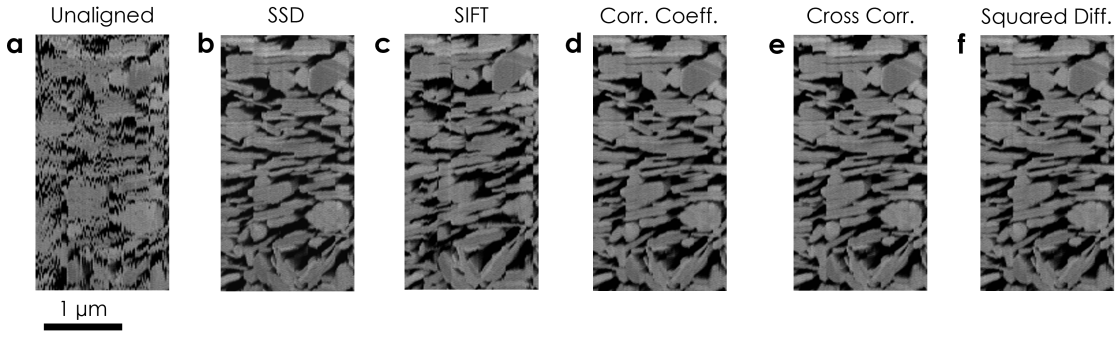



Figure 4.10: **Image stack alignment:** Reconstructed images, showing a view perpendicular to the slicing direction of a FIB-SEM nt image of a AgNS network. **A)** Image of the unalligned image stack.**B)-F)** Images of the same stack after alignment using **B)** Sum of square differences (SSD), **C)** Scale-invariant feature transform (SIFT) **D)** Correlation Coefficient, **E)** Cross-correlation and **F)** Squared difference matching algorithms. All images were aligned in Dragonfly.

FIB-SEM nt is a slice-and-view technique that can have misalignment between adjacent slices. The misalignment can happen for a number of reasons including sample charging, temperature variations, and mechanical vibrations during the imaging procedure.[261] Any value measured in 3D from FIB-SEM nt images will have an error introduced by the misalignment, therefore, the images must be aligned before analysis is carried out. Fig. 4.10 shows the view perpendicular to the slicing direction before alignment, and the same image aligned by a variety of different algorithms. All of these algorithms considerably improve the alignment of the data. The sum of square differences (SSD) algorithm offers the best trade-off between required computational power and quality of alignment, shown in Fig. 4.10B. The SSD algorithm determines the shift required to minimise the sum of the square difference between each pixel in each adjacent slice,[262] the image can then be shifted to this position. This process can be applied to a stack of images. After an image has been aligned and segmented, it can be used to generate 3D images and to calculate a wide variety of material properties. Chapter 5 discusses the morphological parameters of nanosheet networks that can be calculated from an aligned and binarised FIB-SEM nt image.

*"When Pan Gu died, his skull became the top of the sky, his breath became the wind and clouds, his voice the rolling thunder. One eye became the Sun and the other the Moon. His body and limbs turned into five big mountains, and his blood formed the roaring water. His veins became roads and his muscles turned to fertile land. The innumerable stars in the sky came from his hair and beard, and flowers and trees from his skin. His marrow turned to jade and pearls. His sweat flowed like the good rain and the sweet dew that nurtures all things on Earth."*

# 5

# The effect of nanosheet dimensions on network morphology

Solution-processed networks of nanomaterials show promise for a wide range of applications from energy storage, in devices such as batteries and supercapacitors,[137,263] to energy generation, in devices such as catalysts and thermoelectrics.[125,136] They also show promise for application in sensing a wide range of molecules,[264] and in printed electronic devices, such as capacitors, memristors, photodetectors and transistors.[82,138,140,265] In all of these devices, the morphology of the network has an impact on its performance. Despite the importance of network morphology, interrogation of it has proven difficult. Physical measurements allow for the calculation of some network properties such as porosity, pore shape and length, specific surface area (SSA) and nanosheet alignment.[126,170,192,199,201,266] However, these measurements cannot be applied to all networks, with techniques such as MIP and nitrogen adsorption/desorption isotherms requiring thick films (>100 $\mu$m),[199] which are time-consuming to produce and may not be representative of the thin films required for a variety of applications.

Tomography offers a solution to investigate network morphology that is applicable to a variety of materials, and can allow for the calculation of a range of morphological parameters. A wide array of tomography techniques have been developed to investigate a different materials and devices at a range of length scales. When choosing a tomography technique there is a trade-off between resolution and FOV, the best technique to use for a given application offers sufficient resolution and FOV to capture the morphology of the network. Very high resolution techniques such as 3D TEM and atom probe tomography allow for the imaging of individual atoms in small volume (<1 $\mu m^3$).[223,267] On the other hand, micro-X-ray computed tomography (CT) allows for imaging of materials over centimetre scale with a resolution of a few microns.[268] These techniques are not suitable for describing

networks of nanomaterials as they do not offer sufficient FOV and resolution, respectively. 3D images of networks of nanomaterials have been obtained using both nano-X-ray CT and FIB-SEM nt.[201,204,205] FIB-SEM nt generally offers a superior resolution to nano-X-ray CT, a few nanometres vs tens of nanometres, at the cost of a lower FOV, ~600 $\mu m^3$ vs. ~1000000 $\mu m^3$.[267] We suggest that the higher resolution of FIB-SEM nt makes it the ideal technique for imaging networks of nanomaterials, where feature sizes are often on the order of ~50 nm.

This chapter demonstrates the applicability of FIB-SEM nt to characterise the morphology of solution processed nanosheet networks. A wide range of morphological parameters such as network porosity, pore circularity, SSA, and nanosheet and pore tortuosity factor are calculated for size-selected networks of graphene, $WS_2$ and silver nanosheets (AgNSs), finding that the morphological parameters scale with nanosheet dimension. The technique is then extended to image heterostack devices. The penetration of silver nanoparticles (AgNPs) into graphene networks is measured and an electrical short in an out-of-plane $WS_2$ device is imaged, showing the power of this technique to characterise the morphology of a range of materials and devices. All of the work presented in this chapter was done in collaboration with Dr. Cian Gabbett. We shared the workload of producing the inks, depositing and imaging the networks, Cian carried out the image segmentation and Cian, Prof. Jonathan N. Coleman, Prof. Lewys Jones and I all suggested different components of the analysis which was carried out and is presented here.

## 5.1 Materials & Methods

Graphene inks were prepared by LPE as described in Chapter 2.2.3. Graphite powder (Asbury, Grade 3763) was first sonicated in 80 ml of deionised (DI) water (18.2 MΩ.cm) at a concentration of 35 mg.ml$^{-1}$ for 1 h. A horn probe sonic tip (Sonics Vibra-cell VCX-750 ultrasonic processor) at 55% amplitude, with a pulse rate of 6 s on 2 s off was used. The temperature was maintained at 7°C using a chiller. The resulting dispersion was centrifuged for 1 h at 2684× $g$ (Hettich Mikro 220R) to remove potential contaminants from the starting powder. The supernatant was decanted and the sediment redispersed in 80 ml of DI and sodium cholate (DI:SC) (SC, Sigma Aldrich, >99 %) at a concentration of 2 mg.ml$^{-1}$. It was then sonicated for 8 h at an amplitude of 55% with a 4 s on 4 s off pulse rate. The resulting dispersion was separated into size-selected inks by LCC.[130] An initial centrifugation step at 28× $g$ for 2 h was used to isolate unexfoliated material in the sediment. The supernatant was then subjected to additional centrifugation steps at 112× $g$, 252× $g$, 447× $g$, 699× $g$ and 1789× $g$, for 2 h, retaining the sediment at each interval to isolate nanosheet fractions of different sizes. In each case the sediment was redispersed in a 2 mg.ml$^{-1}$ DI:SC solution. The redispersed 112× $g$ ink was subjected to a further centrifugation step at 28× $g$ for 1 h to separate it into two size fractions.

Each ink was then transferred to IPA (Sigma Aldrich, HPLC grade) for spray coating. To remove the SC, dispersions captured below 1066× $g$ were centrifuged at 4052× $g$, while material captured above this speed was centrifuged at 25155× $g$. The supernatant was discarded, and the sediment redispersed in IPA. This step was then repeated.

$WS_2$ inks were produced in a similar manner, however, the sonication of bulk powder (Alfa Aesar, 10 - 20 $\mu$m, 99.8%) was carried out in IPA. The size-selected inks were produced by centrifugation steps at 112× $g$, 252× $g$, 447× $g$, and 4052× $g$.

Size-selected AgNS inks were produced by diluting the purchased dispersion (Tokusen Nano, N300, $l_{NS} \approx$ 300 - 500 nm) in DI water to a concentration of 100 mg.ml$^{-1}$. This stock dispersion was then centrifuged at 28× $g$, 112× $g$, 447× $g$ and 4052× $g$ in 5 min steps. The sediment of the 112× $g$, 447× $g$ and 4052× $g$ steps was collected and redispersed in DI water.

AFM (Bruker Multimode 8, ScanAsyst mode, non-contact) was used to measure the nanosheet thickness and lateral dimensions in the size-selected graphene, $WS_2$ and AgNS inks. Measurements were performed in air under ambient conditions using aluminium coated silicon cantilevers (OLTESPA-R3). The inks were diluted to optical densities < 0.1 at 300 nm and a drop of dispersion (15 $\mu$l) was flash evaporated on pre-heated (175°C) $Si/SiO_2$ wafers. After deposition, the wafers were rinsed with ~15 ml of DI water and ~15 ml of IPA and dried with compressed nitrogen. Typical image sizes ranged from 10 × 10 $\mu$m$^2$ for larger nanosheets to 3 × 3 $\mu$m$^2$ for small nanosheets at scan rates of 0.5 - 0.8 Hz with 1024 lines per image. Previously published length corrections were used to correct lateral dimensions from cantilever broadening.[86,207]

UV-Vis optical spectroscopy (Perkin Elmer 1050 spectrophotometer) was performed to determine the graphene and $WS_2$ ink concentrations using previously developed metrics.[207,209] Inks were diluted to a suitable optical density and extinction spectra were recorded in 1 nm increments using a 4 mm quartz cuvette. The concentration of the size-selected AgNS inks was found by vacuum filtration of a known volume of ink onto an alumina membrane (Whatman Anodisc, 0.02 $\mu$m pore size) and weighing.

Nanomaterial inks were spray coated using a Harder and Steenbeck Infinity Airbrush attached to a computer-controlled Janome JR2300N mobile gantry. A $N_2$ back pressure of 45 psi, nozzle diameter of 0.4 mm and stand-off distance of 100 mm between the nozzle and substrate were used. All traces were patterned using stainless-steel masks while the substrate was heated to 80°C using a hotplate. The size-selected LPE graphene inks were sprayed at a concentration of 0.2 mg.ml$^{-1}$ onto ultrasonically cleaned glass slides with prepatterned gold electrodes (Temescal FC2000 metal evaporation system) to facilitate electrical measurements (presented in Chapter 6). $WS_2$ inks were spray coated at a concentration of 0.5 mg.ml$^{-1}$ onto cleaned glass slides. The AgNS inks were deposited at a concentration of 10 mg.ml$^{-1}$ onto $Al_2O_3$-coated PET (Mitsubishi Paper Mills) at a tem-

perature of 100°C. $WS_2$ heterostack devices were spray-coated onto a purchased ITO:glass substrate (Ossila, 100 nm thick ITO, 2 $\mu\Omega$.m) and a 100 nm gold top electrode was deposited by gold evaporation. AgNP top electrodes were deposited on spray-coated graphene networks by diluting AgNP dispersions (Sigma Aldrich, <50 nm diameter, 30 – 35 wt% in methyltriglycol) to 20 mg.ml$^{-1}$ and deposited using an aerosol jet printer (Optomec AJP300).

For the FIB-SEM nt and SEM microscopy the samples were directly mounted on an aluminium stub using a conductive carbon tab (Ted Pella) and grounded using silver paint (Ted Pella). SEM of the network surfaces was performed using a Carl ZEISS Ultra Plus SEM at an accelerating voltage of 2 kV (5 mm working distance, 30 $\mu$m aperture, Inlens detector). FIB-SEM microscopy of network cross-sections was carried out using a dual beam Carl ZEISS Auriga system. All images were captured at a working distance of 5 mm with a 2 kV accelerating voltage and aperture size of 30 $\mu$m. FIB-SEM nt was performed using ZEISS ATLAS 5 software (Version 5.3.3.31). All materials were imaged using a platinum top pad, with tungsten tracking and auto-focus marks. All milling of network cross-sections was carried out using a 30 kV:600 pA gallium ion beam. The images were captured with a slice thickness of 15 nm.

The generated image stacks for each network were aligned and reconstructed in 3D using Dragonfly (Version 2022.1.0.1231, Object Research Systems). Greyscale network cross-sections were segmented using the trainable WEKA segmentation (TWS) plugin in FIJI.[259,269] Porosity, pore area and circularity were calculated in FIJI.[269] Tortuosity factor and SSA were calculated using Taufactor.[270] Nanosheet length and thickness was calculated using the ridge detection plugin in FIJI.[269,271] Nanosheet orientation was calculated using the 3D distance transform watershed and fit ellipse functions in the Morpholibj plugin in FIJI.[269,272]

## 5.2 Results & Discussion

### 5.2.1 Characterisation of size-selected inks

Graphene dispersions were produced by ultrasonication of graphite powder in a sodium cholate:DI water solution (DI:SC). The resulting ink was then size-selected by LCC.[130] The dispersions were then transferred to IPA. UV-vis spectroscopy was carried out to calculate the ink concentration. The resulting extinction spectra can be seen in Fig. 5.1A. At high wavelengths the extinction spectrum is independent of nanosheet size and all the size-selected inks show similar behaviour. As the centrifuge speed at which the nanosheets are captured at is increased, the intensity of the low-wavelength peak in the extinction spectrum increases. It has been found that the intensity of this peak is related to the thickness of the nanosheets present. Using the nanosheet size-independent extinction coefficient

of graphene, the dispersion concentration was calculated, and each ink was diluted to 0.2 mg.ml$^{-1}$ for spray-coating.[209]

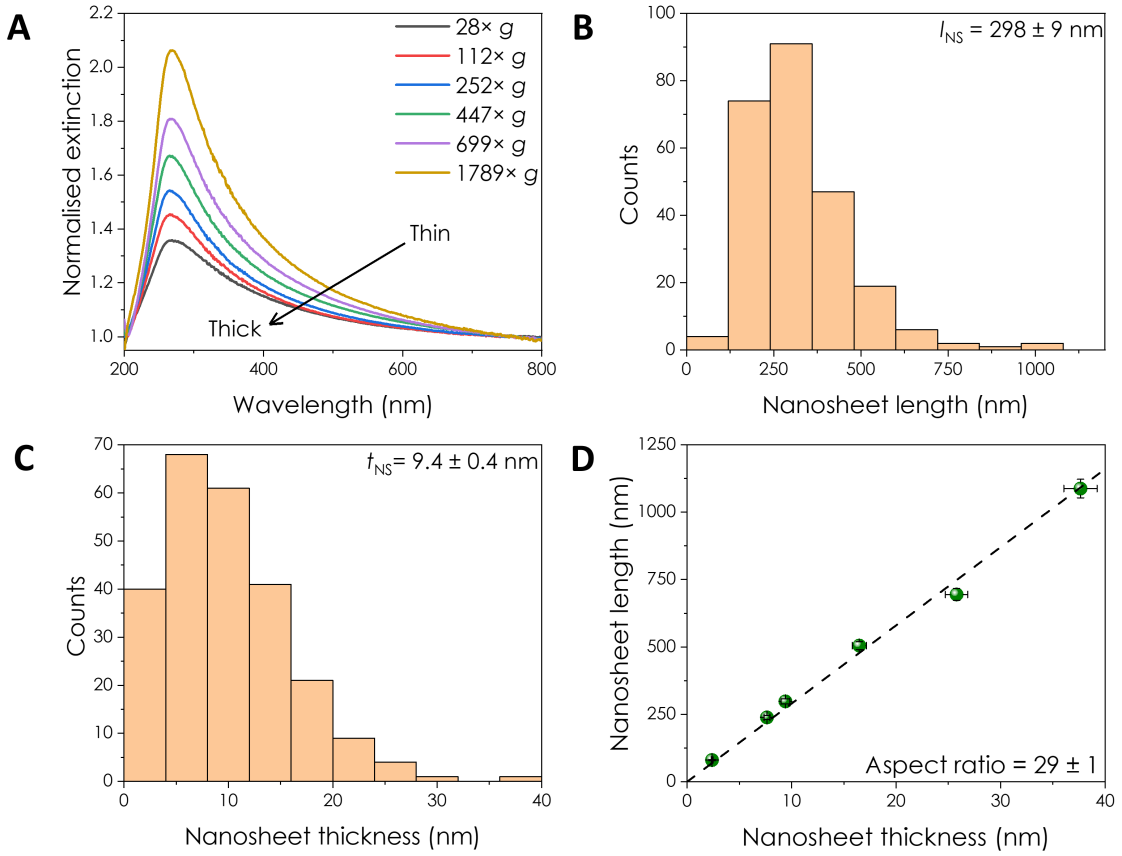



Figure 5.1: **Size-selected graphene ink characterisation: A)** UV-vis spectrum of the size-selected graphene inks in IPA. The spectra were normalised at 750 nm. **B)** Nanosheet length distribution, calculated by AFM, for the ink captured below 447× $g$, showing an average nanosheet length of $l_{NS}$= 298 ± 9 nm. **C)** Nanosheet thickness distribution, calculated by AFM, for the ink captured below 447× $g$, showing an average nanosheet thickness of $t_{NS}$= 9.4 ± 0.4 nm. **D)** Nanosheet length vs. thickness for the size-selected inks. Dashed line shows a linear fit to the data, demonstrating that the nanosheets have a constant aspect ratio of 29 ± 1.

To calculate the length and thickness of the nanosheets, in each of the size-selected inks, AFM was carried out, as described in Chapter 4.1.1. The AFM was done by Dr. Kevin Synnatschke. Representative nanosheet length and thickness distributions can be seen in Fig. 5.1B,C. Both the nanosheet length and thickness are lognormally distributed, as has been found previously for a variety of materials produced by LPE.[86,132] Both measured values decrease with increasing centrifugation speed. The calculated length and thickness of each of the 6 size-selected inks can be seen in Fig. 5.1D. As discussed in Chapter 2.2.3, nanosheets produced by LPE have an approximately constant aspect ratio (nanosheet length divided by nanosheet thickness). Fig. 5.1D shows that the size-selected inks have a constant aspect ratio of 29. This aspect ratio is lower than what has been reported in the literature for LPE graphene produced by ultrasonication of graphite in DI:SC,[86] this may be due to an irreversible re-aggregation of the nanosheets during the transfer from DI:SC to IPA. IPA

is a worse solvent for stabilising graphene than DI:SC; however, removal of the surfactants is required to obtain highly conductive networks.[82,111,126,273]

### 5.2.2 Microscopy of printed networks

The size-selected graphene inks were then spray coated onto glass slides, with predeposited gold electrodes patterned on them; the electrical properties of the networks are discussed in Chapter 6. SEM images of the surface of each of the networks can be seen in Fig. 5.2. From these images the length and morphology of the nanosheets in the network can be seen. The SEM images also show morphological differences between the networks printed from large and small nanosheets. Networks of small nanosheets appear to be more densely packed and have a reduced surface roughness when compared with networks composed of larger nanosheets. However, no quantitative morphological information about the networks can be calculated from surface SEM images.

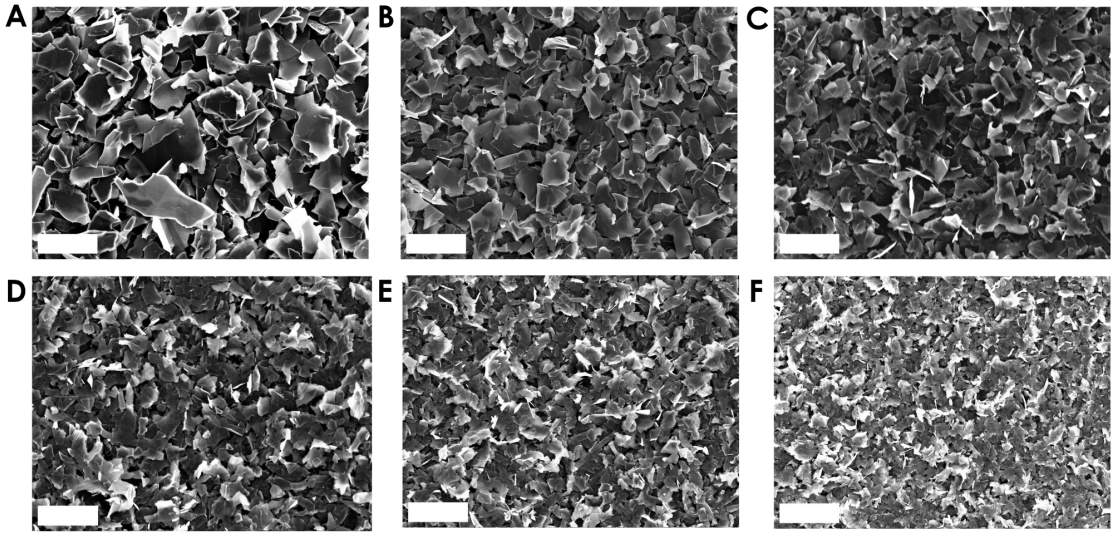



Figure 5.2: **Surface morphology of size-selected graphene networks: A-F)** SEM images of the surface of networks sprayed from the size-selected graphene inks, with decreasing nanosheet size. Scale bar in each image is 2 $\mu$m.

In order to quantitatively interrogate the morphological properties of the printed networks, FIB-SEM nt was carried out on each film. The procedure for FIB-SEM nt is described in Chapter 4.2.3. FIB-SEM nt was carried out with an in-plane pixel size of 5 nm and a slice thickness of 15 nm, giving anisotropic voxels (the 3D analogue of a pixel) with a size of 375 nm$^3$. The images were captured for volumes of approximately 20$\times$ 15$\times$ 2 $\mu$m$^3$, meaning that the images are composed of ~1$\times$ 10$^9$ voxels. For all the FIB-SEM nt data presented in this work, the images were captured using the SE2 detector to minimise the shine-through effect.[255] Individual cross-sections from a subset of the size-selected networks can be seen in Fig. 5.3A. From the individual cross-sections it is clear that the morphology of the networks changes considerably as the size of the constituent nanosheets is decreased. It appears there is a decrease in porosity, as well as pore cross-sectional area,

as the nanosheet size decreased. To gain quantitative information from the images, image processing is required, as discussed in Chapter 4.2.4.

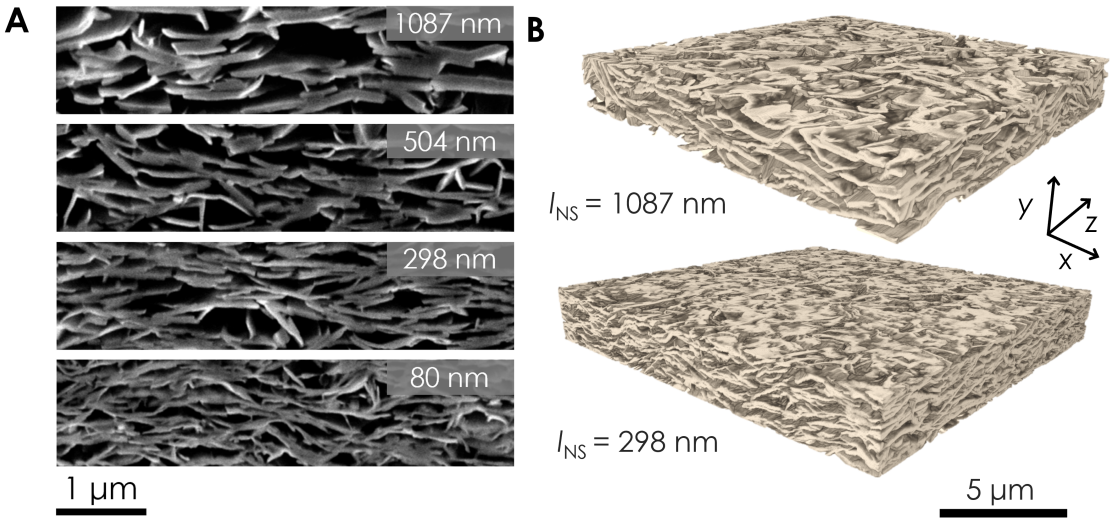



Figure 5.3: **Cross-sections and 3D images of size-selected graphene networks A)** Individual cross-sections of the networks with nanosheet lengths of 1087 nm, 504 nm, 298 nm and 80 nm, showing the variation in morphology as the nanosheet size decreases. **B)** 3D image showing the nanosheet component of networks with nanosheets lengths of 1087 nm and 298 nm. The images have a common scalebar.

After the images were captured they were first aligned using the SSD algorithm in Dragonfly, as discussed in Chapter 4.2.4. Next the brightness and contrast of the images were adjusted to maximise the contrast between the phases. In order to quantitatively determine the properties of the networks, the image stack was then segmented using Trainable WEKA segmentation (TWS). This image segmentation algorithm is described in detail in Chapter 4.2.4. In short, it takes an input of training data and uses a series of different image filters in order to create decision trees which allow for the segmentation of an image into multiple components. The filters used were Gaussian filters, used to reduce the effect of noise, edge detection filters, including Sobel filters and Hessian matrix, used to ensure sharp boundaries between the phases, and textural features, such as the mean and variance, used to improve classification accuracy. Using this algorithm the size-selected graphene networks were separated into nanosheet and pores. A single classification algorithm was trained on a subset of images from each of the graphene networks. The training was repeated until the classification was visibly correct, and the out-of-bag (OOB) error was less than 2%. This classification algorithm was then used to classify all of the images. The resulting probability maps were binarised using the Isodata algorithm in FIJI.[269] The probability maps were used to generate 3D images of the networks in Dragonfly. A section of 2 of the 3D images is shown in Fig. 5.3B. The 3D images highlight that the morphological differences seen in the individual images can be seen across the whole region imaged, with the network composed of smaller nanosheets showing a less open, more condensed structure.

### 5.2.3 Morphological characterisation of printed graphene networks

From the binarised images a large amount of morphological data about the network can be calculated. To explain how this array of morphological information can be extracted from a 3D image, the network composed of nanosheets with length $l_{NS}$= 238 nm will be used as an example. All the morphological parameters are calculated using open source programs, which are accessible to everyone in the scientific community free of charge. The simplest network property to calculate from the binarised images is the porosity. The porosity of a network describes the amount of free space within the network and is calculated as a percentage of the network volume. Fig. 5.4A shows a 3D image of a network split into its nanosheet and pore components, showing the large amount of porosity present in the network. The porosity of the network can be calculated from the binarised images, as the ratio of voxels labelled as pore, to the total number of voxels. The porosity can be calculated for an entire network on a slice by slice basis in any direction. Fig. 5.4B shows the porosity in the network in the FIB slicing (z) direction, showing an average porosity of 41 $\pm$ 1%. The scatter in this data highlights the local inhomogeneity in the network. The inset shows the distribution of slice porosities; the data is normally distributed with a standard deviation of 1%.

Another important network parameter related to the porosity is the network SSA. The SSA of a network describes the surface area of the individual nanosheets which is available for gases or liquids present in the network to interact with. The SSA is a 3D parameter and so can only be calculated from 3D images or by physical measurements. The SSA can be described by the volumetric SSA, which corresponds to the amount of surface area per unit volume, or by the gravimetric SSA, which gives the surface area per unit mass. The volumetric SSA is calculated as area of the interface between the voxels labelled pore and the voxels labelled as nanosheet, divided by the network volume. The SSA was calculated using Taufactor.[270] The volumetric SSA of the network with $l_{NS}$= 238 nm was calculated as 27.7 $\pm$ 0.6 $\mu m^2.\mu m^{-3}$, which can be converted to a gravimetric SSA of 20.6 $\pm$ 0.6 $m^2.g^{-1}$. This value is considerably lower than the theoretical value for a graphene monolayer of 2630 $m^2.g^{-1}$.[29] This low gravimetric SSA is due to the thickness of the nanosheets in the ink, combined with the aggregation of the nanosheets that occurs during printing, which increases the effective thickness of the nanosheets in the networks and decreases the amount of the surface area available. Similar values of gravimetric SSA have been calculated for vacuum-filtered networks of graphene (~40 $m^2.g^{-1}$) and of vanadium oxide (~25 $m^2.g^{-1}$).[199,274]

The pore connectivity describes the total amount of porosity contained within a single connected pore network. It can be defined as the percentage of the total porosity within the region considered that is contained in the largest connected pore network. It is an important parameter as it controls the amount of the network surface area accessible to

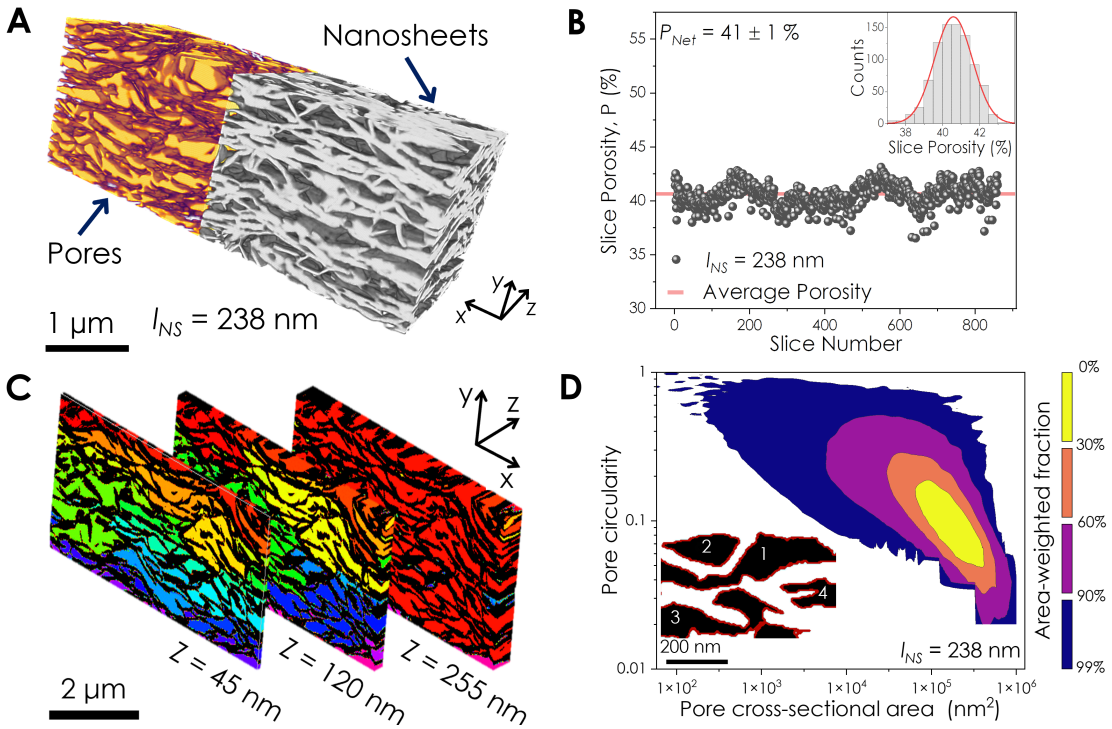



Figure 5.4: **Measuring network porosity: A)** 3D image of a network with $l_{NS}$= 238 nm, split into its nanosheet and pore components. Axes are shown, the z-direction is the FIB slicing direction. **B)** Porosity for the network with $l_{NS}$= 238 nm, in each slice in the z-direction, showing an average porosity of 41 ± 1%. The distribution of slice porosity is shown as an inset, a fit to the data with a normal distribution is shown. **C)** Image showing the increase in pore connectivity, for the network with $l_{NS}$= 238 nm, as the depth considered in the z-direction, is increased. Each colour denotes a single isolated pore network, with 95% of the porosity being contained within a single pore volume when a depth of 255 nm is considered. **D)** Heat map showing the relationship between pore circularity and pore cross-section area for the network with $l_{NS}$= 238 nm. The pore area weighted fraction describes how much of the total porosity is contained within each region. The inset shows 4 labelled isolated pores for which the circularity and pore area was calculated.

materials diffusing through the pores. The pore connectivity of the network was measured using the find connected regions plugin in FIJI,[269] this program finds voxels which are connected within a 3D image. Fig. 5.4C shows the increase in pore connectivity as the depth in the z-direction considered increases. This image shows the pore network, with each isolated pore volume being shown in a different colour. The pore connectivity increases from 4% to 95% as the depth considered is increased from 45 nm to 255 nm, showing the high degree of connectivity of the pores. For this network, and every network considered in this chapter, when the entire network is considered, the pore connectivity is greater than 99% demonstrating that all of the network's SSA is easily accessible.

Within a network, the volume and shape of the pore chambers are important parameters when considering the diffusion of both gases and ions through the material.[275] For the size-selected graphene networks presented here, the pores form a single connected volume, this means that analysis of the pore shape cannot be carried out in 3D without artificially separating the pore volume into chambers. Therefore, to describe the size and shape of

the pores, the pore cross-sectional area and circularity was calculated from each individual cross-sectional image. Here, the minimum pore size that could be measured was taken as 2 pixels, to avoid considering noise, this minimum size corresponds to a pore diameter of ~7 nm. This means only large mesopores (pores with diameters between 2-50 nm) and macropores (pores with diameter above 50 nm) are considered.[276] It has been found for graphene networks that a small portion of the total porosity and SSA is contained within micropores (pores with diameter <2 nm) and mespores,[199] therefore, not measuring these smaller pores is unlikely to significantly effect the calculated values. To compute the shape of the pores, the pore circularity was calculated. Circularity describes how close a shape is to being a circle, with a circularity of 1 denoting a perfect circle, while a circularity of 0 corresponds to a line. The circularity ($C$) of a shape is given by

$$C = \frac{4\pi A}{p^2} \tag{5.1}$$

where $A$ is the shape's area and $p$ is its perimeter. The pore area and circularity were calculated using the analyze particles function in FIJI.[269]

The total number of pores in each image is dominated by small pores, which do not contribute significantly to the porosity of the network. To understand the amount of the total porosity contained within pores of a given shape and size, the area-weighted pore fraction was calculated by taking 3D histograms of pore area vs. pore circularity. The area-weighted pore fraction ($f_a$) was defined as

$$f_a = \frac{N_{bin}A_{bin}}{\sum_{\text{all bins}} N_{bin}A_{bin}} \tag{5.2}$$

where $N_{bin}$ is the number of counts in the bin and $A_{bin}$ is the pore area which the bin corresponds to. This allows for the calculation of the percentage of the total porosity contained within each bin and is shown as a heat map in Fig. 5.4D. From this figure it can be seen that for the network with $l_{NS}$= 238 nm that the majority of the porosity is contained within large area pores with a low circularity, demonstrating that the network porosity is dominated by large slit-like pores.

Another important parameter when considering the diffusion of materials through a network is the tortuosity factor. The tortuosity factor can be defined a variety of different ways, with geometric, electrical, diffusive, and hydraulic tortuosity describing similar but distinct phenomena. Here, we calculate the diffusive tortuosity factor, which describes the increase in the path length that a diffusing species has to travel through a network. The diffusivity of a material in a network ($D_{eff}$) is given by

$$D_{eff} = \frac{D_0 P}{\kappa} \tag{5.3}$$

where $D_0$ is the diffusivity of the material in free space, $P$ is the porosity and $\kappa$ is the

diffusive tortuosity factor.[202] The diffusive tortuosity factor can also be defined as

$$\kappa = \left(\frac{L}{L_0}\right)^2 \tag{5.4}$$

Where $L_0$ is the straight-line path from one side of the network to the other and $L$ is the average distance that a diffusing molecule travels.[202] The diffusive tortuosity factor is an important parameter for catalysis, batteries and gas sensors.[197,277,278] It can be calculated from 3D images using finite element analysis; here a concentration gradient is imposed across the network using Dirichlet boundary conditions, the concentration gradient is allowed to reach a steady state by allowing diffusion through the phase of interest. This was achieved using Taufactor.[270] This program outputs maps showing the diffusive flux through each pixel; this map highlights regions with a high concentration gradient (i.e. regions where a large amount of material is diffusing through a small area) and can be used to visualise bottlenecks to diffusion through the network. The tortuosity factor can be calculated for both the pores and the nanosheets within the network. The diffusive tortuosity is defined identically to the electrical tortuosity, with the difference between the two definitions being the particle that is travelling through the network.[202] Therefore, the calculated nanosheet tortuosity factors can be used to describe the increase in path length that a charge carrier experiences as it travels through a network.The reduction in conductivity of a network due to porosity and tortuosity is given by

$$\sigma_{eff} = \frac{\sigma_0(1-P)}{\kappa} \tag{5.5}$$

where $\sigma_{eff}$ is the conductivity of the network and $\sigma_0$ is the conductivity of the material in the abscence of porosity and tortuosity.

The tortuosity factor for both the nanosheets and pores in the network with $l_{NS}$= 238 nm is shown in Fig. 5.5A, in which, the inset shows regions of high and low diffusive flux in the pore network. Both the nanosheets and the pores show a higher tortuosity factor in the out-of-plane direction than the in-plane direction, suggesting that the nanosheets are primarily aligned in the in-plane direction. The higher out-of-plane tortuosity factor may offer an explanation for the anisotropy in charge and mass transport in networks of 2D materials.[118,279] The considerably lower tortuosity factor for the nanosheets than the pores demonstrates that the nanosheets form a well connected network, with minimal geometrical impedance to charge transport.

It is known that nanosheets aggregate during the deposition process, although, it has proven difficult to calculate the extent to which aggregation occurs.[125] From the individual cross-sectional images the length and thickness of the nanoplatelets within the network can be calculated. In this discussion, nanosheet length and thickness correspond to the length and thickness, measured by AFM, for the size-selected ink, while nanoplatelet length and thickness correspond to the values measured for the objects in the network. The

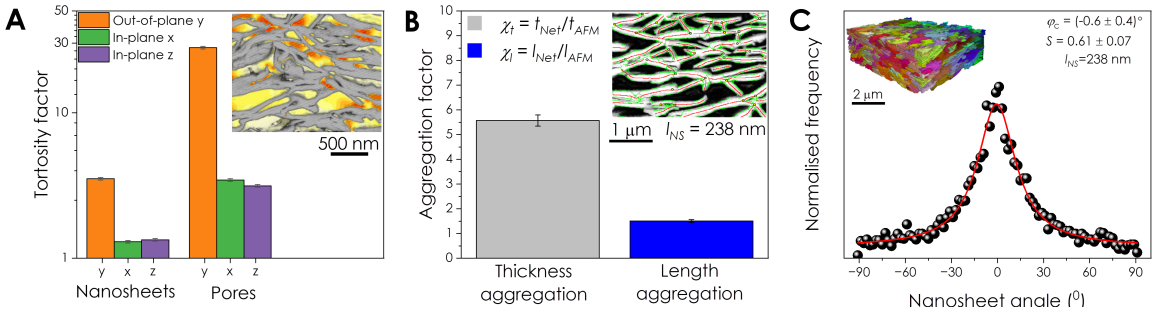



Figure 5.5: **Calculating tortuosity, nanosheet aggregation and alignment: A)** Diffusive tortuosity factor for both pores and nanosheets in each of the three unique directions for the network with $l_{NS}$= 238 nm, calculated using Taufactor.[270] The inset shows the diffusive flux through a region of the pore network (i.e. the amount of material flowing through each pixel per unit time) with yellow denoting area with low flux and red denoting regions with high flux. The regions shown in red are, therefore, bottlenecks to diffusion through the pore network. **B)** Nanosheet aggregation factor in both length and thickness. Calculated by measuring the nanoplatelet thickness ($t_{Net}$) and length ($l_{Net}$) within the network and dividing it by the thickness ($t_{AFM}$) and length ($l_{AFM}$) measured by AFM. Inset shows a region of the network after the ridge detection algorithm has been applied,[269,271] the thickness of the nanosheets is calculated as the width between the green lines and the nanosheet length is calculated as the length of the red lines. **C)** Distribution of the angle between the normal vectors to each nanoplatelet and the substrate normal. The inset shows a section of the network with $l_{NS}$= 238 nm divided into separated nanoplatelets by the 3D distance transform watershed algorithm.

nanoplatelet length and thickness was measured using the ridge detection algorithm in FIJI.[269,271] This algorithm calculates the normal vector to each pixel, it uses sudden changes in the direction of the normal to determine where an object ends.[271] The length and thickness of objects identified by the algorithm can then be calculated. This algorithm was originally developed to determine the length and width of roads from satellite images, here, it is applied to the probability maps created by the segmentation algorithm. A calculated length and thickness distribution can be found in appendix A.2.1. The nanoplatelet length calculated by the algorithm is often lower than the nanosheet length calculated by AFM, as in AFM the longest length of the nanosheet, and the length of the nanosheet perpendicular to its longest length is measured, these two values are then added together and divided by 2 to calculate the nanosheet length. The calculation of the nanoplatelet length considers the length of the nanoplatelet as it appears in each cross-sectional image, leading to the counting of lengths below the nanosheet length. To address this, all nanoplatelet lengths less than 75% of the measured nanosheet length were removed from the calculated length distribution. The mean nanoplatelet length was then calculated from the distribution. The mean nanosheet thickness was calculated by averaging all the measured nanoplatelet thicknesses.

The aggregation of the nanosheets in terms of both length and thickness was then calcu-

lated. The thickness aggregation factor ($\chi_t$) was defined as

$$\chi_t = \frac{t_{Net}}{t_{AFM}} \tag{5.6}$$

where $t_{Net}$ is the nanoplatelet thickness and $t_{AFM}$ is the nanosheet thickness. The length aggregation factor ($\chi_l$) was similarly defined as

$$\chi_l = \frac{l_{Net}}{l_{AFM}} \tag{5.7}$$

where $l_{Net}$ is the nanoplatelet length and $l_{AFM}$ is the nanosheet length. The length and thickness aggregation factors for the network with $l_{NS}$= 238 nm can be seen in Fig. 5.5B. The measured thickness aggregation, 5.6 $\pm$ 0.2, is considerably larger then the length aggregation, 1.5 $\pm$ 0.1, suggesting that during the printing process, the nanosheets aggregate to maximise the basal plane overlap between the nanosheets.

The alignment of the nanosheets within a network is an important parameter for a variety of applications. For electronic applications, nanosheets aligned parallel to the substrate are required to from basal plane aligned networks,which lead to a decrease in the junction resistance and improved charge transport.[82] Basal plane aligned networks also require thinner networks to form a continuous layer, reducing the minimum thickness required to form a capacitor. For batteries, however, nanosheets aligned perpendicular to the substrate create improved rate capacity, as the time for an ion to diffuse into and out of the network is reduced.[280,281] To calculate the alignment of the nanoplatelets in the network, each individual nanoplatelet first has to be identified. This was achieved using a 3D distance transform watershed algorithm, which separates connected objects in a binarised image. The algorithm achieves this by converting the binarised image into a greyscale image, with the greyscale intensity dependent on the distance of each white (nanosheet) pixel from the closest black (pore) pixel, it then floods the image starting at the whitest pixel and working its way downward in grey scale intensity, at the point at which 2 flooded objects meet it creates a boundary between the objects.[282] This was carried out in 3D on the image stack using the 3D distance transform watershed algorithm in the MorpholibJ library in FIJI, with a dynamic setting of 2.[269,272] An image showing the networks separated into individual nanoplatelet components can be seen in the inset in Fig. 5.5C. This method of identifying individual nanoplatelets is not ideal, it cannot accurately calculate the nanoplatelet length or thickness; however, it does group nanoplatelets with the same general orientation together, allowing for calculation of their alignment. To calculate the nanoplatelet orientation, each identified nanoplatelet was fit using the equivalent ellipsoid algorithm in the MorpholibJ library in FIJI.[269,272] The angle that the normal vector of each identified nanoplatelet made with the normal vector of the substrate was calculated, the distribution of normal vectors for the network with $l_{NS}$= 238 nm can be seen in Fig. 5.5C. The distribution is centered on approximately 0° with a FWHM of 29 $\pm$ 1°. This FWHM value is similar to values

previously calculated for graphene networks composed of similar size nanosheets, with a value of 21° measured by AFM for IJP graphene network,[192] and values of 18° calculated from individual cross sectional images of an uncompressed vacuum-filtered graphene network.[199]

A comparison between this method for calculating the nanosheet alignment and an alternative method that calculates the alignment from individual cross-sectional images can be found in appendix A.2.2. Both methods give similar nanosheet alignment distributions. However, as the watershedding method is 3D it allows for calculation of 3D alignment parameters such as the Hermans orientation factor. Within material science the orientation of a group of objects is often described by the Hermans orientation factor ($S$) which is given by

$$S = \frac{3\langle cos^2(\phi)\rangle - 1}{2} \tag{5.8}$$

where $\phi$ is the angle that the object's normal vector makes with the normal vector to the substrate.[283] The direction of a normal vector to an object is dependent on its geometry, with the normal vector to a 2D object pointing perpendicular to its surface.[284] For 2D objects an $S$=1 value describes an object perfectly aligned in the plane, $S$=0 describes objects randomly aligned and $S$= $-\frac{1}{2}$ describes objects aligned perfectly out-of-plane. Using the calculated normal vectors for the network composed of $l_{NS}$= 238 nm yields $S = 0.61 \pm 0.07$. These values are in line with those calculated by wide angle X-ray scattering for vacuum filtered MXene films of 0.79-0.87 as well as GO films 0.67-0.87.[201,266] The lower values calculated here are likely caused by the low aspect ratio of LPE graphene compared to MXenes or GO nanosheets; higher aspect ratios allow nanosheets to conform to each other.[82]

### 5.2.4 The effect of nanosheet length on graphene network morphology

To investigate the effect of nanosheet size on network morphology, each of the properties described in Section 5.2.3 was calculated for each of the size-selected graphene networks imaged. Fig. 5.6A shows the dependency of porosity on nanosheet length, demonstrating that the network porosity decreases as nanosheet length decreases. The decrease in network porosity demonstrates that as the nanosheet size decreases more compact networks are produced, suggesting that smaller nanosheets pack more efficiently. This also suggests that networks of smaller nanosheets may be more conductive, as more densely packed graphene networks have been shown to have superior electrical properties.[199] Decreasing porosity with decreasing nanosheet size for spray-coated graphene networks has also been observed by Clifford *et al.*[126]

Along with the reduction in network porosity with decreasing nanosheet size, the pore size decreases, while the pore circularity increases, as shown in Fig. 5.6B,C respectively. The

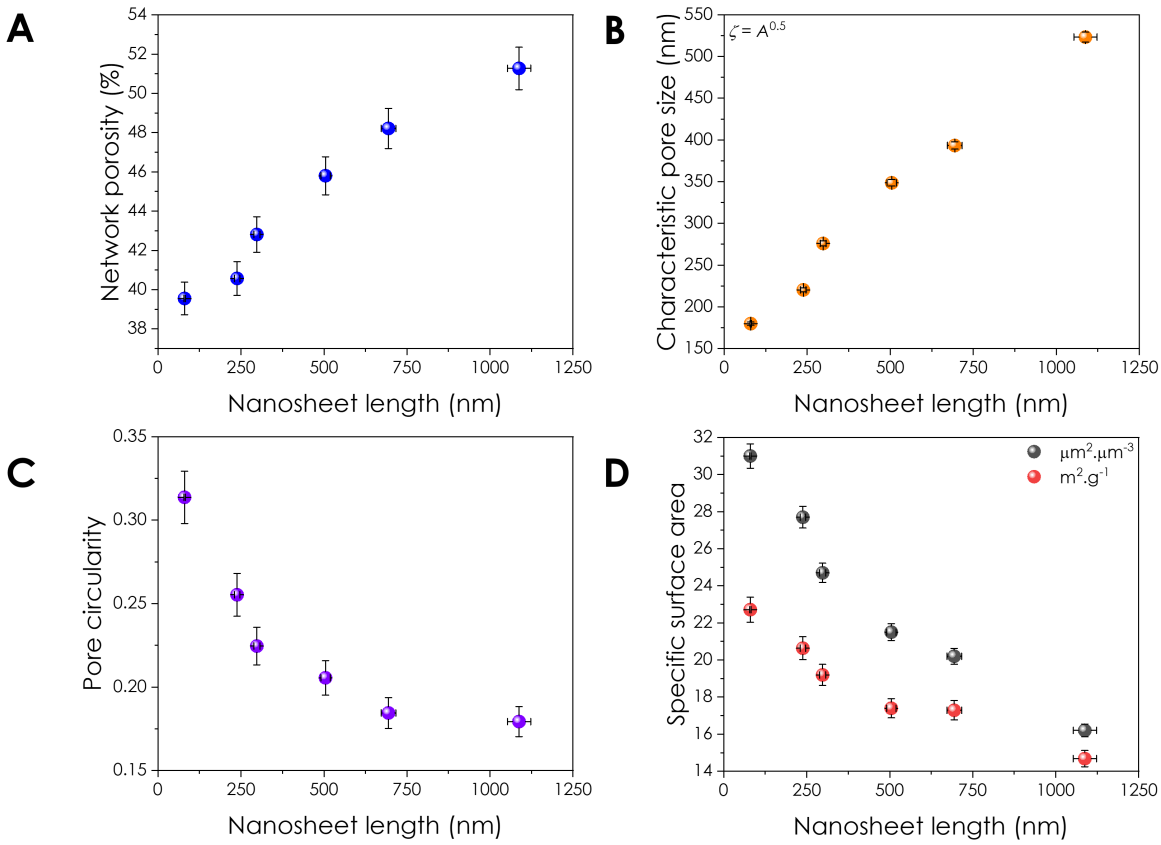



Figure 5.6: **Effect of nanosheet length on the pore volume: A)** Plot of network porosity as a function of nanosheet length. **B)** Characteristic pore length, the square root of pore area, plotted against nanosheet length. **C)** Pore circularity as a function of nanosheet length. **D)** Network volumetric and gravimetric surface area plotted against nanosheet length.

mean pore area and circularity is obtained by calculating the area-weighted pore fraction distributions as shown in Fig. 5.4D. The distribution of pore length and area contained within the 90% area of the heat map is found and the average values of these distributions are calculated for each size-selected network. Area-weighted pore fraction heat maps showing the distribution of pore cross-sectional area and circularity for each of the size-selected networks can be found in appendix A.2.3. The calculated pore area is converted to a characteristic pore size ($\zeta$), the square root of the pore area, as the pore size is a more commonly discussed variable.[285] The decrease in pore size is likely caused by the smaller nanosheets being able to fill the gaps in the network more easily than larger nanosheets. As the pore size decreases the pore circularity increases meaning that the smaller nanosheets produce networks with smaller more circular pores.

Both the gravimetric and volumetric SSA of the networks, as a function of nanosheet length can be seen in Fig.5.6D. Both parameters increase as the nanosheet size is decreased, this is likely driven by the decrease in characteristic pore size, which leads to an increase in the SSA despite the decrease in the porosity for networks composed of smaller nanosheets. For batteries, catalysts and gas sensors, a high SSA means more area available for an electrolyte or gas, to interact with the network.[286,287] For these applications, optimising the nanosheet

dimensions could lead to an increase in SSA and therefore, improved performance.

The nanosheet and pore tortuosity factors are important for the performance of an array of devices from batteries to gas sensors.[197,278,288] The calculated nanosheet and pore tortuosity factors in each of three directions considered, as a function of nanosheet length, are shown in Fig. 5.7A. Here, it can be seen that the nanosheet tortuosity factor increases as nanosheet size increases, while the pore tortuosity factor decreases. These trends can be explained by the Bruggeman equation. It was shown by D. A. G. Bruggeman in 1935 that the pore tortuosity factor of a network composed of regularly shaped objects is given by

$$\kappa = P^{1-\beta} \tag{5.9}$$

where $P$ is the porosity and $\beta$ is a parameter which depends on the shape of the particles in the network.[289,290] For networks composed of spherical particles $\beta$=1.5 while for cylindrical particles $\beta$=2.[290] This equation has been generalised by the addition of a prefactor ($\alpha$), this was done so it would correspond to experimental data.[291] The generalised Bruggeman equation is given by

$$\kappa = \alpha P^{1-\beta} \tag{5.10}$$

While this relation is generally used to describe the dependence of the pore tortuosity factor on the porosity of the network, it can also be used to relate the nanosheet tortuosity to the the nanosheet volume fraction, which is given by 1-Porosity. Pore and nanosheet tortuosity factors in each of the three unique directions, plotted as a function of pore and nanosheet volume fraction, can be seen in Fig. 5.7B. All of the networks appear to follow a generalised Bruggeman relationship. The fit values for $\alpha$ and $\beta$ can be found in Table 5.1. The calculated $\beta$ for the pore volume, 3.3 for the in-plane direction and 5.6 for the out-of-plane direction, are considerably higher than the theoretical values for spherical and cylindrical particles. Calculations have shown that the out-of-plane pore tortuosity factor in a network of ellipsoids increases as the aspect ratio of the ellipsoids increases, the aspect ratio of the nanosheets used may, therefore, explain the large values.[292] The higher Bruggeman exponent for the out-of-plane direction than the in-plane direction for both the nanosheets (1.9 vs. 2.5) and the pores (3.3 vs. 5.6) demonstrates that the out-of-plane tortuosity factors have a stronger dependence on volume fraction, and therefore, on nanosheet length. This suggests that for out-of-plane devices, optimisation of nanosheet length is important for maximising device performance.

Length and thickness aggregation factors as a function of nanosheet length can be seen in Fig. 5.7C, showing an increase in both length and thickness aggregation for the smaller nanosheets. The larger aggregation of smaller nanosheets may occur due to their increased mobility within the ink. For all the nanosheet sizes, the aggregation is greater for thickness than length, suggesting that at all sizes the nanosheets aggregate to maximise basal plane overlap. Furthermore, the aspect ratio of the nanosheets within the network is not constant as it is within the ink, instead the nanoplatelet aspect ratio decreases as the nanosheet length

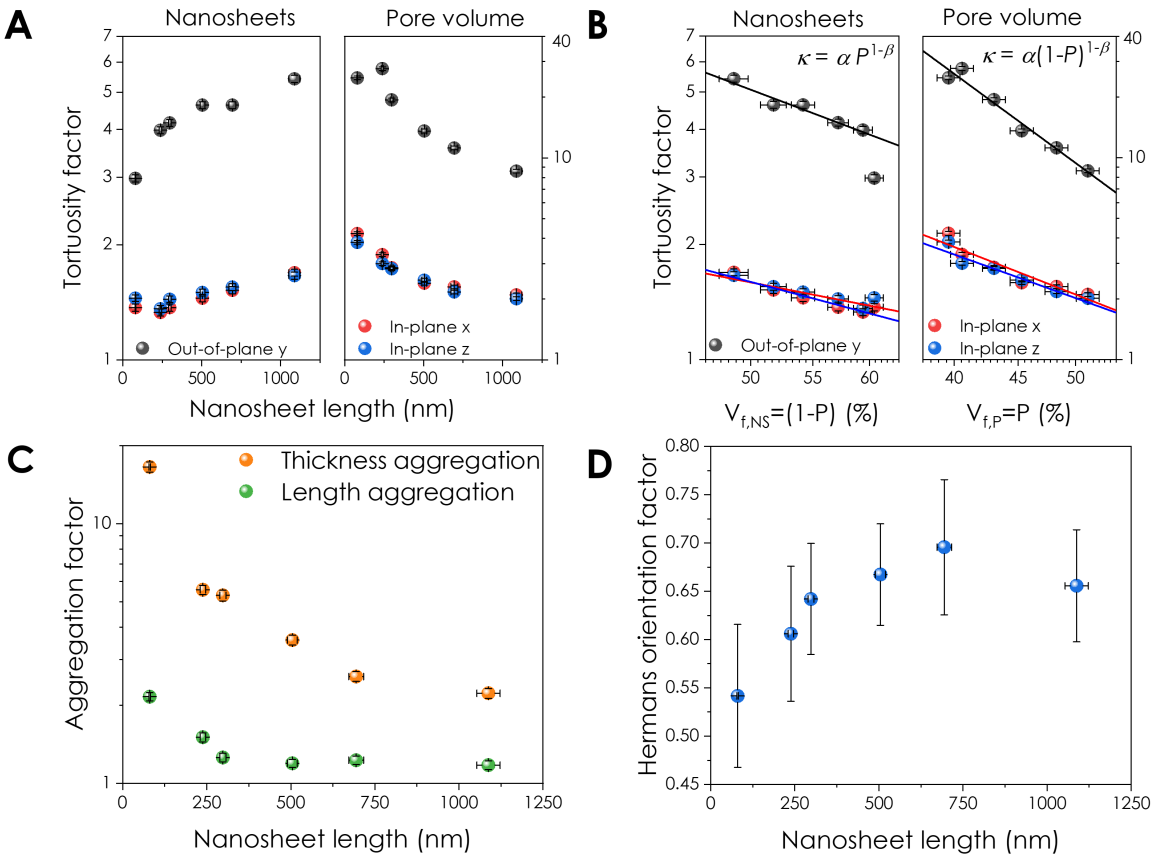



Figure 5.7: **Relationship between nanosheet length and network tortuosity, nanosheet aggregation, and alignment: A)** Pore and nanosheet tortuosity factor, in each of the three unique directions, plotted against nanosheet length. **B)** Pore and nanosheet tortuosity factor, in each of the three unique directions, plotted as a function of nanosheet ($V_{f,NS}$), and pore ($V_{f,P}$) volume fraction respectively. Linear fits corresponding to the generalised Bruggeman equation (Eqn. 5.10) are shown. **C)** Length and thickness aggregation factor of the graphene nanosheets as a function of nanosheet length. **D)** Hermans orientation factor of the graphene nanoplatelets in the network plotted against nanosheet length.

decreases, with the largest nanosheets showing an aspect ratio of 15 $\pm$ 1, half the aspect ratio in the ink, while the smallest nanosheets show an aspect ratio of 4.4 $\pm$ 0.2, 7 times lower than in the ink. Nanoplatelet aspect ratio as a function of nanosheet length can be seen in appendix A.2.1.

The Hermans orientation factor as a function of nanosheet length can be seen in Fig. 5.7D, showing an apparent decrease in nanosheet alignment as the nanosheet length decreases. The same trend has been observed for networks of GO.[293] In the case of GO, this behaviour is likely driven by the nanosheet aspect ratio, larger GO nanosheets often show a higher aspect ratio, improving their ability to conform to each other.[82] However, the LPE graphene nanosheets used here show a constant aspect ratio, which is too low for the nanosheets to conform.[82] It is unclear what drives this decrease in alignment as nanosheet size decreases.

| | | | Bruggeman exponent ($\beta$) | Prefactor ($\alpha$) |
|---|---|---|---|---|
| Graphene | Pores | In-plane | 3.3 ± 0.8 | 0.4 ± 0.2 |
| | | Out-of-plane | 5.6 ± 0.4 | 0.4 ± .02 |
| | Nanosheets | In-plane | 1.9 ± 0.5 | 0.9 ± 1.4 |
| | | Out-of-plane | 2.5 ± 0.3 | 1.2 ± 2.6 |
| $WS_2$ | Pores | In-plane | 2.8 ± 1.1 | 0.6 ± 0.5 |
| | | Out-of-plane | 3.3 ± 0.6 | 1.3 ± 0.7 |
| | Nanosheets | In-plane | 1.55 ± 0.04 | 1.1 ± 0.4 |
| | | Out-of-plane | 3.8 ± 0.5 | 0.8 ± 0.5 |
| AgNS | Pores | In-plane | 5.6 ± 3.2 | 0.007 ± .005 |
| | | Out-of-plane | 6.5 ± 0.8 | 0.020 ± .004 |
| | Nanosheets | In-plane | 3.2 ± 1.3 | 1.3 ± 1.2 |
| | | Out-of-plane | 6.1 ± 4.1 | 4 ± 5 |

Table 5.1: Calculated Bruggeman exponent ($\beta$) and prefactor ($\alpha$) calculated for both nanosheets and pores in the in-plane and out-of-plane direction, for each of the materials presented in this chapter. The pore values were calculated by fitting $\kappa = \alpha P^{(1-\beta)}$ and the nanosheet values were calculated by fitting $\kappa = \alpha(1-P)^{(1-\beta)}$.

### 5.2.5 Morphology of networks of nanomaterials beyond graphene

To investigate how the constituent nanosheets affect the network morphology, 3D images of size-selected AgNS and $WS_2$ networks were captured. An AgNS stock dispersion was purchased, diluted in DI water, size-selected by LCC,[130] and then spray-coated onto PET, coated in $Al_2O_3$ to improve substrate wetting. The $WS_2$ nanosheets were produced in a similar manner to the graphene nanosheets, however, they were exfoliated in IPA instead of SC:DI. The nanosheets were size-selected by LCC.[130] The inks were then spray coated onto cleaned glass slides to produce networks. In each case three size-selected networks were produced.

Representative 3D images and cross-sections of AgNS and $WS_2$ networks can be seen in Fig. 5.8. Further cross-sectional SEM images for each of the networks studied can be found in appendix A.2.4. The $WS_2$ and AgNS network show morphological differences from the graphene networks presented in Fig. 5.3B, and from each other. The AgNSs stack forming large nanoplatelets, due to the thickness of the AgNSs (50-100 nm) some of these nanoplatelets no longer have a 2D geometry. In comparison, the $WS_2$ network shows a morphology more similar to the graphene networks. However, the $WS_2$ networks appear to show a larger porosity than either the graphene or AgNS networks. The high resolution of the $WS_2$ cross-section, shown as an inset in Fig. 5.8B, demonstrates the ability of this technique to image semiconducting, as well as semi-metallic and metallic networks.

To investigate the morphology of the AgNS and $WS_2$ networks, the image processing pipeline that was used for the graphene films was used to create binarised images. Using the binarised images the networks morphologies can be interrogated and compared. Network

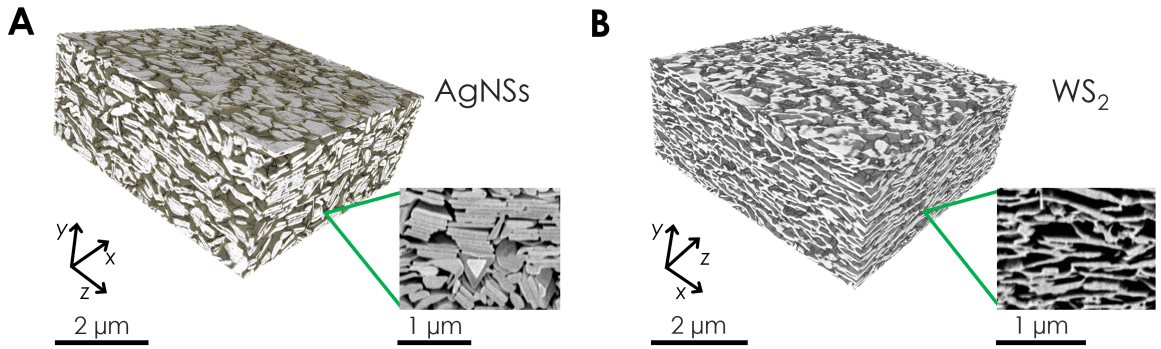



Figure 5.8: **3D imaging materials beyond graphene: A-B)** 3D image of a AgNS and $WS_2$ network, respectively. A section of a cross-section is shown as an inset in each image.

porosity as a function of nanosheet length, for the 3 different materials imaged, is shown in Fig. 5.9A. Power law fits are shown, highlight the dependence of network porosity on nanosheet length for each material. The $WS_2$ networks show a higher porosity than the graphene networks, while the AgNS networks show a lower porosity. The porosity of the $WS_2$ network is below values measured by calculating the density of $WS_2$ networks previously (~60% for a network with $l_{NS}$= ~380 nm), however, surface SEM images of this network suggests that the nanosheets are more poorly aligned than in the networks presented here.[82] Networks of poorly aligned nanosheets are likely to have a higher porosity. The high porosity of the $WS_2$ networks may partially explain the poor performance of LPE $WS_2$ transistors.[170,273,294] The relatively low porosity of the AgNS networks may similarly be related to the high conductivity of spray-coated AgNS networks (~2$\times$ $10^6$ S.m$^{-1}$).[295] The difference in scaling of the porosity with nanosheet length for the 3 materials is also interesting, suggesting that the morphology of the nanosheets may affect the porosity of the networks they produce. The graphene and $WS_2$ networks show a very similar scaling, with the graphene network porosity just downshifted from the $WS_2$ networks, while the AgNS networks seem to show a more gradual change in porosity with nanosheet length.

The network gravimetric SSA of the networks as a function of nanosheet length is shown in Fig. 5.9B. Each of the three materials shows increasing SSA as the nanosheet length decreases. This is in line with measurements of the volumetric capacitance of size-selected $WS_2$ networks, which suggests that the network surface area scales with nanosheet thickness.[125] This data shows that the graphene networks show a considerably higher gravimetric surface area than the $WS_2$ or AgNS networks. This difference in SSA appears to be driven primarily by the difference in density of the constituent materials, $WS_2$ is approximately 3.5 times denser than graphene, while the graphene networks have approximately 3.5 times higher SSA. This very strong scaling suggests that material density has a large impact on the SSA of spray-coated networks. Interestingly the $WS_2$ and graphene show very similar scaling of SSA, with nanosheet length while the AgNS networks show a sharper decrease as nanosheet length increases, suggesting that the morphology of the nanosheets impacts the SSA.

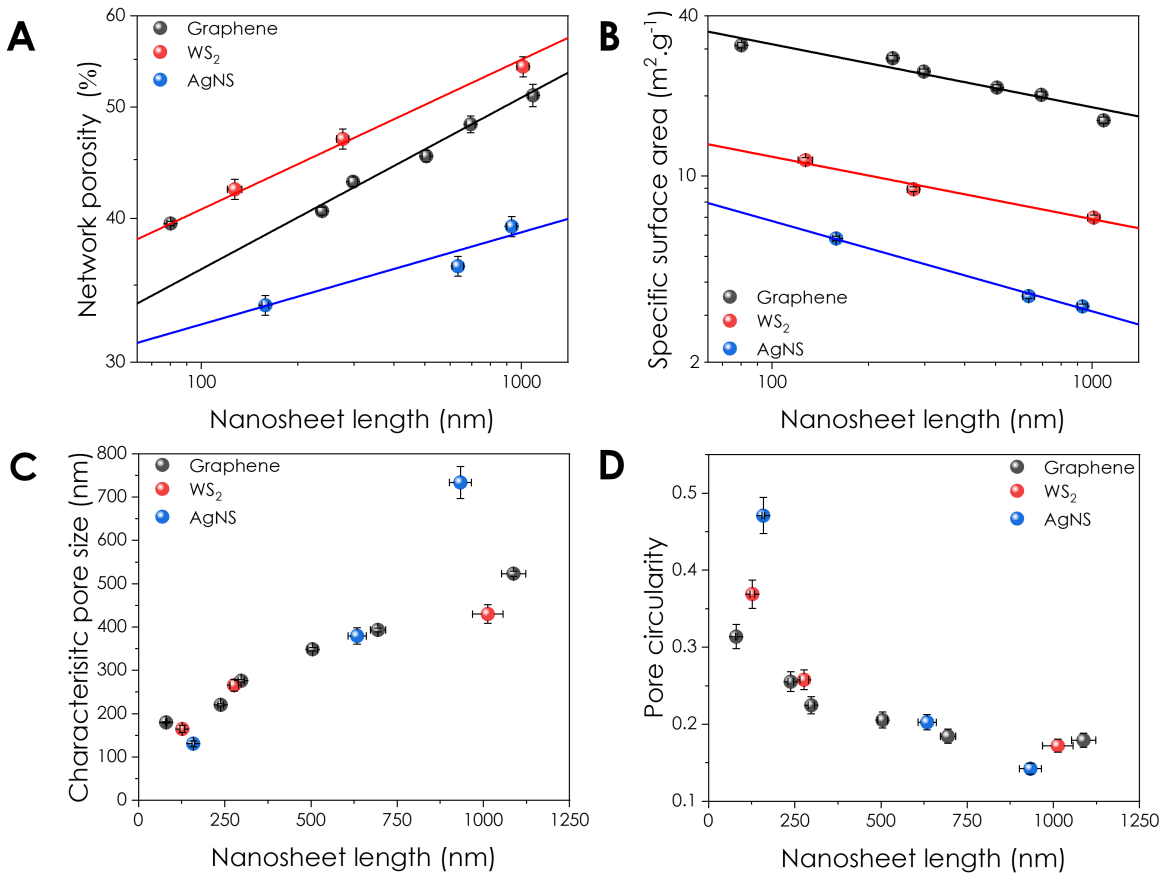



Figure 5.9: **Network pore volume of different materials: A)** Network porosity as a function of nanosheet length for the graphene, $WS_2$ and AgNS networks. Lines shown are fits to a power law, highlighting the dependence of porosity on nanosheet length. **B)** Gravimetric SSA plotted against nanosheet length for the materials imaged. Lines shown are fits to a power law, showing the dependence of SSA on nanosheet length. **C)** Characteristic pore size as a function of nanosheet length for the materials imaged. **D)** Pore circularity plotted against nanosheet length for the materials imaged.

Characteristic pore size and pore circularity for the networks imaged is shown in Fig. 5.9C,D, respectively. Each of the materials show decreasing characteristic pore size, and increasing pore circularity with decreasing nanosheet length, with each of the materials imaged showing very similar values. The AgNS networks show a stronger scaling of both characteristic pore size and pore circularity with nanosheet length than the $WS_2$ or graphene networks. This stronger scaling may partially explain the stronger scaling of SSA with nanosheet length for the AgNS networks.

The tortuosity factor of both the nanosheets and pores in each of the networks imaged was also calculated. The AgNS nanosheet and pore network tortuosity factors are shown in Fig. 5.10A,B. The in-plane nanosheet tortuosity factor increases as nanosheet size increases. The out-of-plane value, however, appears to show a maximum, it is unclear if this is a real effect or simply an outlier. The ratio of in-plane to out-of-plane tortuosity factor of the nanosheets is also notable, showing a reduced value when compared to the graphene networks (1.5 vs. 3). This suggests that the AgNS networks have minimal geometric

impedance to conduction in all directions. The pore tortuosity factor of the networks also shows considerably reduced tortuosity factors compared to the graphene networks in the out-of-plane direction. However, the tortuosity in the in-plane direction is quite similar to the graphene networks. This suggests that the AgNS networks are more isotropic than the graphene networks, which is likely caused by the aggregation of the AgNSs into objects that appear to be isotropic within the network. The smallest AgNS size also shows a different in-plane tortuosity factor in the two in-plane directions, which may suggest that there is inhomogeneity in this network.

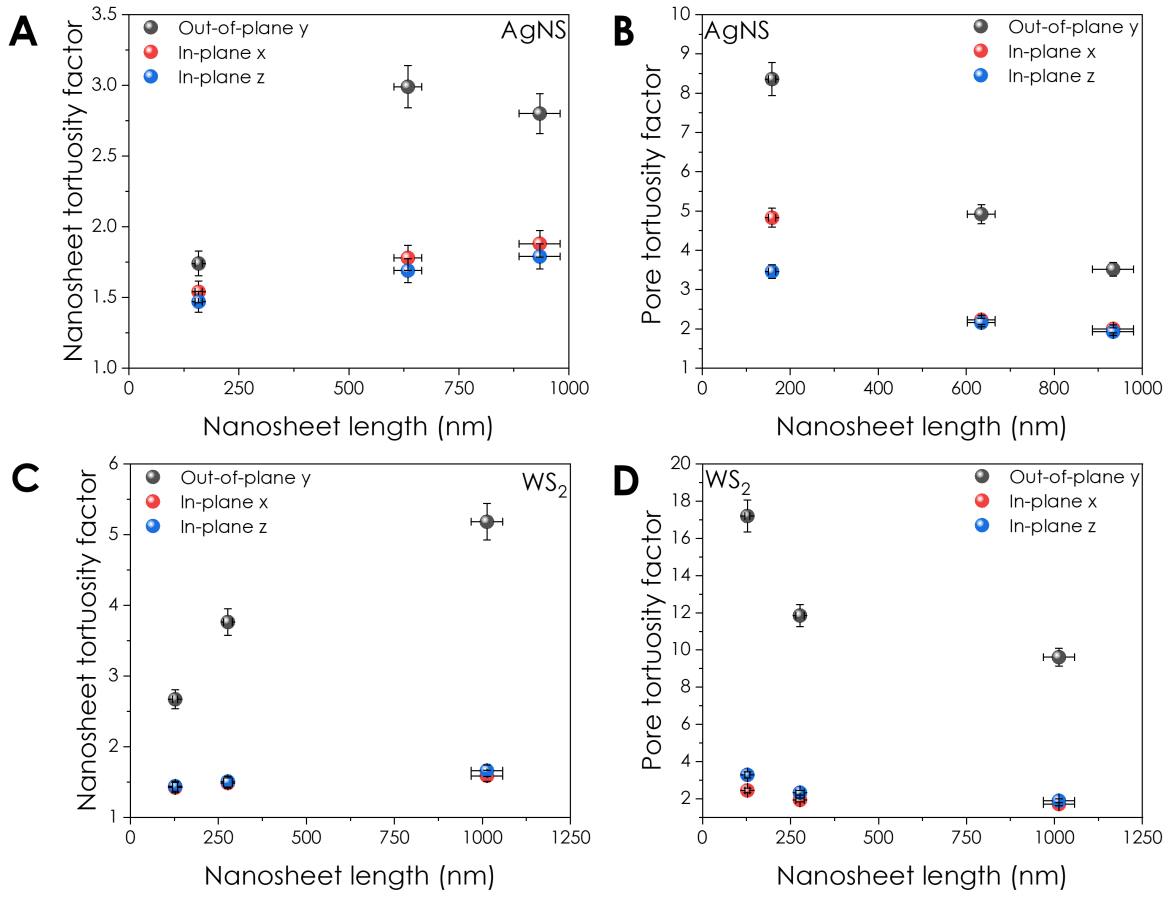



Figure 5.10: **Tortuosity factors of different materials: A-B)** Nanosheet and pore network tortuosity factor, respectively, of the AgNS networks, as a function of nanosheet length. **C-D)** Nanosheet and pore network tortuosity factor, respectively, of the $WS_2$ networks, plotted against nanosheet length

The $WS_2$ nanosheet tortuosity factor is shown in Fig. 5.10C, showing similar behaviour to the graphene networks, with very similar in-plane and out-of-plane tortuosity factors, which further demonstrates the similarities in the morphology of these networks. The pore tortuosity factors of the $WS_2$ networks, however, show differences from the graphene networks, shown in Fig. 5.10D. While the in-plane pore tortuosity factors are similar to the graphene networks the out-of-plane values are lower, suggesting that diffusion through the out-of-plane directions in the networks is considerably less impeded by geometric constraints.

As discussed, the relationship between the tortuosity factor and the volume fraction of mate-

rial should be described by the generalised Bruggeman equation. The calculated Bruggeman parameters for both the nanosheet and pore tortuosity factors, for each of the materials imaged, in both the in-plane and out-of-plane directions are given in Table 5.1. For the AgNS and $WS_2$ networks there are only 3 data points for each fit, causing large uncertainties in the calculated values. Despite the large uncertainties some general trends can be observed. For each material, both the pores and the nanosheets show higher $\beta$ values in the out-of-plane direction than in the in-plane direction. This suggests that the out-of-plane tortuosity factor has a stronger dependence on the volume fill fraction and is likely caused by the nanosheets being primarily aligned in the in-plane direction. The AgNS nanosheet networks appear to show larger $\beta$ values than the $WS_2$ and graphene nanosheet networks in both the in-plane and out-of-plane direction. This suggests that the volume fraction has a greater impact on the tortuosity factors in these networks.

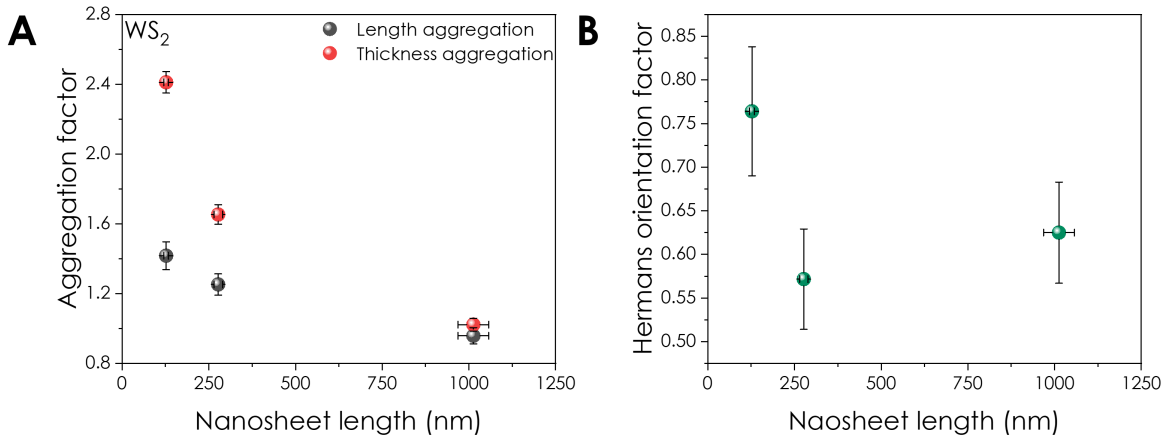



Figure 5.11: **$WS_2$ nanosheet aggregation and alignment: A)** Length and thickness aggregation factor as a function of nanosheet length for $WS_2$ networks imaged. **B)** $WS_2$ nanosheet Hermans orientation factor plotted against nanosheet length.

The techniques used to determine the aggregation and orientation of the graphene nanosheets work on anisotropic materials i.e. materials which are longer than they are thick. They will not work on networks of isotropic materials, as the similar length, width, and thickness of the material makes determining which of the calculated values correspond to the nanosheet length and thickness more difficult. Since the AgNSs aggregate, with some of the AgNS in the network appearing to be isotropic, the nanosheet aggregation and alignment was not calculated for the AgNS networks. The $WS_2$ nanoplatelets in the networks are, however, anisotropic and so the nanosheet aggregation and alignment were calculated for the $WS_2$ networks.

$WS_2$ nanosheet length and thickness aggregation factors are shown in Fig. 5.11A. As with the graphene nanosheets, the aggregation factor increases as the nanosheet length decreases, with the thickness aggregation factor being higher than the length aggregation factor for each of the networks. The $WS_2$ aggregation factors are, however, considerably lower than the graphene values. One possible explanation for the reduced aggregation of the $WS_2$ nanosheets is that the higher density of the $WS_2$ than graphene means the

nanosheets are less mobile within the ink, and therefore, aggregate less during the printing process.

The Hermans orientation factor of $WS_2$ nanosheets as a function of nanosheet length is shown in Fig. 5.11B. The orientation factor shows the opposite trend to the graphene networks, with an apparent increase in nanosheet orientation as the nanosheet length decreases. The orientation of the large $WS_2$ nanosheets agrees within error with the large graphene nanosheets, however as the nanosheet size decreases the orientation of the $WS_2$ nanosheets improves, reaching a maximum of ~0.75. It is not clear what drives this different behaviour between $WS_2$ and graphene.

Beyond networks of 2D materials, we have also applied FIB-SEM nt to networks of Ag-NWs,[296] calculating network porosity and nanowire and pore tortuosity factors. A discussion of the morphology of these networks is beyond the scope of this work.

### 5.2.6 3D imaging of devices

The data presented thus far in this chapter demonstrates how FIB-SEM nt images of printed nanosheet network can be used to characterise a wide range of network properties. However, to form a range of printed devices, printing different materials on top of each other is required.[101,156,170,200,297–299] This section will explore the use of FIB-SEM nt to determine information about the interface between materials.

To investigate the interface between two printed layers, silver nanoparticles (AgNP) were deposited on top of spray-coated graphene networks produced from size-selected inks containing large and small nanosheets. The AgNP are less than 50 nm in diameter and were deposited by aerosol jet printing. The devices were imaged in the same manner as the other networks presented. The networks were produced and imaged by Dr. Cian Gabbett. The images were segmented by four way segmentation, the four phases separated were the nanosheets, pores, AgNPs and the substrate. A section of the 3D image of each device is shown in Fig. 5.12. To visualise the interface between the graphene network and the AgNP network, the graphene network can be removed from the image, so it just shows the AgNP electrode and the substrate. From these images, it appears that the AgNPs penetrate into both the network of small and large nanosheets. However, it appears that the AgNPs penetrate further into the graphene network composed of larger nanosheets and form a rougher interface with this network.

To investigate the interface between the two networks, the volume fraction of the AgNP and graphene as a function of depth from the top of the image was calculated, shown in Fig. 5.12. This was achieved by reslicing the 3D image into an image stack in FIJI,[269] with each image slice being of the xz plane, and moving from one slice to another corresponds to a movement down in y-direction. From these graphs it is clear that there is a much slower transition between the AgNP electrode and the graphene network for the network

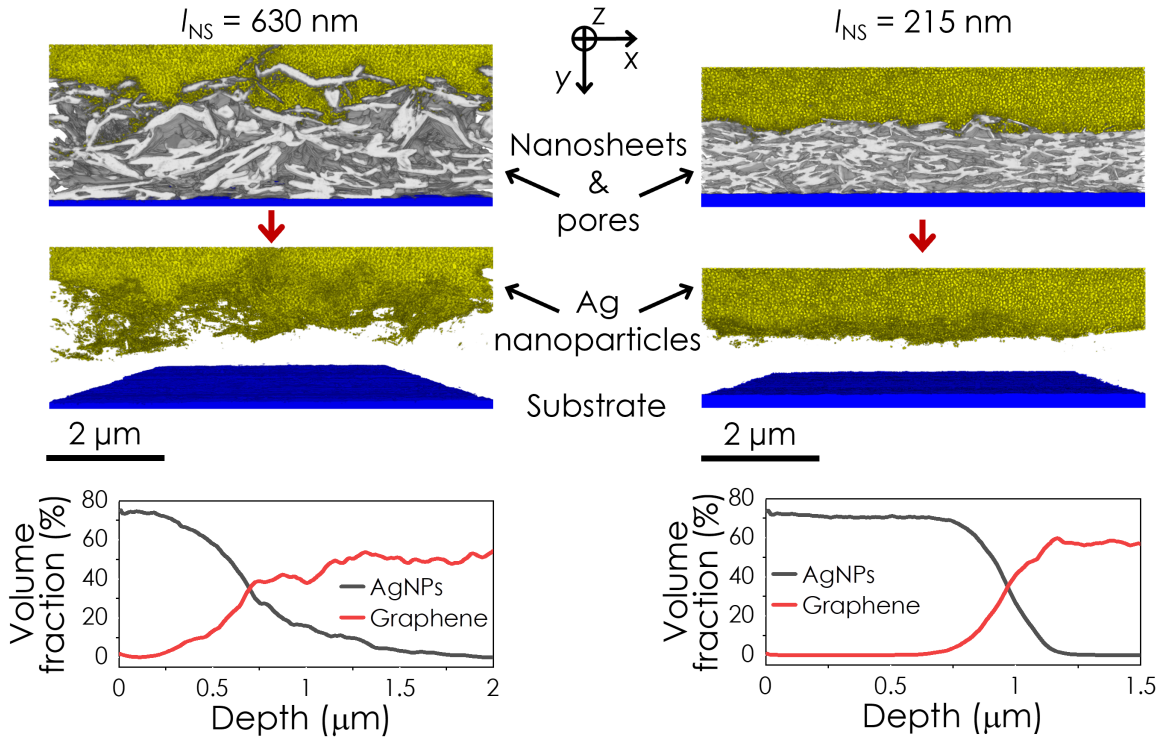



Figure 5.12: **Graphene-silver nanoparticle heterostack:** 3D images of an aerosol jet printed silver nanoparticle (AgNP) top electrode on graphene networks with $l_{NS}$= 630 nm and $l_{NS}$= 215 nm, with the nanosheets present and removed. The graphs show the volume fraction of AgNP and graphene as a function of distance from the top of the image for each heterostack.

composed of larger nanosheets. This slower transition implies that the AgNPs penetrate further into the network composed of larger nanosheets. Interestingly, in both cases the AgNP electrode shows a volume fraction of ~70%, this is above the theoretical packing fraction of randomly packed monodisperse spheres, which is 64%,[300] this deviation is likely due to polydispersity in the AgNPs diameter,[301] which is discussed in appendix A.2.6.

To further investigate the roughness of the interface between the two materials the roughness of the graphene and AgNP network at their interface were calculated. The roughness was calculated by taking the resliced image and encoding the depth of each slice using the Z-stack Depth Colorcode plugin in FIJI.[269] An image of the surface was then produced using the Volume viewer plugin in FIJI.[269] In this image, a pixel's intensity corresponds to its height. Heat maps of the AgNP surface at the interface can be seen in Fig. 5.13. 12 line scans across the surfaces were used to determine the roughness of the graphene networks and the AgNP network at the interface with the graphene network. Representative line scans across both the graphene networks and the AgNP network at the graphene interface are shown in Fig. 5.13. For the network with $l_{NS}$= 615 nm the graphene network has a root mean square (RMS) roughness of $R_{RMS}$=158 ± 48 nm while the AgNP shows a value of $R_{RMS}$=313 ± 55 nm. In comparison, the network composed of the smaller graphene nanosheets has $R_{RMS}$=105 ± 18 nm and AgNP networks shows $R_{RMS}$=102 ± 18 nm. These values clearly show the higher quality of interface between the AgNP and the smaller

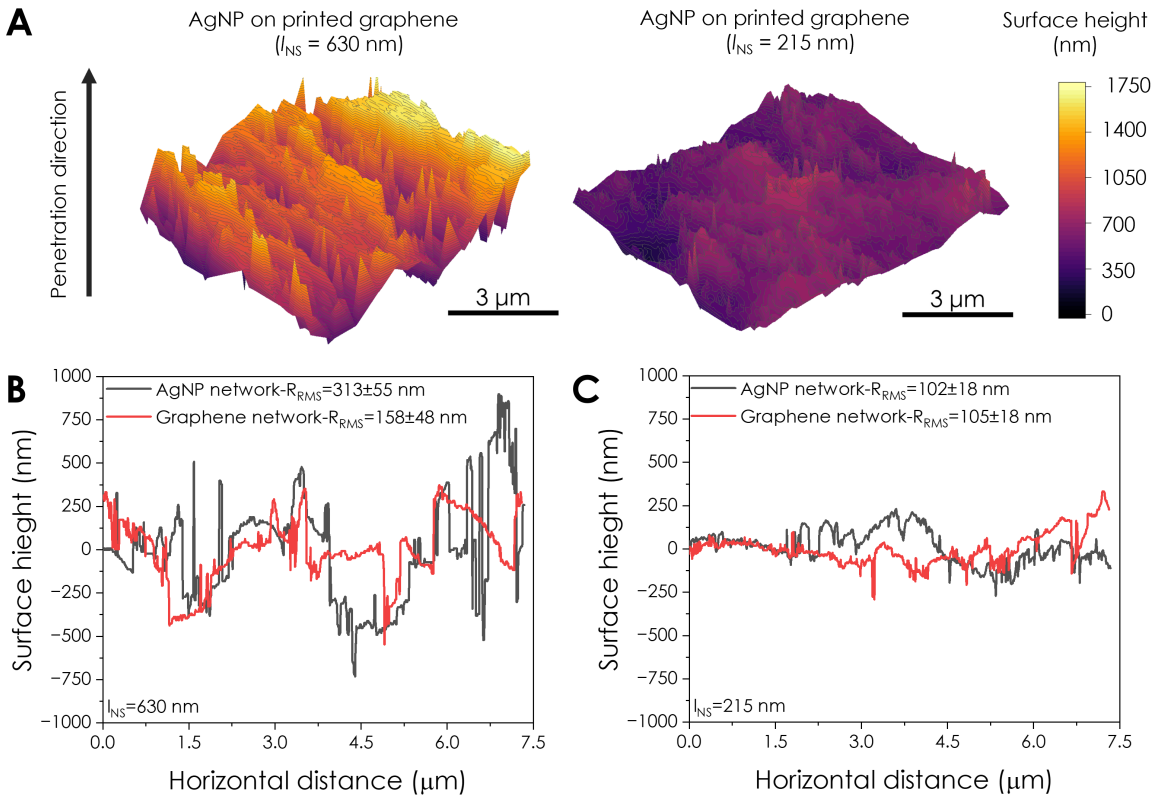



Figure 5.13: **Graphene-silver nanoparticle interface: A)** 3D surface topography maps of the AgNP networks at their interface with the graphene networks printed with lengths of $l_{NS}$= 630 nm and $l_{NS}$= 215 nm. The direction of penetration is shown. The colour scale is common to both images. **B-C)** Representative line scans of the surface height of the both the graphene and the AgNP network at thier interface, for the network composed of graphene nanosheets with $l_{NS}$= 630 nm and $l_{NS}$= 215 nm, respectively. The average network roughnesses at the interface are given for the graphene and AgNP networks are given.

graphene nanosheets, as the network of smaller graphene nanosheets and the AgNP electrode show the same roughness, suggesting that the AgNP sit on top of the graphene network and do not penetrate into the network. In contrast, the network of larger graphene nanosheets has half the surface roughness of the AgNP network, suggesting that the AgNPs penetrate into the network.

The degree of penetration of the AgNP networks into the graphene is important for determining the minimum thickness required for a device to prevent shorting. To calculate the penetration of the AgNP particle into the network the find connected regions plugin in FIJI was used.[269] The penetration depth can be defined as the depth below the lowest point on the surface of the graphene network that a AgNP connected to the AgNP network can be found. Using this definition the AgNPs penetrate 725 nm into the network composed of large nanosheets but do not penetrate at all into the network of smaller graphene nanosheets. It is likely that the difference in the penetration of the AgNPs into the graphene networks is caused by the difference in characteristic pore size between the networks. This larger characteristic pore size in graphene networks composed of larger nanosheets means

that the AgNPs can penetrate further into the network before reaching a bottleneck they cannot pass through. It is likely that if the size of AgNPs used was decreased, that the penetration into both networks would increase. The lower surface roughness of the smaller graphene nanosheet network combined with the reduced material penetration suggests that smaller graphene nanosheets may be superior for printed heterostack devices. The effect of graphene nanosheet size on network electrical properties will be discussed in Chapter 6.

While the AgNP top electrodes on graphene networks demonstrate the ability of FIB-SEM nt to interrogate the interface within a device, the graphene/AgNP heterostacks do not have practical applications. In practical devices the interface betweeen conductive electrodes and semiconducting and insulating materials is of interest. In photodiodes and solar cells in particular a sandwich structure is required, with conductive components above and below a sandwich composed of a semiconducting material, a charge injection material, and a transport layer.[297] To investigate a device with a sandwich structure $WS_2$ nanosheets were printed onto glass coated in indium tin oxide (ITO), a transparent electrode, and a gold electrode was deposited on top of the network by e-beam evaporation. It was found that these devices needed a thickness of approximately 1.6 $\mu$m to prevent shorting between the ITO and the gold electrode. The devices were produced by Dr. Shixin Liu. To understand the cause of this shorting 3D images of the networks were captured.

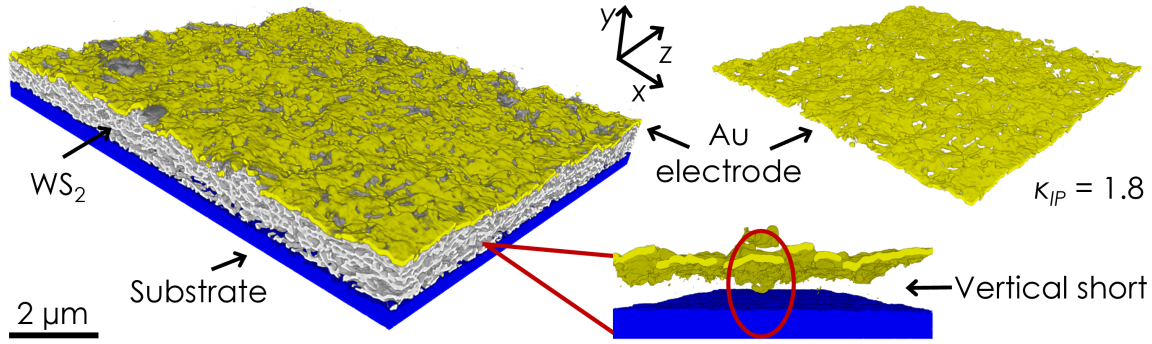



Figure 5.14: **Shorting in a $WS_2$ heterostack:** 3D image of a $WS_2$ network with an ITO bottom electrode and a gold top electrode. A short between the gold electrode and the ITO abd the surface of the gold electrode are shown.

A 3D image of a thin $WS_2$ device (~900 nm) can be seen in Fig. 5.14. In the region imaged a short between the Au electrode and the ITO electrode can be seen. Interestingly, the short is not caused by gold diffusing into the pore network of the $WS_2$ network but is instead caused by a pinhole in the $WS_2$ network. This suggests that the minimum thickness required for the network to prevent shorting is related to the roughness of the underlying network and that shorting could be prevented by improved deposition. Using the same method as for the graphene/AgNP heterostack, the surface roughness of the network was investigated yielding $R_{RMS}$=114 $\pm$ 27 nm, similar to the values calculated for the graphene network. Information about the quality of the gold top electrode can also be obtained from the 3D images. The electrode covers over 98% of the area imaged, with over 99%

of the gold electrode being connected, demonstrating that the gold electrode covers the area of interest. The electrode has an in-plane tortuosity factor of 1.8, suggesting that the electrode is twice as resistive as it would be on a flat surface. The high tortuosity factor of the gold electrode is caused by the roughness of the underlying $WS_2$ network.

In conclusion, we have demonstrated that FIB-SEM nt can be used to determine a wide range of morphological parameters of nanosheet networks. The morphology of size-selected graphene networks was investigated by this method, finding that the porosity and pore size decrease as nanosheet size decreased, while, the pore circularity and SSA increase. The in-plane and out-of-plane tortuosity factor of the nanosheets and pores was calculated, with both following a generalised Bruggeman relationship. It was found that the nanosheet thickness increases more than the nanosheet length during the spray-coating process, with smaller, thinner nanosheets aggregating more than larger, thicker nanosheets. The nanosheet alignment was found to decrease as the nanosheet length decreases. This technique was then extended to size-selected networks of AgNSs and $WS_2$, demonstrating the ability of the technique to interrogate networks of a range of materials. The AgNS and $WS_2$ networks show similar trends with nanosheet length, to the graphene networks, however, the magnitude of the calculated values vary considerably, with $WS_2$ networks being more porous than graphene, while AgNS networks are less porous. Finally, the technique was extended to heterostack devices. First, the interface between an AJP AgNP top electrode and two graphene networks with different nanosheet lengths was investigated. It was found that the AgNPs penetrate further into a network composed of larger nanosheets than a network of smaller nanosheets, with the penetration leading to a far rougher interface between the materials. Shorting in out-of-plane ITO/$WS_2$/Au devices was also investigated, and it was found that the shorting of the devices is driven by pin-holes in the $WS_2$ network. These results demonstrate the ability of FIB-SEM nt to determine a range of morphological parameters of nanosheet networks and their devices.

*"Tao gives birth to one, one gives birth to two, and two to three, three gives birth to all things. All things have yin and yang, filled with Qi that is in harmony."*

Lao Tzu

# 6

# The relationship between nanosheet dimension & network conductivity

The ever increasing demand for cheap consumer electronics has led to an explosion in interest in the field of printed electronics in recent years. This has catalysed a rapid increase of research into solution processing of 2D materials, as they are an ideal candidate for printed flexible electronic devices.[138] Nanosheets exhibit the full range of electrical and optical properties and so can be used to produce a wide range of solution-processed devices from photo-diodes to transistors.[138,297] The solution processing of these nanosheets can be achieved by a variety of methods, allowing for the low-cost production of large quantities of materials.[97]

While nanosheets show great promise for an array of applications, this promise has yet to transfer to nanosheet networks. The electrical properties of nanosheet networks are generally considerably inferior to those of the nanosheets they are composed of, with spray-coated networks of LPE TMD nanosheets showing mobilities 1,000 times lower than the constituent nanosheets.[170] The electrical properties of these networks are defined by 3 factors: the electrical properties of the constituent nanosheets, the junctions between the nanosheets, and the morphology of the network,[82] a method to interrogate the morphology of nanosheet networks has already been presented in Chapter 5. It has been theorised for decades that the junction resistance leads to the inferior performance of nanomaterial networks relative to their constituent materials,[2,82,182] but quantification of the junction resistance and its effect on network conductivity has been limited.

This chapter presents a model to describe conduction in nanosheet networks. The model is derived by considering the voltage drop across each nanosheet and junction and calculating the average number of nanosheets and junctions between the electrodes. The model predicts that the conductivity of nanosheet networks depends strongly on the dimensions of the

nanosheets in the network. To test the validity of the model, the electrical properties of size-selected networks of graphene and $WS_2$ are characterised, showing agreement with the counterintuitive predictions of the model. The model allows for calculation of both the junction resistance and the conductivity of the nanosheets. All of the work presented in this chapter was done in collaboration with Dr. Cian Gabbett. Cian and I shared the workload for the production, deposition and testing of the graphene networks presented here. I produced the $WS_2$ inks, deposited them and tested their electrical properties in consultation with Cian.

## 6.1 Experimental procedure

Graphene and $WS_2$ nanosheets were produced by horn probe sonication (Sonics Vibra-cell VCX-750 ultrasonic processor) of bulk powders. Graphite (Asbury Carbons, grade 3763) was first ultrasonicated in DI water (18.2 MΩ.cm, produced in-house) for 1h at a concentration of 35 mg.mL$^{-1}$, with an amplitude of 55% and a pulse rate of 6 s on and 2 s off. The process temperature was maintained at 7°C using a chiller to prevent overheating of the ultrasonic probe. The resulting dispersions were centrifuged (Hettich Mikro 220R) for 1 h at 2684× $g$ to remove contaminants from the starting material. The supernatant was decanted, and the sediment was redispersed in 80 mL of DI water and SC (>99%, Sigma Aldrich) at a concentration of 2 mg.mL$^{-1}$. The resulting dispersion was sonicated for 8 h, with a 4 s on and 4 s off pulse rate, at an amplitude of 50%. The $WS_2$ nanosheets were produced in a similar manner from commercially sourced powder (10–20 $\mu$m, 99.8% metals basis, Alfa Aesar). However, the ultrasonication was carried out using IPA (HPLC grade, Sigma Aldrich) as the solvent.

The stock dispersions produced by the LPE of the graphite and $WS_2$ powders were size-selected using LCC. Here, a polydisperse parent dispersion is separated into fractions of progressively smaller nanosheets by isolating sediments with increasing RCF.[130] These sediments can then be redispersed in solvents as required. Each stock dispersion was first centrifuged at 28× $g$ for 2 h to remove unexfoliated material. For graphene, the supernatant was centrifuged at 112× $g$, 252× $g$, 447× $g$, 699×$g$ and 1789× $g$ for 2 h. After each step, the sediment was retained and redispersed in a reduced volume of fresh DI:SC solution (2 mg.mL$^{-1}$) to create a size-selected ink. The fraction captured at 112× $g$ was subjected to an additional centrifugation step at 28× g for 1 h to generate a further size fraction. The $WS_2$ stock dispersion was fractionated using upper limits of 112× $g$, 252× $g$, 342× $g$, 699× $g$, 1006× $g$, 1789× $g$ and 4025× $g$. Here, the largest size was split into three fractions by additional centrifugation steps at 28× $g$ and 63× $g$ for 1 h. The smallest of these sizes (63× $g$) was not used. Each sediment was redispersed in IPA.

The size-selected graphene inks were then transferred into IPA for spray-coating. To ensure that their was no loss of material, samples isolated below 1066× $g$ were centrifuged at

4052× $g$ for 2 h. The DI:SC supernatant was discarded, and the sediment was redispersed in IPA. This step was repeated twice to ensure removal of the surfactant. For nanosheet fractions isolated above 1066× $g$, a RCF of 25,155× $g$ was used for the transfer step.

AFM (Bruker Multimode 8, ScanAsyst mode, non-contact) was used to measure the nanosheet thickness and lateral dimensions in the graphene and $WS_2$ inks. Measurements were performed in air under ambient conditions using aluminium coated silicon cantilevers (OLTESPA-R3). The dispersions were diluted with IPA to optical densities <0.1 at 300 nm. A drop of the dilute dispersion (10 $\mu$L) was flash-evaporated on pre-heated (175°C) $Si/SiO_2$ wafers (300 nm oxide layer, 0.5 × 0.5 $cm^2$, MicroChemicals). After deposition, the wafers were rinsed with ~10 mL of water and ~10 mL of IPA and dried with compressed nitrogen. Typical image sizes ranged from 15 × 15 $\mu m^2$ for larger nanosheets to 3 × 3 $\mu m^2$ for small nanosheets at scan rates of 0.4–0.8 Hz with 1024 lines per image. Previously published length corrections were used to correct lateral dimensions from cantilever broadening.[207,209] UV-Vis optical spectroscopy (Perkin Elmer 1050 spectrophotometer) was used to determine the concentration of the inks using previously reported spectroscopic metrics.[207,209] Each ink was diluted to a suitable optical density and extinction spectra were recorded in 1 nm increments using a 4 mm quartz cuvette.

Spray-coating was performed using a Harder and Steenbeck Infinity airbrush attached to a computer-controlled Janome JR2300N mobile gantry. All deposited traces were defined using stainless steel shadow masks, on substrates heated to a temperature of 80°C. A $N_2$ back pressure of 45 psi, nozzle diameter of 400 $\mu$m, and stand-off distance of 100 mm between the nozzle and substrate were used. The size-selected graphene and $WS_2$ inks were diluted to a concentration of 0.2 $mg.mL^{-1}$ and 0.5 $mg.mL^{-1}$ respectively for spray-coating. The traces were patterned onto ultrasonically cleaned glass slides (VWR). Pre-patterned gold bottom electrodes (5 nm/95 nm Ti/Au) were deposited onto the glass substrates to facilitate electrical measurements on the networks using a Temescal FC2000 metal evaporation system.

SEM of the deposited nanosheet networks was performed using a Carl ZEISS Ultra Plus SEM. Samples were mounted on aluminium SEM stubs using conductive carbon tabs (Ted Pella) and grounded using conductive silver paint (PELCO, Ted Pella). All images were captured at an accelerating voltage of 2 kV, using a working distance of 5 mm, and a 30 $\mu$m aperture. The Inlens detector was used for imaging. The thickness of the deposited networks was determined using a combination of contact (graphene) and optical ($WS_2$) profilometry. Contact profilometry was performed using a Bruker Dektak stylus profilometer (10 $\mu$m probe, 19.6 $\mu$N force). An optical profilometer (Profilm3D, Filmetrics) operating in white-light interferometry mode with a 50× objective lens was used for non-contact thickness measurements.

Electrical characterisation of the printed networks was performed in ambient conditions using a Keithley 2612A source-meter connected to a probe station. Prepatterned electrodes

were used to characterise the printed graphene networks using two-terminal measurements in a transmission line geometry. Two-terminal measurements in an interdigitated electrode geometry were used to measure the resistance of the printed $WS_2$ traces.

## 6.2 Results & discussion

### 6.2.1 Model development

Understanding charge transport in nanosheet networks requires a model that describes the essential components of conduction through the network. The existing models can be divided into 2 categories: computational models and simple chain resistor models. Computational models require assumptions about nanosheet orientation and geometry, as well as conduction through the junctions between adjacent nanosheets. While these models have demonstrated some success, they do not generally produce experimentally testable predictions.[302] Chain resistor models have been utilised to model charge transport through networks of 1D and 2D nanomaterials.[82,303] Such models assume that the charge transport takes a single path through the network, they create experimentally testable predictions. As discussed in Chapter 3.3.2, Kelly *et al.* have proposed models for the electrical properties of nanosheet networks under different conditions. These includes networks completely limited by the junctions and networks where both the nanosheets and junctions affects the network conductivity. However, the model for junction and nanosheet limited networks does not correspond with experimental results.[82,126] Therefore, a new model for conduction in nanosheet networks is required.

Here, a model describing charge transport through a nanosheet network is presented, with the full derivation shown in Appendix A.3.1. This model was derived with Dr. Cian Gabbett, Dr. Adam G. Kelly, Emmet Coleman and Prof. Jonathan N. Coleman. The path of a charge carrier through a nanosheet network can be modelled by assuming the charge carrier passes through a series of nanosheet-junction pairs. Each nanosheet has a resistance $R_{NS}$, the charge carrier must then hop across the junction between two nanosheets, this hop has an associated resistance $R_J$, the junction resistance. The path of a charge carrier across two nanosheets is shown in Fig. 6.1A, the charge carrier will travel through several nanosheet-junction pairs between the electrodes as shown in Fig. 6.1B. Assuming that the charge carrier travels halfway through a nanosheet before hopping to the next, we can say that the number of nanosheet-junction pairs ($N$) in the conduction path is given by

$$N \approx \frac{(L\sqrt{\kappa_{NS}})}{(\frac{l_{NS}}{2} + l_J)} \tag{6.1}$$

where $L$ is the electrode separation, $\kappa_{NS}$ is the in-plane nanosheet tortuosity factor, $l_{NS}$ is the nanosheet length and $l_J$ is the junction separation

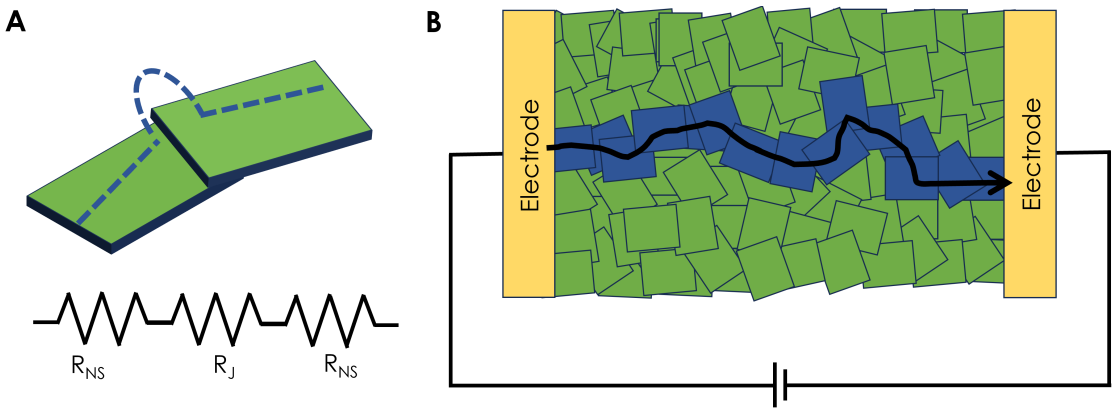



Figure 6.1: **Modelling charge transport: A)** Image showing two nanosheets, with a possible charge carrier path across the network shown as a dashed line. Each nanosheet has an associated resistance $R_{NS}$ and the resistance of the junction between the two nanosheets is denoted as $R_J$. **B)** Schematic showing a possible path, in blue, that a charge carrier travelling from one electrode to another might travel through a nanosheet network.

The voltage drop across a nanosheet-junction pair ($V_P$) is given by $V_P = V_{NS} + V_J = V/N$ where $V_{NS}$ and $V_J$ is the voltage drop across the nanosheet and junction respectively and $V$ is the applied voltage. The voltage drop across a junction can be expressed as

$$V_J \approx \frac{R_J}{R_J + R_{NS}} V \frac{\frac{l_{NS}}{2} + l_J}{L\sqrt{\kappa_{NS}}} \tag{6.2}$$

Similarly, the voltage drop across a nanosheet can be expressed as

$$V_{NS} \approx \frac{R_{NS}}{R_J + R_{NS}} V \frac{\frac{l_{NS}}{2} + l_J}{L\sqrt{\kappa_{NS}}} \tag{6.3}$$

The time taken for a charge carrier to travel across the network ($\tau_{Net}$) is given by

$$\tau_{Net} = \frac{L\sqrt{\kappa_{NS}}}{\mu_{Net} E} = \frac{L^2 \kappa_{NS}}{\mu_{Net} V} \approx N(\tau_{NS} + \tau_J) \tag{6.4}$$

where $\mu_{Net}$ is the network mobility, $E$ is the applied electric field and $\tau_{NS}$ and $\tau_J$ are the time to cross a nanosheet and junction respectively. By calculating $\tau_{NS}$ and $\tau_J$ it can be shown that

$$\mu_{Net} \approx \frac{\left(\frac{l_{NS}}{2} + l_J\right)^2}{\left(\frac{l_{NS}}{2}\right)^2 \left[1 + \frac{R_J}{R_{NS}}\right]} \frac{\mu_{NS}}{\kappa_{NS}\left[1 + \frac{4\mu_{NS} e R_{NS}}{l_{NS}^2}\right]} \tag{6.5}$$

where $\mu_{NS}$ is the nanosheet mobility and $e$ is the charge on an electron. This equation can be simplified by assuming $(l_{NS}/2) \gg l_J$, allowing us to state $l_J \approx 0$. This expression can then be converted to network conductivity ($\sigma_{Net}$) by stating $\sigma_{net} = \mu_{net} n_{net} e$ where $n_{net}$ is the network carrier concentration. The network carrier concentration can be related to the nanosheet carrier concentration ($n_{NS}$) as $n_{Net} = (1 - P) n_{NS}$ where $P$ is the network

porosity.[170] This allows us to state

$$\sigma_{Net} \approx \frac{\sigma_{NS}(1-P)}{\kappa_{NS}\left[1+\frac{R_J}{R_{NS}}\right]\left[1+\frac{4\mu_{NS}eR_{NS}}{l_{NS}^2}\right]} \tag{6.6}$$

Here, the nanosheet resistance will still depend on the nanosheet geometry, if we assume the nanosheets are square then we can state $R_{NS} = (2\sigma_{NS}t_{NS})^{-1}$, allowing us to state

$$\sigma_{Net} \approx \frac{\sigma_{NS}(1-P)}{\kappa_{NS}[1+2R_J\sigma_{NS}t_{NS}]\left[1+\frac{2}{t_{NS}l_{NS}^2n_{NS}}\right]} \tag{6.7}$$

This equation can also be written in terms of resistivity as

$$\rho_{Net} \approx \frac{2t_{NS}\kappa_{NS}}{1-P}[R_{NS}+R_J]\left[1+\frac{2}{n_{NS}t_{NS}l_{NS}}\right] \tag{6.8}$$

These equations are general and should describe the electrical conductivity or resistivity of all nanosheet networks. There are several things worth noting about this derivation. Firstly, while it is assumed here that the charge transport through the nanosheets is classical and can be described by $R_{NS} = (2\sigma_{NS}t_{NS})^{-1}$, the model could instead be restated with a semi-quantum approach by assuming the nanosheet resistance is given by $R_{NS} = R_Q l_{NS}/2\zeta$, where $R_Q$ is the quantum resistance and $\zeta$ is the scattering length, a derivaton of the network conductivity assuming this type of transport can be found in Appendix A.3.1. Secondly, while the derivation was carried out for a nanosheet network, similar equations can be obtained for networks of 1D or 0D nanomaterials by changing the assumptions about the geometry of the material.

In the case of material exfoliated by LPE, the nanosheets have a constant aspect ratio, in this case Eqn. 6.7 can be rewritten to reflect this fact. Network conductivity as a function of nanosheet length can be expressed as

$$\sigma_{Net} \approx \frac{\sigma_{NS}(1-P)}{\kappa_{NS}\left[1+\frac{2R_J\sigma_{NS}l_{NS}}{k_{NS}}\right]\left[1+\frac{2k_{NS}}{l_{NS}^3n_{NS}}\right]} \tag{6.9}$$

where $k_{NS}$ is the nanosheet aspect ratio. Alternatively, network conductivity can be expressed in terms of nanosheet thickness as

$$\sigma_{Net} \approx \frac{\sigma_{NS}(1-P)}{\kappa_{NS}[1+2R_J\sigma_{NS}t_{NS}]\left[1+\frac{2}{t_{NS}^3k_{NS}^2n_{NS}}\right]} \tag{6.10}$$

These equations and Eqn. 6.7 are quite complex, to better understand the predictions of the model, we will now investigate its predictions for two specific cases, nanosheets with high and low carrier densities.

For materials with high carrier densities, $n_{NS} \gg (2/t_{NS}l_{NS}^2)$, meaning that we can state

$2/(t_{NS}l_{NS}^2 n_{NS}) \approx 0$. In this case, we can simplify Eqn. 6.7 to

$$\sigma_{Net} \approx \frac{(1-P)\sigma_{NS}}{\kappa_{NS}(1+2t_{NS}\sigma_{NS}R_J)} \approx \frac{(1-P)\sigma_{NS}k_{NS}}{\kappa_{NS}(k_{NS}+2R_J\sigma_{NS}l_{NS})} \tag{6.11}$$

Interestingly, this suggests that thinner nanosheets should produce more conductive networks. For nanosheets with a constant aspect ratio, which includes nanosheets produced by LPE, this equation implies that smaller nanosheets should yield a more conductive network, despite the fact that the charge carriers will have to travel through more junctions. In the literature, there are two reports of size-selected LPE nanosheet networks showing an increase in network conductivity as nanosheet size decreases: one for graphene and one for $MoS_2$, however, neither report a constant nanosheet aspect ratio, making fitting with this equation impossible.[126,304] There is also a report of size-selected rGO networks that show decreasing network conductivity with decreasing nanosheet length, however, in this case, the nanosheet thickness is constant, and the decrease in conductivity may imply an increase in junction resistance with decreasing nanosheet size.[305] The results of this paper are further discussed in Chapter 7 and in appendix A.4.3.

In the case of a semiconductor with a low carrier concentration, the value of $n_{NS} \ll (2/t_{NS}l_{NS}^2)$ meaning $2/(t_{NS}l_{NS}^2 n_{NS}) \gg 1$. In this case, we can state that

$$\sigma_{Net} \approx \frac{(1-P)n_{NS}t_{NS}l_{NS}^2\sigma_{NS}}{2\kappa_{NS}(1+2\sigma_{NS}t_{NS}R_J)} \approx \frac{(1-P)n_{NS}l_{NS}^3\sigma_{NS}}{2\kappa_{NS}(k_{NS}+2\sigma_{NS}l_{NS}R_J)} \tag{6.12}$$

This equation is more complex than Eqn. 6.11, however, it suggests the network conductivity will depend strongly on nanosheet dimensions. Higgins *et al.* have investigated the effect of nanosheet length on the mobility of ionically gated spray-coated $WS_2$ transistors, finding that transistors made of smaller nanosheets show inferior mobility.[273]

To fully understand the predictions of Eqn. 6.9, the effect of a variety of parameters on the model must be understood. Fig 6.2 shows what the model predicts the effect of varying the junction resistance, nanosheet carrier density, nanosheet mobility and nanosheet aspect ratio would be on the conductivity of nanosheet networks. Here, it can be seen that the model predicts a peak in network conductivity for a given nanosheet length, the position of this peak can be calculated by differentiating Eqn. 6.9, however, the position of the maximum is too complex to be useful for simple analysis. From Fig. 6.2 the effect of the parameters which effect the peak position can be seen. From Fig. 6.2A it can be seen that decreasing the junction resistance causes an increase in the network conductivity without inducing a shift in the position of the maximum conductivity peak. However, changing both the nanosheet carrier density and the nanosheet aspect ratio has a large impact on the peak position. Increasing the nanosheet carrier density causes the maximum conductivity peak to shift to lower nanosheet lengths as can be seen in Fig. 6.2B, this can be understood as a shift from the behaviour described by Eqn. 6.12 to the behaviour described by Eqn. 6.11. Interestingly, changing the nanosheet aspect ratio has the opposite

effect, with networks composed of nanosheets with higher aspect ratios showing a peak at larger nanosheet length values, as can be seen in Fig. 6.2C. Increasing the nanosheet aspect ratio also causes an increase in the maximum conductivity achieved, this might partially explain the higher conductivity of EE nanosheet networks when compared to LPE nanosheet networks. Finally, Fig. 6.2D shows that changing nanosheet mobility has minimal impact on network conductivity when compared to the other parameters, only causing a slight decrease in conductivity at smaller nanosheet lengths. However, decreasing the nanosheet mobility beyond some value appears to lead to a shift in the peak position to lower nanosheet lengths.

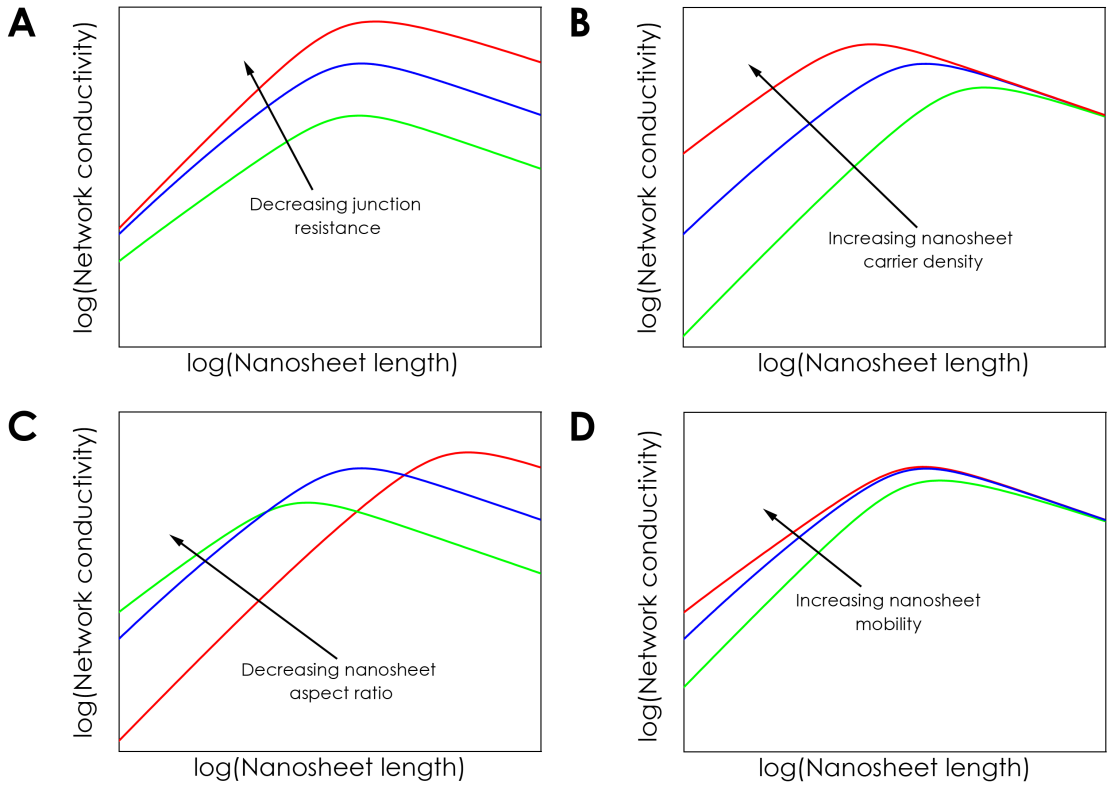



Figure 6.2: **Factors impacting network conductivity:** Network conductivity as a function of nanosheet length calculated from Eqn. 6.9, with changing **A** Junction resistance, **B** nanosheet carrier density, **C** nanosheet aspect ratio, **D** nanosheet mobility. In each case the central (blue) line is the same and the parameter being varied is increased and decreased by an order of magnitude from this value. All of the curves are shown on the same scale. The curves with axes and each of the inputted values is shown in appendix A.3.2.

In order to investigate the validity of Eqn. 6.7 its predictions must be tested against experimental data for size-selected conducting and semiconducting nanosheet networks to see if the predicted behaviour is observed.

### 6.2.2 Electrical properties of size-selected graphene networks

To investigate if Eqn. 6.7 describes the conductivity of conducting nanosheet networks, electrical tests were carried out on size-selected spray-coated graphene networks. The graphene networks used here are the same as those used in Chapter 5, and a full characterisation of the graphene inks and the network morphology can be found in that chapter.

In brief, a stock graphene ink was produced by ultrasonication of graphite powder in a SC:DI solution. Size-selected inks were produced by LCC, and were transferred to IPA.[130] The inks show a constant nanosheet aspect ratio of $k_{NS}$=29. The size-selected inks were then spray-coated onto cleaned glass slide with predeposited gold electrodes, the width of the graphene trace was controlled using a mask. The geometry of the gold electrodes is shown in Fig. 6.3A.

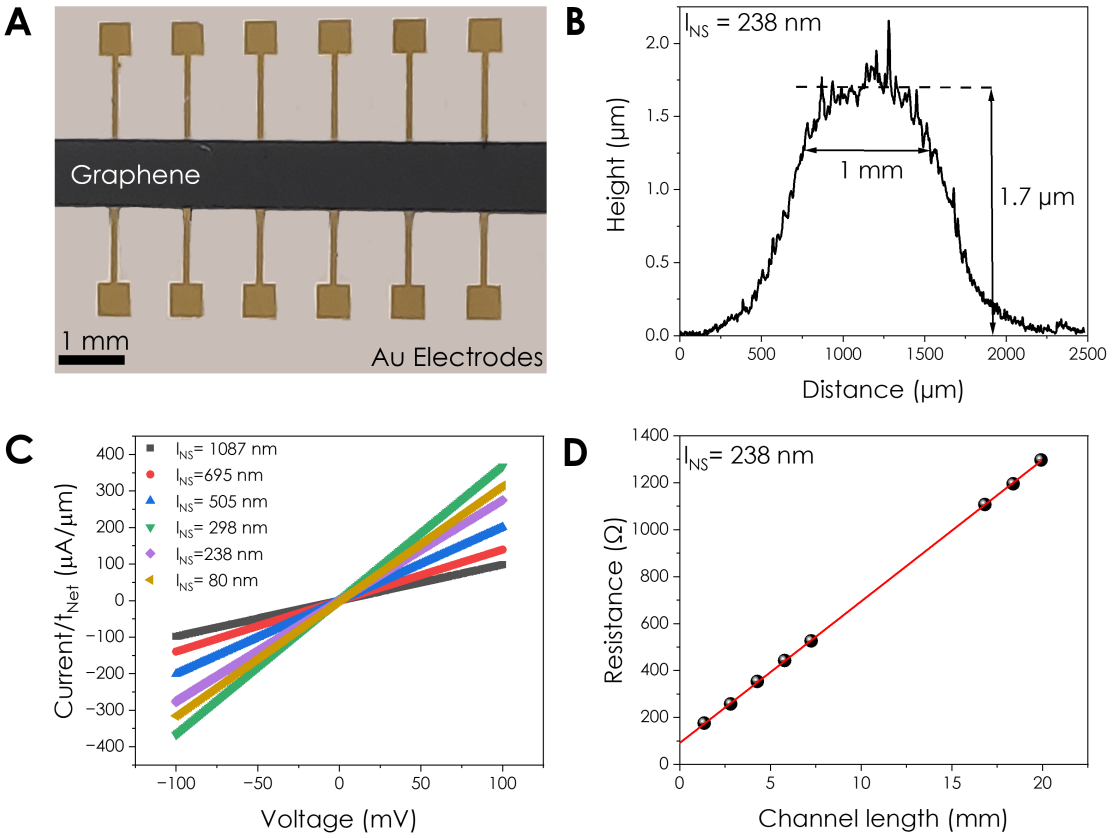



Figure 6.3: **Electrical characterisation of size-selected graphene networks: A)** Image of a section of a printed graphene device showing the graphene trace and the gold electrodes. **B)** Representative stylus profilometry measurement of printed graphene trace with $l_{NS}$= 238 nm, showing the trace has a width of 1 mm and a height of 1.7 $\mu$m. **C)** Current, scaled by network thickness, $t_{Net}$, as a function of applied voltage for the shortest channel length of each of the 6 size-selected networks. **D)** Resistance as a function of channel length for the network with $l_{NS}$=238 nm. The red line shows a linear fit to the data and was used to extract the contact resistance and network conductivity.

To calculate the conductivity of the graphene traces the thickness of each of the networks was measured by stylus profilometry. This technique is similar to contact AFM, the de-

flection of a probe (in this case 12.5 $\mu$m in diameter) as it is moves across the surface of the network is measured. A representative profilometry profile can be seen in Fig. 6.3B. The thickness of the trace was measured between each of the gold electrodes to ensure the network thicknesses were uniform. The resistance between the first electrode and every subsequent electrode was then measured. The measured current, scaled by network thickness, as a function of applied voltage is shown in Fig. 6.3C, each of the curves is linear in the measured range, allowing for calculation of network resistance.

The network conductivity was calculated by plotting resistance as a function of channel length, a representative graph is shown in Fig. 6.3D. The resistance scaled linearly with channel length for each of the networks, demonstrating that the spray-coated traces are homogeneous. A linear fit to the data can be used to calculate both the contact resistance, and the network resistance as a function of channel length. The network conductivity can be calculated using Eqn. 3.2, as discussed in Chapter 3.

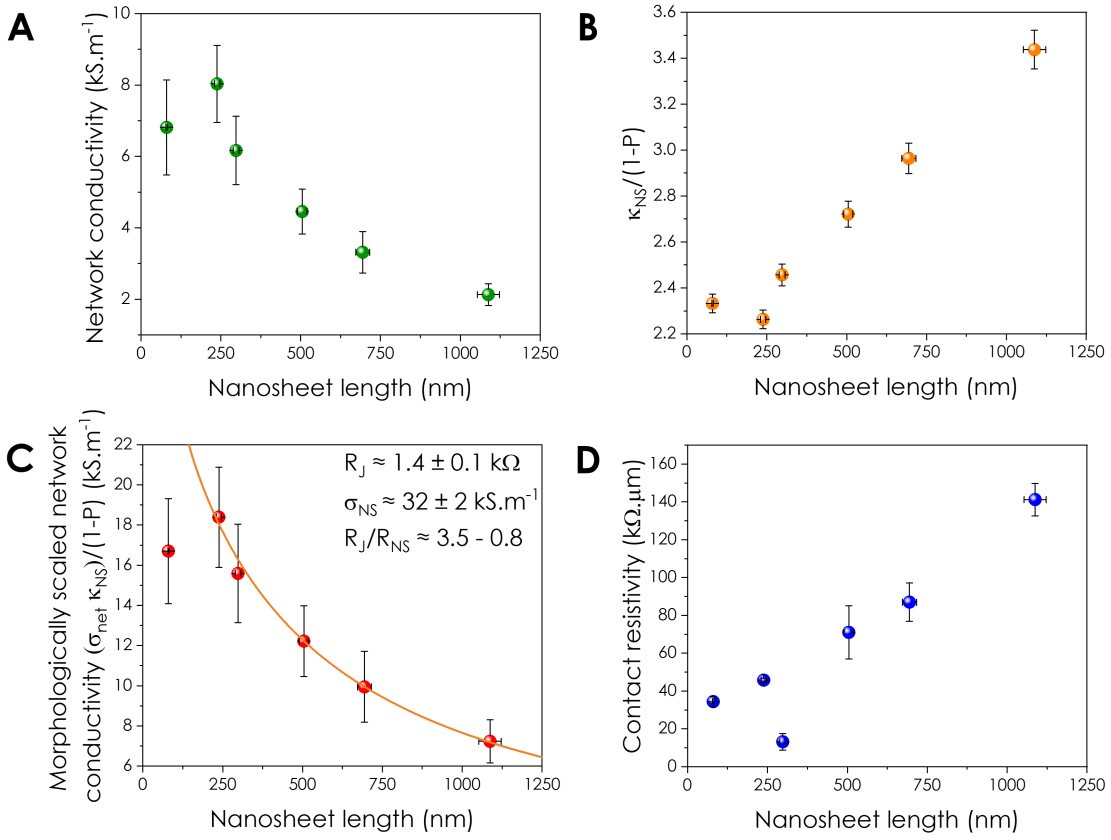



Figure 6.4: **Nanosheet length dependent conductivity of graphene networks: A)** Conductivity of spray-coated graphene networks plotted against nanosheet length. **B)** In-plane nanosheet tortuosity factor, $\kappa_{NS}$, divided by 1-porosity, (1-$P$), as a function of nanosheet length. A discussion of this data can be found in Chapter 5. **C)** Conductivity of the graphene networks scaled by $\kappa_{NS}/(1-P)$, to account for network morphology, plotted against nanosheet length. Fit to Eqn. 6.7 is shown, yielding $R_J = 1.4 \pm 0.1$ kΩ and $n_{NS} = (1.0 \pm 0.1) \times 10^{24}$ m$^{-3}$. Using the calculated data the ratio between the nanosheet and junction resistance for each size-selected network is calculated. **D)** Contact resistivity of the graphene networks with the gold electrodes as a function of nanosheet length.

Graphene network conductivity as a function of nanosheet length is shown in Fig. 6.4A, there

is a general trend of increasing network conductivity as nanosheet length decreases, which is in line with the prediction of Eqn. 6.11. This demonstrates that by controlling nanosheet dimensions the network's electrical properties can be optimised, with a four-fold reduction in nanosheet length leading to a factor of 4.5 increase in network conductivity.

Eqn. 6.7 predicts that the conductivity of a nanosheet network is affected by 3 factors: the network morphology, the nanosheet properties, and the junction resistance. As the graphene network conductivity, shown in Fig 6.4A, is calculated from the same samples as the morphology data presented in Chapter 5, the effect of changing nanosheet length on the network structure can be quantified. The two morphological parameters that Eqn. 6.7 suggests reduce conductivity are the network porosity and nanosheet tortuosity factor, as $\kappa_{NS}/(1-P)$. This parameter, which will be referred to as the morphological scaling factor is shown in Fig. 6.4B. The magnitude of this scaling factor decreases as the nanosheet length decreases, dropping by by a factor of ~1.6 over the nanosheet length range considered. It is clear from this data that the morphology has a large impact on the conductivity of the networks; in the absence of other effects eliminating porosity and reducing the in-plane tortuosity factor to 1 would lead to a 3.5 fold increase in the network conductivity. This analysis only considers the effect of porosity and tortuosity, other morphological parameters, such as nanosheet alignment, may affect the network conductivity by varying the junction resistance.

Fig. 6.4C shows the graphene network conductivity with the impact of porosity and tortuosity removed. As the morphological scaling factor shows the opposite trend to the network conductivity as a function of nanosheet length, removing its affect reduces the rate of increase in conductivity with nanosheet length. However, it is clear that even with the effect of morphology removed, nanosheet length still has a large effect on the network conductivity. The fit of Eqn. 6.7 to the morphologically scaled conductivity data is shown in Fig. 6.4C, the data was fit excluding the network printed with the smallest nanosheets, as this data point is an outlier. For the fit the nanosheet mobility was fixed to 2,000 $cm^2.V^{-1}.s^{-1}$ the value reported for graphite,[306] this value was fixed as the fit depends very weakly on the nanosheet mobility as can be seen from Fig. 6.2D. The value of the nanosheet aspect ratio was fixed at 29, the value measured for these nanosheets in Chapter 5. The fit yields yields a nanosheet carrier concentration value of $n_{NS} = (1.0 \pm 0.1) \times 10^{24}$ $m^{-3}$, and a junction resistance of $1.4 \pm 0.1$ kΩ. The calculated carrier concentration combined with the nanosheet mobility gives a nanosheet conductivity of $32 \pm 2$ $kS.m^{-1}$, slightly below the value generally reported for graphite, which varies between 50-170 $kS.m^{-1}$.[28] The calculated value may be lower than literature values due to limitations with the model or due to the exfoliation process creating defects in the nanosheets.[307] The value of the junction resistance is in line with other reported values for the junction resistance of graphene networks, which varies between 0.5-10 kΩ.[26,82,199]

Using the calculated values for the nanosheet conductivity and junction resistance, the ratio

of nanosheet to junction resistance can be estimated. This parameter describes whether the network conductivity is limited by the nanosheets, the junctions, or is affected by both, which is important when trying to optimise network conductivity. If networks are nanosheet-limited ($R_J/R_{NS} < 0.1$), then improving nanosheet conductivity, for example, by doping the nanosheets, is the best route for optimisation. However, if the network is junction-limited ($R_J/R_{NS} > 10$), network conductivity can be improved by optimising the junctions in the network, perhaps by improving the alignment of the nanosheets by compression, or by cross-linking the nanosheets.[186,187] For the size-selected graphene networks, the ratio of junction to nanosheet resistance varies between 0.8-3.5, suggesting the networks are nanosheet- and junction-limited. Therefore, optimisation of these networks could be achieved both by increasing nanosheet conductivity and reducing the junction resistance.

One assumption of applying Eqn. 6.7 to the length dependent graphene data is that the junction resistance is the same in each of the networks. The good fit of the equation to the data suggests that this assumption is true. This may imply that the nanosheets have point-like contacts with adjacent nanosheets, with no variation in junction area with increasing nanosheet size. Alternatively, the data presented in Chapter 5 shows that the aggregation of the nanosheets increases as the nanosheet length decreases. This increase in aggregation factor may imply that as a nanosheets length decreases its overlap area with adjacent nanosheets, as a percentage of nanosheet area, increases, leading to minimal change in junction area as nanosheet length decreases.

The fit shown in Fig. 6.4C does not include the smallest nanosheet length, which is an outlier to the trend. One possible explanation for why very small graphene nanosheets may not obey Eqn. 6.7 is that graphene shows a layer-dependent band gap for nanosheets thinner than ~10 layers,[308] the smallest nanosheets here are $2 \pm 1$ layers thick, therefore, band mismatch between adjacent nanosheets may cause an increase in the junction resistance.[191]

The contact resistance between the graphene networks and the gold electrodes was also calculated. For 2D materials, the contact resistance is generally normalised by the contact width, giving the contact resistivity. The dependence of the contact resistivity on nanosheet length is shown in Fig. 6.4D. The contact resistance decreases as nanosheet length decreases, varying by approximately a factor of 5 over the nanosheet length range considered, excluding the outlier at $l_{NS}$=298 nm. This decrease in contact resistance may be driven by the porosity of the networks at the base, the smaller nanosheets show a lower porosity, meaning there will be a larger contact area between the network and the gold, reducing the contact resistance.

To the best of the author's knowledge this is the first report of contact resistance between a printed graphene network and gold electrodes. The calculated contact resistance values are considerably higher than the values in the literature for individual graphene nanosheets and gold, which vary between 50-1200 $\Omega.\mu$m.[309] There are a number of possible reasons for the high contact resistance, the first is the high porosity of the networks, which will

reduce the contact area between the graphene nanosheets and the electrode. Secondly, due to the exfoliation and printing process there may be residual solvent or surfactants between the nanosheets and the gold, decreasing the quality of the contact.

### 6.2.3 Electrical properties of size-selected $WS_2$ networks

The data presented in Fig. 6.4 demonstrates that Eqn. 6.7 describes conduction in networks of conductive nanosheets. Evidence of the generality of the equation would be if it could describe the conductivity of a semiconducting nanosheet network as well. To this end, the nanosheet length dependent conductivity of networks of $WS_2$, a semiconducting layered material, was investigated.

Size-selected $WS_2$ inks were produced in IPA in a similar manner to the graphene. Normalised extinction spectra of the size-selected inks are shown in Fig. 6.5A and shows the same nanosheet length-dependent trend as other LPE size-selected $WS_2$ inks.[130,207] The nanosheets captured at low centrifugation speeds are large and thick and so the extinction spectra at low wavelengths are dominated by scattering.[216] As the centrifugation speed at which the nanosheets are captured at increases, the nanosheet thickness decreases, and scattering has less of an effect on the spectra at high wavelengths, in this case, the nanosheets show a well defined excitonic peak at ~630 nm. The UV-vis spectra were used to calculate the ink concentration using previously published spectroscopic metrics.[207]

The length and thickness of the nanosheets in the majority of the inks was calculated by AFM. A representative nanosheet length distribution can be seen in Fig. 6.5B. The AFM was carried out by Dr. Kevin Synnatschke. The data is lognormally distributed as has been found for nanosheets produced by LPE previously.[86,132] Nanosheet length as a function of the upper RCF the nanosheets were captured at is shown in Fig. 6.5C. There is a power-law relationship between nanosheet length and upper centrifugation speed, as described by Ogilvie *et al.*;[131] this relationship was used to extract the mean nanosheet length for the two inks for which AFM was not carried out due to time constraints.

The length and thickness of the size-selected $WS_2$ nanosheets are shown in Fig. 6.5D. The nanosheets show a constant aspect ratio of 15. This aspect ratio is below the theoretical value for LPE $WS_2$ nanosheets, as the nanosheets were exfoliated in IPA. While IPA is capable of stabilising $WS_2$ it does lead to a lower aspect ratio than other solvents.[86,118] The benefit of using IPA is that no solvent exchange is step required before printing, and there will be no surfactant or polymer molecules on the nanosheet surface, which could lead to an increase in the junction resistance.[82]

The size-selected inks were spray-coated onto cleaned microscope slides with 5 pre-patterned interdigitated gold electrodes deposited on them. The electrodes had a channel length of 50 $\mu$m and a channel width of 19.55 mm. Representative SEM images of the surface of a network composed of small and large nanosheets is shown in Fig. 6.6A. The morphology of

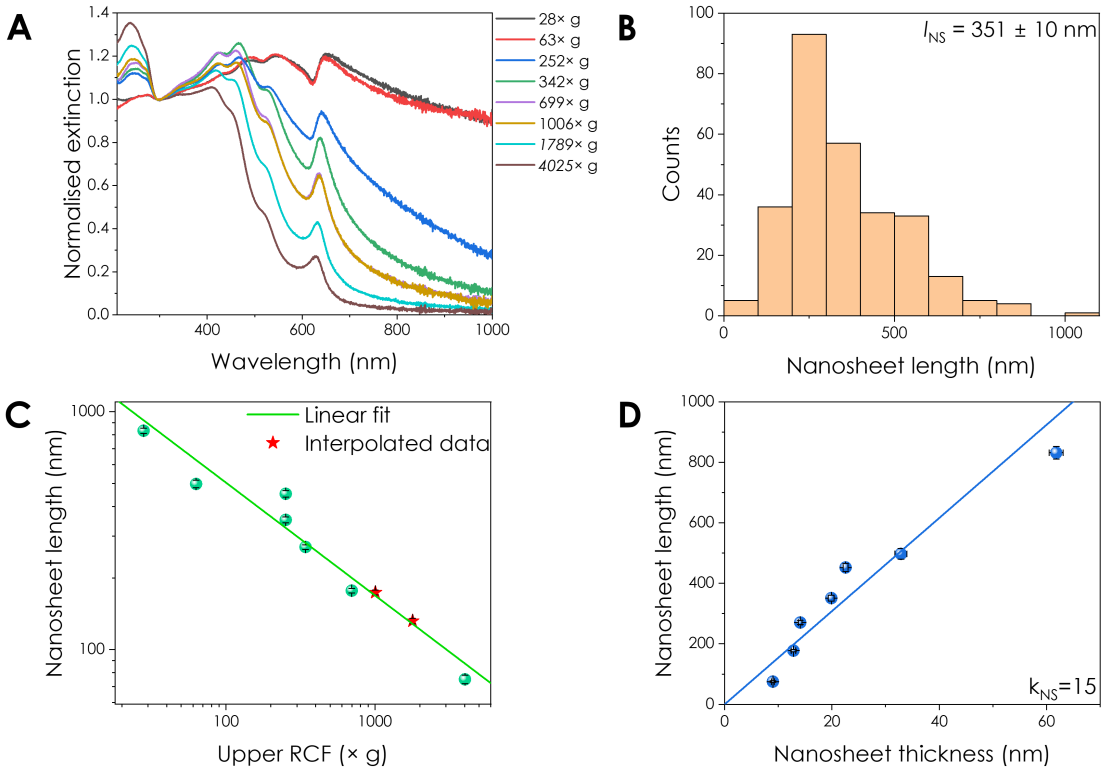



Figure 6.5: **Size-selected $WS_2$ inks: A)** UV-vis spectra of size-selected $WS_2$ inks, normalised to the local minimum at 235 nm. The upper RCF the nanosheets were captured at is shown. **B)** Representative nanosheet length distribution measured by AFM, for the nanosheets captured below 699× g. **C)** Average nanosheet length for each size-selected ink, as a function of the upper RCF, the ink was captured at. The line shown is a linear fit to the data. The two data points shown as red stars are extrapolated lengths based on the linear fit. **D)** Nanosheet length as a function of nanosheet thickness. A linear fit to the data gives an average nanosheet aspect ratio of 15.

these networks is similar to that of the $WS_2$ networks discussed in Chapter 5, due to time constraints 3D imaging and analysis was not carried out on each of the networks presented here.

The thickness of each of the printed networks was calculated by white-light optical profilometry. This is a non-contact profilometry technique that uses the interference fringes created by the reflection of a white light from each point on the surface to measure the height of the surface at that point. A movable stage is used to find the height at which there is maximum interference of the reflected light, the height of the stage at this point can be related to the height of the sample. This technique has been used to calculate the thickness of printed nanosheet networks.[80,310] A representative optical profilometry scan of the film with $l_{NS}$= 177 nm is shown in Fig. 6.6B.

IV curves were measured for each size-selected network. Representative IV curves, with the current normalised by network thickness, for four of the size-selected $WS_2$ networks are shown in Fig. 6.7A. While some of the IV curves show non-linear behaviour at high voltages, they are all linear at low voltages. All the IV curves were fit between -1 V and 1 V, where they are all linear, to calculate the network resistance. The calculated network

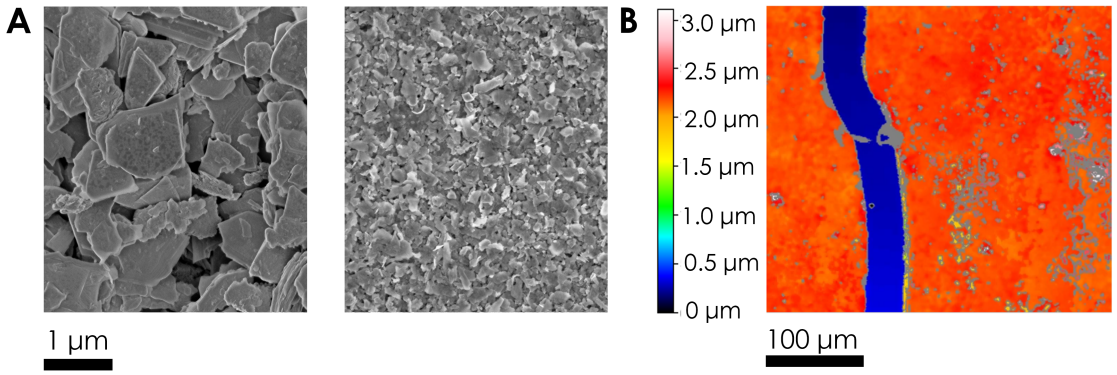



Figure 6.6: **Spray-coated $WS_2$ networks: A)** Representative SEM images of the surface of sprayed coated $WS_2$ networks with $l_{NS}$= 497 nm and $l_{NS}$= 132 nm, on a common scale. **B)** Optical profilometry of the sample with $l_{NS}$= 177 nm. The region in blue is the substrate and the remainder of the area is the network surface. The network thickness was calculated as 2.1 $\pm$ 0.4 $\mu$m.

resistances and thicknesses were combined to determine the $WS_2$ network conductivity, which is plotted as a function of nanosheet length in Fig. 6.7B. The data shows the opposite trend to the graphene data, with a peak in conductivity for large nanosheets and a decrease in conductivity as nanosheet length decreases. The change in conductivity here is far larger than is observed for graphene networks with approximately an order of magnitude change in conductivity when the nanosheet length is decreased from 497 $\pm$ 18 nm to 75 $\pm$ 3 nm. The very strong scaling of $WS_2$ network conductivity with nanosheet length suggests that for semiconducting nanosheets optimisation of nanosheet dimensions is integral for device optimisation. The large change in conductivity cannot be explained by changes in morphology, the data presented in Chapter 5 suggests that the morphological scaling factor varies from 3.6 $\pm$ 0.2 to 2.5 $\pm$ 0.1 for the networks presented here. The change in conductivity can, however, be explained using Eqn. 6.7, which suggests different behaviour for high and low carrier density materials. A fit of the $WS_2$ network conductivity data with Eqn. 6.7 is shown in Fig. 6.7B. Here, the nanosheet mobility was fixed at 60 $cm^2.V^{-1}.s^{-1}$, the value reported for LPE $WS_2$ nanosheets,[170] and the network porosity and tortuosity values were fixed at 50% and 1.5, based on the values calculated in Chapter 5. The fit yields a junction resistance value of 17 $\pm$ 3 G$\Omega$ and a nanosheet carrier concentration of (6 $\pm$ 1) $\times 10^{-20}$ $m^{-3}$, corresponding to a nanosheet conductivity of 0.6 $\pm$ 0.1 $S.m^{-1}$. This calculated nanosheet carrier density is in-line literature values for LPE $WS_2$, which vary between (0.3 - 20) $\times$ $10^{20}$ $m^{-3}$.[117,118,170,294]

The calculated junction resistance of 17 $\pm$ 3 G$\Omega$ is considerably larger than the value calculated for graphene, it is possible that this can be partially explained by a reduction in junction overlap area. In Chapter 5, we show that the thickness aggregation factor of graphene nanosheets is higher than that of $WS_2$. This suggests that there is larger overlap between adjacent graphene sheets, which is likely to lead to lower resistance junctions.[82] However, it seems improbable that a variation in junction area could explain the magnitude of the difference.

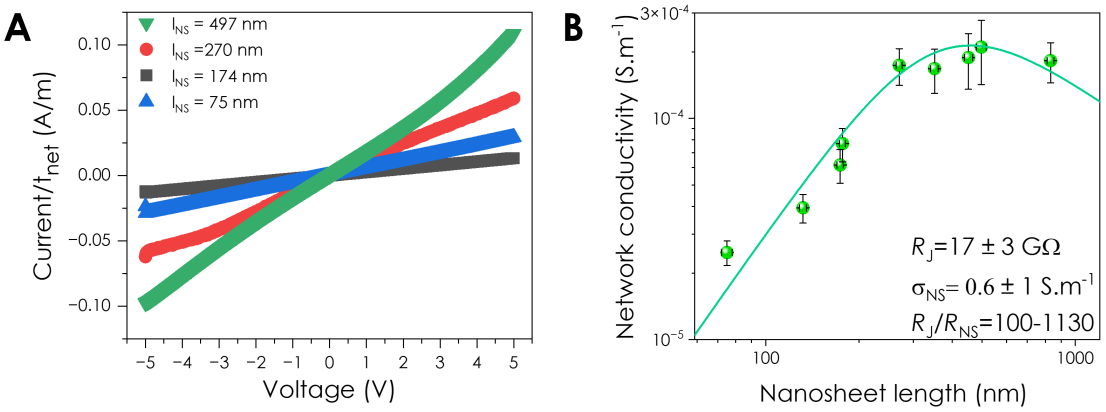



Figure 6.7: **Size-selected tungsten disulphide network conductivity: A)** Current, normalised by network thickness, as a function of applied voltage for a representative subset of the size-selected $WS_2$ networks. **B)** Network conductivity as a function of nanosheet length for size-selected $WS_2$ networks.

The large calculated junction resistance in the $WS_2$ networks leads to very large values of $R_J/R_{NS}$ ranging between 100-1130. This demonstrates that the very low mobilities reported for LPE $WS_2$ networks ($1\times10^{-3}$ - 0.1 $cm^2.V^{-1}.s^{-1}$) are caused in part by the presence of highly resistive junctions.[117,170,273,294] This suggests that optimisation of the mobility of LPE $WS_2$ nanosheet networks could be achieved by methods to reduce the junction resistance, such as cross-linking of the nanosheets (which has proven effective for LPE $MoS_2$ networks[184,186]) or by improving the overlap between adjacent nanosheets through network compression.[187] The latter method of improving $WS_2$ network conductivity is discussed in Chapter 8.2.

Here, we have demonstrated the applicability of Eqn. 6.7 to describe the nanosheet length dependent conductivity of spray-coated networks of graphene, a semi-metal, and $WS_2$, a semiconductor, suggesting that the equation is applicable to networks of a variety of nanosheets. Further work in the group by Dr. Cian Gabbett has demonstrated that this equation can be used to describe the nanosheet length dependent conductivity of networks printed from AgNSs and $WSe_2$, AgNSs are metallic while $WSe_2$ is semiconducting.[295] The relationship between nanosheet conductivity and the junction resistance, calculated by fitting Eqn. 6.7 to nanosheet length dependent conductivity data for each material, is shown in Fig. 6.8. Here, we can see that the junction resistance shows a clear dependence on nanosheet conductivity, suggesting that the junction resistance may be related to the conductivity of the material in the network. As discussed in Chapter 3.3.2, this effect has also been found for CNT networks; using C-AFM it has been found that an argon treatments leads to a factor of 3 decrease in nanotube conductivity, which causes a factor of 5 increase in junction resistance.[190]

Further work in the group by Emmet Coleman has shown that Eqn. 6.7 can be rewritten to describe conduction in networks of 1D nanomaterials. This version of the equation agrees with experimental results for silver nanowire networks, showing that network conductivity

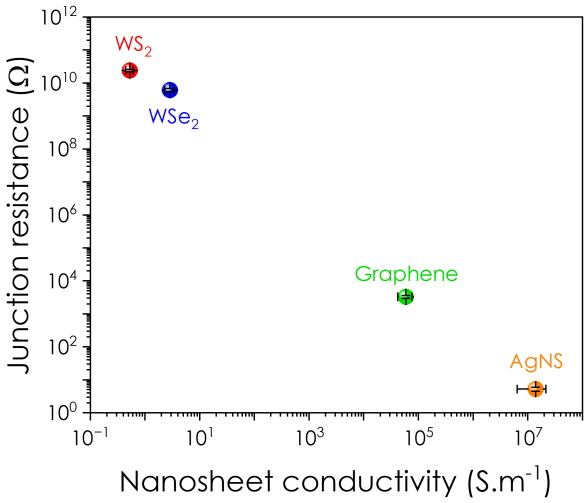



Figure 6.8: **Material conductivity and junction resistance:** Junction resistance as a a function of nanosheet conductivity calculated by fitting nanosheet length dependent conductivity data using Eqn. 6.7. Length dependent conductivity for AgNS and $WSe_2$ networks is presented in ref.[295]

is inversely proportional to the nanowire length.[295] Additional work in the group by Eoin Caffrey has found that Eqn. 6.7 can be used to model the dependence of the network gauge factor (a measure of the sensitivity of a strain sensor) on nanosheet thickness for printed graphene strain sensors. This work uses LPE graphene exfoliated in NMP and finds values of $\sigma_{NS}$ (~35 kS.m$^{-1}$) and $R_J$ (~9 kΩ), similar to the values obtained here.[310] Recent work by coworkers at Universidad de los Andes has tested the effect of nanosheet size on the conductivity of networks of chemically exfoliated $MoS_2$ and $WS_2$. They found that the nanosheet length dependent conductivity of their networks is also described by Eqn. 6.7.[311]

In conclusion, we have derived an equation that describes the effect of nanosheet dimensions, network morphology, and junction resistance on the conductivity of nanosheet networks. The equation can be rewritten for nanosheets with a constant aspect ratio, as is the case for LPE nanosheets, to relate network conductivity to nanosheet length. The equation describes the nanosheet length dependent conductivity of spray-coated graphene networks, where the network conductivity increases with decreasing nanosheet length. Using the derived equation, we calculate that the resistance of the junctions between nanosheets is 1.4 ± 0.1 kΩ and the conductivity of the graphene nanosheets is 32 ± 2 kS.m$^{-1}$, suggesting that the resistance of both the nanosheets and the junctions affect the network's electrical properties. The derived equation also predicts the nanosheet length dependent electrical properties of spray-coated $WS_2$ networks, where the network conductivity shows a peak at large nanosheet lengths and decreases rapidly for smaller nanosheets. We calculate that the conductivity of the $WS_2$ nanosheets as 0.6 ± 0.1 S.m$^{-1}$ while the junction resistance is 17 ± 3 GΩ, suggesting that the electrical properties of these networks is completely dominated by the junctions between the nanosheets, which severely reduces the mobility of these networks. The applicability of the derived equation to describe the conductivity

of networks of graphene, a semi-metal, and $WS_2$, a semiconductor, demonstrates its explanatory power. Furthermore, the conduction model can be used to determine the ideal nanosheet dimensions to optimise the electrical performance of nanosheet networks and improve their device performance.

*"The first of Ohrmazd's creatures of the world was the sky, and his good thought, by good procedure, produced the light of the world, along with which was the good religion of the Mazdayasnians; this was because the renovation which happens to the creatures was known to him! ... Of Ohrmazd's creatures of the world, the first was the sky; the second, water; the third, earth; the fourth, plants; the fifth, animals; the sixth, mankind."*

Joseph H Peterson

# 7

# The morphological & electrical properties of mechanically exfoliated nanosheet networks

There has been an explosion of interest in the solution-processing of nanosheets since it was discovered that graphene could be dispersed in a liquid in 2008.[81] Solution-processed nanosheets can be printed into networks to form functional electrical devices.[57] While solution processing has numerous advantages for the mass production of nanosheets, it also has limitations. Nanosheets produced by solution-processing often show defects introduced by the exfoliation procedure.[104] Furthermore, solution processing consumes large amounts of time and energy, requiring the exfoliation of material, size-selecting it and then often re-dispersing it in a new solvent, before the material can be deposited to form a device.[57,134] Recently, a method of mass-producing mechanically exfoliated nanosheets, dubbed massive parallel mechanical exfoliation (MPME), has been proposed. This method allows the production of networks of mechanically exfoliated nanosheets in a low cost, simple and scalable process. It can be applied to conducting, semiconducting and insulating nanosheets allowing for the formation of a range of devices.[5]

However, the electrical properties of MPME nanosheet networks are currently inferior to solution-processed networks, with a literature report for thin MPME $MoS_2$ networks showing mobilities of 0.03-1.36 $cm^2.V^{-1}.s^{-1}$, well below the state of the art for solution-processed $MoS_2$ networks.[5,108] The reason for the inferior electrical properties is not clear. In this chapter, the morphological and electrical properties of thick MPME networks of $MoS_2$ nanosheets are investigated. The morphology is investigated by FIB-SEM nt, finding the networks show low porosity, high nanosheet alignment and a low surface roughness. These excellent morphological properties do not confer excellent electrical properties however,

with the networks showing a mobility above the literature for MPME $MoS_2$ networks, but below values regularly achieved for solution-processed $MoS_2$.[5,101,105,108] The poor electrical properties of these networks are investigated using EIS, which can be used to calculate the nanosheet and junction resistance in the network.[295] Finally EIS is used to understand the temperature dependent conduction mechanism in these networks, allowing for interrogation of the dependence of the nanosheet conductivity and junction resistance on temperature. The results suggest that the low mobility of the networks can be attributed to the low mobility of the $MoS_2$ nanosheets,

## 7.1 Experimental procedure

The nanosheet films of $MoS_2$ were produced by MPME, which is an automated exfoliation method based on in-contact rolling of the two parallel cylinders. First, Nitto SPV 224 tapes were placed onto cylinders via previously attached double-sided tapes, with their adhesive side facing outwards. Next, the bulk crystal, obtained from Prof. Zdeněk Sofer, or powder of $MoS_2$ (10–20 $\mu$m, 99.8% metals basis, Alfa Aesar), were uniformly transferred onto one of the Nitto tapes, over an area of 3 $cm^2$. For the exfoliation of powder material, we formed a fringe on one of the cylinders by sprinkling them onto the cylinder. The cylinders were then rolled in contact for 20 s using a drill motor to obtain a large area nanosheet film (~13 $cm^2$) on the acceptor nitto tape. To transfer the films, the Nitto tape was adhered onto a glass substrate and annealed at 110°C for 5 min. Several transfers can be performed to increase the film thickness. Interdigitated electrodes (5 nm/95 nm Ti/Au) were deposited, through a custom shadow mask, on the top of the networks using a Temescal FC2000 metal evaporation system.

Raman spectroscopy was carried out using a Renishaw Raman spectrometer, utilising a 532 nm laser and equipped with a 100× objective. To minimise potential thermal damage, the incident laser power was kept at approximately 1 mW. AFM (Bruker Multimode 8, ScanAsyst mode, non-contact) was used to measure the thickness and lateral dimensions of the nanosheets produced. Measurements were performed in air, under ambient conditions, using aluminium coated silicon cantilevers (OLTESPA-R3) on a sparse film deposited using a single transfer step. Previously published length corrections were used to correct lateral dimensions from cantilever broadening.[86,207]

Film thickness and surface roughness measurements were conducted using the Filmetrics Profilm 3D Optical Profiler. Nanosheet networks deposited on glass slides, were scratched using a tweezers, to have regions of the top surface and the underlying substrate visible in the field of view of the 50x objective lens. The height at each pixel was stitched into a 3D reconstruction of the surface, which was levelled using the ProfilmOnline software. Step heights were determined using the histogram function, which plots each pixel height value, giving a bimodal distribution, with the difference between the peaks in the distribution

giving the thickness of the network. Surface roughness calculations were also computed using the surface roughness function.

Surface SEM and FIB-SEM nt was carried out using a Zeiss Aruiga dual beam Ga FIB-SEM at an accelerating voltage of 2 kV with an aperture of 30 $\mu$m. FIB-SEM nt was carried out using Zeiss' Atlas 5 software (Version 5.3.3.31). It was carried out by depositing a 20 x 15 $\mu$m metal pad into which lines were etched in a specific geometry, the lines were then filled with a second metal and then more of the first metal was deposited on top. For the network composed of powder $MoS_2$ nanosheets, platinum was used as the first metal and tungsten as the second while for the network composed of crystal $MoS_2$ nanosheets, tungsten was used as the first metal and platinum as the second. Slicing was done using a 600 pA beam. The distance between the slices was set as 15 nm. Brightness and contrast of the images was altered in Fiji,[269] and the images were then segmented into substrate, nanosheets, pores and surface using the TWS plugin in Fiji.[259,269] Porosity and surface roughness was measured in Fiji, nanosheet alignment was measured using the orientationJ plugin in FIJI,[269,312] tortuosity factors were measured using Taufactor.[270]

Electrical measurements were carried out using interdigitated electrodes (5 nm/95 nm Ti/Au) deposited on top of the networks using a gold evaporator (FC-2000 Temescal Evaporator). The electrode geometry was defined by a 50 $\mu$m thick stainless-steel mask. IV curves were measured using a Keithly 2612A source-meter. Transistor measurements were carried out by drop-casting the ionic liquid (IL) 1-ethyl-3-methylimidazolium bis(trifluoromethylsulfonyl)imide (EMIM-TFSI, Sigma-Aldrich) onto the network, the IL was then dried by leaving for 12 hours under vacuum at a temperature of 70°C. The sample was returned to room temperature and pressure, and 3 probe measurements were carried out using a Keithley 2612A source-meter, connected to a Janis probe station. Measurements were carried out by sweeping the gate voltage from -3 V to 3 V, with a source drain voltage of 1 V, at a scan rate of 50 mV/s. Room temperature EIS spectra were measured using a Keysight E4990E, with a test fixture (16047E) and spring-loaded gold probes to contact the sample. Measurements were carried out in potentiostatic mode at a voltage of 50 mV between 20 Hz and 30 MHz at a precision speed of 3. Temperature dependent impedance was carried out using a broadband Alpha High-Resolution impedance Analyzer (Novocontrol GmbH, Germany) in potentiostatic mode with a voltage of 100 mV, a frequency range of 100 Hz to 10 MHz and a temperature range of 20°C to -120°C. Sample temperature was measured using a sample holder containing a 100 Ω Pt resistor, the sample was measured in a double wall cryostat. Temperature was controlled using a flow of $N_2$ produced by evaporating liquid nitrogen from a dewar (Apollo 50 by Messer Griesheim GmbH).

## 7.2 Results & discussion

### 7.2.1 Material characterisation

$MoS_2$ nanosheets were exfoliated by MPME, this technique is outlined in Fig. 7.1A. The layered material to be exfoliated is attached to tape on a roller. The roller is then rotated in contact with another roller, with tape attached to it. The rollers are rotated for 20 s using a drill. This process leads to the transfer of nanosheets from one roller to the other. The ratio of the radii of the rollers is important to preventing the same point on the rollers repeatedly coming in contact, in this work a ratio of 53:23 was used. The material is exfoliated using "Nitto" tape, this tape is commonly used in the exfoliation of layered materials as it is leaves minimal residue on the nanosheets. It is a thermal release tape, so the material can be transferred to a substrate by heating the substrate to 110°C and leaving the tape attached for 5 minutes. The MPME networks presented in this work were produced by Yigit Sozen, in Prof. Andres Castellanos-Gomez group, in the Instituto de Ciencia de Materiales de Madrid.

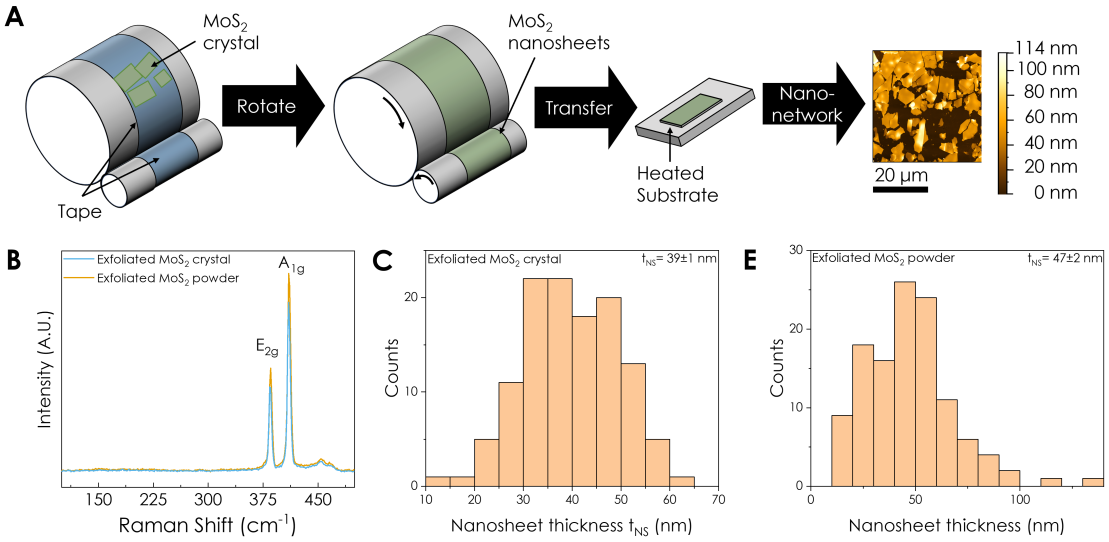



Figure 7.1: **Mechanical exfoliation of $MoS_2$ nanosheets: A)** Schematic explaining the process of MPME. The material to be exfoliated is attached to tape on a roller. The roller is then rotated in contact with another roller, with tape attached, leading to the transfer of nanosheets. The exfoliation material can then be transferred to a substrate. The final image shows an AFM image of the exfoliated nanosheets. **B)** Raman spectra obtained from $MoS_2$ crystal (c) and powder (p) exfoliated by MPME. The $A_{1g}$ and $E_{2g}$ peaks are labelled. **C-D)** Nanosheet thickness distributions, calculated by AFM, for the c- and p-$MoS_2$ nanosheets, exfoliated by MPME, respectively.

$MoS_2$ nanosheets were exfoliated from natural $MoS_2$ crystal, provided by Prof. Zdeněk Sofer. These crystals are used for EE exfoliation of $MoS_2$ by a number of groups and the nanosheets produced from them show high carrier densities.[101,105,106,108,313] For comparison $MoS_2$ nanosheets were also exfoliated from commercially sourced $MoS_2$ powder (Alfa Aesar). Hereafter, networks composed of nanosheets exfoliated by MPME from $MoS_2$ powder will

be referred to as MPME p-$MoS_2$ networks, and networks composed of nanosheets exfoliated from the $MoS_2$ crystals will be referred to as MPME c-$MoS_2$ networks. Raman spectra of the $MoS_2$ nanosheets exfoliated from both the crystal and the powder are shown in Fig. 7B, the Raman spectroscopy was carried out by Dr. Tian Carey. Nanosheets exfoliated from both starting materials show the characteristic $A_{1g}$ and $E_{2g}$ vibrational modes of 2H $MoS_2$, with the position of the peaks suggesting that the nanosheets show bulk thickness.[314] There is no evidence for the presence of the $J_2$ or $J_3$ mode associated with the 1T phase, which appear between 200 and 350 $cm^{-1}$.[315] The higher intensity of the p-$MoS_2$ signal can be attributed to the thicker film used in this case.[316] The spectra are otherwise identical, showing the same peak position and FWHM, suggesting that the nanosheets are of similar quality.[317]

To better understand the length and thickness of the nanosheets produced, AFM was carried out. Nanosheet thickness distributions for the c- and p-$MoS_2$ nanosheets are shown in Fig. 7.1C,D. The AFM was carried out by Anthony Dawson. The thickness of the nanosheets exfoliated from the $MoS_2$ crystal are normally distributed and show an average thickness of 39 $\pm$ 1 nm, while the nanosheets exfoliated from the powder appear to be log-normally distributed with a mean thickness of 47 $\pm$ 2 nm. The nanosheet length distributions are shown in appendix A.4.1, both appear to be log-normally distributed and show an average length of 3.6 $\pm$ 0.1 $\mu$m and 2.9 $\pm$ 0.2 $\mu$m for the c- and p-$MoS_2$ nanosheets, respectively. These length and thickness values lead to nanosheet aspect ratios of 97 $\pm$ 4 and 70 $\pm$ 4, for the c- and p-$MoS_2$ nanosheets, respectively. These aspect ratios are higher than the value that can be obtained by LPE of $MoS_2$ (~50),[86] but is below the aspect ratios typically obtained by EE which range between 100-500.[100,105–107,318] The aspect ratio of the nanosheets is lower than EE due to their high thickness, with the nanosheets lengths being considerably larger than the values generally obtained from EE. It is unclear what drives the difference in length and thickness of the nanosheets obtained from the different starting materials. The difference in length may be driven by differences in the crystal grain size of the starting material but this cannot explain the difference in thickness of the nanosheets. Further research into what affects the size and thickness of the nanosheets is required as both nanosheet length and thickness affect network properties, as discussed in Chapter 5 and 6.

### 7.2.2 The morphology of mechanically exfoliated networks

To produce functional devices from MPME networks repeat depositions are required to increase the film thickness. The mobility of a single deposit of MPME $MoS_2$ varies between 0.03-1.36 $cm^2.V^{-1}.s^{-1}$,[5] to produce electronic devices from a technique consistent device performance is required. The thickness of the devices produced by this technique can be increased by repeatedly depositing material in the same area. In this work, networks produced by 5 and 6 depositions of MPME c-$MoS_2$ nanosheets will be discussed and compared

to a 10 depositions MPME p-$MoS_2$ network. The thickness of the networks was measured by optical profilometry in the same manner as described in Chapter 6. Optical profilometry was carried out by Eoin Caffrey.

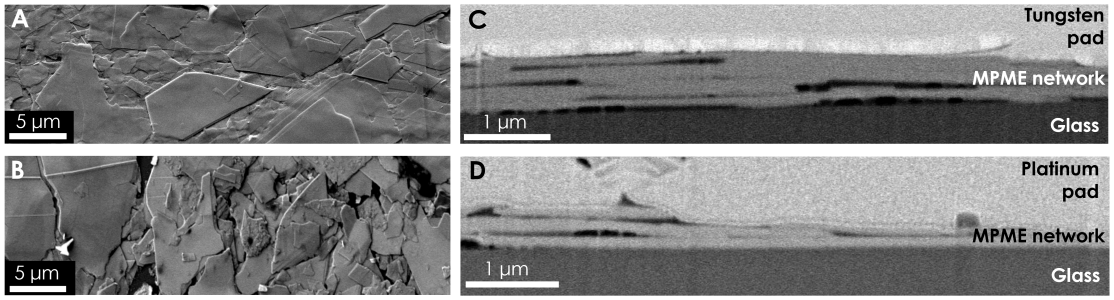



Figure 7.2: **Networks of mechanical exfoliated $MoS_2$: A-B)** SEM of the surface of a MPME c- and p-$MoS_2$ networks, respectively. **C-D)** Cross-sectional SEM images showing the internal structure of a MPME c- and p-$MoS_2$ network, respectively.

SEM images of the surface of a MPME c- and p-$MoS_2$ network are shown in Fig. 7.2A,B. These images show that the networks are composed of well-aligned nanosheets with a broad range of nanosheet lengths, which form a basal plane aligned network. It appears that the c-$MoS_2$ nanosheets are more well-aligned than the p-$MoS_2$ nanosheets, which may be due to the superior aspect ratio of these nanosheets.[82] As discussed in Chapter 5, a limited amount of information can be obtained from surface images, so FIB-SEM nt was carried out on a MPME c- and p-$MoS_2$ network. Representative cross-sections of both networks are shown in Fig. 7.2C,D. Both networks show similar morphologies with low porosities, small slit like pores and large overlap area between adjacent nanosheets. The images of the MPME p-$MoS_2$ network were obtained with a platinum top pad, which shows limited contrast with the $MoS_2$, for this reason it was not used for further analysis.

The FIB-SEM nt images of the MPME c-$MoS_2$ network were aligned using Dragonfly and segmented using TWS, as discussed in Chapter 4.2.4. A four way segmentation was carried out, separating the nanosheets, pores, substrate, and tungsten pad. Sections of the 3D volumes of the nanosheets and pores are shown in Fig. 7.3. From the nanosheet volume it is clear that the MPME networks are composed of well-aligned nanosheets, with a low surface roughness. The nanosheets show a low in-plane tortuosity factor of $1.10 \pm 0.05$, suggesting that there is minimal convolution of the conduction path through the network. The pore volume shows that while pores exist throughout the network, they are not evenly distributed, instead there are regions with very low porosity and regions with a high degree of porosity. This effect can further be seen in the data presented in Fig. 7.3C, which shows the porosity as a function of slice number in the slicing direction. This data shows a wide distribution of porosity with slice number varying from a maximum of 15% to a minimum of 8%, with an average value of $11 \pm 2\%$, the slice porosity distribution is shown as an inset. This large variation in porosity between slices suggests that the network is not homogeneous over the length scale considered and instead show large local morphological variations. While this increases the error in the calculated morphological parameters, the FIB-SEM nt data

can still be used to gain an understanding of the network's morphology.

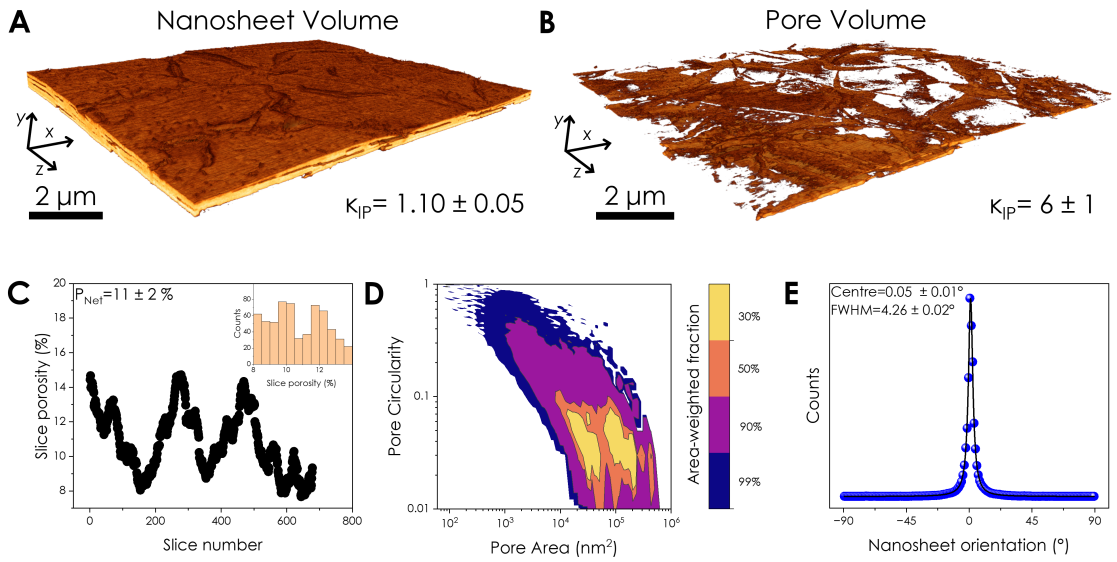



Figure 7.3: **Tomography of a mechanical exfoliated $MoS_2$ network: A-B)** 3D image of the nanosheet and pore volume of a MPME c-$MoS_2$ network. **C)** Porosity as a function of slice number in the slicing direction for the MPME c-$MoS_2$ network. The inset shows the distribution of slice porosity. **D)** Pore area-weighted heat map showing pore circularity as a function of pore area. **E)** Nanosheet orientation calculated from cross-sectional images. The fit to a Cauchy-Lorentz function is shown, wit the calculated centra and FWWHM of the distribution given.

Despite the local variations in morphology the pore volume shows a high degree of connectivity with 90% of the porosity contained in a single connected pore volume. The pore volume shows an in-plane tortuosity factor of 6 ± 1, considerably higher than was measured for the networks presented in Chapter 5. This large value suggests that the diffusivity of species through the pore network will be severely reduced by convolution of the diffusion path. Here, due to the low thickness of the network (~230 nm), there was an insufficient volume to accurately calculate the out-of-plane tortuosity factors. Due to the pore connectivity the pore size and shape was analysed in the same manner as in Chapter 5, the pore area and circularity are shown as area-weighted pore fraction heat map in Fig. 7.3D. This distribution shows both similarities and differences from the distributions for LPE graphene, $WS_2$ and the AgNSs presented in Chapter 5 and appendix A.2.3. As with the other heat maps presented in this work the porosity is contained predominantly in large area, low circularity pores. However, unlike the materials presented in Chapter 5, the 50% band is not approximately linear but instead shows a broad distribution of at large area low circularity pores. From this heat map the average pore area was calculated as 40,000 ± 1000 $nm^2$, corresponding to a characteristic pore length of 200 ± 30 nm. This value is smaller than the average pore size for all but the networks composed of the smallest nanosheets of each material presented in Chapter 5. This demonstrates the very small area of the pores in these networks. The pores show an average pore circularity of 0.19 ± 0.01, which is similar to the values to the pore circularity obtained for the largest nanosheets of the materials investigated in Chapter 5. This demonstrates that the MPME network is composed of

small, slit-like pores.

Due to the difficultly in identifying individual nanosheets, the nanosheet alignment could not be calculated in 3D and thus the Hermans orientation factor could not be calculated. Instead the nanosheet alignment was calculated for the nanosheets from the individual, cross-sections using the OrientationJ plugin in FIJI.[269,312] This algorithm finds the direction that maximises the derivative of the image in a local area. This algorithm yields similar results to the 3D distance transform watershed used in Chapter 5 and a comparison between the two methods for size-selected graphene networks can be found in appendix A.2.2. The distribution of nanosheet angle is shown in Fig. 7.3E. The distribution is centred around 0° showing that the nanosheets are primarily aligned with the substrate, it shows a FWHM of 4.26 $\pm$ 0.02°, well below the values calculated for the LPE graphene networks, which varied between 23-39°, this value is also below the values calculated for IJP MXene and EE $MoS_2$ networks of 5° and 9°.[192] This demonstrates the excellent nanosheet alignment which is obtained by this technique, this alignment is likely achieved as each layer of nanosheets is pressed into the layer before.

The surface roughness of the network was also calculated from the 3D image, using the method described in Chapter 5. Calculating the roughness from line scans yields an average root mean square roughness of 74 $\pm$ 8 nm. As a comparison optical profilometry was also carried out, giving a surface roughness of 70 nm, showing excellent agreement. The calculated surface roughness is below the value calculated for LPE graphene (105 nm and 158 nm) and $WS_2$ (114 nm) networks presented in Chapter 5 and the value for an EE graphene network (122 nm), measured by the same method.[296] The value is above the value calculated for transfer (9 nm) and screen printed (32 nm) LPE graphene networks.[319,320] The low surface roughness of these networks makes them an ideal candidate for the formation of printed heterostacks, as different material can be stacked on top of each other, with minimal interfacial roughness.

### 7.2.3 Network electrical properties

The low porosity, high degree of nanosheet alignment, and large overlap area between adjacent nanosheets suggest that the MPME networks should show excellent electrical properties.[82] To investigate this interdigitated electrodes (IDEs) (5 nm/95 nm Ti/Au) were deposited on the top of the network by gold evaporation, channel length dependent IDEs were deposited on the MPME c-$MoS_2$ networks, while on the MPME p-$MoS_2$ network 5 IDEs with a fixed channel length of 50 $\mu$m were deposited. IV curves for the MPME c-$MoS_2$ network composed of 5 depositions are shown in Fig. 7.4A. While the IV curves are non-linear at high voltages they are linear between -0.25 and 0.25 V and a linear fit to the data in this range was used to calculate the device resistance. The resistance of the MPME c-$MoS_2$ networks, as a function of channel length is shown in Fig. 7.4B. There is a clear difference in the channel length dependent scaling between the 5 and 6 deposition

samples. The sample composed of 6 depositions shows an approximately linear relationship between channel length and resistance, with a power law fit to the resistance vs channel length data yielding a slope of 0.9 $\pm$ 0.1. This is the behaviour that would be expected for a sample above the bulk conductivity thickness. The 5 depositions sample, however, shows a non-linear scaling of resistance with channel length, with a power law fit giving a slope of 3.0 $\pm$ 0.2, which may be due to it not being at the bulk conductivity thickness. Samples below the bulk conductivity thickness can show power-law relationships between conductivity ($\sigma$) and channel length ($L$), given by

$$\sigma \propto L^{-\gamma} \tag{7.1}$$

where $\gamma$ is the channel length percolation exponent (CLPE) as discussed in Chapter 3.3.1.[180] A fit to the conductivity vs channel length data is shown in appendix A.4.2. The fit yields $\gamma$=2.0 $\pm$ 0.2, which is below the theoretical value for a 3D system of $\gamma$=2.3, at the percolation threshold.[180] The sample is likely to be close to bulk conductivity thickness, as it shows a higher conductivity at the smallest channel length than the 6 depositions sample (0.80 $\pm$ 0.05 S.m$^{-1}$ vs 1.0 $\pm$ 0.1 S.m$^{-1}$). Therefore, $\gamma$ should be considerably lower than the theoretical value at the percolation threshold. The MPME p-$MoS_2$ sample is thicker than the 5 and 6 deposition sample and so should be above the bulk conductivity thickness. Its conductivity, (5.2 $\pm$ 0.3) $\times 10^{-4}$ S.m$^{-1}$, is considerably lower than the MPME c-$MoS_2$ networks, however, the value is above the value obtained for LPE $MoS_2$ (~$1\times10^{-6}$ S.m$^{-1}$).[170,321–324]

The mobility of MPME $MoS_2$ networks has been shown to increase after annealing.[5] To investigate this effect the samples were annealed under vacuum at increasing temperatures. The conductivity of the networks as a function of annealing temperature is shown in Fig. 7.4C, as the conductivity of the 5 deposition sample decreases with channel length its conductivity was calculated just considering the smallest channel length. A trend of increasing conductivity as annealing temperature is increased can be seen, with the conductivity increasing by approximately an order magnitude for each of the samples, reaching a maximum at 300°C, with a slight decrease afterwards. A similar effect with annealing has been found for EE $MoS_2$ networks, which have been found to show a maximum mobility after annealing at 200°C and a decrease thereafter.[100] The maximum conductivities of the MPME c-$MoS_2$ networks is considerably higher than has been achieved for LPE $MoS_2$ networks (~$1\times10^{-6}$ S.m$^{-1}$) and is similar to values reported for EE $MoS_2$ networks, which have reached values as high as 40 S.m$^{-1}$.[170,192,295] The maximum value for the MPME p-$MoS_2$ network, however, is considerably lower than the c-$MoS_2$ networks, reaching a maximum of (1.0 $\pm$ 0.1) $\times 10^{-2}$ S.m$^{-1}$, while this value is superior to LPE $MoS_2$ networks,[170,321–324] it falls considerably below the values for EE $MoS_2$ networks.[170,192,295]

The CLPE of the 5 deposition MPME c-$MoS_2$ network also changes as the annealing temperature increases, with the value of $\gamma$ decreasing from 2.0 $\pm$ 0.2 for the as-deposited

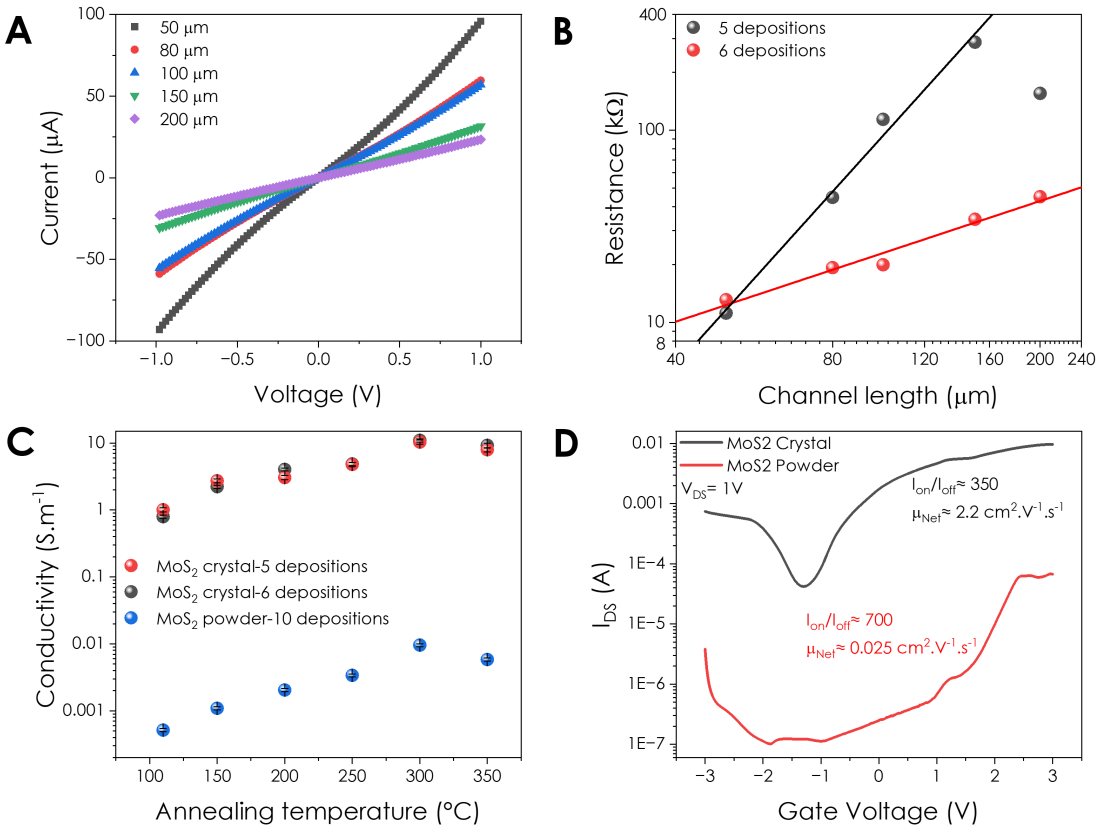



Figure 7.4: **D.C. characterisation of mechanical exfoliated $MoS_2$ networks: A)** IV curves as a function of channel length for the MPME c-$MoS_2$ network with 5 depositions. **B)** Resistance as a function of channel length for a 5 and 6 deposition MPME c-$MoS_2$ network. A fit to a power law is shown for both samples. **C)** Conductivity as a function of annealing temperature for the MPME $MoS_2$ networks. The conductivity of the 5 deposition sample was calculated for the shortest channel length **D)** Transfer curves for a MPME c- and p-$MoS_2$ network. The networks were gated using an IL.

film to $1.3 \pm 0.2$ after the network was annealed at 300°C. This decrease may be related to a reduction in the ratio of the nanosheet to junction resistance ($R_J/R_{NS}$), computational studies suggest that the channel width percolation exponent of CNT networks decreases as $R_J/R_{NS}$ decreases.[325] The dependence of the CLPE on the annealing temperature can be found in appendix A.4.2.

To investigate the difference between the MPME c- and p-$MoS_2$ networks, IL gated transistor measurements were carried out. The IL EMIM-TFSI was drop cast onto the network, the network was then annealed at 70°C under vacuum for 12 hours to remove water. The IL measurements were carried out on a 5 deposition MPME c-$MoS_2$ network and a 10 deposition MPME p-$MoS_2$ network, both with 50 $\mu$m channel IDEs. A representative transfer curve for both samples is shown in Fig. 7.4D, the measurements were carried out with a sweep rate of 50 mV/s, with a source-drain voltage of 1 V. Both transistors show n-type switching behaviour, with the crystal sample showing an on/off ratio of 350 while the powder sample is double that at 700.

To calculate the mobility of the networks, the capacitance of the device must be calculated.

It has been shown that the volumetric capacitance ($C_v$) of a network depends on the thickness of the nanosheets in the network as

$$C_v = \frac{2\epsilon_r\epsilon_0(1-P))}{\lambda t_{NS}} \tag{7.2}$$

where $\epsilon_r$ is the relative permittivity for the double layer, $\epsilon_0$ is the permittivity of free space, $P$ is the porosity, $t_{NS}$ is the nanosheet thickness and $\lambda$ is the electrical double layer thickness.[125] This equation can be combined with literature values for the volumetric capacitance of $MoS_2$ with EMIM-TFSI to estimate the volumetric capacitance of these devices.[105,106] This yields a MPME c-$MoS_2$ network mobility of 2.2 $\pm$ 0.3 $cm^2.V^{-1}.s^{-1}$, while for the MPME p-$MoS_2$ network a value of 0.025 $\pm$ 0.002 $cm^2.V^{-1}.s^{-1}$ is obtained. As discussed in Chapter 6, the network mobility value ($\mu_{Net}$) can be combined with the network conductivity ($\sigma_{Net}$) and the porosity to calculate the nanosheet carrier concentration ($n_{NS}$) according to the formula $\sigma_{Net} = \mu_{Net} n_{NS}(1-P)$, yielding $n_{NS}$=(1.4 $\pm$ 0.2)$\times 10^{22}$ $m^{-3}$ for the p-$MoS_2$ and $n_{NS}$=(6 $\pm$ 1)$\times 10^{23}$ $m^{-3}$ for the c-$MoS_2$. Both values are in line with previous reports for mechanically exfoliated $MoS_2$, which range between $10^{22}$-$10^{23}$ $m^{-3}$ depending on the starting material.[326,327] The carrier concentration of the c-$MoS_2$ nanosheets also agrees with literature for the carrier concentration of EE $MoS_2$ nanosheets,[105] suggesting that there is no doping effect from the EE process.

The large difference between the mobility of the MPME p- and c-$MoS_2$ networks is surprising as the morphology of the networks is very similar. The powder nanosheets are smaller than the crystal nanosheets (2.9 $\mu$m vs 3.6 $\mu$m), which could cause a decrease in junction area and therefore, an increase in the junction resistance. An alternative explanation is that the high nanosheet conductivity of the c-$MoS_2$ nanosheets, caused by there higher carrier concentration, leads to a reduction in the junction resistance, as discussed in Chapter 6 there seems to be a relationship between nanosheet conductivity and junction resistance.

While the mobility of the MPME c-$MoS_2$ network is considerably higher than the powder network, it is lower than the majority of reports for EE $MoS_2$ networks which range between 0.7-80 $cm^2.V^{-1}.s^{-1}$.[100,101,105,107,108,295,313,328] To understand this inferior performance to the MPME networks, the nanosheet and junction resistance within the networks needs to be understood. In Chapter 6 a method for calculating the junction resistance by varying nanosheet dimensions was presented, there are 2 limitations to this technique. Firstly, it is very time consuming to produce and deposit size-selected nanosheet network. Secondly, for novel deposition techniques, such as MPME, techniques to control the length and thickness of the exfoliated nanosheets have to be developed before this technique can be used. Therefore, a method to measure the nanosheet and junction resistance within a network would be ideal.

EIS has been used to measure the ratio of nanotube bundle to junction resistance for bundles of CNTs.[174] Here, we will apply this technique to calculate the nanosheet and junction resistance within the MPME c-$MoS_2$ networks. Fig. 7.5A,B shows the real and imaginary

components of the EIS spectra of the 5 deposition MPME c-$MoS_2$ network measured at different channel lengths. To extract information about the networks from these spectra an equivalent circuit model is required. Moore *et al.* have suggested that the impedance of a nanosheet network can be modelled as a Randles circuit which is a resistor in series with a resistor and capacitor in parallel with each other, a circuit diagram of this circuit is shown as an inset in Fig. 7.5C. Here the resistor in series, corresponds to the nanosheets, and the resistor and capacitor in parallel correspond to the resistance and capacitance of the junctions. The values measured by fitting the network EIS spectra are not the nanosheet and junction properties, but are instead network properties, which are created by the current path being averaged over a large number of nanosheets and junctions. In networks there will be a distribution of junction resistances and capacitances, this can be accounted for by changing the capacitor to a constant phase element, the impedance of a constant phase element is given by $Z_{CPE} = (Y_0(i\omega)^n)^{-1}$, where $\omega$ is the frequency of the applied signal, and $Y_0$ is a constant, and $n$ describes the distribution of junction resistances and capacitance, with $n$=1 describing a single value and $n$=0 describing a flat line distribution,[329] a more in-depth discussion can be found in the appendix A.4.4. Replacing a capacitor with a constant phase element is often done in electrochemical impedance spectroscopy.[172] This circuit shows an impedance ($Z$) of

$$Z = R_S + \frac{R_P[1 + (\omega R_P C_P)^n cos\frac{n\pi}{2}]}{1 + 2(\omega R_P C_P)^n cos\frac{n\pi}{2} + (\omega R_P C_P)^{2n}} - i\left(\frac{R_P(\omega R_P C_P)^n sin\frac{n\pi}{2}}{1 + 2(\omega R_P C_P)^n cos\frac{n\pi}{2} + (\omega R_P C_P)^{2n}}\right) \tag{7.3}$$

where $R_S$ and $R_P$ are the resistance of the resistor in series and parallel, respectively, and $C_P$ is capacitance of the capacitor.

EIS cannot be used to investigate the electrical properties of the MPME p-$MoS_2$ network as its resistance is too high. The IDEs used to measure the samples act as capacitor during the impedance measurement and if the samples resistance is too high then the background impedance is lower than the samples at high frequencies, causing it to dominate the measured values. For the IDEs used in this work, the background impedance reaches a minimum value of ~6 kΩ at 30 MHz. This prevents measurement of the MPME p-$MoS_2$ network and measurement of the MPME c-$MoS_2$ networks before annealing. The background spectra of the IDE can be found in appendix A.4.2.

Fitting Eqn. 7.3 to the real and imaginary component of the EIS spectra allows for calculation of $R_S$, $R_P$, $C_P$ and $n$. The calculated values of $R_S$ and $R_P$ for the 5 and 6 deposition MPME c-$MoS_2$ networks are shown in Fig. 7.5C,D. The value of $n$ is discussed below and $C_P$ is shown in appendix A.4.1. Despite the non-linear scaling of the resistance of the 5 depositions sample, $R_S$ varies linearly with channel length. As this value is related to the nanosheet resistance, its y-intercept corresponds to twice the contact resistance, yielding a contact resistivity value of 1.0 ± 0.4 MΩ.$\mu$m, this value is higher than the values reported

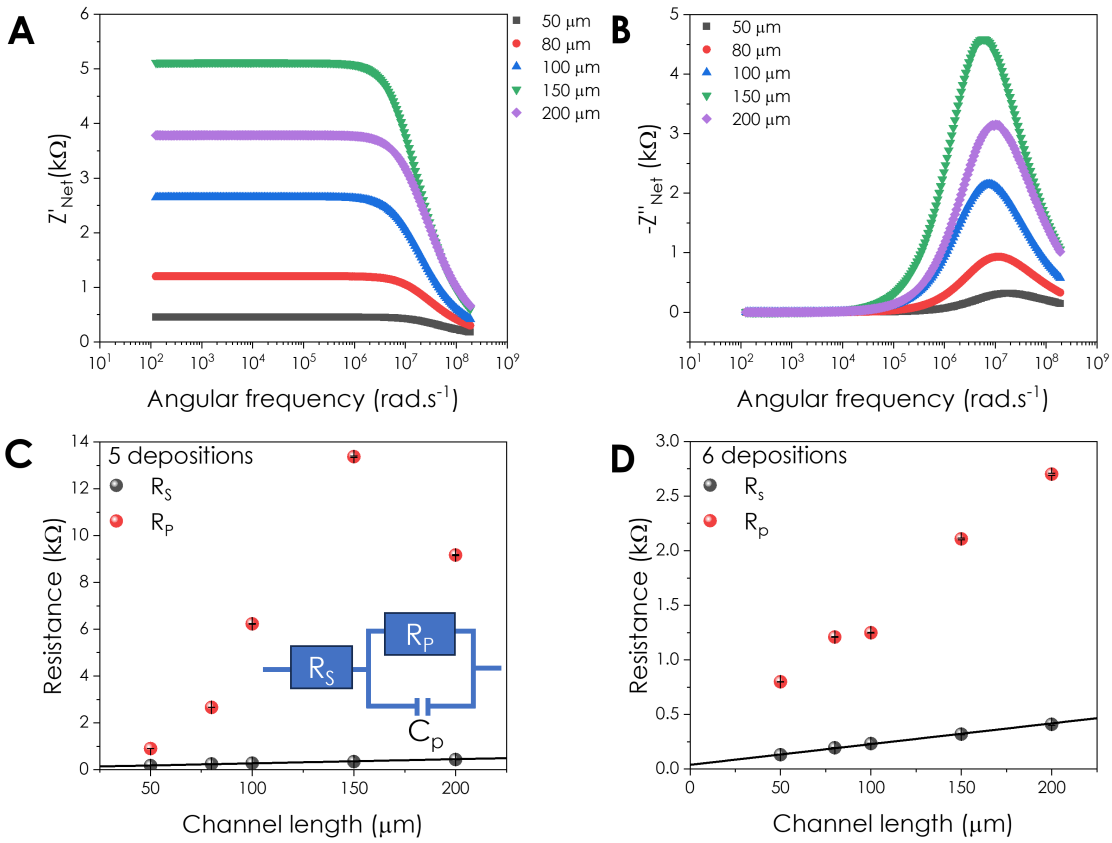



Figure 7.5: **Electrical impedance spectroscopy of mechanical exfoliated $MoS_2$ networks: A-B)** Real and imaginary components of the EIS spectra of the 5 deposition MPME c-$MoS_2$ network. **C-D)** Series and parallel resistance, calculated by fitting the EIS spectra, for 5 and 6 deposition MPME c-$MoS_2$ networks, respectively. A Randles circuit is shown as an inset, the spectra were fit with a Randles circuit with the capacitor replaced with a constant phase element. The line shows a linear fit to the $R_S$ data, the intercept of which is $2R_C$.

for EE $MoS_2$ networks with pure Au contacts (100-400 kΩ.$\mu$m).[295,328] The higher contact resistance here can be explained by the presence of a 5 nm Ti layer between the network and the Au, Ti has been shown to have a higher contact resistance with $MoS_2$ than Au.[330] The 5 nm Ti layer is used to improve the adhesion of the gold to the glass. The use of $R_S$ allows for a more accurate calculation of $R_C$ than can be obtained by plotting resistance vs channel length as it is not affected by local variations in the junction resistance. Unlike $R_S$, $R_P$ does not show a linear scaling with channel length, for the 5 depositions samples, which suggests that the non-linear scaling of resistance with channel length for this sample is driven by an increase in the average junction resistance in the conduction path. For the 6 deposition sample both $R_S$ and $R_P$ scale linearly with channel length.

Fits to network EIS spectra allow for the calculation of $R_S$, $R_P$ $C_P$ and $n$, however, it would be preferable to convert these values to those of the nanosheet-junction pair as this would offer information about the material in the network. In Chapter 6, it was shown that the

network resistivity ($\rho_{Net}$) can be expressed as

$$\rho_{Net} \approx \frac{2t_{NS}\kappa_{NS}}{1-P}[R_{NS}+R_J]\left[1+\frac{2}{n_{NS}t_{NS}l_{NS}}\right] \tag{7.4}$$

where $t_{NS}$ and $l_{NS}$ are the average nanosheet thickness and length, respectively, $\kappa_{NS}$ is the in-plane tortuosity factor, P is the porosity, and $R_{NS}$ and $R_J$ are the nanosheet and junction resistance respectively. If instead of the resistivity of the network, we consider its impedance ($Z_{Net}$), the impedance of the nanosheet-junction pair ($Z_{NS-J}$) can replace the nanosheet and junction resistance, allowing us to state

$$Z_{Net} \approx \frac{L}{wt_{Net}}\frac{2t_{NS}\kappa_{NS}}{1-P}[Z_{NS-J}]\left[1+\frac{2}{n_{NS}t_{NS}l_{NS}^2}\right] \tag{7.5}$$

where $L$ and $w$ are the channel length and width respectively and $t_{Net}$ is the network thickness. This equation can then be rewritten in terms of $Z_{NS-J}$

$$Z_{NS-J} = (Z_{Net}-2R_C)\frac{wt_{net}}{L}\frac{1-P}{2t_{NS}\kappa_{NS}}\left[1+\frac{2}{n_{NS}t_{NS}l_{NS}^2}\right]^{-1} \tag{7.6}$$

where $R_c$ is the contact resistance. This equation allows for the conversion of network impedance to nanosheet-junction impedance. The contact resistance has to be subtracted from the impedance values before the conversion to remove its effect on the value of $R_{NS}$. The conversion of network to nanosheet-junction impedance is outlined in Fig. 7.6. This conversion allows for the calculation of $R_{NS}$, $R_J$, and $C_J$, where $C_J$ is the junction capacitance, which can be related to the junction area. This conversion has been shown to be effective for EE $MoS_2$ networks, with the calculated values agreeing with vales calculated from kelvin probe force microscopy and terahertz spectroscopy.[295]

The calculated nanosheet and junction resistance as a function of channel length for the 5 and 6 deposition sample are shown in Fig. 7.7A,B. In both cases the nanosheet resistance is approximately constant with channel length with average values of $R_{NS}$= 87 $\pm$ 12 k$\Omega$ and $R_{NS}$= 120 $\pm$ 20 k$\Omega$ for the 5 and 6 deposition sample, respectively. The discrepancy in the calculated values may partially be explained by the fact that the 5 deposition sample is not at bulk conductivity, while the derivation of Eqn. 7.6 assumes the network is above bulk conductivity thickness. For this reason we will consider $R_{NS}$ values calculated for the 6 deposition sample. The $R_{NS}$ values corresponds to a nanosheet conductivity 110 $\pm$ 20 S.m$^{-1}$, considerably higher than the value calculated for LPE $WS_2$ nanosheets (0.6 $\pm$ 0.1 S.m$^{-1}$) in Chapter 6. This value is below the value of 230 S.m$^{-1}$ calculated by the same method for EE nanosheets, however, it is in agreement with values reported for thick mechanically exfoliated $MoS_2$ nanosheets (5-300 S.m$^{-1}$).[326] Combining this value with the calculated nanosheet concentration gives a nanosheet mobility of 11 $\pm$ 3 cm$^2$.V$^{-1}$.s$^{-1}$, this value is below the values generally reported for $MoS_2$ nanosheets. However, the mobility of $MoS_2$ nanosheets has been found to be thickness dependent, with bulk mechanically exfoliated

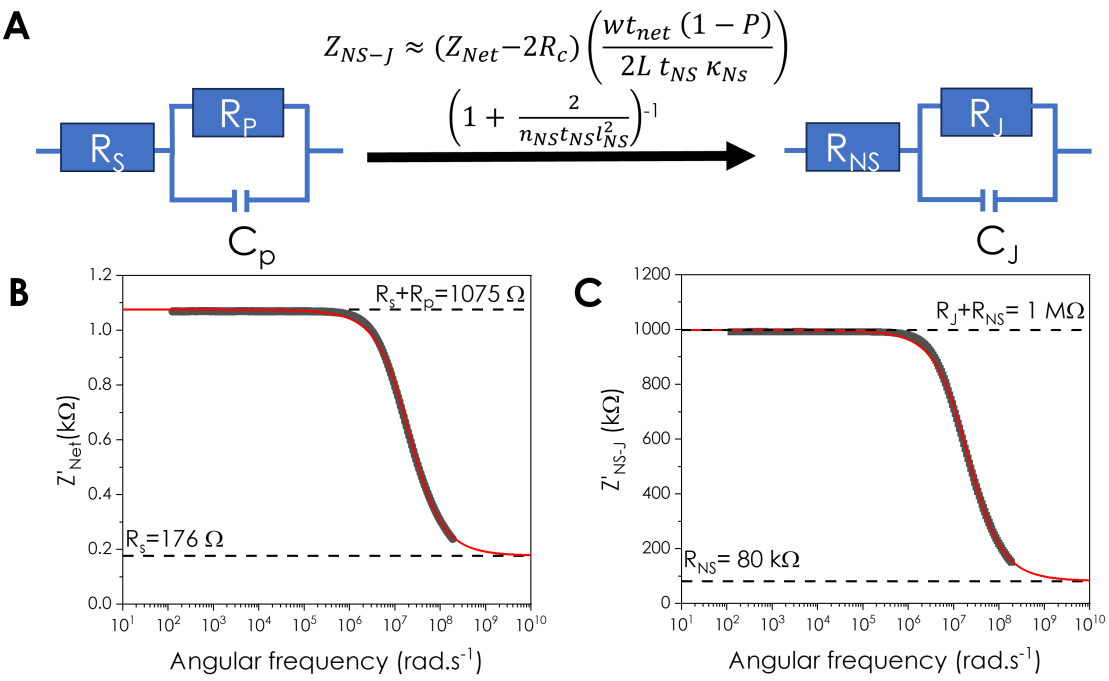



Figure 7.6: **Converting from network to nanosheet-junction impedance: A)** Schematic explaining the method of converting from network to nanosheet-junction impedance. **B)** Real component of network impedance spectra showing the fit of Eqn. 7.3 and the calculated values. **C)** The real impedance spectra, shown in B, converted to nanosheet-junction impedance with the calculated values of $R_J$ and $R_{NS}$ shown.

$MoS_2$ nanosheets showing a mobility of ~20 $cm^2.V^{-1}.s^{-1}$, similar to the value obtained here.[54]

The average $R_J$ for the 6 deposition network is 890 ± 130 kΩ, below the value of EE $MoS_2$ networks (2.9 MΩ) calculated by the same method. This lower junction resistance could be driven by a larger overlap between adjacent nanosheets. The junction capacitance can be used to calculate the junction area, assuming the junctions act as a parallel plate capacitors. The junction capacitance for the 6 deposition sample as a function of channel length is shown in Fig. 7.7, the average value is 35 ± 4 fF. Taking the nanosheet separation as 0.6 nm, the value in $MoS_2$ nanosheets,[100] and assuming the permittivity of the junction is the same as the permittivity of free space, yields a junction area of 2.4 ± 0.3 $\mu m^2$, this is considerably larger than the value of 0.4 $\mu m^2$ calculated for EE $MoS_2$ nanosheets. To consider the relationship between junction resistance and junction area, we can calculate the junction resistance multiplied by the junction area, which gives 2,100 ± 400 kΩ.$\mu m^2$ for the MPME c-$MoS_2$ network in comparison to a value of 1,160 ± 70 kΩ.$\mu m^2$ for the EE $MoS_2$ network. The factor of 2 difference between these values suggests that the junction resistance does not scale inversely with junction area. Junction resistance as a function of junction area is shown in appendix A.4.3. This is further supported by data on the dependence of network conductivity on nanosheet length in IJP rGO networks by He *et al.* This work examines networks of ML rGO nanosheets broken apart using sonic energy, therefore, the variation in conductivity is driven by changes in junction resistance and not by

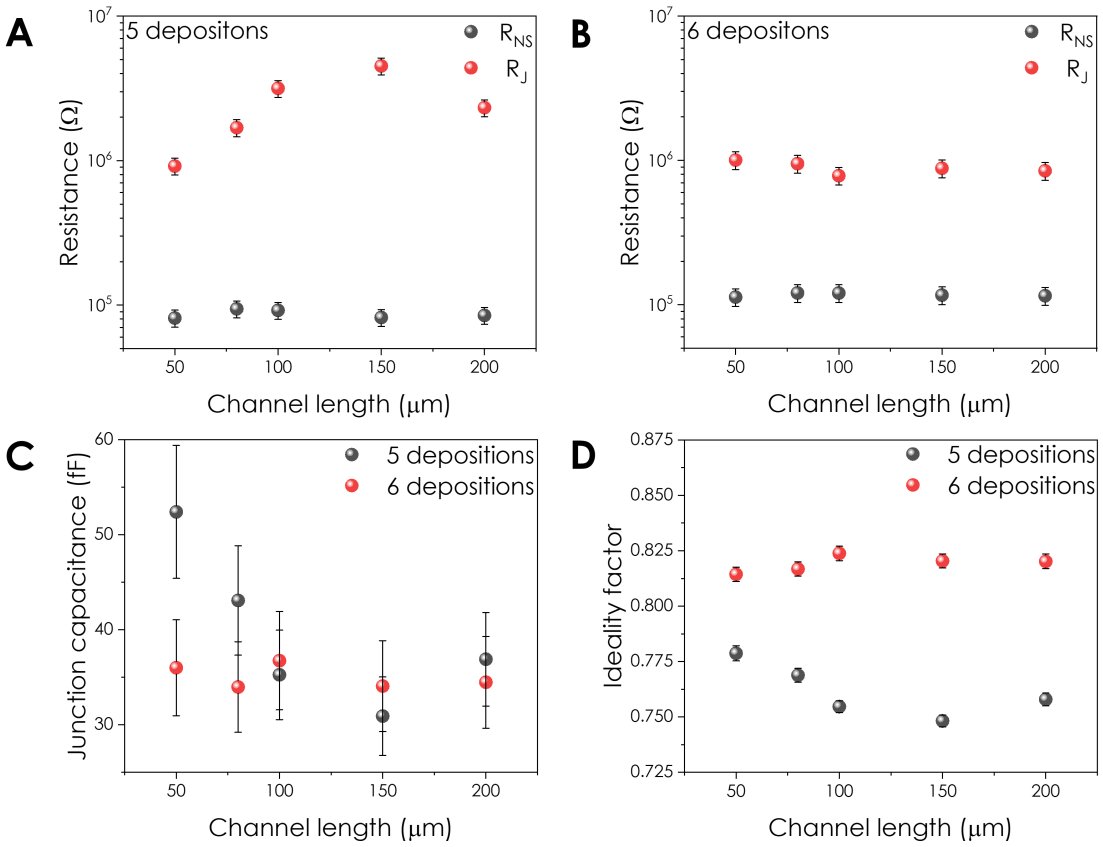



Figure 7.7: **Nanosheet and junction properties: A-B)**Nanosheet and Junction resistance as a function of channel length for sample composed of 5 and 6 deposition, respectively. **C)** Junction capacitance as a function of channel length. **D)** Ideality parameter as a function of channel length.

a change in nanosheet thickness, which drives the variation in conductivity seen in Chapter 6. The data shows network conductivity scaling very weakly with nanosheet length,[305] a fit to data extracted from the paper is shown in appendix A.4.3, finding $\sigma_{Net} \propto l_{NS}^{0.1}$. As junction area is likely to scale with nanosheet length squared, this suggests a weak scaling of junction resistance with junction area in rGO networks.

The calculated values can be used to determine the nanosheet-junction resistance ratio, giving a value of $R_J/R_{NS}$=8 $\pm$ 2, suggesting that the networks are nanosheet- and junction-limited. For these networks, the low nanosheet mobility causes the low network mobility, despite the relatively low value of $R_J$. Therefore, to optimise the mobility of the MPME c-$MoS_2$ networks control over the nanosheet thickness is required. This will yield 2 benefits, firstly, Eqn. 6.11 suggests that for nanosheets with a high carrier concentration the network mobility will increase with decreasing nanosheet thickness. Secondly thinner nanosheets are likely to have a higher mobility and this will increase network mobility.[54]

The final piece of information that can be extracted from fitting the EIS spectra is the ideality factor, n. The ideality factor gives information about the distribution of junction resistances and capacitances,[329] with the ideality parameter of the 6 deposition sample having a value of 0.82 $\pm$ 0.01. This value is below the value of 0.985 calculated for EE

$MoS_2$ networks and suggests that there is a far broader distribution of junction resistances in the channel. The distribution of the junction resistances and capacitances for the range of n values calculated in this chapter can be seen in appendix A.4.4. The decrease in the ideality factor implies that the junctions in the MPME networks are not as homogeneous as LS networks of EE $MoS_2$ nanosheets presented in Gabbett & Kelly *et al*.[295]

While the values calculated for the 5 deposition sample have an increased error due to percolation effects, several interesting trends can still be observed in the data. The calculated junction resistance of the sample shows a strong channel length dependence with a factor of ~5 increase as the channel length increases from 50 to 150 $\mu$m, this increase coincides with a decrease in the junction capacitance and the ideality parameter. The decrease in junction resistance as channel length is increased, shown in Fig. 7.7A, suggests that the non-linear scaling of conductivity with channel length for this sample can be explained by an increase in the number of highly resistive junctions in the charge carriers path as channel length increases. This can most reliably be seen from the ideality factor, shown in Fig. 7.7D, which does not vary with the transformation from network to nanosheet-junction impedance. The ideality parameter decreases as channel length increases, suggesting that there is an increase in the distribution of the junction resistances in the conduction path as the channel length increases. Classical percolation theory assumes that all the resistors have the same resistance, while here, the non-linear scaling is partially, if not completely, caused by an increase in the distribution of the resistances at higher channel lengths. Research considering a distribution of resistances in percolative systems found that increasing the distribution of resistances in the network increases the value of the percolation exponent.[181] The high value for $\gamma$ obtained might, therefore, be explained by the fact that the percolation like behaviour observed in these networks is in part driven by an increase in the distribution of junction resistances with channel length.

The difference in the behaviour of the junction resistance, capacitance and ideality factor with channel length, between 5 and 6 deposition sample, suggests that the 6 deposition sample is sufficiently homogeneous to have a junction resistance distribution that is independent of the channel length, while for the 5 deposition sample there is an increase in the effective junction resistance experienced by a charge carrier as the channel length increases. To fully understand this effect thinner samples are required.

Now that we have an understanding of the junction resistance of the MPME c-$MoS_2$ networks we should once again consider the MPME p-$MoS_2$ networks. If we assume that the mobility of p-$MoS_2$ nanosheets is the same as in the c-$MoS_2$ nanosheets, we can calculate the nanosheet conductivity and then use Eqn. 6.7 to estimate the junction resistance, which yields a value of 1.9 $\pm$ 0.4 S.m$^{-1}$ and 200 $\pm$ 40 M$\Omega$, respectively. Given the similar morphologies of the networks the large difference between the junction resistances suggests that the junction resistance is related to the nanosheet conductivity. Fig. 7.8 shows junction resistance as a function of nanosheet conductivity calculated in this work

and in Gabbett & Kelly *et al.*,[295] showing that increasing nanosheet conductivity leads to a decrease in junction resistance. This data, also shows the improvements that can be obtained by increasing junction overlap area, the junction resistance of the MPME c-$MoS_2$ network is lower than the EE LS $MoS_2$ network and the junction resistance of the MPME p-$MoS_2$ network is lower than the LPE $WSe_2$, despite in both cases the former having a lower nanosheet conductivity. However, it seems that the junction resistance is related to the nanosheet conductivity, although there is insufficient data here to understand the nature of this relationship.

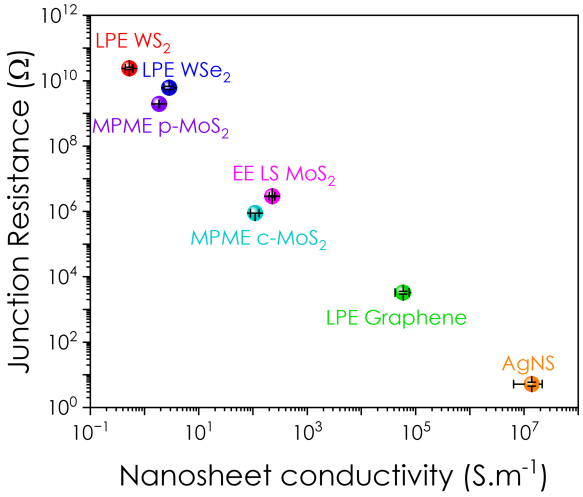



Figure 7.8: **Nanosheet conductivity and junction resistance:** Junction resistance as a function of nanosheet conductivity. The data is calculated by fitting network conductivity vs nanosheet length data for the LPE $WS_2$, LPE $WSe_2$, LPE graphene and AgNS and by EIS for the EE LS $MoS_2$ and MPME c-$MoS_2$ networks. The powder MPME $MoS_2$ sample is estimated assuming the mobility is the same as in the crystal MPME $MoS_2$ nanosheets

### 7.2.4 Temperature dependence of electrical properties

EIS allows for the measurement of the nanosheet and the junction resistance of a network, however, it does not offer an insight into the conduction mechanism. To gain a better understanding of the conduction mechanism in the MPME c-$MoS_2$ networks, temperature dependent EIS measurements were carried out on the 5 deposition sample, on the 50 $\mu$m channel length. The temperature dependent measurements were carried out by Emmet Coleman. It was found that the silver paint (PELCO high performance silver paste (Ted Pella)) that was used for the temperature dependent EIS measurements doped the networks, leading to a factor of 3 increase in the conductivity of the network, the increase was temporary and the networks returned to their original conductivity after approximately a week. This silver paint was used as it shows a lower thermal expansion than the standard silver paint used to contact the electrodes in this work. To investigate the doping caused by this silver paint, channel length dependent EIS measurements were carried out on the sample before the temperature dependent measurements. Fig. 7.9A shows the nanosheet resistance with the standard and the temperature dependent contacts, showing that there

is no measurable change in the nanosheet resistance. However, there is a change in the junction resistance as can be seen in Fig. 7.9B, with a decrease of approximately a factor of 3 for each of the channel lengths, with the temperature dependent contacts. This change in junction resistance is not driven by an increase in junction area as there is no increase in the junction capacitance, as can be seen in Fig. 7.9C. Interestingly, the doping causes an increase in the ideality factor, shown in Fig. 7.9D, suggesting that the distribution of junction resistances and capacitances narrows due to the doping. This is likely driven by a decrease in highly resistive junctions in the conduction path. The difference in the junction resistance and capacitance distributions can be seen in appendix A.4.4. The doping does not lead to a measurable change in the CLPE.

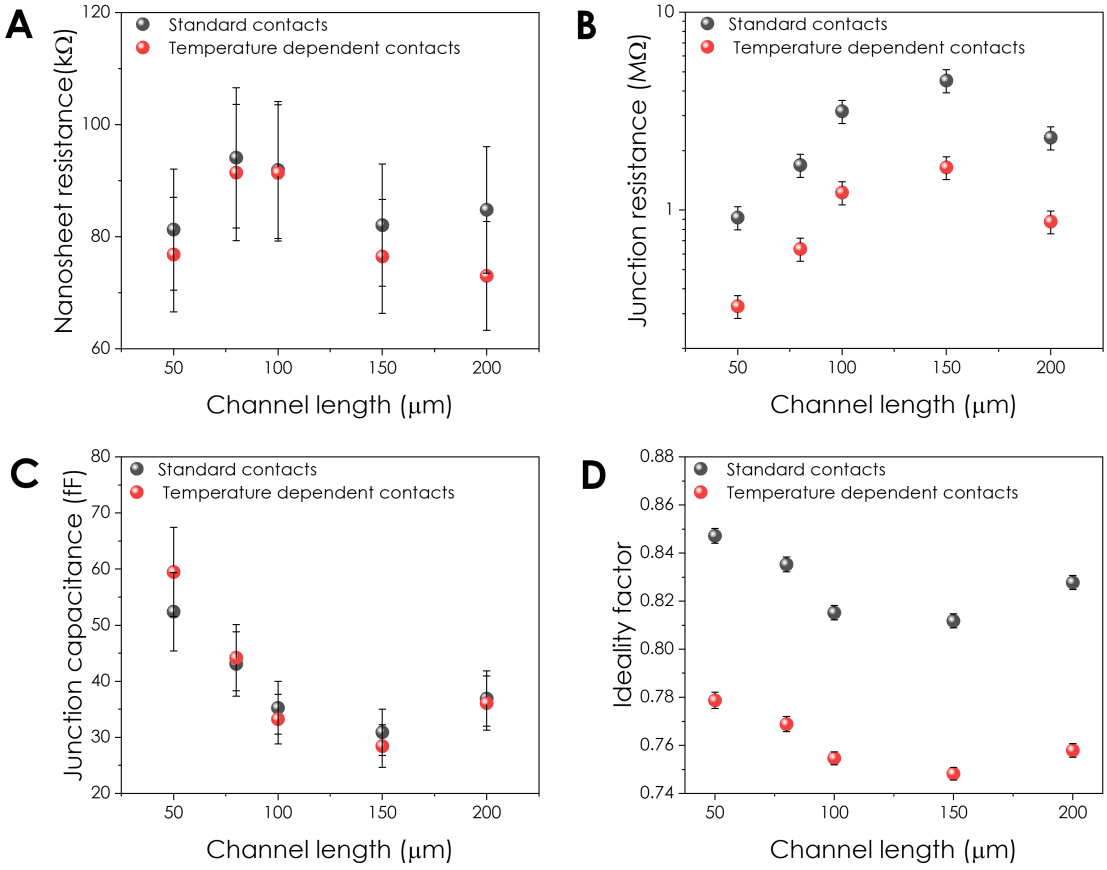



Figure 7.9: **Network doping: A-D)** Nanosheet resistance, junction resistance, junction capacitance and ideality factor, respectively, as a function of channel length, for the samples with standard painted silver contacts and the temperature dependent painted silver contacts.

It is unclear what causes this large decrease in junction resistance. It has recently been found that a variety of solvents can dope $MoS_2$ nanosheets, which may explain the effect observed here,[331] with the increase in nanosheet conductivity being too small to be measured by impedance but leading to a large decrease in the junction resistance. This large decrease in junction resistance would suggest that there has been an improvement in the network mobility, demonstrating the improvements that could be made in these devices if the doping level could be controlled.

Despite this doping effect temperature dependent EIS spectra can still be used to determine

information about the conduction mechanism in the MPME networks. EIS spectra taken at different temperatures are shown in Fig. 7.10A. From the spectra it can be seen that there is an increase in network resistance as the temperature decreases. Network resistance can be calculated by averaging the low frequency plateau, allowing for the calculation of network conductivity as a function of temperature. Conductivity as a function of temperature is shown Fig. 7.10B, showing that network conductivity decreases as the temperature decreases, as is generally found for nanosheet networks.[101,170,184,192,193,295] As discussed in Chapter 3.3.2 the conduction mechanism in nanosheet networks is generally described by hopping mechanisms. For a hopping mechanism the temperature dependent network conductivity ($\sigma$) is given by

$$\sigma(T) = \sigma_0 \exp\left[-\left(\frac{T_0}{T}\right)^{\alpha}\right] \tag{7.7}$$

where T is the temperature, $\alpha$ tells you the hopping mechanism, $\sigma_0$ and $T_0$ are constants which depends on the hopping mechanism. To accurately determine which hopping mechanism is occurring reduced activation energy analysis is often used.[184,192,193]The reduced activation energy ($W$) is defined as

$$W = \frac{d\sigma}{dT} \tag{7.8}$$

The slope of fits to a plot of ln($W$) vs ln($T$) indicates which conduction mechanism is present. A plot of ln($W$) vs ln($T$) is shown in Fig. 7.10C. The plot shows a change from one conduction mechanism to another, with a transition temperature of 195 K. There is a large amount of scatter in the data. The slope of the plot at high temperature is 0.85 $\pm$ 0.03, which likely implies Miller-Abrahams hopping (MAH) or nearest-neighbour hopping, both of which occurs when $\alpha$=1. At lower temperatures the plot shows a considerable amount of scatter, with the data at very low temperatures showing a slope of above 1, which is not possible as the maximum slope for a hopping mechanism is 1. It is possible that this large amount of scatter is caused by an increase in the error in the measurement temperature at lower temperatures. The slope of the plot in this region varies depending on the data points fit, fitting the data points closest to the transition temperature yields a slope of 0.29 $\pm$ 0.06, which could imply 2D-variable range hopping (VRH), where $\alpha$=0.33, or 3D-VRH, where $\alpha$=0.25.

Once the temperature dependent conduction mechanism has been determined, fitting the network conductivity vs temperature data allows for the determination of values relating to the conduction. Fig. 7.10D shows the conductivity as a function of 1/T, fit with the MAH mechanism at high temperatures. We believe that the data is described by MAH and not NNH as NNH describes the hopping of charge carriers when there is uniform spatial distribution of sites in a narrow energy range, while MAH models the hoping of charge carriers between 2 localised states when there is a distribution of separations and energy differences between the states.[332] We believe that the MAH mechanism more likely explains

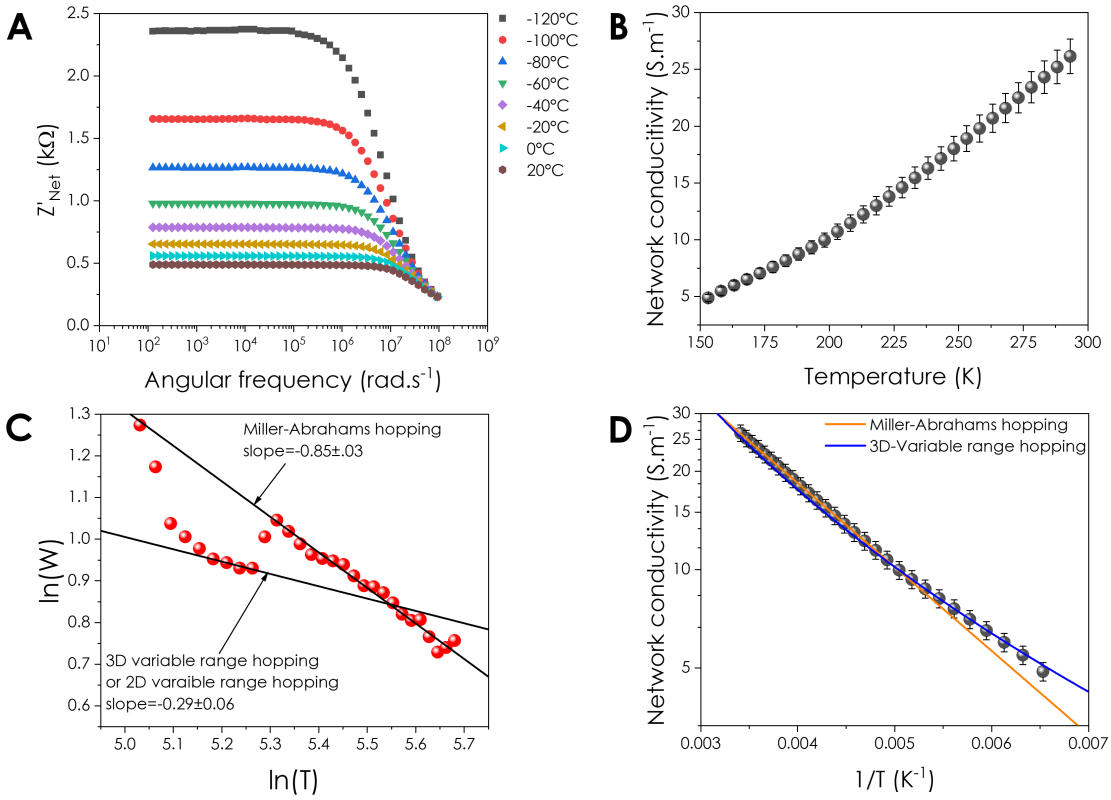



Figure 7.10: **Temperature dependent impedance: A)** Real component of the network impedance spectra measured at a variety of different temperatures for the 5 deposition MPME c-$MoS_2$ sample. **B)** Conductivity as a function of temperature calculated from the low frequency plateau of the data shown in A. **C)** Reduced activation energy plot used to determine the conduction mechanism in the network. At high temperatures the plot shows Miller-Abrahams hopping (MAH) behaviour while at low temperatures the behaviour could be explained by 2D- or 3D-variable range hoping (VRH). **D)** Network conductivity vs 1/T, with fits to MAH and 3D-VRH shown.

the type of hoping that occurs between nanosheets. Fitting this hopping mechanism yields the activation energy of the hops, which in this case gives a value of 50 meV. This value is below the value reported for IJP EE $MoS_2$ nanosheet networks (96 meV) but above the value reported for LS EE $MoS_2$ networks (44 meV).[192,295] The low activation energy likely contributes to the low junction resistance in the networks.

In the low temperature regime Fig. 7.10C suggests that the conduction mechanism could be described by 2D- or 3D-VRH. To determine which of these conduction mechanisms is occurring the data was fit for both the conduction mechanisms and the fit parameters were used to calculate the localisation length. The localisation length corresponds to the region in which electrons are confined by the wavefunction and should be similar to the Bohr radius of an $MoS_2$ atom (0.45 nm).[295] Fits to both the 2D- and 3D-VRH can be found in appendix A.4.5. Fitting to the 2D-VRH yields a localisation length of $1\times10^{-4}$ nm, while fitting to the 3D-VRH mechanism yields a localisation length of 0.44 nm. From these values it is clear that the hopping mechanism at low temperature in the network is described by 3D-VRH, this mechanism has been found for IJP and LS EE $MoS_2$ networks

at low temperatures.[192,295] In this case a version of the 3D-VRH mechanism which has been adapted for 2D materials was used.[295] The calculated localisation length is in line with values calculated for $MoS_2$ nanosheets, which vary between 0.2-3 nm.[192,295,333–335] In a VRH model, charge carriers hop from one state to another energetically favourable state, with larger hops than occur during MAH, the dimensionality of the mechanism indicates in which directions the hopping can occur.[295]

While the temperature dependent conductivity data allows for the calculation of the conduction mechanism it does not allow for an understanding of the temperature dependent properties of the either the nanosheets or the junctions, these properties can be determined from temperature dependent nanosheet-junction EIS spectra, a sub-set of which are shown in Fig. 7.11A. From these spectra the temperature dependence of both the nanosheets and junctions can be calculated. The dependence of both nanosheet and junction resistance on temperature is shown in Fig. 7.11B. Interestingly, they show opposite behaviour, with the nanosheet resistance decreasing as temperature decreases, while the junction resistance increases. It is clear from this data that the networks transition from nanosheet- and junction-limited at room temperature to junction-limited at low temperatures.

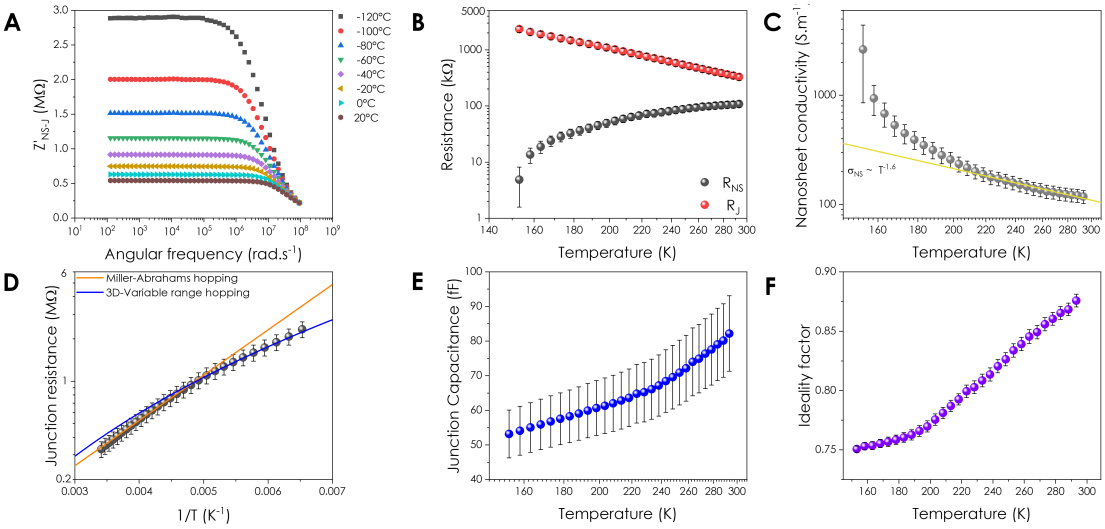



Figure 7.11: **Temperature dependence of nanosheet and junctions: A)** Real component of the nanosheet-junction EIS spectra measured at a variety of different temperatures. **B)** Nanosheet and junction resistance as a function of temperature. **C)** Nanosheet conductivity as a function of temperature. Fit to the high temperature regime shows $\sigma_{NS} \propto T^{-1.6}$. **D)** Junction resistance as a function of inverse temperature. The fit to both both MAH at high temperature and 3D-VRH at low termperature are shown. **E)** Junction capacitance as a a function of temperature. **F)** Ideality factor as a function of temperature.

To understand the charge transport mechanism within the networks we will now consider the temperature dependence of both the nanosheets and the junctions. Nanosheet conductivity as a function of temperature is shown in Fig. 7.11C. The $MoS_2$ nanosheet conductivity increases as the temperature decreases. Increasing mobility as temperature decreases is seen for materials where the conductivity is limited by phonon-scattering of the charge carriers. In this scenario the conductivity scales as $\sigma \propto T^{-\beta}$.[54] At high temperature a

value of $\beta$=1.6 $\pm$ 0.1 was calculated, in line with literature reports for $MoS_2$ which range between 0.5-2.6[54,195,336,337] and similar to a value of 1.1 for EE nanosheets, measured by the same method.[295] At lower temperatures the rate of increase in conductivity increases, this is unusual behaviour for $MoS_2$, which generally shows a decrease in the dependence of mobility on temperature at lower temperatures.[195] This behaviour may be partially explained by the same effect which causes the scatter in the reduced activation energy plot, however, the deviation begins at higher temperature and so this effect is unlikely to completely explain it. This deviation may also be driven by contact resistance effects. The EIS spectra were converted from network to nanosheet-junction assuming a constant contact resistance, however, contact resistance is a temperature dependent value. In most materials the contact resistance decreases as temperature increases due to an increase in thermionic carrier emission, this has been observed for $MoS_2$.[338] However, in materials where the mobility is strongly dependent on temperature, as is seen here, the contact resistance can decrease as temperature decreases due to a decrease in scattering at the contact.[339] Decreasing contact resistance with decreasing temperature has been observed for $MoS_2$ with a range of contact materials, including Ti/Au.[340,341] As the nanosheet resistance decreases the impact on the contact resistance on the measured value increases, and so variations in contact resistance could lead to large errors in values measured at lower temperatures. The calculated series resistance from the network EIS spectra, can be found in appendix A.4.6. This data shows that the series resistance approaches the room temperature contact resistance at lower temperatures.

Junction resistance as a function of temperature is shown in Fig. 7.11D. The junction resistance is likely to show the same hopping mechanisms as the network, as the network resistance is dominated by the junction resistance, especially at low temperatures. Fitting the junction resistance vs temperature data, at high temperatures, with the MAH mechanism allows for the calculation of the activation energy associated with the hop across the junction. This yields a value of 64 meV, higher than was calculated for the network activation energy. This calculated value is larger than the value calculated for EE LS $MoS_2$ nanosheets (55 meV), this is interesting as the junction resistance and junction area is smaller in the networks presented here than in the EE LS $MoS_2$ networks.[295] This suggests that the activation energy for hopping across a junction does not solely control the value of the junction resistance at room temperature. In the low temperature regime the junction resistance data can be fit with 3D-VRH, the fit to the data is shown in Fig. 7.11D. From this fit the localisation length can be calculated, yielding a value of 0.4 nm, in agreement with the value calculated for the network. Using the 3D-VRH model the energy of the hops can be calculated at a given temperature, at 195 K, the temperature that there is the transition from MAHto 3D-VRH the energy of the hops is 46 meV, below the MAH energy. The average hopping distance can also be calculated from the 3D-VRH model, yielding a value of 1.6 nm, which is in-line with previously calculated values for EE LS $MoS_2$ 2.3 nm and 2.5 nm for cross-linked LPE $MoS_2$ networks.[184,295] This value is larger than the thickness

separation between the layers in an $MoS_2$ crystal, this occurs as the VRH model describes a charge carrier hopping from one energetically favourable trap state to another, even if separated by a large distance.

The junction capacitance and ideality factor also varies with temperature, as shown in Fig. 7.11E,F, respectively, both decrease as the temperature decreases. The decrease in the junction capacitance with temperature suggests that there is a reduction in the junction area as the temperature decreases, it is not clear what causes this decrease. The decrease in ideality factor suggests that as the temperature decreases that there is an increase in the distribution of the junctions resistances in the charge carriers path. The decrease in junction area combined with the increase in the junction resistance likely leads to the decrease in the ideality factor as there is an increase in highly resistive junctions in the conduction path.

In conclusion, we have investigated the morphological and electrical properties of mechanically exfoliated networks of $MoS_2$ produced from both natural $MoS_2$ crystals and from commercially available $MoS_2$ powder. The exfoliation yields large area, thick, high aspect nanosheets. Networks can be produced by repeat deposition of these nanosheets. The networks show a low porosity of $11 \pm 2\%$, a high degree of nanosheet alignment and a low surface roughness making them an ideal candidate for electronic devices. The networks show increasing conductivity with annealing, up to a temperature of 300°C, however, they show low mobilities of $2.2 \pm 0.3$ $cm^2.V^{-1}.s^{-1}$ and $0.025 \pm 0.002$ $cm^2.V^{-1}.s^{-1}$ for the samples exfoliated from the crystal and powder respectively. Using the model developed in Chapter 6 and EIS the nanosheet and junction resistance were calculated for the samples exfoliated from the crystal $MoS_2$. This yielded a nanosheet conductivity of $110 \pm 20$ $S.m^{-1}$ and a junction resistance of $890 \pm 130$ kΩ, suggesting the networks are nanosheet and junction limited. The calculated nanosheet resistance suggests that the nanosheets show a low mobility, which is likely caused by the thickness of the nanosheets. Therefore, to increase the mobility of devices produced by this method, the thickness of the nanosheets needs to be reduced. EIS measurements also revealed that a sample composed of 5 depositions showed a variation in junction resistance with channel length, while a sample composed of 6 depositions did not, suggests that 6 depositions are required to obtain a homogenous network. Finally, temperature dependent measurements were carried out, finding that the network conductivity is strongly dependent on temperature. Temperature dependent EIS measurements show that the nanosheet conductivity is limited by phonon scattering while the junctions transitioning from MAH to 3D-VRH. In theMAH regime the junction resistance has an activation energy of 64 meV. From the 3D-VRH, a localisation length of the electron in $MoS_2$ was calculated as 0.4 nm .

*"Who truly knows, who here could proclaim:*
*whence this creation flows, where is its origin?*
*. . . Only He (Brahman) in highest heaven, who is of this the witness.*
*He alone knows, unless...He knows it not."*

The Rigveda, translated by Martin R. Wolff

# 8

# Conclusions & Future Work

## 8.1 Conclusions

The discovery of the stability of individual layers of 2D materials led to a great deal of research into these materials, with 2D materials showing promise for an almost endless array of applications. One method to produce devices from nanosheets is through the formation of solution-processed nanosheet networks, which offer promise in a range of devices from batteries to catalysts to electronic devices. This work focuses on the development of techniques to understand the properties of nanosheet networks so that they can be optimised, fulfil their promise, and transition from devices of interest to the scientific community to commercially available products.

One of the main factors which limits the applicability of nanosheet networks for a variety of applications is the morphology of the network. Control over morphological parameters such as porosity and nanosheet alignment is important for device optimisation, however, measuring the network morphology has proven difficult. FIB-SEM nt is presented as a solution, allowing for the calculation of an array of network morphological parameters, including network porosity, nanosheet alignment, nanosheet and pore tortuosity factors, and nanosheet aggregation. The effectiveness of this technique was demonstrated by investigating the morphology of size-selected networks of graphene, $WS_2$ and AgNSs. For each of the materials it was found that the size of the constituent nanosheets affected the morphology of the network, with each material showing similar but distinct morphological properties. The technique was then applied to printed heterostack devices. The interface between size-selected graphene networks and a printed AgNP top electrode was investigated, finding that the interfacial roughness and penetration depth was affected by the nanosheet size. The morphology of an ITO/$WS_2$/Au out-of-plane device was also investigated, finding that the network's surface roughness led to the formation of electrical shorts within the device.

As well as affecting network morphology, reports suggest that nanosheet size also affects network electrical properties. The electrical properties of nanosheet networks are known to be limited by the resistance of the junctions between the nanosheets. To understand the effect of network morphology, nanosheet size and the junction resistance on network conductivity a model describing the charge transport in the networks was developed. This model suggests that the relationship between nanosheet length and network conductivity is dependent on the nanosheet carrier concentration. To investigate this the conductivity of size-selected networks of graphene and $WS_2$ were measured. It was found that the conductivity of the graphene networks increased with decreasing nanosheet size, in line with predictions from the model. Using the model the nanosheet conductivity was calculated as 32 $\pm$ 2 kS.m$^{-1}$, while the junction resistance was calculated as 1.4 $\pm$ 0.1 k$\Omega$. In contrast, the $WS_2$ network conductivity showed a peak at large nanosheets lengths and a rapid decrease as nanosheet length was decreased. This behaviour is also in line with predictions from the model, allowing for the calculation of a $WS_2$ nanosheet conductivity of 0.6 $\pm$ 0.1 S.m$^{-1}$ and a junction resistance of 17 $\pm$ 3 G$\Omega$. These results demonstrate the validity of the derived model, and the importance of controlling nanosheet dimensions for optimising network electrical properties.

While solution-processed nanosheet networks show promise for a range of applications, networks of mechanically exfoliated nanosheets can be produced in a more cost-effective manner. If the electrical properties of these networks could be optimised then they might offer a superior method for the production of low-cost electronic devices. The electrical and morphological properties of mechanically exfoliated networks of $MoS_2$ nanosheets produced from natural $MoS_2$ crystal and commercial $MoS_2$ powder was investigated. The morphology of the networks was investigated by FIB-SEM nt, finding that the networks were composed of well aligned nanosheets, with the networks showing a low porosity of 11 $\pm$ 2%. The electrical properties of the networks was found to depend on the starting material. IL gated transistor measurements were used to calculate the mobility of the networks, the networks produced from $MoS_2$ crystal and $MoS_2$ powder had a mobility of 2.2 $\pm$ 0.3 cm$^2$.V$^{-1}$.s$^{-1}$ and 0.025 $\pm$ 0.002 cm$^2$.V$^{-1}$.s$^{-1}$, respectively. To understand the low mobility of these devices, the nanosheet and junction resistance were calculated by combining EIS with the model derived for the network conductivity. This yielded a nanosheet conductivity of 110 $\pm$ 20 S.m$^{-1}$ and a junction resistance of 890 $\pm$ 130 k$\Omega$, which suggests that the low mobility of the devices is caused by the low mobility of $MoS_2$ nanosheets, as well as the junctions in the network. This technique was then used to measure the temperature dependent electrical properties of the networks, finding the nanosheet conductivity increases as temperature decreases, while the junctions resistance is described by Miller-Abrahams hopping at high temperature, with an activation energy of 64 meV, and 3D-variable range hopping at low temperature.

## 8.2 Future work

### 8.2.1 Mechanically exfoliated $MoS_2$ networks

The data presented in Chapter 7 offers insight into the morphology and electrical properties of MPME networks of $MoS_2$ and makes suggestions about how the electrical properties of these networks could be improved. However, it does raise several questions which could not be answered in the time frame of this project. Firstly, the channel length dependent percolation effect is interesting; it has only been observed once before for nanosheet networks.[184] To further investigate this effect the dependence of the channel length dependent percolation exponent on sample thickness should be investigated. If the channel length dependent scaling is a percolation effect, the percolation exponent should increase as the network thickness is decreased.[325] To investigate this effect the channel length dependent scaling of network conductivity for samples with less than 5 depositions will be investigated. The data obtained from these experiments will allow for a greater understanding of this effect and could allow for the expansion of Eqn. 7.3 to describe networks below the percolation threshold.

Secondly, the data presented shows that the use of a water based silver paint leads to an increase in the conductivity of the network. Control over the doping of nanosheet networks is of interest as it would allow for further control over the electrical properties of the network. As discussed in Chapter 6 the nanosheet length dependent electrical properties of a network depend on the charge carrier concentration and so control over the doping level could allow for control over the nanosheet length dependent electrical properties of a material. Therefore, the cause of this doping requires further investigation.

Finally, the temperature dependent data presented in Chapter 7 shows a large amount of scatter. It is unclear if this scatter is due to the instrumentation used for the measurement or if it is related to the sample. To determine if there is a problem with the instrumentation, an alternative thermometer will be used to double check the measured temperature. A circuit of resistor and capacitors will then be used to ensure the impedance spectra measured by the instrument at low temperature are accurate. If this does not explain the noise in the data then a different sample will be used to see if the scatter is repeatable and contains information about charge transport in the networks.

### 8.2.2 Factors affecting junction resistance

In Chapter 6 and 7 different methods to measure the nanosheet and junction resistance within a network are proposed. Using these methods the junction resistance can be calculated for a range of materials. Fig. 7.8 shows the relationship between nanosheet conductivity and junction resistance for the materials tested by these methods thus far showing a relationship between nanosheet conductivity and junction resistance. The cause of the de-

crease in junction resistance with increasing nanosheet conductivity is unclear and requires further investigation. To investigate this effect populating the nanosheet conductivity vs junction resistance graph over a broad range of nanosheet conductivities is required, this would require the production of nanosheets with a broad range of conductivities.

Furthermore, Fig. 7.8 also suggests that there is a relationship between junction resistance and junction area. Therefore, the relationship between junction area and junction resistance should be investigated. Some work on this has already been carried out by measuring EIS spectra of a $MoS_2$ network at different strains, the strain causes a decrease in junction area and therefore an increase in the junction resistance.[342] A more thorough study could be carried out by controlling the size of large area nanosheets by scission, as has previously been carried out for GO,[305] and measuring the junction area and junction resistance of networks composed of the different size nanosheets by EIS. An alternative method would be to use compression of an LPE network to increase the junction area and then through fitting of Eqn. 6.7 and applying EIS the effect of the increase in junction area on junction resistance could be understood.

### 8.2.3 Compression of spray-coated networks

Chapter 7 demonstrates the ability of EIS to calculate both the nanosheet and junction resistance in nanosheet networks. This method can allow for in-situ testing of the effect of various stimuli on the properties of nanosheet networks. This technique was not applied to the LPE $WS_2$ presented in Chapter 6 as the resistance of the sample was too high, meaning that EIS just measures the capacitance of the electrodes. To more fully understand charge transport in nanosheet techniques the application of EIS to spray-coated LPE $WS_2$ networks would be useful. One method which could allow for a sufficient improvement in network conductivity so that EIS could be used is network compression, as discussed in Chapter 3.8 compression can lead to large increases in network conductivity.

It has recently been found that compression of spray-coated graphene networks made in a similar method to the networks shown in Chapter 5 and 6 can lead to a factor of 9 reduction in sheet resistance, which is likely to correspond to a factor of 18 improvement of conductivity due to the removal of the porosity from the network, reducing the thickness by a factor of 2.[343] The data presented in Chapter 6 suggests spray-coated $WS_2$ networks are more junction limited than graphene networks and therefore compression may lead to a larger increase in conductivity.

To investigate the effect of compression on $WS_2$ networks, a size-selected $WS_2$ network was produced in the same manner as Chapter 6. In this case the ink was captured between $28\times$ $g$ and $447\times$ $g$ to have a sufficient amount of mass to spray-coat thick films. The ink was then spray-coated onto PET coated in $Al_2O_3$. The networks were then compressed using a hydraulic press. In this case the networks were compressed at ~200 MPa for 100 s. This large

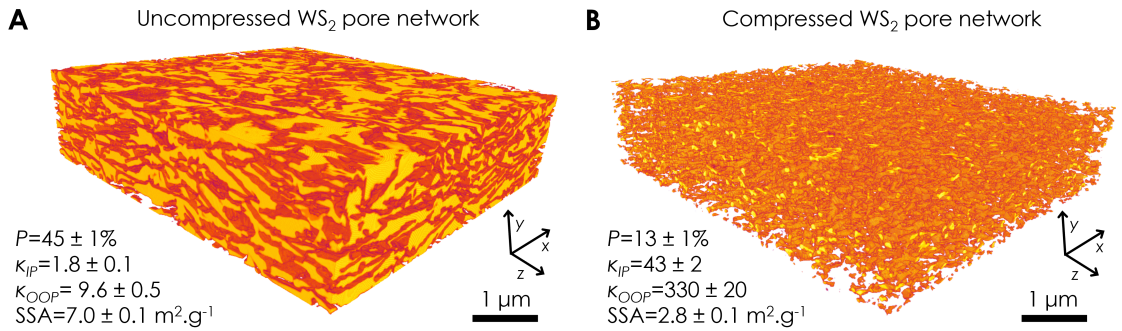



Figure 8.1: **Morphology of compressed network: A)** 3D image of the pore network of a $WS_2$ network, printed from nanosheets with $l_{NS}$=1012 nm. The morphology of this network is discussed in Chapter 5. **B)** 3D image of a compressed $WS_2$ network.

pressure was used as it has been found that $MoS_2$ networks partially relax after compression up to a pressure of 20 MPa.[343] To determine the effectiveness of the compression, FIB-SEM nt was carried out on a compressed network. 3D images of the network were produced in the same manner as described in Chapter 5. A section of the pore volume of the compressed network and the pore volume from the $WS_2$ network with $l_{NS}$=1012 nm presented in Chapter 5 are shown in Fig. 8.1, showing the densification of the network which occurs after compression. The compressed network has a porosity of 13 $\pm$ 1% and a SSA of 2.8 $m^2.g^{-1}$, well below and above the values measured for the $WS_2$ networks presented in Chapter 5, respectively. The network shows a pore connectivity of 90%, demonstrating that despite the densification the pores still remain connected. The compression also increases the pore tortuosity factors, with the in-plane pore tortuosity factor increasing to 43 $\pm$ 2 and the out-of-plane value increasing to 330 $\pm$ 20. In comparison the nanosheet tortuosity factors decreased to 1.11 $\pm$ 0.06 in the in-plane direction and 1.29 $\pm$ 0.07 in the out-of plane direction. The very similar nanosheet tortuosity demonstrates the high degree of nanosheet alignment. There was also a decrease in pore size, with the compressed networks have a characteristic pore length of 71 $\pm$ 14 nm and a pore circularity of 0.61 $\pm$ 0.01.

The reduction in porosity and nanosheet tortuosity factor should produce an improvement in network conductivity, with the morphological scaling factor decreasing from 3.5 to 1.3. To investigate the improvement in network conductivity from compression, electrical tests were performed on a network before and after compression. These tests show that the conductivity of the network increases by a factor of ~80, with the post compression network showing a conductivity of ~$3\times10^{-2}$ $S.m^{-1}$. This result suggests that compression can be used to produce LPE nanosheet networks that are conductive enough for EIS to determine the nanosheet and junction resistance. To this end, a spray-coated LPE $WS_2$ network that was ~22 $\mu$m thick was produced and compressed. The modulus of the EIS spectrum of a thin $WS_2$ network before compression, the thick network after compression, and the background are shown in Fig. 8.2A. The impedance of the compressed network is below the substrate impedance. The imaginary component of the network EIS spectrum is shown in Fig. 8.2B, showing that the peak is in the measured range, suggesting that fits to the data

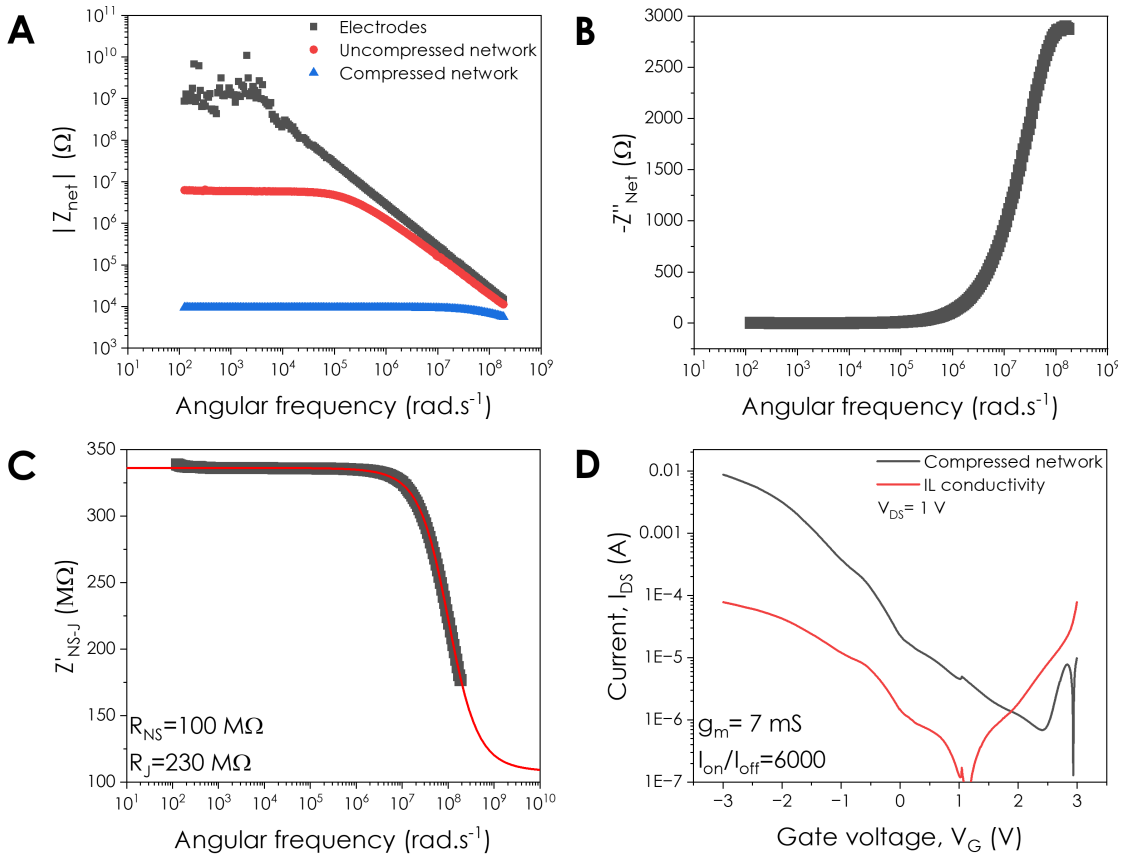



Figure 8.2: **Electronics of compressed network: A)** Impedance modulus of a thin uncompressed $WS_2$ network, a thick compressed $WS_2$ network and the electrodes used for the measurement. **B)** Imaginary component of the network EIS spectrum, showing that the peak is in the measured frequency range. **C)** Real component of the nanosheet-junction impedance spectrum showing the fit of Eqn. 7.3. The average nanosheet and junction resistance for the device is shown. **D)** Transfer curve for the compressed network, gated with an IL. The gate-source voltage is also shown.

will be accurate. The converted real component of the impedance spectrum is shown in Fig. 8.2C. The conversion was carried out using the carrier concentration calculated in Chapter 6, assuming a nanosheet thickness of 400 nm, an aspect ratio of 15, and that the network thickness decreased by a factor of 2 after compression. Fitting the real component of the nanosheet-junction impedance spectrum shown in Fig. 8.2C leads to an average junction resistance of 230 MΩ and a nanosheet resistance of 100 MΩ, which corresponds to a nanosheet conductivity of 0.2 $S.m^{-1}$, a factor of 3 lower than the value measured by fitting the length dependent data in Chapter 6. Since this was carried out on a standard mask and not a length dependent mask the contact resistance was not measured, meaning that this value likely underestimates the nanosheet conductivity. The networks show a junction capacitance of 45 aF, which corresponds to a junction area of 3,000 $nm^2$. An average ideality parameter of 0.84 $\pm$ 0.01 was measured, suggesting that there is a distribution of junction resistances and capacitances.

The large decrease in the junction resistance suggests that there should be a large increase in the network mobility. To investigate if this occurs IL gated transistor measurements were

carried on a network after compression. The transfer curve is shown in Fig. 8.2D, showing that the network is p-type, with any n-type behaviour being masked by the conductivity of the IL. Fitting the data yields a transconductance of 7 mS, which is in agreement with the value measured for an uncompressed $WS_2$ network.[170] As discussed in Chapter 7, the volumetric capacitance of a nanosheet network is related to the nanosheet thickness, it is likely that an increase in nanosheet thickness due to compression is masking the improvement in network mobility.

To expand on this work, the effect of compression pressure on the change in network morphology should be investigated. The compression could also be expanded to size-selected graphene networks. This would be of interest as reducing the junction resistance should reduce the slope of the network conductivity vs. nanosheet length plot, meaning that highly conductive networks could be produced from both thick and thin nanosheets.

# Appendix

## A.1 Supplementary information for theory chapters

### A.1.1 Aspect ratio of nanosheets produced by LPE

As demonstrated by Backes *et al.*[86] and discussed in Chapter 2.2.3, the nanosheets produced by LPE show a constant aspect ratio ($k_{NS}$) which is given by

$$k_{NS} \approx 2a\frac{Y_{In-plane}}{Y_{Out-of-plane}}\langle N\rangle^{b-1} \tag{A.1}$$

here, we will show the derivation of this equation.

Assuming that the energy for exfoliation a sheet from its parent crystal ($E_{Peeling}$) and the energy to tear a nanosheet ($E_{Tearing}$) does not depend on the nanosheet size or shape, and that the energy for these two processes is related by a constant ($a$), we can state

$$\langle E_{Peeling}\rangle = a \times \langle E_{Tearing}\rangle \tag{A.2}$$

This equation can be expressed as the peeling ($E_S$) and tearing ($E_E$) energy and the nanosheet dimensions as

$$2\langle A_S\rangle E_S = \frac{2aE_E\langle A_E\rangle}{2} \tag{A.3}$$

where $A_E$ is the area of edges created and $A_S$ is the new surface area created by the peeling of a nanosheet from the parent crystal. The factor of 2 on the left hand side of the equation is to denote that the peeling of a nanosheet from its parent crystal creates new surface for both the nanosheet and the crystal. The factor of 0.5 on the right hand side describes the fact that the nanosheet may be torn from the edge as well as the centre of the parent crystal and so the amount of new edge area created will be on average approximately half the edge area of the nanosheet .

If we assume that the edge area is given by a small area around the perimeter then the edge area is given by the nanosheet perimeter ($P$) times the nanosheet thickness ($t_{NS}$) which is given by the layer number ($N$) and the ML thickness ($d_0$) as $t_{NS} = Nd_0$. Allowing us to state

$$\langle A_E\rangle = \langle PN\rangle d_0 \tag{A.4}$$

If we sub this value for $\langle A_E \rangle$ into Eqn. A.3, then we can state

$$\langle A_S \rangle = \frac{a d_0}{2} \frac{E_E}{E_S} \langle PN \rangle \tag{A.5}$$

From AFM images the nanosheet length ($l_{NS}$), width ($w_{NS}$) and thickness can be calculated. Here, we will assume that the nanosheet are elliptical in shape. In the case of a low aspect ratio ellipse, its area is given by

$$\langle A_S \rangle = \frac{\pi}{4} \langle l_{NS} w_{NS} \rangle \tag{A.6}$$

While the perimeter of a low aspect ratio ellipse is given by $P = \pi \langle \sqrt{l_{NS} w_{NS}} \rangle$ meaning we can state

$$\langle PN \rangle = \pi \langle N \sqrt{l_{NS} w_{NS}} \rangle \tag{A.7}$$

subbing the values for $\langle A_S \rangle$ and $\langle PN \rangle$ into Eqn. A.6, allows us to state

$$\langle l_{NS} w_{NS} \rangle = 2 a h_0 \frac{E_E}{E_S} \langle N \sqrt{l_{NS} w_{NS}} \rangle \tag{A.8}$$

To calculate the value of $\langle N \sqrt{l_{NS} w_{NS}} \rangle$ , we will assume that it can be described by

$$\langle N \sqrt{l_{NS} w_{NS}} \rangle = \langle N \rangle^b \sqrt{\langle l_{NS} w_{NS} \rangle} \tag{A.9}$$

This relationship has found to describe a wide range of LPE materials with the value of b generally being close to 1 and never being larger than 1.5.[86] Using this assumption we can state

$$\langle l_{NS} w_{NS} \rangle = \left( 2 a d_0 \frac{E_E}{E_S} \right)^2 \langle N \rangle^{2b} \tag{A.10}$$

We can then rearrange this equation to write it in terms of nanosheet aspect ratio ($k_{NS}$) as

$$k_{NS} = \frac{\sqrt{\langle l_{NS} w_{NS} \rangle}}{\langle N \rangle d_0} = 2 a \frac{E_E}{E_S} \langle N \rangle^{b-1} \tag{A.11}$$

as b is close to 1 this suggests that the nanosheets have an approximately constant aspect ratio which is related to the ratio of the peeling to tearing energy. It has been shown by DFT that for graphene, this ratio is the same as the ratio of the in-plane ($Y_{in-plane}$) to the out-of-plane ($Y_{out-of-plane}$) Youngs modulus.[86] This allows us to state

$$k_{NS} \approx 2 a \frac{Y_{in-plane}}{Y_{out-of-plane}} \langle N \rangle^{b-1} \tag{A.12}$$

This equation suggests that the aspect ratio of nanosheets that can be obtained by the application of energy which is equally divided between peeling and tearing nanosheets ($a$=1) is a constant governed by the properties of the material.

### A.1.2 Size of nanosheets obtained by LCC

Ogilvie *et al.*[131] have derived the equation for the size of nanosheets obtained by LCC, showing that the volume of nanosheets obtained is given by

$$V_{NS} = \left( \frac{\pi \eta h}{10(\rho_{2D} - \rho_l) R g t} \right)^{\frac{3}{2}} \tag{A.13}$$

Here we will show the derivation of this equation.

The force that an nanosheet experiences due to centrifugation ($F_g$) is given by

$$F_g = \rho_{2D} V_{NS} R g \tag{A.14}$$

where $\rho_{2d}$ and $V_{NS}$ are the density of the nanosheet and its volume, R is the RCF and g is the acceleration due to gravity. The buoyant force on the nanosheets ($F_b$) in the liquid is given by

$$F_b = \rho_l V_{NS} R g \tag{A.15}$$

where $\rho_l$ is the density of the liquid. If $F_g > F_b$ then the nanosheet will move down in the liquid. This downward motion will be acted against by a drag force ($F_d$). Stokes law states that the drag force for a sphere is given by

$$F_d = 6\pi \eta r \nu \tag{A.16}$$

where $r$ is the radius of the sphere, $\eta$ is the solvents viscosity and $\nu$ is the velocity of the sphere. If the volume of a nanosheet is modelled as a sphere with radius $r = V_{NS}^{\frac{1}{3}}$, we can state that the drag force on the nanosheet is given by $F_d = 6\pi \eta V_{NS}^{\frac{1}{3}} \nu$. When the nanosheet is at terminal velocity the force on the nanosheet is $F_d = F_g - F_b$, which is given by

$$6\pi \eta V_{NS}^{\frac{1}{3}} \nu = (\rho_{2D} - \rho_l) V_{NS} R g \tag{A.17}$$

which means we can state the terminal velocity of the nanosheets is given by

$$\nu = \frac{(\rho_{2D} - \rho_l) V_{NS}^{\frac{2}{3}} R g}{6\pi \eta} \tag{A.18}$$

Using the velocity we can calculate the sedimentation time for a nanosheet ($t$) from the top of a centrifuge tube

$$t = \frac{h}{\nu} = \frac{6\pi \eta h}{(\rho_{2D} - \rho_l) V_{NS}^{\frac{2}{3}} R g} \tag{A.19}$$

where $h$ is the height of the liquid in the centrifuge tube. This can then be re-expressed in

terms of the volume of the nanosheet as

$$V_{NS} = \left( \frac{\pi \eta h}{10(\rho_{2D} - \rho_l) R g t} \right)^{\frac{3}{2}} \tag{A.20}$$

While this model assumes that the nanosheets are spherical, it seems to agree with experimental results with show a power-law trend of nanosheet volume with $Rt$

# A.2 Supplementary information for Chapter 5

## A.2.1 Nanoplatelet length and thickness distributions

It is known that LPE nanosheets aggregate during the printing process. While this has been observed, measurements of the extent of the aggregation has proven difficult.[125] In this work, we measure the thickness of the nanoplatelets in the network using the ridge detection algorithm in FIJI.[269,271] This algorithm measures the thickness and length of objects in an image and identifies where it believes there are junctions between the objects. The algorithm was applied to the probability maps obtained from TWS after the images had been segmented. The application of the algorithm to a cross-section from the network with $l_{NS}$= 238 nm is shown in Fig. A.1A. Here, the green lines show where the algorithm believes the edge of the object is, the thickness of the object is the average distance between the green lines. The red line shows the centre of object, the object length is measured as the length of the red line and the dots show where the algorithm believes there are junctions between the nanosheets. As the algorithm was used to meaure the nanosheet length in each cross-section, nanosheet lengths less than the length measured by AFM were included, to create a length comparable to the AFM length any nanosheet less than 75% of the nanosheet length was not included in the distribution or the calculation of average nanoplatelet length. Due to the nanosheet aggregation during the printing process the identified junctions are not related to the junctions that a charge carrier has to pass through has it travels through the network but instead just denote the end of a nanoplatelet in a given cross-section.

The aggregation of the nanosheets during the printing process causes an increase in their aspect ratio as they aggregate more with thickness than they do with length. Nanoplatlet aspect ratio as a function of nanosheet length is shown in Fig. A.2, showing that the nanoplatelet aspect ratio decreases significantly as the nanosheet length decreases, with the aspect ratio decreasing from 15, approximately half the value of the nanosheets in the ink, to ~4, 7 times lower than the value in the ink. This aggregation of the nanosheets may have an impact in the performance of devices as it considerably reduces the SSA of the network.

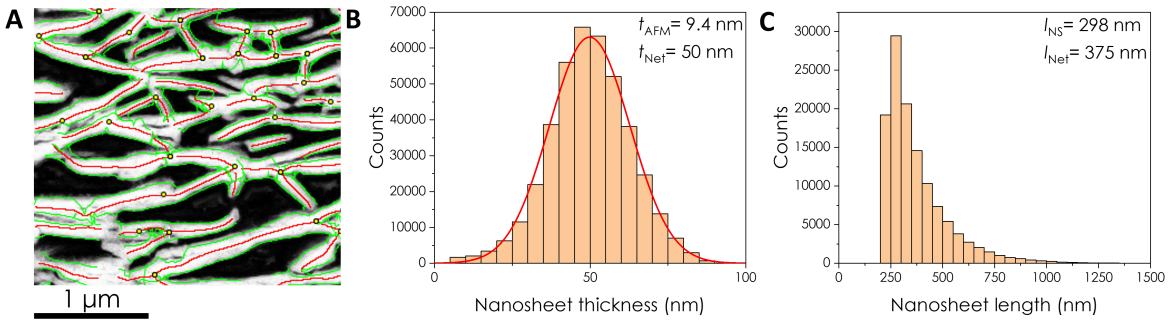



Figure A.1: **Nanoplatelet length and thickness distributions: A)** Probability map of cross-section of the graphene network with $l_{NS}$= 238 nm, with the ridge detection algorithm applied. **B)** Distribution of the thickness of the nanoplatelets in the network for the network with $t_{NS}$=9.4 nm. **C)** Distribution of the length of the nanoplatelets in the network for the network with $l_{NS}$=298 nm, any nanosheet lengths less than 75% of this nanosheet length were not included in this distribution.

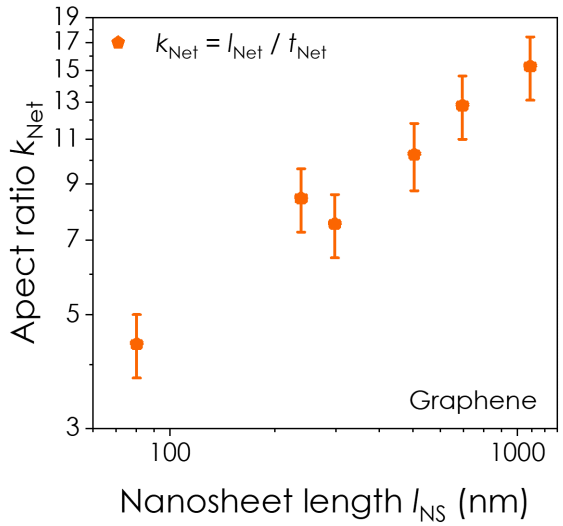



Figure A.2: **Nanoplatelet aspect ratio:** Aspect ratio of the nanoplatelets within the network

### A.2.2 Nanosheet alignment measurements

Measuring the alignment of objects from an image is usually carried out in 2D, however, in Chapter 5 we present a method for measuring alignment in 3D allowing for the calculation of the Hermans orientation factor. To demonstrate the efficacy method we will compare it to a method that has previously been used for calculating the alignment of vacuum filtered and 3D printed graphene nanosheets.[199,205] OrientationJ is a plugin in FIJI,[269,312] which uses a structure tensor to determine the orientation of objects in an image. A structure tensor is a matrix which can be used to determine the gradient of an image and can be used to detect edges. The plugin used requires an estimate of the thickness of the objects in the image to apply a Gaussian filter to the image. The plugin then outputs a histogram giving the object orientation and an image showing the orientation of the objects. The orientation histogram for a large and small graphene nanosheet network is shown in Fig. A.3, the distributions are fit with the Cauchy-Lorentz function.

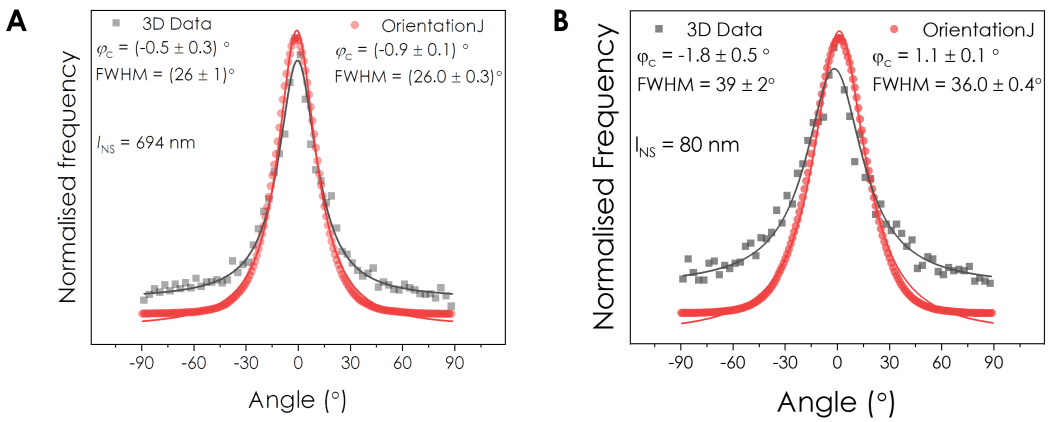



Figure A.3: **Nanosheet orientation: A-B)** Nanosheet orientation distribution calculated using the OrientationJ plugin in FIJI and by the 3D distance transform watershed followed by fitting with equivalent ellipsoid functions in MorpholibJ in FIJI,[269,272,312] for the network with $l_{NS}$=694 nm and $l_{NS}$=80 nm, respectively. The data is fit with a Cauchy-Lorentz function and the FWHM and the centre point of the distributions are shown.

In Chapter 5 the orientation of the $WS_2$ and graphene nanoplatelets was measured by seperating the nanoplatelets using 3D using a distance transform watershed algorithm and finding their orientation by fitting them with equivalent ellipses, both calculations were carried out using the morpholibJ library in FIJI.[269,272] This algorithm separates joined objects in a binarised 3D image by considering there distance from an edge. This algorithm is designed for the separation of isotropic objects and not anisotropic objects, therefore, to demonstrate its validity we compare it with the distributions calculated using the structure tensor method described above. Both methods yield distribtuions which are centered about 0°, for the large nanosheets the FWHM of the distributions agree, while for the smallest nanosheet the 3D method leads to a slightly larger FWHM. The similarity of these results suggests that the 3D method is capable of determining the orientation of the objects in the network.

### A.2.3 Pore area and circularity distributions

The pore volumes within the networks presented in Chapter 5 show a very high degree of connectivity with all of the networks showing connectivity above 99%. This makes analysis of the pore volumes impossible in 3D, so the area and circularity of the pores was calculated from each cross-sectional image. As the pore networks are dominated by small pores which do not contribute significantly to the overall porosity of the networks the area-weighted pore fraction was calculated for each of the networks.

The area-weighted pore fraction for each of the size-selected graphene networks presented in Chapter 5 are shown in Fig. A.4. Here it can be seen that the 30% area weighted faction band shifts to smaller pore areas and and circularities as nanosheet size decreases. For each network there for each of the networks that 90% of the porosity is contained within a an approximately linear band at low circularities and large pore area. The distribution

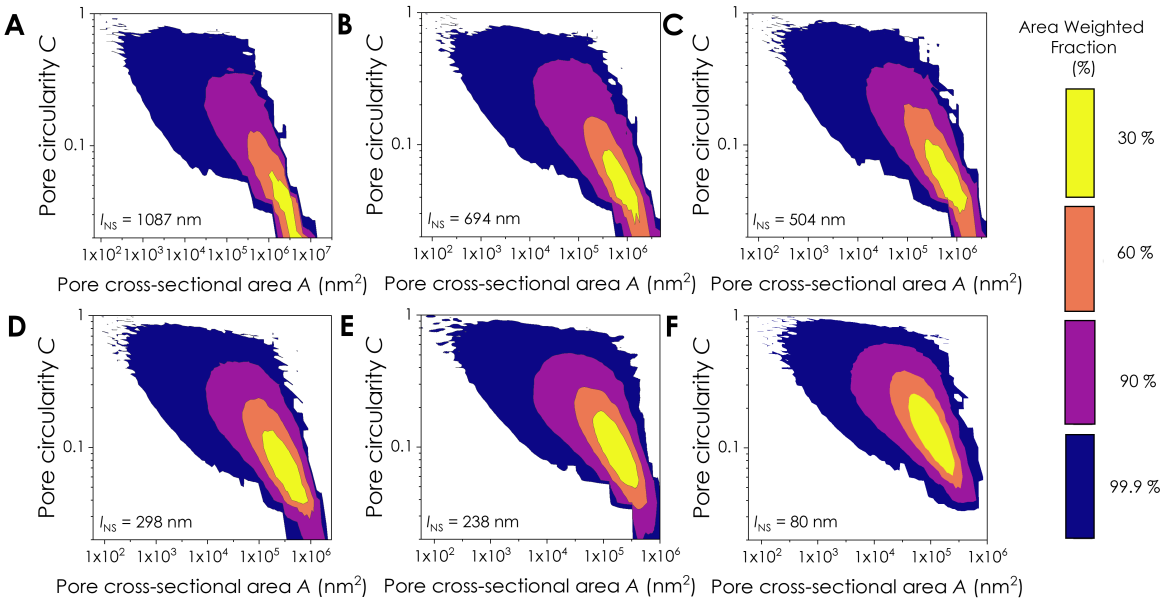



Figure A.4: **Graphene network pore volume: A-F)** Area-weighted pore fraction heat maps, showing the amount of the porosity contained within different regions as a function of the pore area an pore circularity, for each of the size-selected graphene networks. The nanosheet length in each of the networks is shown.

of bins within these bands was used to calculate the average pore cross-sectional area and the circularity. A representative pore area and pore circularity distribution is shown in Fig. A.2.3.

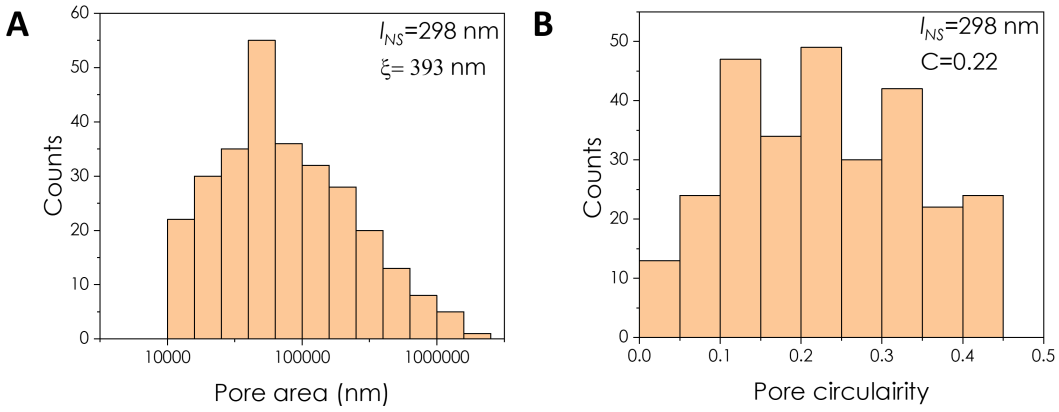



Figure A.5: **Graphene network pore volume: A)** Pore area distribution on a semi-log scale, for the network with $l_{NS}$ = 298 nm. **B)** Pore circularity distribution for the same network.

Area-weighted heat maps were calculated for the $WS_2$ and AgNSs networks presented in Chapter 5 and are shown in Fig. A.6. These heat maps show the same general trend as the graphene with a decreasing pore circularity and area as the nanosheet size is decreased. The AgNS networks composed of larger nanosheets appears to be dominated by very large pores, with very low circularities which are at the limit of what can be detected using this technique. For each of these networks the average pore circularity and characteristic pore length was calculated in the same way as described above for the graphene networks .

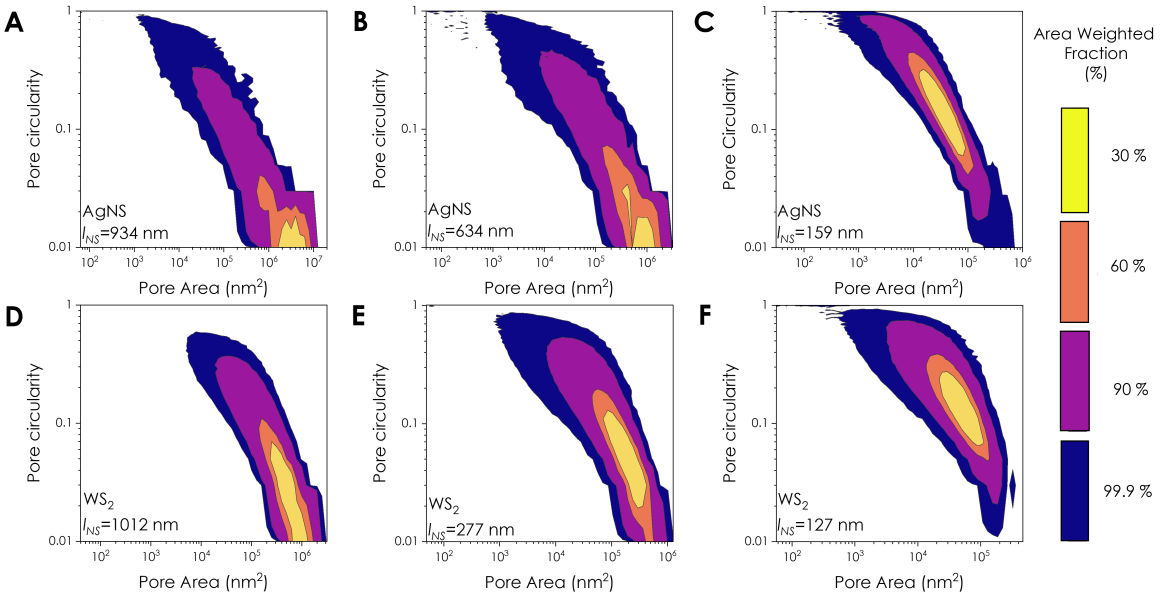



Figure A.6: **AgNS and $WS_2$ pore volume: A-C)** Area-weighted pore fraction heat maps, showing the amount of the porosity contained within different regions as a function of the pore area and pore circularity, for each of the size-selected AgNS networks with decreasing nanosheet size. **D-F)** Area-weighted pore fraction heat maps, showing the amount of the porosity contained within different regions as a function of the pore area and pore circularity, for each of the size-selected $WS_2$ networks with decreasing nanosheet size.

### A.2.4 Cross-sections of AgNS and $WS_2$ networks

In Chapter 5 the morphology of size-selected AgNS and $WS_2$ networks is discussed. However, individual cross-sections of the size-selected networks is not presented so that the effect of nanosheet size on network morphology can be easily visualised. Fig. A.7 shows representative cross-sections for each of the size-selected $WS_2$ and AgNS networks, showing that their is a clear change in morphology as nanosheet size decreases.

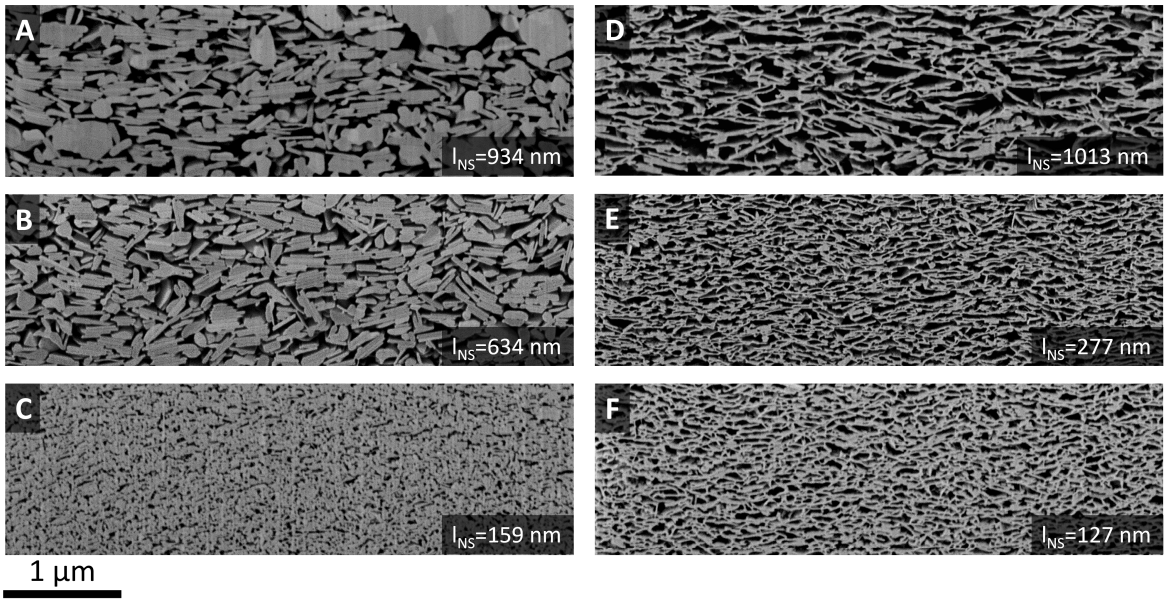



Figure A.7: **Cross-sections of $WS_2$ and AgNS networks: A-C)** SEM cross-section images of the size-selected networks of AgNSs presented in Chapter 5. **D-F)** SEM cross-section images of the size-selected networks of $WS_2$ presented in Chapter 5.

### A.2.5 Volumetric SSA

The relationship between nanosheet length and network gravimetric SSA is shown in Chapter 5, this data suggests that the difference in the SSA of the 3 networks is driven by the density of the materials in the network. At first glance this might imply that all the network show similar trends in volumetric SSA, however, this is not the case. The volumetric SSA of the networks imaged is shown in Fig. A.8. Here, it can be seen that the graphene and $WS_2$ show similar scaling with nanosheet length, while the AgNSs show a different trend. The very similar scaling of gravimetric SSA with nanosheet length is created by the fact that the density of the network is related to the porosity.

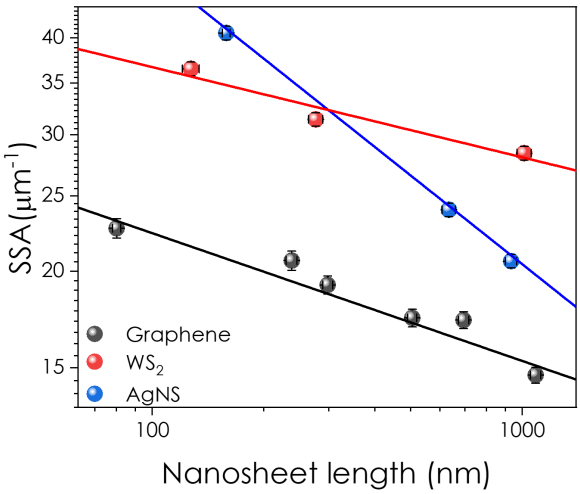



Figure A.8: **Volumetric SSA:** Volumetric SSA of the 3 materials imaged in Chapter 5 as a function of nanosheet length.

### A.2.6 Graphene network with AgNP top electrode

In Chapter 5.2.6 it is found the porosity of AJP AgNP electrodes is (71 ± 2)%. This value is higher than would be expected for randomly packed mono-disperse spheres, where calculations suggest a value of 64%,[300] and higher than would be obtained from body centered cubic packing. but is below what would be obtained for face centered packing of spheres. Fig A.9 shows that the spheres are randomly packed, the relatively low porosity can therefore be understood by polydispersity in the diameter of the spheres. For polydisperse spheres the packing fraction can reach values of 70%.[301] The nanoparticles were used as purchased (Sigma Aldrich, 736465) and no information was available about the polydispersity of the nanoparticle's diameter. It is also possible that the low diameter of the spheres (<50 nm) relative to the resolution of the images leads to an overestimation of the packing fraction.

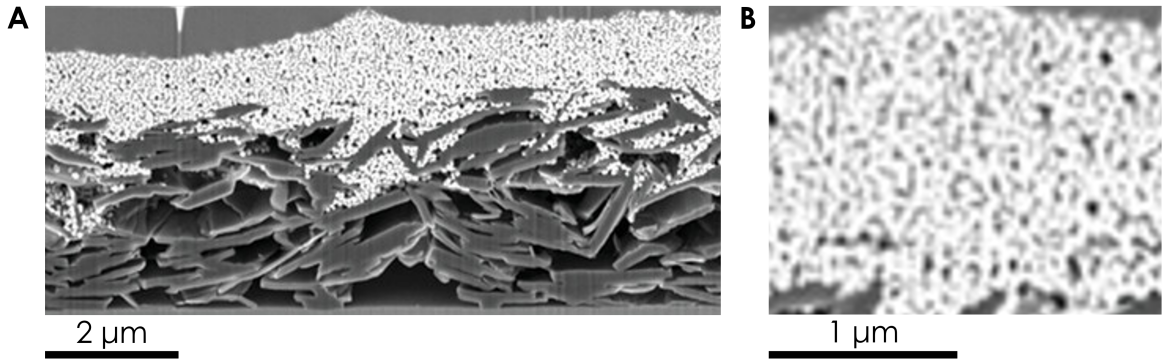



Figure A.9: **Cross-section of graphene network with AgNP top electrode: A** Cross-section of graphene network with $l_{NS}$= 630 nm with an AJP AgNP top electrode. **B** Magnified region of the AgNP network showing the packing of the NPs.

## A.3 Supplementary information for Chapter 6

### A.3.1 Derivation of network conductivity equation

Chapter 6 demonstrates that Eqn. 6.7 can be used to describe the nanosheet length dependent conductivity of both graphene and $WS_2$. The main points of the derivation are shown in that chapter, here, the derivation is presented more fully. As discussed in Chapter 6 this model, assumes that the network is composed of a series of nanosheet-junction pairs that a charge carrier must travel through in order to traverse the network. The number of nanosheet-junction pairs ($N$) that a charge carrier has to pass through in a nanosheet network is given by

$$N \approx \frac{L_{Ch}}{d_{NS} + l_J} \tag{A.21}$$

where $d_{NS}$ and $l_J$ is the average distance that a charge carrier travels through a nanosheet and junction and $L_{CH}$ is the effective channel length. The increase in effective channel length ($L_{Ch}$) for a charge carrier in a network due to convolution of the conduction path is

given by the square root of the in-plane nanosheet tortuosity factor $\sqrt{\kappa_{NS}}$, so the effective channel length is given by $L_{Ch} = L\sqrt{\kappa_{NS}}$, where L is the electrode separation. If we assume that the average distance that a charge carrier travels through a nanosheet is half the nanosheet length ($l_{NS}$) then we can say

$$N \approx \frac{(L\sqrt{\kappa_{NS}})}{(\frac{l_{NS}}{2} + l_J)} \tag{A.22}$$

The voltage drop that is associated with travelling across nanosheet-junction pair ($V_P$) is given by $V_P = V/N = V_J + V_{NS}$. Here, $V_{NS}$ and $V_J$ are the average voltage drop for a charge carrier travelling across a nanosheet and a junction respectively. The voltage drop across a junction is given by

$$V_J = \frac{R_J}{R_J + R_{NS}} \frac{V}{N} \tag{A.23}$$

Where $R_{NS}$ and $R_J$ are the resistance of the nanosheet and the junction respectively. The voltage drop across the nanosheet is similarly given by

$$V_{NS} = \frac{R_{NS}}{R_J + R_{NS}} \frac{V}{N} \tag{A.24}$$

Using these equation the properties of the network can be calculated. The time for a charge carrier to travel from one electrode ($\tau_{Net}$) to another is given by

$$\tau_{Net} = \frac{L}{\mu_{Net} E_A} = \frac{L^2}{\mu_{Net} V} \tag{A.25}$$

where $E_A = V/L$ is the applied field. The time for a charge carrier to cross the network can also be expressed in terms of the average time for a charge carrier to cross a nanosheet ($\tau_{NS}$) and a junction ($\tau_J$) as

$$\tau_{Net} \approx N(\tau_{NS} + \tau_J) = \frac{L_{Ch}}{\frac{l_{NS}}{2} + l_J}(\tau_{NS} + \tau_J) \tag{A.26}$$

Using the same equation for $\tau_{NS}$ as $\tau_{Net}$, we can state

$$\tau_{NS} = \frac{\frac{l_{NS}}{2}}{\mu_{NS} E_{NS}} = \frac{(\frac{l_{NS}}{2})^2}{\mu_{NS} V_{NS}} = \frac{(\frac{l_{NS}}{2})^2}{\mu_{NS}} \frac{R_J + R_{NS}}{R_{NS}} \frac{L_{Ch}}{(\frac{l_{NS}}{2} + l_J)V} \tag{A.27}$$

Where $E_{NS}$ is the electric field across a nanosheet and $\mu_{NS}$ is the mobility of charge carrier in the nanosheet. $\tau_J$ can be calculated by considering the current flowing through the network as

$$\tau_J = \frac{e}{I_J} = \frac{eR_J}{V_J} = e(R_J + R_{NS}) \frac{L_{Ch}}{(\frac{l_{NS}}{2} + l_J)V} \tag{A.28}$$

where $e$ is the charge on an electron. Subbing the equations for $\tau_{NS}$ and $\tau_J$ into Eqn. A.25

gives

$$\tau_{Net} = \frac{L^2}{\mu_{Net} V} \approx \frac{L_{Ch}}{\frac{l_{NS}}{2} + l_J} \left[ \frac{l_{NS}^2}{4\mu_{NS}} \frac{R_J + R_{NS}}{R_{NS}} \frac{L_{Ch}}{(\frac{l_{NS}}{2} + l_J)V} + e(R_J + R_{NS}) \frac{L_{Ch}}{(\frac{l_{NS}}{2} + l_J)V} \right] \tag{A.29}$$

This equation can then be rearranged in terms of network mobility and using the fact that $\kappa_{NS} = (L_{Ch}/L)^2$, which gives

$$\frac{1}{\mu_{Net}} \approx \kappa_{NS} \frac{R_J + R_{NS}}{(\frac{l_{NS}}{2} + l_J)^2} \left[ \frac{l_{NS}^2}{4\mu_{NS} R_{NS}} + e \right] \tag{A.30}$$

Which can be used to obtain an expression for network mobility

$$\mu_{Net} \approx \frac{(\frac{l_{NS}}{2} + l_J)^2}{\left(\frac{l_{NS}}{2}\right)^2 \left[1 + \frac{R_J}{R_{NS}}\right]} \frac{\mu_{NS}}{\kappa_{NS} \left[1 + \frac{4\mu_{NS} e R_{NS}}{l_{NS}^2}\right]} \tag{A.31}$$

If we assume that the $\frac{l_{NS}}{2} >> l_J$, that is that the average distance the charge carrier travels through a nanosheet is far greater than the average distance travelling through a junction, then we can state

$$\mu_{Net} \approx \frac{\mu_{NS}}{\kappa_{NS} \left(1 + \frac{R_J}{R_{NS}}\right) \left[1 + \frac{4 R_{NS} e \mu_{NS}}{l_{NS}^2}\right]} \tag{A.32}$$

If we assume that the nanosheets are square then we can write $R_{NS}$ in terms of the nanosheet size

$$R_{NS} = \frac{\frac{l_{NS}}{2}}{l_{NS} t_{NS} \sigma_{NS}} = \frac{1}{2 t_{NS} \sigma_{NS}} \tag{A.33}$$

This can be combined with the equation for nanosheet conductivity $\sigma_{NS} = \mu_{NS} n_{NS} e$ where $n_{NS}$ is the nanosheet carrier concentration to further simplify Eqn. A.32 to

$$\mu_{Net} \approx \frac{\mu_{NS}}{\kappa_{NS} \left(1 + 2 t_{NS} \sigma_{NS} R_J\right) \left[1 + \frac{2}{t_{NS} l_{NS}^2 n_{NS}}\right]} \tag{A.34}$$

Using the relationship between network mobility and network conductivity ($\sigma_{Net}$)

$$\sigma_{Net} = \mu_{Net} n_{Net} e = \mu_{Net} n_{NS} (1 - P) e \tag{A.35}$$

where $P$ is the porosity.[170] The equation can be written in terms of network conductivity as

$$\sigma_{Net} \approx \frac{\sigma_{NS}(1 - P)}{\kappa_{NS}[1 + 2 R_J \sigma_{NS} t_{NS}] \left[1 + \frac{2}{t_{NS} l_{NS}^2 n_{NS}}\right]} \tag{A.36}$$

Which is the equation used to fit the nanosheet length dependent conductivity data in Chapter 6.

### Derivation considering quantum like transport

The derivation shown in appendix A.3.1 assumes that the charge transport in the nanosheets can be considered to be classical with the nanosheet resistance given by Eqn. A.33. However, the derivation up to that point is general and we can assume a semi-quatnum transport, where the the nanosheet resistance is given by

$$R_{NS} = \frac{R_Q l_{NS}}{2\zeta} \tag{A.37}$$

where $R_Q$ is the quantum resistance and $\zeta$ is the scattering length. Using this expression for nanosheet resistance an alternative model can be derived.

Without the assumption about the conduction in nanosheets being classical Eqn. 6.7 can be expressed as

$$\sigma_{NS} = \frac{\sigma_{NS}(1-P)}{\kappa_{NS}\left(1+\frac{R_J}{R_{NS}}\right)\left[1+\frac{4R_{NS}}{n_{NS}l_{NS}^2}\right]} \tag{A.38}$$

Replacing $R_{NS}$ with Eqn. A.37, allows us to state

$$\sigma_{NS} = \frac{(1-P)\sigma_{NS}}{\kappa_{NS}\left(1+\frac{2R_J\zeta}{R_Q l_{NS}}\right)\left[1+\frac{2R_Q}{n_{NS}l_{NS}\zeta}\right]} \tag{A.39}$$

While this equation is similar to the one obtained by assuming classical transport, it suggests a very weak dependence of network conductivity on nanosheet length and cannot explain the strong dependence's observed both in the literature and in this work[93,126,304]

## A.3.2 Understanding the implications of Eqn. 6.7

In order to understand the implications of Eqn. 6.7 it is graphed with varying some of its parameters in Fig. 6.2, here, these graphs are replicated in Fig. A.10 with axes labels and the relevant values included so the position of the peak in conductivity can be understood. The values used for the blue (central) curve in each case can be found in table A.1. The values were chosen as they are representative of the values that can be achieved for LPE and EE nanosheets.

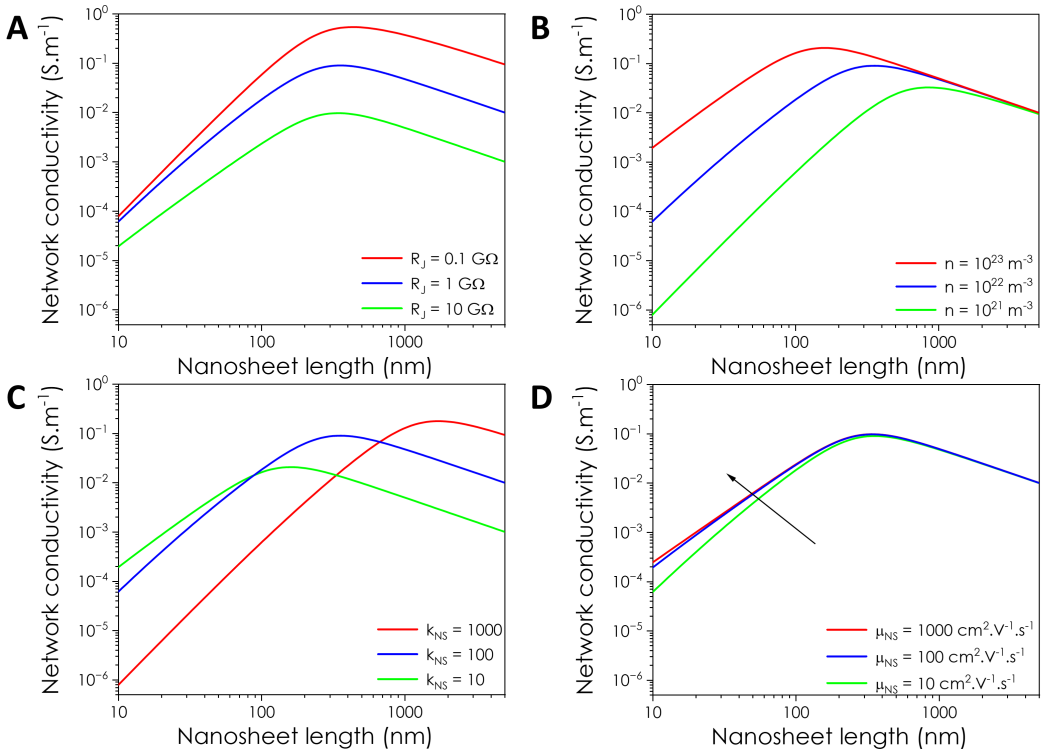



Figure A.10: **Factors impacting network conductivity:** Network conductivity as a function of nanosheet length calculated from Eqn. 6.7, with changing **A)** junction resistance, **B)** nanosheet carrier density, **C)** nanosheet aspect ratio, **D)** nanosheet mobility. In each case the central (blue) line is the same and the parameter being varied is increased and decreased by an order of magnitude from this value. The values for the blue curves are given in table A.1

| Parameter | Value |
|---|---|
| Porosity, $P$ | 0 |
| Tortuosity, *kappa* | 1 |
| Junction resistance , $R_J$ | 1 GΩ |
| Nanosheet carrier density, $n_{NS}$ | $1 \times 10^{22}$ m$^{-3}$ |
| Nanosheet mobility, $\mu_{NS}$ | 10 cm$^{-2}$.V$^{-1}$.s$^{-1}$ |
| Nanosheet aspect ratio, $K_{NS}$ | 100 |

Table A.1: Table with the values inputted to Eqn. 6.7 to generate the blue (central) curve in Fig. 6.2 and A.10.

## A.4 Supplementary information for Chapter 7

### A.4.1 Nanosheet dimension distributions

The dimension of nanosheets produced by MPME is important for the electrical properties of the networks produced. The thickness of the nanosheets is of particular importance and

are shown in Fig. 7.1. However, the nanosheet length is also important as the junction area will be related to the nanosheet size. Fig. A.11A,C shows the distribution of nanosheet length for the c-$MoS_2$ and p-$MoS_2$, respectively, showing that MPME of $MoS_2$ powder produces smaller nanosheets.

The aspect ratio of the nanosheets produced is also important, with the aspect ratio effecting the mechanics of the nanosheet.[82] The aspect ratio of the nanosheets exfoliated from c- and p-$MoS_2$ are shown in Fig. A.11B,D, respectively. The aspect ratio of the nanosheets are higher than can be achieved by LPE of $MoS_2$ and the powder aspect ratio is higher than the aspect ratio that has been achieved for EE p-$MoS_2$ without high temperature annealing (~50).[103] It is possible that repeated exfoliation steps could increase the aspect ratio of the nanosheets further so that they could be competitive with EE nanosheets.

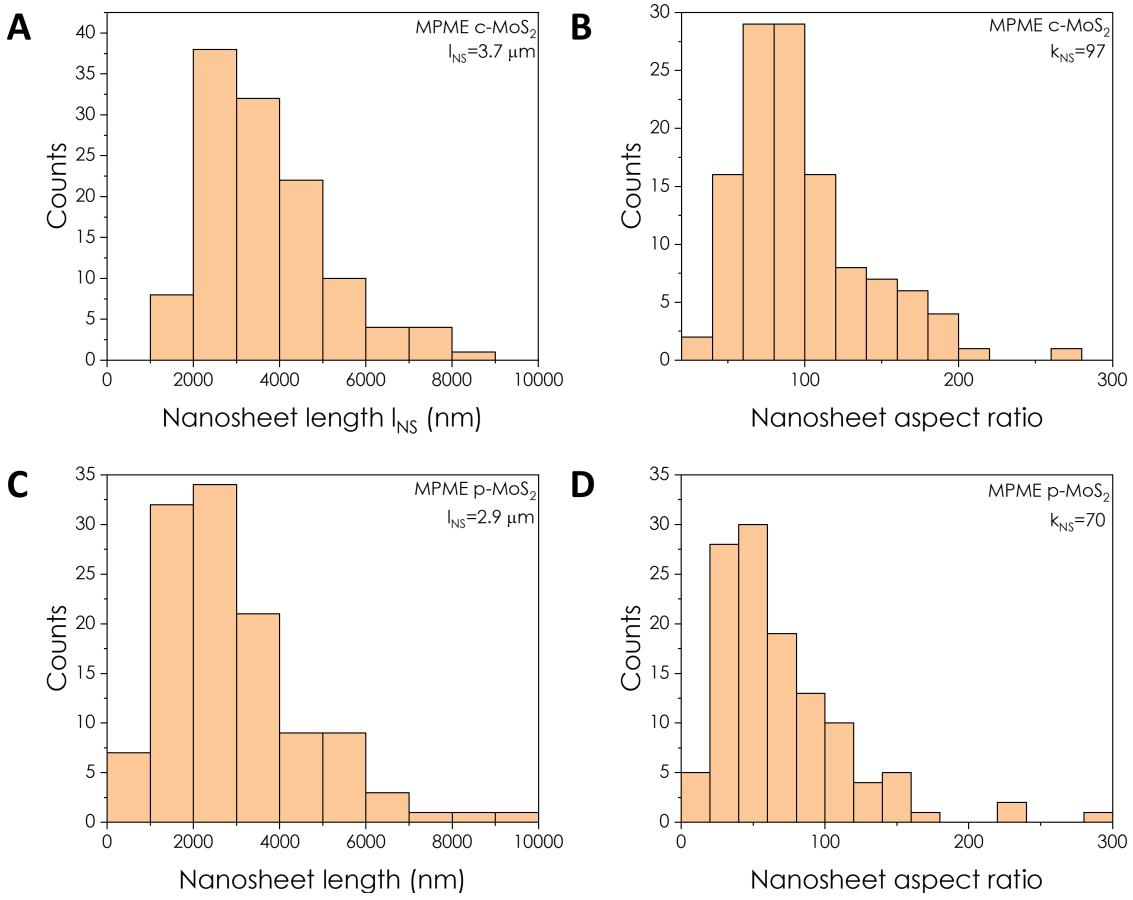



Figure A.11: **Length and aspect ratio of MPME $MoS_2$ nanosheets: A-B)** Nanosheet length and aspect ratio distribution for c-$MoS_2$ nanosheets. **C-D)** Nanosheet length and aspect ratio distribution for p-$MoS_2$ nanosheets.

## Parallel capacitance values

The values of $R_S$, $R_P$ and $n$, extracted from the network EIS spectra, for both the 5 and 6 deposition MPME c-$MoS_2$ networks are shown in Chapter 7. However, the parallel capacitance of the networks are not discussed. $C_P$ as a function of channel length for both networks is shown in Fig. A.12. showing that the parallel capacitance decreases as the

channel length decreases. Unlike the value of $R_P$ the variation in channel length is similar for both networks, with the 6 deposition sample showing a slightly slower decrease.

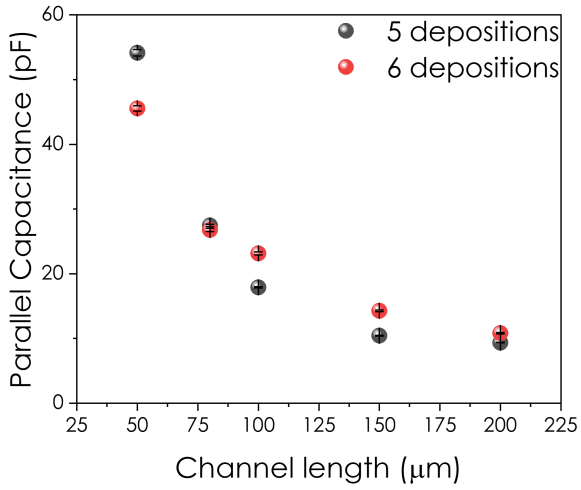



Figure A.12: **Parallel capacitance:** Parallel capacitance values for the 5 and 6 deposition MPME c-$MoS_2$ networks as a function of channel length.

### A.4.2 Channel length percolation scaling

The 5 deposition MPME c-$MoS_2$ network shows a scaling of conductivity with channel length which could be explained by a percolation effect in these networks. The channel length percolation exponent (CLPE) ($\gamma$), describes this non-linear scaling. To investigate this effect the CLPE was calculated for the network after annealing at each temperature. A linear fit to each of the conductivity vs. channel length plots at each temperature is shown in Fig. A.13A. In each case the 200 $\mu$m channel length was excluded from the fit as it is an outlier. It is not clear why the 200 $\mu$m sample is an outlier but percolation plots are prone to scatter due to their very strong dependence on network thickness.

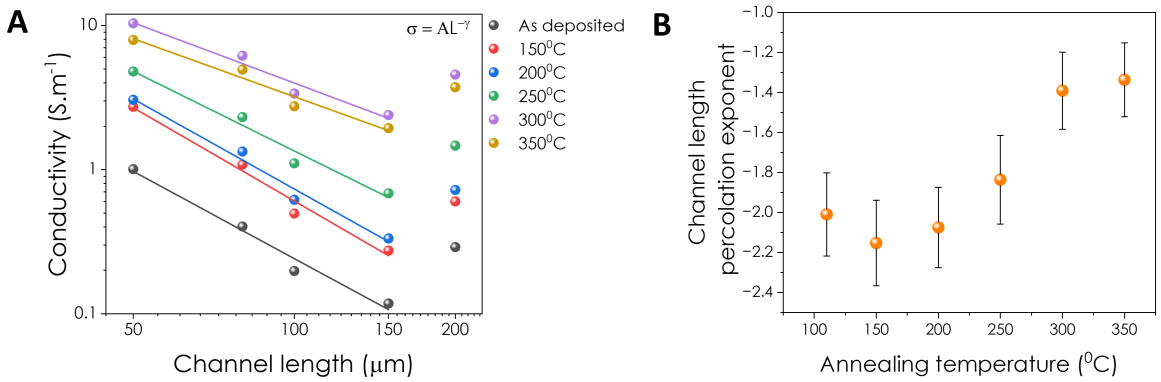



Figure A.13: **Channel length percolation: A)** Network conductivity of the 5 deposition MPME c-$MoS_2$ network as a function of channel length, after annealing at different temperatures. A power law fit is shown. **B)** Channel length percolation exponent (CLPE) as a function of annealing temperature.

The value of the CLPE decreases as the annealing temperature is increased, as can be seen

in Fig. A.13B. This may be caused by a reduction in the ratio of nanosheet-junction resistance. Computational studies on channel width percolation in CNT networks have found that the channel width percolation exponent is dependent on the ratio of junction to nanotube resistance, with networks with lower ratios showing lower percolation exponents.[325] This suggests that the increase in conductivity with annealing temperature is caused by a reduction in the junction resistance.

## Limitation of impedance spectroscopy

EIS has 2 major limitations for investigating the nanosheet and junction resistance in nanosheet networks. The first is that it can only measure materials with a high junction resistance. The peak of the measurement in the imaginary component of the EIS spectra has to be within the frequency range of the instrument. The peak position of a randles circuit is given by $\tau = (R_P C_P)^{-1} = (R_J C_J)^{-1}$.[295] Therefore, to measure the nanosheet and junction resistance of conductive materials a very high frequency impedance analyser is required.

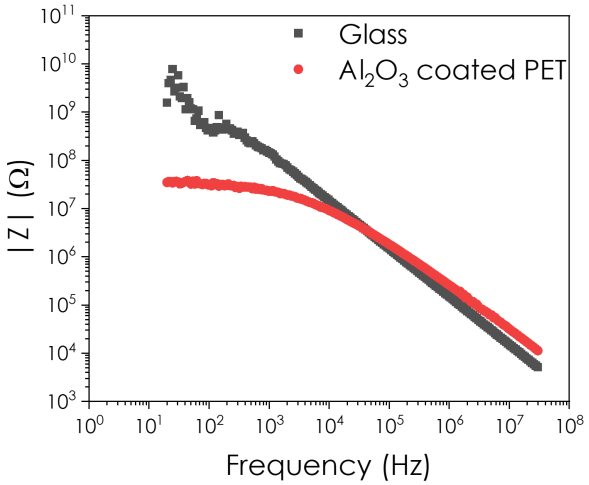



Figure A.14: **Impedance background:** Modulus of EIS spectra of the 50 $\mu$m channel length IDEs used throughout this work on both glass, and PET coated in $Al_2O_3$.

The other limitation of EIS for measuring nanosheet and junction resistance is that the electrodes used to measure the impedance will have there own impedance spectra, this background spectra can have quite low resistance at high frequencies. The impedance spectra for the 50 $\mu$m channel length IDE used throughout this work on both glass and $Al_2O_3$ coated PET is shown in Fig. A.14. In both cases the electrodes act as a capacitor, showing a reduced impedance as a the resistance increases, with the glass reaching a minimum of ~6 kΩ and the PET reaching a minimum of ~10 kΩ. To obtain a network impedance spectra which gives information about the nanosheet and junction resistances, the impedance of the sample must be below these values at high frequencies.

### A.4.3 The relationship between junction area and junction resistance

It is generally presumed that the junction resistance is related to the junction area,[82] however, investigating the nature of this relationship has proven difficult. Strain measurements offer one method to investigate this effect. A recent study expanded the model derived in Chapter 6 to LPE graphene strain sensors , and found that the gauge factor (change in resistance as a function of strain) of a junction was 8.7, suggesting that reducing junction area increases the junction resistance.[310] However, in this case it is not clear how much the junction area changes in this case.

Further evidence for the relationship between junction resistance and junction area can be found in a report of IJP rGO networks, where the size of the GO nanosheets was controlled by sonication induced scission. In this case the GO nanosheets are predominantly MLs and so the thickness should be approximately constant as the nanosheet length decreases. Network conductivity as a function of nanosheet length for these networks is shown in Fig. A.15A. The network conductivity decreases slowly with nanosheet length, a power law fit to the data finds $\sigma_{Net} \propto l_{NS}^{0.1}$, if we assume that the junction area ($A_J$) is proportional to the nanosheet length squared ($A_J \propto l_{NS}^2$) and that the network is junction-limited, then $\sigma_{Net} \propto A_J^{0.05}$. This is a very weak scaling, however, it may partially be explained by large nanosheets leading to a large junction area in these networks. Furthermore the high conductivity of these networks likely means they are not junction-limited. The final data point is an outlier, which may suggest a different behaviour at small junction areas.

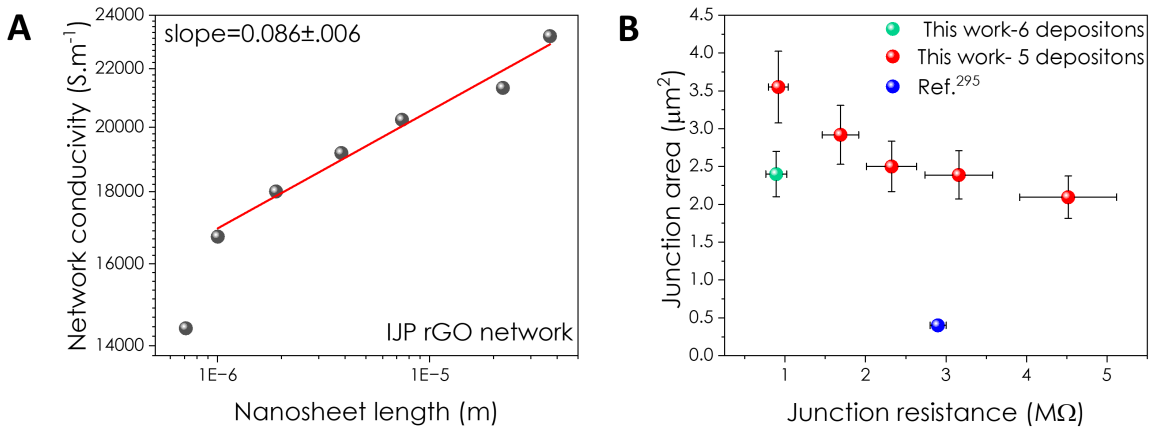



Figure A.15: **Junction resistance and area: A)** Network conductivity of an rGO network as a function of nanosheet length. Here, the nanosheet length is decreased by sonication induced scission of ML GO nanosheets so the decrease in conductivity is likely driven by a reduction in nanosheet area and not nanosheet thickness as is seen in Chapter 6. **B)** Junction resistance as a function of junction area for the 5 and 6 depsotions MPME c-$MoS_2$ network and an EE LS $MoS_2$ network presented in ref.[295]

Junction resistance as a function of junction area for $MoS_2$, measured by EIS, is shown in Fig. A.15B. Here, it can be seen that there is a decrease in junction resistance as the junction area decreases. For the 5 deposition sample the increased error due to the channel

length percolation effect makes interpretation of these results difficult. However, this data data does suggest that junction area is not inversely proportional to junction resistance. Further information about the relationship between junction area and junction resistance can be obtained from the distribution of junction resistance and junction areas.

### A.4.4 Junction resistance and capacitance distributions

The equivalent circuit used to fit the EIS spectra in this work uses an equivalent circuit which contains a constant phase element. Boukamp has shown that a constant phase element implies that there is a distribution of resistance and capacitances in a resistor network.[329] The distribution of junction resistance and capacitances ($G$) is given by

$$G(R_J C_J) = \frac{\sin(n\pi)}{2\pi(\cosh[n\ln(\langle R_J C_J\rangle / R_J C_J] + \cos(n\pi))} \tag{A.40}$$

where $n$ is the ideality parameter, and $R_J$ and $C_J$ are the junction resistance and capacitance, respectively. The distribution of junction resistance and capacitance for the $n$ values obtained in this work and in ref.[295] are shown in Fig. A.16

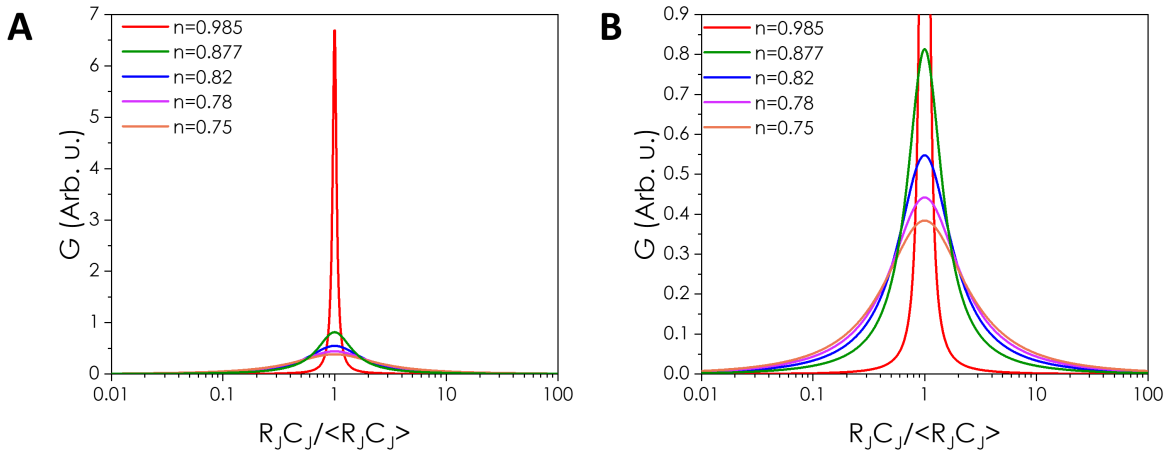



Figure A.16: **Junction resistance and capacitance distributions: A)** Distribution of junction resistance and capacitances calculated using A.40, for the n values calculated in this work and the value calculated in ref.[295] as a comparison. **B)** Same figure as A, with a reduced y axis so the differences in the distributions can be seen more clearly.

The difference in distribution of the 6 deposition MPME c-$MoS_2$ network (n=0.82) and the EE LS $MoS_2$ (n=0.985) can clearly be seen, with the MPME network showing a far broader distribution in junction resistances and capacitances. The values of 0.877 and 0.75 correspond to the values measured for the 5 depositions MPME c-$MoS_2$ network at 20°C and -120°C, respectively. These 2 curves show the large increase in the distribution of junction resistances and capaictances as temperature decreases. Finally, the 5 deposition sample shows n=0.78 at the 50 $\mu$m channel length and n=0.75 at a channel length of 150 $\mu$m, suggesting a minor broadening of the distribution as the channel length decreases.

The implication of the broad distribution of junction resistance and capacitances should

be considered. The low n values obtained in this work, suggests that $\langle R_J C_J \rangle / (R_J C_J)$ can take a range of values, with a considerable portion of the distribution being below 0.1 and above 10 for the 6 deposition MPME c-$MoS_2$ network. As junction capacitance is directly proportional to junction area, this implies that junction resistance is not inversely proportional to junction area, as if this was the case $\langle R_J C_J \rangle / (R_J C_J)$ would be a constant and fitting the EIS spectra would yield n=1.

### A.4.5 Fitting temperature dependent network conductivity data

The reduced activation energy plot for the temperature dependent conductivity, presented in Fig. 7.10C, suggests that the temperature dependent conductivity of MPME c-$MoS_2$ network is given by 2D or 3D VRH at low temperature. If the range that is fit is extended slightly then a slope of -0.54 $\pm$ 0.09 is obtained, shown in Fig. A.17A, which suggests that the hopping could be described by Efros–Shklovskii variable range hopping (ES-VRH), which should show a slope of 0.5. While it seems unlikely that this fit is correct as it fits the data as it begins deviating towards non-physical values. The fit of ES-VRH, 3D-VRH and 2D-VRH to the temperature dependent conductivity data is examined in this section.

From a VRH mechanism the localisation length of electrons within a system can be calculated by fitting the temperature dependent conductivity data. The fit of the 3D-VRH hopping mechanism to the data points for which the reduced activation energy plot suggests 3D-VRH is a possible mechanism, is shown in Fig. A.17B. This plot shows a slope of 37.68 $\pm$ 0.07 $K^{-0.25}$. To calculate the localisation length from the slope must be combined with the model for 3D-VRH. Here, the model describing 3D-VRH between 2 thick nanosheets presented by Gabbett & Kelly *et al.*[295] is used. This model has some minor distinctions from the standard 3D-VRH mechanism. Standard 3D-VRH describes the hopping of charge carriers from one localised state to another and so considers the density of states (DOS) of these localised states, in nanosheet networks the charge carrier hops from one nanosheet to another and so the DOS at the bottom of the conduction band is where the charge carriers hop from. This DOS is calculated using the model for the DOS in a 2D electron gas ($g_{2D}$) given by

$$g_{2D} = \frac{m}{\pi \hbar^2} \tag{A.41}$$

where $m$ is the effective mass of the charge carrier. This can be converted to a 3D DOS ($g_{3D}$) by dividing by the ML thickness ($d_0$)

$$g_{3D} = \frac{m}{\pi \hbar^2 d_0} \tag{A.42}$$

Using this expression the 3D-VRH mechanism for a nanosheet network can be expressed

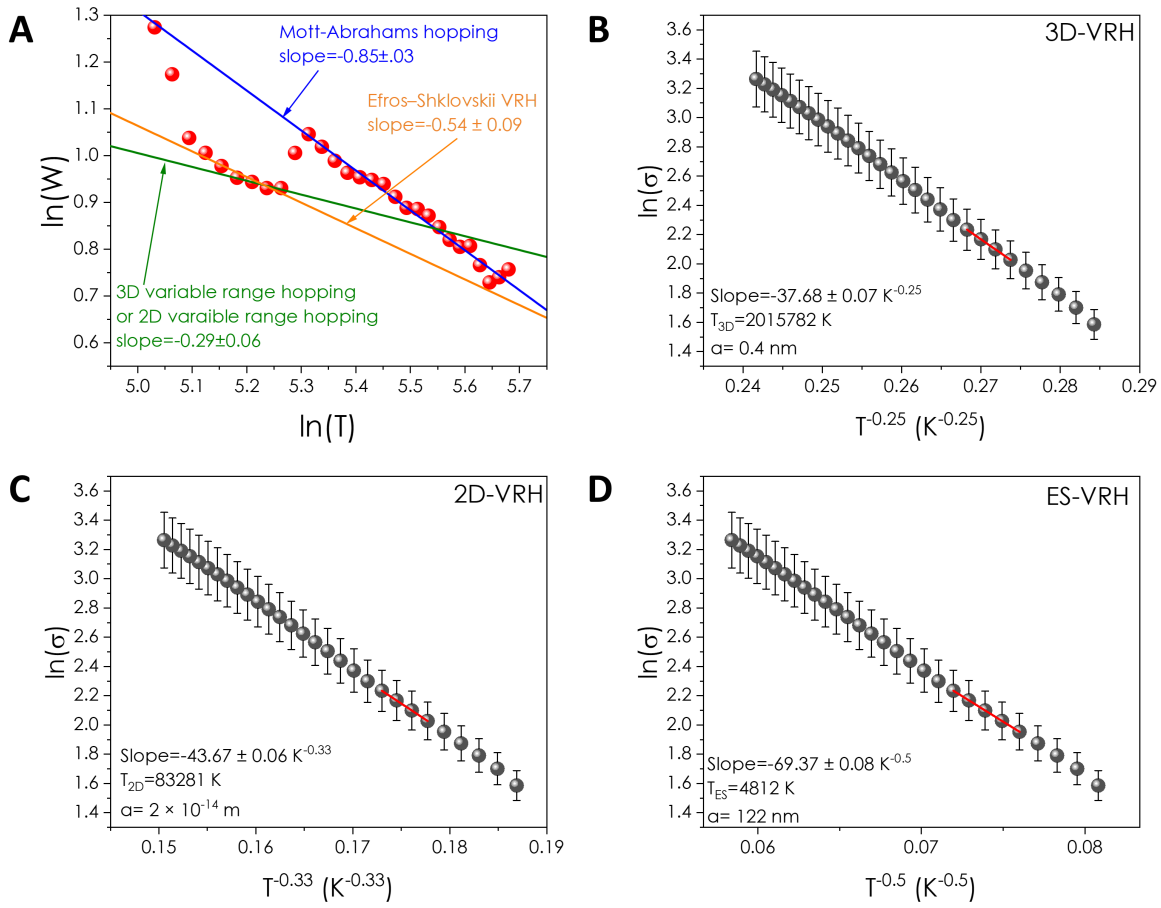



Figure A.17: **Temperature dependent mechanism analysis: A)** Reduced activation energy plot for the 5 deposition MPME c-$MoS_2$ network. The fit to the high temperature data shows MAH, while the fits at low temperature could show 2D-VRH, 3D-VRH or ES-VRH. **B)** Natural log of conductivity vs. temperature to the power of -$\frac{1}{4}$. The fit to 3D-VRH for the data points suggested in A and the corresponding localisation length are shown. **C)** Natural log of conductivity vs. temperature to the power of -$\frac{1}{3}$, The fit to 2D-VRH for the data points suggested in A and the corresponding localisation length are shown. **D)** Natural log of conductivity vs. temperature to the power of -$\frac{1}{2}$, The fit to ES-VRH for the data points suggested in A and the corresponding localisation length are shown.

as

$$\sigma = \sigma_{3D} \exp\left(\frac{2l_J}{a}\right) \exp\left[\frac{T_{3D}}{T}\right]^{\frac{1}{4}} \tag{A.43}$$

where $l_J$ is the distance between the sheets, $a$ is the localisation length, $\sigma_{3D}$ is a constant and and $T_{3D}$ is a constant given by

$$T_{3D} = \frac{76\pi\hbar^2 d_0}{k_B a^3 m} \tag{A.44}$$

where $k_B$ is the Boltzmann constant. Using this equation and the effective mass of an electron in an $MoS_2$ flake as 0.7 times the mass of an electron the localisation length was calculated as 0.4 nm.[295]

The fit of the temperature dependent conductivity data to the 2D-VRH mechanism is shown

in Fig. A.17C. The 2D-VRH mechanism is similarly given by

$$\sigma = \sigma_{2D} \exp\left[\frac{T_{2D}}{T}\right]^{\frac{1}{3}} \tag{A.45}$$

where $\sigma_{2D}$ is a constant and $T_{2D}$ is a constant given by

$$T_{2D} = \frac{13.8}{k_B N_F a^2} \tag{A.46}$$

where $N_F$ is the density of localised states.[344] Using the assumption described above for the density of states of a 2D material we can state

$$T_{2D} = \frac{13.8\pi\hbar^2 d_0}{k_B m a^2} \tag{A.47}$$

using this model to calculate the localisation length gives a value of $2 \times 10^{-14}$ m, which is not a physically sensible result and so we can state 2D-VRH is not occurring.

The final mechanism which could be occurring is ES-VRH. This model is different from Mott-VRH as it assumes that the interaction between charge carriers in the material leads to the opening of a Coloumb gap at the Fermi level. The fit of ES-VRH to the temperature dependent conductivity data is shown in Fig. A.17D. In this case the conductivity is given by

$$\sigma = \sigma_{ES} \exp\left[\frac{T_{ES}}{T}\right]^{\frac{1}{2}} \tag{A.48}$$

where $\sigma_{ES}$ is a constant and $T_{ES}$ is a constant given by

$$T_{ES} = \frac{2.8e^2}{\epsilon k_B a} \tag{A.49}$$

where $e$ is the charge an the electron and $\epsilon$ is the permittivity of the material.[345] Taking the permittivity of a junction as the permittivity of free space this yields a localisation length of 122 nm. This value is considerably large than the Bohr radius of an $MoS_2$ atom and suggests that the electrons exist in small delocalised regions before hopping between the nanosheets. This value fort the localisation length is larger than literature values calculated for ES-VRH.[346]

### A.4.6 Unconverted temperature dependent impedance fits

One of the causes of error in the calculated nanosheet temperature dependent conductivity is that the value of $R_S$, the series resistance, approaches the value of $2R_C$, the room temperature contact resistance, at low temperatures. The value of $R_S$ and $R_P$ as a function of temperature and the value of $2R_C$ at room temperature is shown in Fig. A.18. From this data it is clear that $R_S$ approaches the room temperature value of $2R_C$. As discussed

in Chapter 7, the contact resistance of material where the conductivity is limited by charge scattering can decrease as temperature decreases. Therefore, the assumption of a constant contact resistance with decreasing temperature is likely to increase the error in the calculated nanosheet conductivity, especially at low temperatures, where the measured value of $2R_C$ is a large component of the measured $R_S$. When converting the temperature dependent EIS spectra the room temperature contact resistance was subtracted from each spectra.

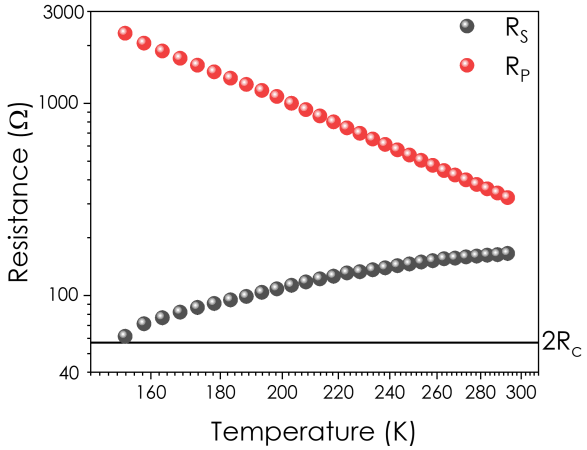



Figure A.18: **Unconverted temperature dependent EIS fit values:** Parallel and series resistance for the unconverted EIS spectra. The value of $2R_C$ at room temperature is also shown.

# Bibliography


[1] W. Wu, *Printed Electronics Technologies*. Royal Society of Chemistry, 2022.

[2] Z. Lin, Y. Huang, and X. Duan, "Van der Waals thin-film electronics," *Nature Electronics*, vol. 2, 2019.

[3] M. S. Fuhrer, J. Nygård, L. Shih, M. Forero, Y. G. Yoon, M. S. Mazzoni, H. J. Choi, J. Ihm, S. G. Louie, A. Zettl, and P. L. McEuen, "Crossed nanotube junctions," *Science*, vol. 288, pp. 494–497, 4 2000.

[4] A. Buldum and J. P. Lu, "Contact resistance between carbon nanotubes," *Physical Review B*, vol. 63, no. 16, p. 161403, 2001.

[5] Y. Sozen, J. J. Riquelme, Y. Xie, C. Munuera, and A. Castellanos-Gomez, "High-throughput mechanical exfoliation for low-cost production of van der Waals nanosheets," *Small Methods*, vol. 7, p. 2300326, 10 2023.

[6] D. Schaming and H. Remita, "Nanotechnology: from the ancient time to nowadays," *Foundations of Chemistry*, vol. 17, pp. 187–205, 7 2015.

[7] E. A. Rohlfing, . D. M. Cox, . A. Kaldor, E. A. Rohlfing, D. M. Cox, and A. Kaldor, "Production and characterization of supersonic carbon cluster beams," *The Journal of Chemical Physics*, vol. 81, pp. 3322–3330, 10 1984.

[8] S. Iijima, "Helical microtubules of graphitic carbon," *Nature 1991 354:6348*, vol. 354, pp. 56–58, 1991.

[9] X. Zhao, Y. Liu, S. Inoue, T. Suzuki, R. O. Jones, and Y. Ando, "Smallest carbon nanotube is 3 Å in diameter," *Physical Review Letters*, vol. 92, p. 125502, 3 2004.

[10] K. S. Novoselov, A. K. Geim, S. V. Morozov, D. Jiang, Y. Zhang, S. V. Dubonos, I. V. Grigorieva, and A. A. Firsov, "Electric field in atomically thin carbon films," *Science*, vol. 306, pp. 666–669, 10 2004.

[11] L. J. Ji, Y. Qin, D. Gui, W. Li, Y. Li, X. Li, and P. Lu, "Quantifying the exfoliation ease level of 2D materials via mechanical anisotropy," *Chemistry of Materials*, vol. 30, pp. 8732–8738, 12 2018.

[12] N. Mounet, M. Gibertini, P. Schwaller, D. Campi, A. Merkys, A. Marrazzo, T. Sohier, I. E. Castelli, A. Cepellotti, G. Pizzi, and N. Marzari, "Two-dimensional materials from high-throughput computational exfoliation of experimentally known compounds," *Nature Nanotechnology 2018 13:3*, vol. 13, pp. 246–252, 2 2018.

[13] A. H. C. Neto, F. Guinea, N. M. Peres, K. S. Novoselov, and A. K. Geim, "The electronic properties of graphene," *Reviews of Modern Physics*, vol. 81, pp. 109–162, 1 2009.

[14] L. Kurpaska, M. Frelek-Kozak, M. Wilczopolska, W. Bonicki, R. Diduszko, A. Zaborowska, E. Wyszkowska, M. Clozel, A. Kosinska, I. Cieslik, M. Duchna, I. Jozwik, W. Chmurzynski, G. Olszewski, B. Zajac, and J. Jagielski, "Structural and mechanical properties of different types of graphite used in nuclear applications," *Journal of Molecular Structure*, vol. 1217, p. 128370, 10 2020.

[15] L. Zhao, B. Ding, X.-Y. Qin, Z. Wang, W. Lv, Y.-B. He, Q.-H. Yang, F. Kang, L. Zhao, B. C. Ding, X.-Y. Qin, Z. J. Wang, W. Lv, Y.-B. He, F. Y. Kang, and Q.-H. Yang, "Revisiting the roles of natural graphite in ongoing lithium-ion batteries," *Advanced Materials*, vol. 34, p. 2106704, 5 2022.

[16] B. J. D. B. ernal, "The structure of graphite," *Proceedings of the Royal Society of London. Series A, Containing Papers of a Mathematical and Physical Character*, pp. 749–773, 12 1924.

[17] P. R. Wallace, "The band theory of graphite," *Physical Review*, vol. 71, p. 622, 5 1947.

[18] C. M. O'Leary, B. Haas, C. T. Koch, P. D. Nellist, and L. Jones, "Increasing spatial fidelity and snr of 4D-STEM using multi-frame data fusion," *Microscopy and Microanalysis*, vol. 28, pp. 1417–1427, 8 2022.

[19] N. D. Mermint, "Crystalline order in two dimensions," *Physical review*, vol. 176, 1968.

[20] J. C. Meyer, A. K. Geim, M. I. Katsnelson, K. S. Novoselov, T. J. Booth, and S. Roth, "The structure of suspended graphene sheets," *Nature 2006 446:7131*, vol. 446, pp. 60–63, 3 2007.

[21] A. Ravi, M. K. P. Kumar, M. Y. Rekha, M. S. Santosh, and C. Srivastava, "Graphene based nanocomposites: Synthesis, properties and application as electrochemical sensors," *Comprehensive Analytical Chemistry*, vol. 91, pp. 1–20, 1 2020.

[22] F. Banhart, J. Kotakoski, and A. V. Krasheninnikov, "Structural defects in graphene," *ACS Nano*, vol. 5, pp. 26–41, 1 2011.

[23] F. Farjadian, S. Abbaspour, M. A. A. Sadatlu, S. Mirkiani, A. Ghasemi, M. Hoseini-Ghahfarokhi, N. Mozaffari, M. Karimi, and M. R. Hamblin, "Recent developments in graphene and graphene oxide: Properties, synthesis, and modifications: A review," *ChemistrySelect*, vol. 5, pp. 10200–10219, 9 2020.

[24] C. Lee, X. Wei, J. W. Kysar, and J. Hone, "Measurement of the elastic properties and intrinsic strength of monolayer graphene," *Science*, vol. 321, pp. 385–388, 7 2008.

[25] K. I. Bolotin, K. J. Sikes, Z. Jiang, M. Klima, G. Fudenberg, J. Hone, P. Kim, and H. L. Stormer, "Ultrahigh electron mobility in suspended graphene," *Solid State Communications*, vol. 146, pp. 351–355, 6 2008.

[26] P. N. Nirmalraj, T. Lutz, S. Kumar, G. S. Duesberg, and J. J. Boland, "Nanoscale mapping of electrical resistivity and connectivity in graphene strips and networks," *Nano Letters*, vol. 11, pp. 16–22, 1 2011.

[27] L. Chen, P. Cheng, K. Wu, E. Y. Andrei, G. Li, X. Du, N. García, P. Esquinazi, J. Barzola-Quiquia, and S. Dusari, "Evidence for semiconducting behavior with a narrow band gap of bernal graphite," *New Journal of Physics*, vol. 14, p. 053015, 5 2012.

[28] M. Cermak, N. Perez, M. Collins, and M. Bahrami, "Material properties and structure of natural graphite sheet," *Scientific Reports 2020 10:1*, vol. 10, pp. 1–12, 10 2020.

[29] S. Zhang, H. Wang, J. Liu, and C. Bao, "Measuring the specific surface area of monolayer graphene oxide in water," *Materials Letters*, vol. 261, p. 127098, 2 2020.

[30] X. Tang, M. Debliquy, D. Lahem, Y. Yan, and J. P. Raskin, "A review on functionalized graphene sensors for detection of ammonia," *Sensors 2021, Vol. 21, Page 1443*, vol. 21, p. 1443, 2 2021.

[31] A. Ilnicka and J. P. Lukaszewicz, "Graphene-based hydrogen gas sensors: A review," *Processes 2020, Vol. 8, Page 633*, vol. 8, p. 633, 5 2020.

[32] M. Carbone, L. Gorton, and R. Antiochia, "An overview of the latest graphene-based sensors for glucose detection: the effects of graphene defects," *Electroanalysis*, vol. 27, pp. 16–31, 1 2015.

[33] J. Chang, G. Zhou, E. R. Christensen, R. Heideman, and J. Chen, "Graphene-based sensors for detection of heavy metals in water: A review," *Analytical and Bioanalytical Chemistry*, vol. 406, pp. 3957–3975, 4 2014.

[34] R. F. Frindt, "Crystals of $MoS_2$ several molecular layers thick," *J. Appl. Phys*, vol. 37, pp. 1928–1929, 1966.

[35] S. A. Han, R. Bhatia, and S. W. Kim, "Synthesis, properties and potential applications of two-dimensional transition metal dichalcogenides," *Nano Convergence*, vol. 2, pp. 1–14, 12 2015.

[36] B. Radisavljevic, A. Radenovic, J. Brivio, V. Giacometti, and A. Kis, "Single-layer $MoS_2$ transistors," *Nature nanotechnology*, vol. 6, no. 3, pp. 147–150, 2011.

[37] C. J. Shearer, A. D. Slattery, A. J. Stapleton, J. G. Shapter, and C. T. Gibson, "Accurate thickness measurement of graphene," *Nanotechnology*, vol. 27, p. 125704, 2 2016.

[38] S. Manzeli, D. Ovchinnikov, D. Pasquier, O. V. Yazyev, and A. Kis, "2D transition metal dichalcogenides," *Nature Reviews Materials 2017 2:8*, vol. 2, pp. 1–15, 6 2017.

[39] M. Acerce, D. Voiry, and M. Chhowalla, "Metallic 1T phase $MoS_2$ nanosheets as supercapacitor electrode materials," *Nature Nanotechnology 2015 10:4*, vol. 10, pp. 313–318, 3 2015.

[40] S. A. Han, R. Bhatia, and S. W. Kim, "Synthesis, properties and potential applications of two-dimensional transition metal dichalcogenides," *Nano Convergence*, vol. 2, pp. 1–14, 12 2015.

[41] A. Coogan and Y. K. Gun'ko, "Solution-based "bottom-up" synthesis of group vi transition metal dichalcogenides and their applications," *Cite this: Mater. Adv*, vol. 2, p. 146, 2021.

[42] M. Chhowalla, H. S. Shin, G. Eda, L. J. Li, K. P. Loh, and H. Zhang, "The chemistry of two-dimensional layered transition metal dichalcogenide nanosheets," *Nature Chemistry 2013 5:4*, vol. 5, pp. 263–275, 3 2013.

[43] J. Kang, S. Tongay, J. Zhou, J. Li, and J. Wu, "Band offsets and heterostructures of two-dimensional semiconductors," *Applied Physics Letters*, vol. 102, 1 2013.

[44] J. A. Wilson and A. D. Yoffe, "The transition metal dichalcogenides discussion and interpretation of the observed optical, electrical and structural properties," *Advances in Physics*, vol. 18, pp. 193–335, 1969.

[45] A. Splendiani, L. Sun, Y. Zhang, T. Li, J. Kim, C. Y. Chim, G. Galli, and F. Wang, "Emerging photoluminescence in monolayer $MoS_2$," *Nano Letters*, vol. 10, pp. 1271–1275, 4 2010.

[46] A. Kuc, N. Zibouche, and T. Heine, "Influence of quantum confinement on the electronic structure of the transition metal sulfide $TiS_2$," *Physical Review B - Condensed Matter and Materials Physics*, vol. 83, p. 245213, 6 2011.

[47] A. Splendiani, L. Sun, Y. Zhang, T. Li, J. Kim, C. Y. Chim, G. Galli, and F. Wang, "Emerging photoluminescence in monolayer $MoS_2$," *Nano Letters*, vol. 10, pp. 1271–1275, 4 2010.

[48] J. Hong, Z. Hu, M. Probert, K. Li, D. Lv, X. Yang, L. Gu, N. Mao, Q. Feng, L. Xie, J. Zhang, D. Wu, Z. Zhang, C. Jin, W. Ji, X. Zhang, J. Yuan, and Z. Zhang, "Exploring atomic defects in molybdenum disulphide monolayers," *Nature Communications 2015 6:1*, vol. 6, pp. 1–8, 2 2015.

[49] R. Addou, S. McDonnell, D. Barrera, Z. Guo, A. Azcatl, J. Wang, H. Zhu, C. L. Hinkle, M. Quevedo-Lopez, H. N. Alshareef, L. Colombo, J. W. Hsu, and R. M. Wallace, "Impurities and electronic property variations of natural $MoS_2$ crystal surfaces," *ACS Nano*, vol. 9, pp. 9124–9133, 9 2015.

[50] Y. Park, N. Li, D. Jung, L. T. Singh, J. Baik, E. Lee, D. Oh, Y. D. Kim, J. Y. Lee, J. Woo, S. Park, H. Kim, G. Lee, G. Lee, and C. C. Hwang, "Unveiling the origin of n-type doping of natural $MoS_2$: carbon," *npj 2D Materials and Applications 2023 7:1*, vol. 7, pp. 1–7, 9 2023.

[51] H. P. Komsa and A. V. Krasheninnikov, "Native defects in bulk and monolayer $MoS_2$ from first principles," *Physical Review B - Condensed Matter and Materials Physics*, vol. 91, p. 125304, 3 2015.

[52] T. Zhang, K. Fujisawa, F. Zhang, M. Liu, M. C. Lucking, R. N. Gontijo, Y. Lei, H. Liu, K. Crust, T. Granzier-Nakajima, H. Terrones, A. L. Elías, and M. Terrones, "Universal in situ substitutional doping of transition metal dichalcogenides by liquid-phase precursor-assisted synthesis," *ACS Nano*, vol. 14, pp. 4326–4335, 4 2020.

[53] R. A. Wells, N. J. Diercks, V. Boureau, Z. Wang, Y. Zhao, S. Nussbaum, M. Esteve, M. Caretti, H. Johnson, A. Kis, and K. Sivula, "Composition-tunable transition metal dichalcogenide nanosheets via a scalable, solution-processable method," *Nanoscale Horizons*, 2024.

[54] M. W. Lin, I. I. Kravchenko, J. Fowlkes, X. Li, A. A. Puretzky, C. M. Rouleau, D. B. Geohegan, and K. Xiao, "Thickness-dependent charge transport in few-layer $MoS_2$ field-effect transistors," *Nanotechnology*, vol. 27, p. 165203, 3 2016.

[55] A. Rai, H. C. Movva, A. Roy, D. Taneja, S. Chowdhury, and S. K. Banerjee, "Progress in contact, doping and mobility engineering of $MoS_2$: An atomically thin 2D semiconductor," *Crystals 2018, Vol. 8, Page 316*, vol. 8, p. 316, 8 2018.

[56] X. Cui, G. H. Lee, Y. D. Kim, G. Arefe, P. Y. Huang, C. H. Lee, D. A. Chenet, X. Zhang, L. Wang, F. Ye, F. Pizzocchero, B. S. Jessen, K. Watanabe, T. Taniguchi, D. A. Muller, T. Low, P. Kim, and J. Hone, "Multi-terminal transport measurements of $MoS_2$ using a van der Waals heterostructure device platform," *Nature Nanotechnology 2015 10:6*, vol. 10, pp. 534–540, 4 2015.

[57] F. Bonaccorso, A. Bartolotta, J. N. Coleman, and C. Backes, "2D-crystal-based functional inks," *Advanced Materials*, vol. 28, pp. 6136–6166, 8 2016.

[58] M. Yi and Z. Shen, "A review on mechanical exfoliation for the scalable production of graphene," *Journal of Materials Chemistry A*, vol. 3, pp. 11700–11715, 5 2015.

[59] K. S. Novoselov, V. I. Fal'Ko, L. Colombo, P. R. Gellert, M. G. Schwab, and K. Kim, "A roadmap for graphene," *Nature 2012 490:7419*, vol. 490, pp. 192–200, 10 2012.

[60] J. H. Lee, S. J. Park, and J. W. Choi, "Electrical property of graphene and its application to electrochemical biosensing," *Nanomaterials 2019, Vol. 9, Page 297*, vol. 9, p. 297, 2 2019.

[61] P. C. Shen, Y. Lin, H. Wang, J. H. Park, W. S. Leong, A. Y. Lu, T. Palacios, and J. Kong, "CVD technology for 2-D materials," *IEEE Transactions on Electron Devices*, vol. 65, pp. 4040–4052, 10 2018.

[62] N. Briggs, S. Subramanian, Z. Lin, X. Li, X. Zhang, K. Zhang, K. Xiao, D. Geohegan, R. Wallace, L. Q. Chen, M. Terrones, A. Ebrahimi, S. Das, J. Redwing, C. Hinkle, K. Momeni, A. V. Duin, V. Crespi, S. Kar, and J. A. Robinson, "A roadmap for electronic grade 2D materials," *2D Materials*, vol. 6, p. 022001, 1 2019.

[63] Y. Zhan, Z. Liu, S. Najmaei, P. M. Ajayan, and J. Lou, "Large-area vapor-phase growth and characterization of $MoS_2$ atomic layers on a sio2 substrate," *Small*, vol. 8, pp. 966–971, 4 2012.

[64] K. Kang, S. Xie, L. Huang, Y. Han, P. Y. Huang, K. F. Mak, C. J. Kim, D. Muller, and J. Park, "High-mobility three-atom-thick semiconducting films with wafer-scale homogeneity," *Nature 2015 520:7549*, vol. 520, pp. 656–660, 4 2015.

[65] T. Liang, M. R. Habib, H. Xiao, S. Xie, Y. Kong, C. Yu, H. Iwai, D. Fujita, N. Hanagata, H. Chen, Z. Feng, and M. Xu, "Intrinsically substitutional carbon doping in CVD-grown monolayer $MoS_2$ and the band structure modulation," *ACS Applied Electronic Materials*, vol. 2, pp. 1055–1064, 4 2020.

[66] D. Ghoshal, R. Kumar, and N. Koratkar, "Controlled Re doping in $MoS_2$ by chemical vapor deposition," *Inorganic Chemistry Communications*, vol. 123, p. 108329, 1 2021.

[67] Y. Yang, H. Pu, J. Di, Y. Zang, S. Zhang, and C. Chen, "Synthesis and characterization of monolayer Er-doped $MoS_2$ films by chemical vapor deposition," *Scripta Materialia*, vol. 152, pp. 64–68, 7 2018.

[68] M. R. Laskar, D. N. Nath, L. Ma, E. W. Lee, C. H. Lee, T. Kent, Z. Yang, R. Mishra, M. A. Roldan, J. C. Idrobo, S. T. Pantelides, S. J. Pennycook, R. C. Myers, Y. Wu, and S. Rajan, "P-type doping of $MoS_2$ thin films using Nb," *Applied Physics Letters*, vol. 104, 3 2014.

[69] O. C. Compton and S. T. Nguyen, "Graphene oxide, highly reduced graphene oxide, and graphene: Versatile building blocks for carbon-based materials," *Small*, vol. 6, pp. 711–723, 3 2010.

[70] M. Naguib, V. N. Mochalin, M. W. Barsoum, and Y. Gogotsi, "25th anniversary article: Mxenes: A new family of two-dimensional materials," *Advanced Materials*, vol. 26, pp. 992–1005, 2 2014.

[71] J. H. Zhan, Z. D. Zhang, X. F. Qian, C. Wang, Y. Xie, and Y. T. Qian, "Solvothermal synthesis of nanocrystalline $MoS_2$ from $MoO_3$ and elemental sulfur," *Journal of Solid State Chemistry*, vol. 141, pp. 270–273, 11 1998.

[72] P. Zhou, I. Tanghe, P. Schiettecatte, D. V. Thourhout, Z. Hens, and P. Geiregat, "Ultrafast carrier dynamics in colloidal $WS_2$ nanosheets obtained through a hot injection synthesis," *Journal of Chemical Physics*, vol. 151, p. 164701, 10 2019.

[73] R. Mastria, R. Scarfiello, D. Altamura, C. Giannini, A. Liscio, A. Kovtun, G. V. Bianco, G. Bruno, V. Grillo, A. H. Tavabi, R. E. Dunin-Borkowski, C. Nobile, A. Cola, P. D. Cozzoli, S. Gambino, and A. Rizzo, "In-plane aligned colloidal 2D $WS_2$ nanoflakes for solution-processable thin films with high planar conductivity," *Scientific Reports 2019 9:1*, vol. 9, pp. 1–13, 6 2019.

[74] Q. Yu and Y. Yang, "Synthesis of two-dimensional metallic nanosheets: From elemental metals to chemically complex alloys," *ChemNanoMat*, vol. 6, pp. 1683–1711, 12 2020.

[75] R. K. Sharma, S. Yadav, S. Dutta, H. B. Kale, I. R. Warkad, R. Zboril, R. S. Varma, and M. B. Gawande, "Silver nanomaterials: synthesis and (electro/photo) catalytic applications," *Chemical Society Reviews*, vol. 50, pp. 11293–11380, 10 2021.

[76] L. Scarabelli, M. Sun, X. Zhuo, S. Yoo, J. E. Millstone, M. R. Jones, and L. M. Liz-Marzán, "Plate-like colloidal metal nanoparticles," *Chemical Reviews*, vol. 123, pp. 3493–3542, 4 2023.

[77] F. Cheng, J. W. Betts, S. M. Kelly, and A. L. Hector, "Green synthesis of highly concentrated aqueous colloidal solutions of large starch-stabilised silver nanoplatelets," *Materials Science and Engineering: C*, vol. 46, pp. 530–537, 1 2015.

[78] J. Jain, S. Arora, J. M. Rajwade, P. Omray, S. Khandelwal, and K. M. Paknikar, "Silver nanoparticles in therapeutics: Development of an antimicrobial gel formulation for topical use," *Molecular Pharmaceutics*, vol. 6, pp. 1388–1401, 10 2009.

[79] A. G. Kelly, J. O'reilly, C. Gabbett, B. Szydłowska, D. O'suilleabhain, U. Khan, J. Maughan, T. Carey, S. Sheil, P. Stamenov, J. N. Coleman, A. G. Kelly, J. O'reilly, C. Gabbett, B. Szydłowska, J. Maughan, T. Carey, S. Sheil, P. Stamenov, J. N. Coleman, and U. Khan, "Highly conductive networks of silver nanosheets," *Small*, vol. 18, p. 2105996, 4 2022.

[80] A. G. Kelly, S. Sheil, D. A. Douglas-Henry, E. Caffrey, C. Gabbett, L. Doolan, V. Nicolosi, and J. N. Coleman, "Transparent conductors printed from grids of highly conductive silver nanosheets," *ACS Applied Materials & Interfaces*, vol. 15, no. 33, pp. 39864–39871, 2023.

[81] Y. Hernandez, V. Nicolosi, M. Lotya, F. M. Blighe, Z. Sun, S. De, I. T. McGovern, B. Holland, M. Byrne, Y. K. Gun'ko, J. J. Boland, P. Niraj, G. Duesberg, S. Krishnamurthy, R. Goodhue, J. Hutchison, V. Scardaci, A. C. Ferrari, and J. N. Coleman, "High-yield production of graphene by liquid-phase exfoliation of graphite," *Nature Nanotechnology 2008 3:9*, vol. 3, pp. 563–568, 8 2008.

[82] A. G. Kelly, D. O'suilleabhain, C. Gabbett, and J. N. Coleman, "The electrical conductivity of solution-processed nanosheet networks," *Nature reviews materials*, 2021.

[83] Z. Li, R. J. Young, C. Backes, W. Zhao, X. Zhang, A. A. Zhukov, E. Tillotson, A. P. Conlan, F. Ding, S. J. Haigh, K. S. Novoselov, and J. N. Coleman, "Mechanisms of liquid-phase exfoliation for the production of graphene," *ACS Nano*, vol. 14, pp. 10976–10985, 9 2020.

[84] Y. No and Y. Son, "Effects of probe position of 20 khz sonicator on sonochemical oxidation activity," *Japanese Journal of Applied Physics*, vol. 58, p. SGGD02, 5 2019.

[85] H. Tao, Y. Zhang, Y. Gao, Z. Sun, C. Yan, and J. Texter, "Scalable exfoliation and dispersion of two-dimensional materials – an update," *Physical Chemistry Chemical Physics*, vol. 19, pp. 921–960, 1 2017.

[86] C. Backes, D. Campi, B. M. Szydlowska, K. Synnatschke, E. Ojala, F. Rashvand, A. Harvey, A. Griffin, Z. Sofer, N. Marzari, J. N. Coleman, and D. D. O'Regan, "Equipartition of energy defines the size-thickness relationship in liquid-exfoliated nanosheets," *ACS Nano*, 2019.

[87] K. Synnatschke, N. M. Badlyan, A. Wrzesińska, G. L. Onrubia, A.-L. Hansen, S. Wolff, H. Tornatzky, W. Bensch, Y. Vaynzof, J. Maultzsch, *et al.*, "Sonication-assisted liquid phase exfoliation of two-dimensional $CrTe_3$ under inert conditions," *Ultrasonics Sonochemistry*, vol. 98, p. 106528, 2023.

[88] R. Tian, J. N. Coleman, H. Kaur, A. Roy, M. McCrystall, D. V. Horvath, G. L. Onrubia, R. Smith, M. Ruether, A. Griffin, C. Backes, and V. Nicolosi, "Production of quasi-2D platelets of nonlayered iron pyrite ($FeS_2$) by liquid-phase exfoliation for high performance battery electrodes," *ACS Nano*, vol. 14, pp. 13418–13432, 10 2020.

[89] H. Kaur, J. N. Coleman, H. Kaur, and J. N. Coleman, "Liquid-phase exfoliation of nonlayered non-van-der-waals crystals into nanoplatelets," *Advanced Materials*, vol. 34, p. 2202164, 9 2022.

[90] F. Zhang, L. She, C. Jia, X. He, Q. Li, J. Sun, Z. Lei, and Z. H. Liu, "Few-layer and large flake size borophene: preparation with solvothermal-assisted liquid phase exfoliation," *RSC Advances*, vol. 10, pp. 27532–27537, 7 2020.

[91] J.-Y. Chung, Y. Yuan, T. P. Mishra, C. Joseph, P. Canepa, P. Ranjan, E. H. S. Sadki, S. Gradečak, and S. Garaj, "Structure and exfoliation mechanism of two-dimensional boron nanosheets," *Nature Communications*, vol. 15, no. 1, p. 6122, 2024.

[92] K. R. Paton, E. Varrla, C. Backes, R. J. Smith, U. Khan, A. O'Neill, C. Boland, M. Lotya, O. M. Istrate, P. King, T. Higgins, S. Barwich, P. May, P. Puczkarski, I. Ahmed, M. Moebius, H. Pettersson, E. Long, J. Coelho, S. E. O'Brien, E. K. McGuire, B. M. Sanchez, G. S. Duesberg, N. McEvoy, T. J. Pennycook, C. Downing, A. Crossley, V. Nicolosi, and J. N. Coleman, "Scalable production of large quantities of defect-free few-layer graphene by shear exfoliation in liquids," *Nature Materials 2014 13:6*, vol. 13, pp. 624–630, 4 2014.

[93] M. J. Large, S. P. Ogilvie, A. A. Graf, P. J. Lynch, M. A. O'Mara, T. Waters, I. Jurewicz, J. P. Salvage, and A. B. Dalton, "Large-scale surfactant exfoliation of graphene and conductivity-optimized graphite enabling wireless connectivity," *Advanced Materials Technologies*, vol. 5, p. 2000284, 7 2020.

[94] W. Zhao, M. Fang, F. Wu, H. Wu, L. Wang, and G. Chen, "Preparation of graphene by exfoliation of graphite using wet ball milling," *Journal of Materials Chemistry*, vol. 20, pp. 5817–5819, 7 2010.

[95] T. Carey, A. Alhourani, R. Tian, S. Seyedin, A. Arbab, J. Maughan, L. Šiller, D. Horvath, A. Kelly, H. Kaur, E. Caffrey, J. M. Kim, H. R. Hagland, and J. N. Coleman, "Cyclic production of biocompatible few-layer graphene ink with in-line shear-mixing for inkjet-printed electrodes and li-ion energy storage," *npj 2D Materials and Applications 2022 6:1*, vol. 6, pp. 1–11, 1 2022.

[96] P. Joensen, R. F. Frindt, and S. R. Morrison, "Single-layer $MoS_2$," *Materials Research Bulletin*, vol. 21, pp. 457–461, 4 1986.

[97] M. Zhao, C. Casiraghi, and K. Parvez, "Electrochemical exfoliation of 2D materials beyond graphene," *Chemical Society Reviews*, 2024.

[98] Y. Zhang, Y. Xu, R. Liu, and Y. Niu, "Synthesis of high-quality graphene by electrochemical anodic and cathodic co-exfoliation method," *Chemical Engineering Journal*, vol. 461, p. 141985, 4 2023.

[99] N. Imanishi, M. Toyoda, Y. Takeda, and O. Yamamoto, "Study on lithium intercalation into $MoS_2$," *Solid State Ionics*, vol. 58, no. 3-4, pp. 333–338, 1992.

[100] Z. Lin, Y. Liu, U. Halim, M. Ding, Y. Liu, Y. Wang, C. Jia, P. Chen, X. Duan, C. Wang, *et al.*, "Solution-processable 2D semiconductors for high-performance large-area electronics," *Nature*, vol. 562, no. 7726, pp. 254–258, 2018.

[101] O. Song, D. Rhee, J. Kim, Y. Jeon, V. Mazánek, A. Söll, Y. A. Kwon, J. H. Cho, Y.-H. Kim, Z. Sofer, *et al.*, "All inkjet-printed electronics based on electrochemically exfoliated two-dimensional metal, semiconductor, and dielectric," *npj 2D Materials and Applications*, vol. 6, no. 1, p. 64, 2022.

[102] R. A. Wells, M. Zhang, T. H. Chen, V. Boureau, M. Caretti, Y. Liu, J. H. Yum, H. Johnson, S. Kinge, A. Radenovic, and K. Sivula, "High performance semiconducting nanosheets via a scalable powder-based electrochemical exfoliation technique," *ACS Nano*, vol. 16, pp. 5719–5730, 4 2022.

[103] N. D. Wilson, M. Ozhukil Valappil, B. Y. Martin, T. Siu, J. Pennings, M. Mackintosh, M. N. Almadhoun, J. Ouyang, N. Graddage, and M. A. Pope, "Toward scalable electrochemical exfoliation of molybdenum disulfide powder through an accessible electrode design," *Small Methods*, p. 2400298, 2024.

[104] J. Munuera, J. Paredes, S. Villar-Rodil, M. Ayán-Varela, A. Pagán, S. Aznar-Cervantes, J. Cenis, A. Martínez-Alonso, and J. Tascón, "High quality, low oxygen content and biocompatible graphene nanosheets obtained by anodic exfoliation of different graphite types," *Carbon*, vol. 94, pp. 729–739, 2015.

[105] T. Carey, O. Cassidy, K. Synnatschke, E. Caffrey, J. Garcia, S. Liu, H. Kaur, A. G. Kelly, J. Munuera, C. Gabbett, *et al.*, "High-mobility flexible transistors with low-temperature solution-processed tungsten dichalcogenides," *ACS nano*, vol. 17, no. 3, pp. 2912–2922, 2023.

[106] T. Carey, J. Maughan, L. Doolan, E. Caffrey, J. Garcia, S. Liu, H. Kaur, C. Ilhan, S. Seyedin, and J. N. Coleman, "Knot architecture for biocompatible and semiconducting 2D electronic fiber transistors," *Small Methods*, p. 2301654, 2024.

[107] J. Neilson, M. P. Avery, and B. Derby, "Tiled monolayer films of 2D molybdenum disulfide nanoflakes assembled at liquid/liquid interfaces," *ACS applied materials & interfaces*, vol. 12, no. 22, pp. 25125–25134, 2020.

[108] Y. A. Kwon, J. Kim, S. B. Jo, D. G. Roe, D. Rhee, Y. Song, B. Kang, D. Kim, J. Kim, D. W. Kim, *et al.*, "Wafer-scale transistor arrays fabricated using slot-die printing of molybdenum disulfide and sodium-embedded alumina," *Nature Electronics*, vol. 6, no. 6, pp. 443–450, 2023.

[109] K. Parvez, R. Worsley, A. Alieva, A. Felten, and C. Casiraghi, "Water-based and inkjet printable inks made by electrochemically exfoliated graphene," *Carbon*, vol. 149, pp. 213–221, 2019.

[110] R. Safitri, A. Suriani, Y. Htwe, W. Dwandaru, V. V. Kumar, K. Ali, M. Othman, S. Alluqmani, M. Azlan, M. Mamat, *et al.*, "Recent development of electrochemically exfoliated graphene and its hybrid conductive inks for printed electronics applications," *Synthetic Metals*, p. 117707, 2024.

[111] Y. Hernandez, M. Lotya, D. Rickard, S. D. Bergin, and J. N. Coleman, "Measurement of multicomponent solubility parameters for graphene facilitates solvent discovery," *Langmuir*, vol. 26, pp. 3208–3213, 3 2010.

[112] J. Fernandes, S. S. Nemala, G. D. Bellis, and A. Capasso, "Green solvents for the liquid phase exfoliation production of graphene: The promising case of cyrene," *Frontiers in Chemistry*, vol. 0, p. 311, 4 2022.

[113] J. Sherwood, M. D. bruyn, A. Constantinou, L. Moity, C. R. McElroy, T. J. Farmer, T. Duncan, W. Raverty, A. J. Hunt, and J. H. Clark, "Dihydrolevoglucosenone (cyrene) as a bio-based alternative for dipolar aprotic solvents," *Chemical Communications*, vol. 50, pp. 9650–9652, 7 2014.

[114] J. Adam, M. Singh, A. Abduvakhidov, M. R. D. Sorbo, C. Feoli, F. Hussain, J. Kaur, A. Mirabella, M. Rossi, A. Sasso, M. Valadan, M. Varra, G. Rusciano, and C. Altucci, "The effectiveness of cyrene as a solvent in exfoliating 2D tmds nanosheets," *International Journal of Molecular Sciences*, vol. 24, p. 10450, 7 2023.

[115] Z. S. Baird, P. Uusi-Kyyny, J. P. Pokki, E. Pedegert, and V. Alopaeus, "Vapor pressures, densities, and pc-saft parameters for 11 bio-compounds," *International Journal of Thermophysics*, vol. 40, pp. 1–36, 11 2019.

[116] W.-W. Liu, B.-Y. Xia, X.-X. Wang, and J.-N. Wang, "Exfoliation and dispersion of graphene in ethanol-water mixtures," *Frontiers of Materials Science*, vol. 6, pp. 176–182, 2012.

[117] A. G. Kelly, V. Vega-Mayoral, J. B. Boland, and J. N. Coleman, "Whiskey-phase exfoliation: exfoliation and printing of nanosheets using irish whiskey," *2D Materials*, vol. 6, p. 045036, 9 2019.

[118] S. Liu, E. X. Ding, A. G. Kelly, L. Doolan, C. Gabbett, H. Kaur, J. Munuera, T. Carey, J. Garcia, and J. N. Coleman, "Solution processed, vertically stacked hetero-structured diodes based on liquid-exfoliated $WS_2$ nanosheets: from electrode-limited to bulk-limited behavior," *Nanoscale*, vol. 14, pp. 15679–15690, 11 2022.

[119] M. J. Rosen and J. T. Kunjappu, *Surfactants and interfacial phenomena*. John Wiley & Sons, 2012.

[120] M. Lotya, Y. Hernandez, P. J. King, R. J. Smith, V. Nicolosi, L. S. Karlsson, F. M. Blighe, S. De, W. Zhiming, I. T. McGovern, G. S. Duesberg, and J. N. Coleman, "Liquid phase production of graphene by exfoliation of graphite in surfactant/water solutions," *Journal of the American Chemical Society*, vol. 131, pp. 3611–3620, 3 2009.

[121] B. Derjaguin and L. Landau, "Theory of the stability of strongly charged lyophobic sols and of the adhesion of strongly charged particles in solutions of electrolytes," *Progress in Surface Science*, vol. 43, pp. 30–59, 5 1993.

[122] E. J. W. Verwey, "Theory of the stability of lyophobic colloids," *The Journal of Physical Chemistry*, vol. 09, p. 36, 1947.

[123] R. J. Smith, M. Lotya, and J. N. Coleman, "The importance of repulsive potential barriers for the dispersion of graphene using surfactants," *New Journal of Physics*, vol. 12, p. 125008, 12 2010.

[124] A. Griffin, K. Nisi, J. Pepper, A. Harvey, B. M. Szydłowska, J. N. Coleman, and C. Backes, "Effect of surfactant choice and concentration on the dimensions and yield of liquid-phase-exfoliated nanosheets," *Chemistry of Materials*, vol. 32, pp. 2852–2862, 4 2020.

[125] Z. Gholamvand, D. McAteer, A. Harvey, C. Backes, and J. N. Coleman, "Electrochemical applications of two-dimensional nanosheets: The effect of nanosheet length and thickness," *Chemistry of Materials*, vol. 28, pp. 2641–2651, 5 2016.

[126] K. Clifford, S. P. Ogilvie, A. A. Graf, H. J. Wood, A. C. Sehnal, J. P. Salvage, P. J. Lynch, M. J. Large, and A. B. Dalton, "Emergent high conductivity in size-selected graphene networks," *Carbon*, vol. 218, p. 118642, 1 2024.

[127] P. Li, A. Kumar, J. Ma, Y. Kuang, L. Luo, and X. Sun, "Density gradient ultracentrifugation for colloidal nanostructures separation and investigation," *Science Bulletin*, vol. 63, pp. 645–662, 5 2018.

[128] M. S. Arnold, S. I. Stupp, and M. C. Hersam, "Enrichment of single-walled carbon nanotubes by diameter in density gradients," *Nano Letters*, vol. 5, pp. 713–718, 4 2005.

[129] A. A. Green and M. C. Hersam, "Solution phase production of graphene with controlled thickness via density differentiation," *Nano Letters*, vol. 9, pp. 4031–4036, 12 2009.

[130] C. Backes, B. M. Szydłowska, A. Harvey, S. Yuan, V. Vega-Mayoral, B. R. Davies, P. L. Zhao, D. Hanlon, E. J. Santos, M. I. Katsnelson, W. J. Blau, C. Gadermaier, and J. N. Coleman, "Production of highly monolayer enriched dispersions of liquid-exfoliated nanosheets by liquid cascade centrifugation," *ACS Nano*, vol. 10, pp. 1589–1601, 1 2016.

[131] S. P. Ogilvie, M. J. Large, M. A. O'Mara, P. J. Lynch, C. L. Lee, A. A. King, C. Backes, and A. B. Dalton, "Size selection of liquid-exfoliated 2D nanosheets," *2D Materials*, vol. 6, p. 031002, 4 2019.

[132] H. Chacham, J. C. Santos, F. G. Pacheco, D. L. Silva, R. M. Martins, J. P. Del'boccio, E. M. Soares, R. Altoé, C. A. Furtado, F. Plentz, B. R. Neves, and L. G. Cançado, "Controlling the morphology of nanoflakes obtained by liquid-phase exfoliation: Implications for the mass production of 2D materials," *ACS Applied Nano Materials*, vol. 3, pp. 12095–12105, 12 2020.

[133] H. Yang, Y. Hernandez, A. Schlierf, A. Felten, A. Eckmann, S. Johal, P. Louette, J.-J. Pireaux, X. Feng, K. Mullen, *et al.*, "A simple method for graphene production based on exfoliation of graphite in water using 1-pyrenesulfonic acid sodium salt," *Carbon*, vol. 53, pp. 357–365, 2013.

[134] J. R. Downing, S. Diaz-Arauzo, L. E. Chaney, D. Tsai, J. Hui, J. W. T. Seo, D. R. Cohen, M. Dango, J. Zhang, N. X. Williams, J. H. Qian, J. B. Dunn, and M. C. Hersam, "Centrifuge-free separation of solution-exfoliated 2D nanosheets via cross-flow filtration," *Advanced Materials*, vol. 35, pp. 1–13, 2023.

[135] Y. Li, Y. Liu, S. R. A. Bhuiyan, Y. Zhu, and S. Yao, "Printed strain sensors for on-skin electronics," *Small Structures*, vol. 3, p. 2100131, 2 2022.

[136] M. Burton, G. Howells, J. Atoyo, M. Carnie, M. Burton, M. Carnie, G. Howells, and J. Atoyo, "Printed thermoelectrics," *Advanced Materials*, vol. 34, p. 2108183, 5 2022.

[137] J. P. Mensing, T. Lomas, and A. Tuantranont, "2D and 3D printing for graphene based supercapacitors and batteries: A review," *Sustainable Materials and Technologies*, vol. 25, p. e00190, 9 2020.

[138] S. Conti, G. Calabrese, K. Parvez, L. Pimpolari, F. Pieri, G. Iannaccone, C. Casiraghi, and G. Fiori, "Printed transistors made of 2D material-based inks," *Nature Reviews Materials*, vol. 8, no. 10, pp. 651–667, 2023.

[139] Y. Nalawade, J. Pepper, A. Harvey, A. Griffin, D. Caffrey, A. G. Kelly, and J. N. Coleman, "All-printed dielectric capacitors from high-permittivity, liquid-exfoliated biocl nanosheets," *ACS Applied Electronic Materials*, vol. 2, pp. 3233–3241, 10 2020.

[140] X. Chen, X. Wang, Y. Pang, G. Bao, J. Jiang, P. Yang, Y. Chen, T. Rao, and W. Liao, "Printed electronics based on 2D material inks: Preparation, properties, and applications toward memristors," *Small Methods*, vol. 7, pp. 1–21, 2023.

[141] M. A. Soltan, *An investigation into the history of the airbrush and the impact of the conservation treatment of airbrushed canvas paintings*. PhD thesis, The university of Northumbria, 2015.

[142] L. Nayak, S. Mohanty, S. K. Nayak, and A. Ramadoss, "A review on inkjet printing of nanoparticle inks for flexible electronics," *Journal of Materials Chemistry C*, vol. 7, pp. 8771–8795, 7 2019.

[143] T. Carey, C. Jones, F. L. Moal, D. Deganello, and F. Torrisi, "Spray-coating thin films on three-dimensional surfaces for a semitransparent capacitive-touch device," *ACS Applied Materials and Interfaces*, vol. 10, pp. 19948–19956, 6 2018.

[144] Y. Zheng, S. Li, W. Shi, and J. Yu, "Spray-coated nanoscale conductive patterns based on in situ sintered silver nanoparticle inks," *Nanoscale Research Letters*, vol. 9, pp. 1–7, 12 2014.

[145] N. Ferrer-Anglada, M. Kaempgen, V. Skákalová, U. Dettlaf-Weglikowska, and S. Roth, "Synthesis and characterization of carbon nanotube-conducting polymer thin films," *Diamond and Related Materials*, vol. 13, pp. 256–260, 2 2004.

[146] V. Scardaci, R. Coull, P. E. Lyons, D. Rickard, J. N. Coleman, V. Scardaci, P. E. Lyons, N. Coleman, and D. Rickard, "Spray deposition of highly transparent, low-resistance networks of silver nanowires over large areas," *Small*, vol. 7, pp. 2621–2628, 9 2011.

[147] Y. L. Dong and B. Pan, "A review of speckle pattern fabrication and assessment for digital image correlation," *Experimental Mechanics 2017 57:8*, vol. 57, pp. 1161–1181, 5 2017.

[148] C. Gabbett, *Electrical , Mechanical & Morphological Characterisation of Nanosheet Networks*. PhD thesis, Trinity College Dublin, 2021.

[149] H. Shi and C. Kleinstreuer, "Simulation and analysis of high-speed droplet spray dynamics," *Journal of Fluids Engineering*, vol. 129, pp. 621–633, 5 2007.

[150] X. Shen, C. M. Ho, and T. S. Wong, "Minimal size of coffee ring structure," *Journal of Physical Chemistry B*, vol. 114, pp. 5269–5274, 4 2010.

[151] S. Pinilla, J. Coelho, K. Li, J. Liu, and V. Nicolosi, "Two-dimensional material inks," *Nature Reviews Materials*, vol. 7, pp. 717–735, 2022.

[152] N. Wilkinson, M. Smith, R. W. Kay, and R. Harris, "A review of aerosol jet printing—a non-traditional hybrid process for micro-manufacturing," *The International Journal of Advanced Manufacturing Technology*, vol. 105, pp. 4599–4619, 2019.

[153] E. B. Secor, "Principles of aerosol jet printing," *Flexible and Printed Electronics*, vol. 3, no. 3, p. 035002, 2018.

[154] B. N. Smith, P. Ballentine, J. L. Doherty, R. Wence, H. A. Hobbie, N. X. Williams, and A. D. Franklin, "Aerosol jet printing conductive 3D microstructures from graphene without post-processing," *Small*, vol. 20, p. 2305170, 3 2024.

[155] M. Smith, Y. S. Choi, C. Boughey, and S. Kar-Narayan, "Controlling and assessing the quality of aerosol jet printed features for large area and flexible electronics," *Flexible and Printed Electronics*, vol. 2, p. 015004, 2 2017.

[156] S. Lu, B. N. Smith, H. Meikle, M. J. Therien, and A. D. Franklin, "All-carbon thin-film transistors using water-only printing," *Nano Letters*, vol. 23, pp. 2100–2106, 3 2023.

[157] Q. Huang and Y. Zhu, "Printing conductive nanomaterials for flexible and stretchable electronics: A review of materials, processes, and applications," *Advanced Materials Technologies*, vol. 4, p. 1800546, 5 2019.

[158] A. Mahajan, C. D. Frisbie, and L. F. Francis, "Optimization of aerosol jet printing for high-resolution, high-aspect ratio silver lines," *ACS applied materials & interfaces*, vol. 5, no. 11, pp. 4856–4864, 2013.

[159] W. D. Callister Jr and D. G. Rethwisch, *Callister's materials science and engineering*. John Wiley & Sons, 2020.

[160] I. S. Grant and W. R. Phillips, *Electromagnetism*. John Wiley & Sons, 2013.

[161] G. Reeves and H. Harrison, "Obtaining the specific contact resistance from transmission line model measurements," *IEEE Electron device letters*, vol. 3, no. 5, pp. 111–113, 1982.

[162] S. Conti, L. Pimpolari, G. Calabrese, R. Worsley, S. Majee, D. K. Polyushkin, M. Paur, S. Pace, D. H. Keum, F. Fabbri, G. Iannaccone, M. Macucci, C. Coletti, T. Mueller, C. Casiraghi, and G. Fiori, "Low-voltage 2D materials-based printed field-effect transistors for integrated digital and analog electronics on paper," *Nature Communications 2020 11:1*, vol. 11, pp. 1–9, 7 2020.

[163] S. M. Sze, *Semiconductor devices: physics and technology*. John Wiley & sons, 2008.

[164] A. Allain, J. Kang, K. Banerjee, and A. Kis, "Electrical contacts to two-dimensional semiconductors," *Nature Materials 2015 14:12*, vol. 14, pp. 1195–1205, 11 2015.

[165] "Transitor image." `https://electronics-bani.tistory.com/19`. Accessed: 15-07-2024.

[166] Q. Zhou, S. M. Koh, T. Thanigaivelan, T. Henry, and Y. C. Yeo, "Contact resistance reduction for strained n-mosfets with silicon-carbon source/drain utilizing aluminum ion implant and aluminum profile engineering," *IEEE Transactions on Electron Devices*, vol. 60, pp. 1310–1317, 2013.

[167] N. Pimparkar, Q. Cao, J. A. Rogers, and M. A. Alam, "Theory and practice of "striping" for improved on/off ratio in carbon nanonet thin film transistors," *Nano Research*, vol. 2, pp. 167–175, 3 2009.

[168] F. Torrisi, T. Hasan, W. Wu, Z. Sun, A. Lombardo, T. S. Kulmala, G. W. Hsieh, S. Jung, F. Bonaccorso, P. J. Paul, D. Chu, and A. C. Ferrari, "Inkjet-printed graphene electronics," *ACS Nano*, vol. 6, pp. 2992–3006, 4 2012.

[169] F. Torricelli, D. Z. Adrahtas, Z. Bao, M. Berggren, F. Biscarini, A. Bonfiglio, C. A. Bortolotti, C. D. Frisbie, E. Macchia, G. G. Malliaras, I. McCulloch, M. Moser, T. Q. Nguyen, R. M. Owens, A. Salleo, A. Spanu, and L. Torsi, "Electrolyte-gated transistors for enhanced performance bioelectronics," *Nature Reviews Methods Primers 2021 1:1*, vol. 1, pp. 1–24, 10 2021.

[170] A. G. Kelly, T. Hallam, C. Backes, A. Harvey, A. S. Esmaeily, I. Godwin, J. Coelho, V. Nicolosi, J. Lauth, A. Kulkarni, S. Kinge, L. D. Siebbeles, G. S. Duesberg, and J. N. Coleman, "All-printed thin-film transistors from networks of liquid-exfoliated nanosheets," *Science*, vol. 356, pp. 69–73, 4 2017.

[171] H. Jo, J. H. Choi, C. M. Hyun, S. Y. Seo, D. Y. Kim, C. M. Kim, M. J. Lee, J. D. Kwon, H. S. Moon, S. H. Kwon, and J. H. Ahn, "A hybrid gate dielectrics of ion gel with ultra-thin passivation layer for high-performance transistors based on two-dimensional semiconductor channels," *Scientific Reports 2017 7:1*, vol. 7, pp. 1–6, 10 2017.

[172] S. Wang, J. Zhang, O. Gharbi, V. Vivier, M. Gao, and M. E. Orazem, "Electrochemical impedance spectroscopy," *Nature Reviews Methods Primers 2021 1:1*, vol. 1, pp. 1–21, 6 2021.

[173] M. Gerstl, E. Navickas, G. Friedbacher, F. Kubel, M. Ahrens, and J. Fleig, "The separation of grain and grain boundary impedance in thin yttria stabilized zirconia (ysz) layers," *Solid State Ionics*, vol. 185, pp. 32–41, 3 2011.

[174] M. P. Garrett, I. N. Ivanov, R. A. Gerhardt, A. A. Puretzky, and D. B. Geohegan, "Separation of junction and bundle resistance in single wall carbon nanotube percolation networks by impedance spectroscopy," *Applied Physics Letters*, vol. 97, 10 2010.

[175] S. He, Y. Yuan, A. Nag, S. Feng, N. Afsarimanesh, T. Han, S. C. Mukhopadhyay, and D. R. Organ, "A review on the use of impedimetric sensors for the inspection of food quality," *International Journal of Environmental Research and Public Health 2020, Vol. 17, Page 5220*, vol. 17, p. 5220, 7 2020.

[176] D. C. Moore, A. Jawaid, R. Busch, M. Brothers, P. Miesle, A. Miesle, R. Rao, J. Lee, L. K. Beagle, M. Motala, S. G. Wallace, J. R. Downing, A. Roy, C. Muratore, M. C. Hersam, R. Vaia, S. Kim, N. R. Glavin, D. C. Moore, A. Jawaid, R. Busch, P. Miesle, A. Miesle, R. Rao, J. Lee, L. K. Beagle, M. Motala, A. Roy, R. Vaia, N. R. Glavin, M. Brothers, S. Kim, S. G. Wallace, J. R. Downing, M. C. Hersam, and C. Muratore, "Ultrasensitive molecular sensors based on real-time impedance spectroscopy in solution-processed 2D materials," *Advanced Functional Materials*, p. 2106830, 2021.

[177] E. Caffrey, J. R. Garcia, D. O'Suilleabhain, C. Gabbett, T. Carey, and J. N. Coleman, "Quantifying the piezoresistive mechanism in high-performance printed graphene strain sensors," *ACS Applied Materials & Interfaces*, p. acsami.1c21623, 1 2022.

[178] C. Kocabas, N. Pimparkar, O. Yesilyurt, S. J. Kang, M. A. Alam, and J. A. Rogers, "Experimental and theoretical studies of transport through large scale, partially aligned arrays of single-walled carbon nanotubes in thin film type transistors," *Nano Letters*, vol. 7, pp. 1195–1202, 5 2007.

[179] P. J. Flory, "Molecular size distribution in three dimensional polymers. i. gelation1," *Journal of the american chemical society*, vol. 63, no. 11, pp. 3083–3090, 1941.

[180] D. Stauffer and A. Aharony, *Introduction to percolation theory*. Taylor & Francis, 2018.

[181] P. M. Kogut and J. P. Straley, "Distribution-induced non-universality of the percolation conductivity exponents," *Journal of Physics C: Solid State Physics*, vol. 12, no. 11, p. 2151, 1979.

[182] E. S. Snow, J. P. Novak, P. M. Campbell, and D. Park, "Random networks of carbon nanotubes as an electronic material," *Applied Physics Letters*, vol. 82, pp. 2145–2147, 3 2003.

[183] Q. Cao, H. S. Kim, N. Pimparkar, J. P. Kulkarni, C. Wang, M. Shim, K. Roy, M. A. Alam, and J. A. Rogers, "Medium-scale carbon nanotube thin-film integrated circuits on flexible plastic substrates," *Nature 2008 454:7203*, vol. 454, pp. 495–500, 7 2008.

[184] S. Ippolito, F. Urban, W. Zheng, O. Mazzarisi, C. Valentini, A. G. Kelly, S. M. Gali, M. Bonn, D. Beljonne, F. Corberi, J. N. Coleman, H. I. Wang, and P. Samorì, "Unveiling charge-transport mechanisms in electronic devices based on defect-engineered $MoS_2$ covalent networks," *Advanced Materials*, vol. 35, 2023.

[185] E. Yakimchuk, R. Soots, I. Kotin, and I. Antonova, "2D printed graphene conductive layers with high carrier mobility," *Current Applied Physics*, vol. 17, pp. 1655–1661, 12 2017.

[186] S. Ippolito, A. G. Kelly, R. F. de Oliveira, M.-A. Stoeckel, D. Iglesias, A. Roy, C. Downing, Z. Bian, L. Lombardi, Y. A. Samad, V. Nicolosi, A. C. Ferrari, J. N. Coleman, and P. Samorì, "Covalently interconnected transition metal dichalcogenide networks via defect engineering for high-performance electronic devices," *Nature Nanotechnology*, pp. 1–7, 2 2021.

[187] K. Arapov, G. Bex, R. Hendriks, E. Rubingh, R. Abbel, G. de With, and H. Friedrich, "Conductivity enhancement of binder-based graphene inks by photonic annealing and subsequent compression rolling," *Advanced Engineering Materials*, vol. 18, pp. 1234–1239, 7 2016.

[188] K. Lee, B. M. Szydłowska, O. Hartwig, K. Synnatschke, B. Tywoniuk, T. Hartman, T. Tomašević-Ilić, C. P. Gabbett, J. N. Coleman, Z. Sofer, M. Spasenović, C. Backes, and G. S. Duesberg, "Highly conductive and long-term stable films from liquid-phase exfoliated platinum diselenide," *Journal of Materials Chemistry C*, vol. 11, pp. 593–599, 1 2023.

[189] A. Znidarsic, A. Kaskela, P. Laiho, M. Gaberscek, Y. Ohno, A. G. Nasibulin, E. I. Kauppinen, and A. Hassanien, "Spatially resolved transport properties of pristine and doped single-walled carbon nanotube networks," *Journal of Physical Chemistry C*, vol. 117, pp. 13324–13330, 6 2013.

[190] P. N. Nirmalraj, P. E. Lyons, S. De, J. N. Coleman, and J. J. Boland, "Electrical connectivity in single-walled carbon nanotube networks," *Nano Letters*, vol. 9, pp. 3890–3895, 12 2009.

[191] Z. Zhu, J. S. Kim, M. J. Moody, and L. J. Lauhon, "Edge and interface resistances create distinct trade-offs when optimizing the microstructure of printed van der Waals thin-film transistors," *ACS Nano*, vol. 17, pp. 575–586, 1 2022.

[192] E. Piatti, A. Arbab, F. Galanti, T. Carey, L. Anzi, D. Spurling, A. Roy, A. Zhussupbekova, K. A. Patel, J. M. Kim, D. Daghero, R. Sordan, V. Nicolosi, R. S. Gonnelli, and F. Torrisi, "Charge transport mechanisms in inkjet-printed thin-film transistors based on two-dimensional materials," *Nature Electronics 2021 4:12*, vol. 4, pp. 893–905, 12 2021.

[193] A. Kovtun, A. Candini, A. Vianelli, A. Boschi, S. Dell'Elce, M. Gobbi, K. H. Kim, S. L. Avila, P. Samorì, M. Affronte, A. Liscio, and V. Palermo, "Multiscale charge transport in van der Waals thin films: Reduced graphene oxide as a case study," *ACS Nano*, vol. 15, pp. 2654–2667, 2 2021.

[194] N. D. Cottam, F. Wang, J. S. Austin, C. J. Tuck, R. Hague, M. Fromhold, W. Escoffier, M. Goiran, M. Pierre, O. Makarovsky, L. Turyanska, N. D. Cottam, M. Fromhold, O. Makarovsky, F. Wang, J. S. Austin, C. J. Tuck, R. Hague, L. Turyanska, W. Escoffier, M. Goiran, and M. Pierre, "Quantum nature of charge transport in inkjet-printed graphene revealed in high magnetic fields up to 60 t," *Small*, p. 2311416, 2024.

[195] B. Radisavljevic and A. Kis, "Mobility engineering and a metal–insulator transition in monolayer $MoS_2$," *Nature Materials 2013 12:9*, vol. 12, pp. 815–820, 6 2013.

[196] J. Xue, S. Huang, J. Y. Wang, and H. Q. Xu, "Mott variable-range hopping transport in a $MoS_2$ nanoflake," *RSC Advances*, vol. 9, pp. 17885–17890, 6 2019.

[197] R. Tian, S. H. Park, P. J. King, G. Cunningham, J. Coelho, V. Nicolosi, and J. N. Coleman, "Quantifying the factors limiting rate performance in battery electrodes," *Nature Communications 2019 10:1*, vol. 10, pp. 1–11, 4 2019.

[198] W.-Y. Lai, P. W. Huang, J. Kang, Q. Zhang, Y. Wang, S. W.-Y. Lai, Y.-Z. Zhang, Y. Wang, T. Cheng, L.-Q. Yao, X. Li, and W. H. ab, "Printed supercapacitors: materials, printing and applications," *Chemical Society Reviews*, vol. 48, pp. 3229–3264, 6 2019.

[199] S. Barwich, J. M. de Araújo, A. Rafferty, C. G. da Rocha, M. S. Ferreira, and J. N. Coleman, "On the relationship between morphology and conductivity in nanosheet networks," *Carbon*, vol. 171, pp. 306–319, 1 2021.

[200] T. Carey, S. Cacovich, G. Divitini, J. Ren, A. Mansouri, J. M. Kim, C. Wang, C. Ducati, R. Sordan, and F. Torrisi, "Fully inkjet-printed two-dimensional material field-effect heterojunctions for wearable and textile electronics," *Nature Communications 2017 8:1*, vol. 8, pp. 1–11, 10 2017.

[201] S. Wan, X. Li, Y. Chen, N. Liu, Y. Du, S. Dou, L. Jiang, and Q. Cheng, "High-strength scalable mxene films through bridging-induced densification," *Science*, vol. 374, pp. 96–99, 10 2021.

[202] J. Fu, H. R. Thomas, and C. Li, "Tortuosity of porous media: Image analysis and physical simulation," *Earth-Science Reviews*, vol. 212, p. 103439, 1 2021.

[203] T. M. Heenan, C. Tan, J. Hack, D. J. Brett, and P. R. Shearing, "Developments in x-ray tomography characterization for electrochemical devices," *Materials Today*, vol. 31, pp. 69–85, 12 2019.

[204] C. Forró, S. J. Ihle, A. M. Reichmuth, H. Han, F. Stauffer, S. Weaver, A. Bonnin, M. Stampanoni, K. Tybrandt, and J. Vörös, "Visualizing and analyzing 3d metal nanowire networks for stretchable electronics," *Advanced Theory and Simulations*, vol. 3, p. 2000038, 8 2020.

[205] S. Tagliaferri, G. Nagaraju, A. Panagiotopoulos, M. Och, G. Cheng, F. Iacoviello, and C. Mattevi, "Aqueous inks of pristine graphene for 3D printed microsupercapacitors with high capacitance," *ACS Nano*, vol. 15, pp. 15342–15353, 9 2021.

[206] K. A. Sierros, H. Loh, S. Gyawali, and A. D. Bristow, "Morphology-dependent terahertz electrical conductivity of liquid-exfoliated graphite," *Optical Materials Express, Vol. 14, Issue 2, pp. 505-518*, vol. 14, pp. 505–518, 2 2024.

[207] K. Synnatschke, P. A. Cieslik, A. Harvey, A. Castellanos-Gomez, T. Tian, C. J. Shih, A. Chernikov, E. J. Santos, J. N. Coleman, and C. Backes, "Length- and thickness-dependent optical response of liquid-exfoliated transition metal dichalcogenides," *Chemistry of Materials*, vol. 31, pp. 10049–10062, 2019.

[208] D. Hanlon, C. Backes, E. Doherty, C. S. Cucinotta, N. C. Berner, C. Boland, K. Lee, A. Harvey, P. Lynch, Z. Gholamvand, S. Zhang, K. Wang, G. Moynihan, A. Pokle, Q. M. Ramasse, N. McEvoy, W. J. Blau, J. Wang, G. Abellan, F. Hauke, A. Hirsch, S. Sanvito, D. D. O'Regan, G. S. Duesberg, V. Nicolosi, and J. N. Coleman, "Liquid exfoliation of solvent-stabilized few-layer black phosphorus for applications beyond electronics," *Nature Communications 2015 6:1*, vol. 6, pp. 1–11, 10 2015.

[209] C. Backes, K. R. Paton, D. Hanlon, S. Yuan, M. I. Katsnelson, J. Houston, R. J. Smith, D. McCloskey, J. F. Donegan, and J. N. Coleman, "Spectroscopic metrics allow in situ measurement of mean size and thickness of liquid-exfoliated few-layer graphene nanosheets," *Nanoscale*, vol. 8, pp. 4311–4323, 2 2016.

[210] P. Eaton and P. West, *Atomic force microscopy*. Oxford university press, 2010.

[211] Y. Feng and W. H. Roos, "Atomic force microscopy: An introduction," *Methods in Molecular Biology*, vol. 2694, pp. 295–316, 2024.

[212] J. Li, M. M. Naiini, S. Vaziri, M. C. Lemme, and M. Östling, "Inkjet printing of $MoS_2$," *Advanced Functional Materials*, vol. 24, pp. 6524–6531, 11 2014.

[213] JASCO, "Instrumentation of a uv-visible spectrophotometer." `https://jascoinc.com/learning-center/theory/spectroscopy/uv-vis-spectroscopy/instrumentation/`. Accessed:30/07/24.

[214] J. M. Hollas, *Modern spectroscopy*. John Wiley & Sons, 2004.

[215] N. Kubetschek, C. Backes, and S. Goldie, "Algorithm for reproducible analysis of semiconducting 2D nanomaterials based on uv-vis spectroscopy," *Advanced Materials Interfaces*, p. 2400311, 2024.

[216] A. Harvey, C. Backes, J. B. Boland, X. He, A. Griffin, B. Szydlowska, C. Gabbett, J. F. Donegan, and J. N. Coleman, "Non-resonant light scattering in dispersions of 2D nanosheets," *Nature Communications 2018 9:1*, vol. 9, pp. 1–11, 11 2018.

[217] K. J. I. Ember, M. A. Hoeve, S. L. McAughtrie, M. S. Bergholt, B. J. Dwyer, M. M. Stevens, K. Faulds, S. J. Forbes, and C. J. Campbell, "Raman spectroscopy and regenerative medicine: a review," *npj Regenerative Medicine 2017 2:1*, vol. 2, pp. 1–10, 5 2017.

[218] L. G. Cançado, V. P. Monken, J. L. E. Campos, J. C. Santos, C. Backes, H. Chacham, B. R. Neves, and A. Jorio, "Science and metrology of defects in graphene using raman spectroscopy," *Carbon*, vol. 220, p. 118801, 2 2024.

[219] W. Jiang, M. Lin, Z. Yi, H. Li, and S. Wu, "Parameter determination using 3D FIB-SEM images for development of effective model of shale gas flow in nanoscale pore clusters," *Transport in Porous Media*, vol. 117, pp. 5–25, 3 2017.

[220] R. Hu, S. Jin, and G. Sha, "Application of atom probe tomography in understanding high entropy alloys: 3d local chemical compositions in atomic scale analysis," *Progress in Materials Science*, vol. 123, p. 100854, 1 2022.

[221] F. Wankmüller, J. Szász, J. Joos, V. Wilde, H. Störmer, D. Gerthsen, and E. Ivers-Tiffée, "Correlative tomography at the cathode/electrolyte interfaces of solid oxide fuel cells," *Journal of Power Sources*, vol. 360, pp. 399–408, 8 2017.

[222] R. Moroni, M. Börner, L. Zielke, M. Schroeder, S. Nowak, M. Winter, I. Manke, R. Zengerle, and S. Thiele, "Multi-scale correlative tomography of a li-ion battery composite cathode," *Nature Publishing Group*, pp. 1–9, 2016.

[223] B. Gault, A. Chiaramonti, O. Cojocaru-Mirédin, P. Stender, R. Dubosq, C. Freysoldt, S. K. Makineni, T. Li, M. Moody, and J. M. Cairney, "Atom probe tomography," *Nature Reviews Methods Primers 2021 1:1*, vol. 1, pp. 1–30, 7 2021.

[224] R. L. Mitchell, M. Coleman, P. Davies, L. North, E. C. Pope, C. Pleydell-Pearce, W. Harris, and R. Johnston, "Macro-to-nanoscale investigation of wall-plate joints in the acorn barnacle semibalanus balanoides: Correlative imaging, biological form and function, and bioinspiration," *Journal of the Royal Society Interface*, vol. 16, 8 2019.

[225] G. Hübschen, I. Altpeter, R. Tschuncky, and H.-G. Herrmann, *Materials characterization using nondestructive evaluation (NDE) methods*. Woodhead publishing, 2016.

[226] M. Dunlap and J. Adaskaveg, "Introduction to the scanning electron microscope," *Theory, practice, & procedures. Facility for Advance Instrumentation. UC Davis*, vol. 52, 1997.

[227] D. C. Joy and J. B. Pawley, "High-resolution scanning electron microscopy," *Ultramicroscopy*, vol. 47, pp. 80–100, 11 1992.

[228] F. Zupanič, "Extracting electron backscattering coefficients from backscattered electron micrographs," *Materials Characterization*, vol. 61, pp. 1335–1341, 12 2010.

[229] N. Barthe, S. Maîtrejean, N. Carvou, and A. Cardona, "High-resolution beta imaging," in *Handbook of Radioactivity Analysis: Volume 2*, pp. 669–727, Elsevier, 2020.

[230] K. Wandelt, *Encyclopedia of interfacial chemistry: surface science and electrochemistry*. Elsevier, 2018.

[231] M. Ezzahmouly, A. Elmoutaouakkil, M. Ed-Dhahraouy, H. Khallok, A. Elouahli, A. Mazurier, A. ElAlbani, and Z. Hatim, "Micro-computed tomographic and SEM study of porous bioceramics using an adaptive method based on the mathematical morphological operations," *Heliyon*, vol. 5, p. e02557, 12 2019.

[232] L. Reimer and L. Reimer, "Detectors and signal processing," *Scanning Electron Microscopy: Physics of Image Formation and Microanalysis*, pp. 176–226, 1985.

[233] H. Seiler, "Secondary electron emission in the scanning electron microscope," *Journal of Applied Physics*, vol. 54, pp. R1–R18, 11 1983.

[234] B. J. Griffin, "A comparison of conventional everhart-thornley style and in-lens secondary electron detectors—a further variable in scanning electron microscopy," *Scanning*, vol. 33, pp. 162–173, 5 2011.

[235] K. Kumagai and T. Sekiguchi, "Sharing of secondary electrons by in-lens and out-lens detector in low-voltage scanning electron microscope equipped with immersion lens," *Ultramicroscopy*, vol. 109, pp. 368–372, 3 2009.

[236] J. I. Goldstein, D. E. Newbury, J. R. Michael, N. W. Ritchie, J. H. J. Scott, and D. C. Joy, *Scanning electron microscopy and X-ray microanalysis*. springer, 2017.

[237] P. Baatsen, S. Gabarre, K. Vints, R. Wouters, D. Vandael, R. Goodchild, S. Munck, and N. V. Gounko, "Preservation of fluorescence signal and imaging optimization for integrated light and electron microscopy," *Frontiers in Cell and Developmental Biology*, vol. 9, p. 737621, 12 2021.

[238] A. Yoshida and Y. Hishiyama, "Optimum acceleration voltage for SEM observation of carbon fiber," *TANSO*, vol. 1987, no. 130, pp. 110–117, 1987.

[239] M. D. Bachmann and M. D. Bachmann, "Focused ion beam micro-machining," *Manipulating Anisotropic Transport and Superconductivity by Focused Ion Beam Microstructuring*, pp. 5–33, 2020.

[240] C. A. Volkert and A. M. Minor, "Focused ion beam microscopy and micromachining," *MRS bulletin*, vol. 32, no. 5, pp. 389–399, 2007.

[241] B. I. Prenitzer, C. A. Urbanik-Shannon, L. A. Giannuzzi, S. R. Brown, R. B. Irwin, T. L. Shofner, and F. A. Stevie, "The correlation between ion beam/material interactions and practical fib specimen preparation," *Microscopy and Microanalysis*, vol. 9, pp. 216–236, 6 2003.

[242] M. F. Hayles, D. J. Stokes, D. Phifer, and K. C. Findlay, "A technique for improved focused ion beam milling of cryo-prepared life science specimens," *Journal of Microscopy*, vol. 226, pp. 263–269, 6 2007.

[243] R. J. Young and J. Puretz, "Focused ion beam insulator deposition," *Journal of Vacuum Science and Technology B: Microelectronics and Nanometer Structures Processing, Measurement, and Phenomena*, vol. 13, pp. 2576–2579, 11 1995.

[244] J. Melngailis, "Focused ion beam induced deposition: A review," *Electron-Beam, X-Ray, and Ion-Beam Submicrometer Lithographies for Manufacturing*, vol. 1465, pp. 36–49, 1991.

[245] A. Motayed, A. V. Davydov, M. D. Vaudin, I. Levin, J. Melngailis, and S. N. Mohammad, "Fabrication of gan-based nanoscale device structures utilizing focused ion beam induced Pt deposition," *Journal of Applied Physics*, vol. 100, p. 24306, 7 2006.

[246] C. Fager, M. Röding, A. Olsson, N. Lorén, C. V. Corswant, A. Särkkä, and E. Olsson, "Optimization of FIB–SEM tomography and reconstruction for soft, porous, and poorly conducting materials," *Microscopy and Microanalysis*, vol. 26, pp. 837–845, 8 2020.

[247] F. Kleiner, C. Rößler, F. Vogt, A. Osburg, and H. M. Ludwig, "Reconstruction of calcium silicate hydrates using multiple 2D and 3D imaging techniques: Light microscopy, $\mu$-ct, SEM, FIB-nT combined with EDX," *Journal of Microscopy*, vol. 286, pp. 102–107, 5 2022.

[248] M. Cantoni, A. Nakajo, G. Rinaldi, S. Diethelm, J. van Herle, and F. Pérez-Willard, "Characterization of solid oxide electrolysis cell by advanced FIB-SEM tomography," tech. rep., Centre Interdisciplinaire de Microscopie Électronique, École Polytechnique Fédérale de Lausanne (EPFL), 2010.

[249] M. Röding, C. Fager, A. Olsson, C. Von Corswant, E. Olsson, and N. Loren, "Three-dimensional reconstruction of porous polymer films from FIB-SEM nanotomography data using random forests," *Journal of Microscopy*, vol. 281, no. 1, pp. 76–86, 2021.

[250] M. D. Uchic, L. Holzer, B. J. Inkson, E. L. Principe, and P. Munroe, "Three-dimensional microstructural characterization using focused ion beam tomography," *MRS Bulletin*, vol. 32, pp. 408–416, 1 2007.

[251] Y. Zhang, C. Kong, R. S. Davidsen, G. Scardera, L. Duan, K. T. Khoo, D. N. Payne, B. Hoex, and M. Abbott, "3D characterisation using plasma FIB-SEM: A large-area tomography technique for complex surfaces like black silicon," *Ultramicroscopy*, vol. 218, p. 113084, 11 2020.

[252] M. F. Hayles and D. A. de Winter, "An introduction to cryo-FIB-SEM cross-sectioning of frozen, hydrated life science samples," *Journal of Microscopy*, vol. 281, pp. 138–156, 2 2021.

[253] Z. A. Khan, P. A. G. Salaberri, T. M. M. Heenan, al, M. Agnaou, M. A. Sadeghi, G. Lieser, L. de Biasi, and M. Scheuermann, "Kintsugi imaging of battery electrodes: Distinguishing pores from the carbon binder domain using Pt deposition," *Journal of The Electrochemical Society*, vol. 169, p. 070512, 7 2022.

[254] N. Yao, C. Harrison, D. Adamson, M. Park, P. Chaikin, and R. Register, "Sampling depth controlled by accelerating voltage in a low voltage sem," *Microscopy and Microanalysis*, vol. 3, no. S2, pp. 1241–1242, 1997.

[255] D. Roldán, C. Redenbach, K. Schladitz, M. Klingele, and M. Godehardt, "Reconstructing porous structures from FIB-SEM image data: Optimizing sampling scheme and image processing," *Ultramicroscopy*, vol. 226, p. 113291, 7 2021.

[256] R. C. Gonzalez, *Digital image processing*. Pearson education india, 2018.

[257] G. W. Zack, W. E. Rogers, and S. A. Latt, "Automatic measurement of sister chromatid exchange frequency.," *http://dx.doi.org/10.1177/25.7.70454*, vol. 25, pp. 741–753, 7 1977.

[258] H. M. Zelelew and A. T. Papagiannakis, "A volumetrics thresholding algorithm for processing asphalt concrete x-ray ct images," *International Journal of Pavement Engineering*, vol. 12, pp. 543–551, 12 2011.

[259] I. Arganda-Carreras, V. Kaynig, C. Rueden, K. W. Eliceiri, J. Schindelin, A. Cardona, and H. S. Seung, "Trainable weka segmentation: a machine learning tool for microscopy pixel classification," *Bioinformatics*, vol. 33, pp. 2424–2426, 8 2017.

[260] M. Belgiu and L. Drăgu, "Random forest in remote sensing: A review of applications and future directions," *ISPRS Journal of Photogrammetry and Remote Sensing*, vol. 114, pp. 24–31, 4 2016.

[261] I. Reimers, I. Safonov, A. Kornilov, and I. Yakimchuk, "Two-stage alignment of FIB-SEM images of rock samples," *Journal of Imaging 2020, Vol. 6, Page 107*, vol. 6, p. 107, 10 2020.

[262] M. B. Hisham, S. N. Yaakob, R. A. Raof, A. B. Nazren, and N. M. Embedded, "Template matching using sum of squared difference and normalized cross correlation," *2015 IEEE Student Conference on Research and Development, SCOReD 2015*, pp. 100–104, 2015.

[263] S. D. Kim, A. Sarkar, and J.-H. Ahn, "Graphene-based nanomaterials for flexible and stretchable batteries," *Small*, vol. 17, no. 48, p. 2006262, 2021.

[264] C. Yang, M. E. Denno, P. Pyakurel, and B. J. Venton, "Recent trends in carbon nanomaterial-based electrochemical sensors for biomolecules: A review," *Analytica chimica acta*, vol. 887, pp. 17–37, 2015.

[265] G. Ersu, Y. Sozen, E. Sánchez-Viso, S. Kuriakose, B. H. Juárez, F. J. Mompean, M. Garcia-Hernandez, L. Visscher, A. J. Magdaleno, F. Prins, *et al.*, "Pen plotter as a low-cost platform for rapid device prototyping with solution-processable nanomaterials," *Advanced Engineering Materials*, vol. 25, no. 14, p. 2300226, 2023.

[266] Y. Cao, Z. Xiong, F. Xia, G. V. Franks, L. Zu, X. Wang, Y. Hora, S. Mudie, Z. He, L. Qu, *et al.*, "New structural insights into densely assembled reduced graphene oxide membranes," *Advanced Functional Materials*, vol. 32, no. 42, p. 2201535, 2022.

[267] D. Kulkarni, S. J. Normile, L. G. Connolly, and I. V. Zenyuk, "Development of low temperature fuel cell holders for operando x-ray micro and nano computed tomography to visualize water distribution," *Journal of Physics: Energy*, vol. 2, no. 4, p. 044005, 2020.

[268] P. J. Withers, C. Bouman, S. Carmignato, V. Cnudde, D. Grimaldi, C. K. Hagen, E. Maire, M. Manley, A. D. Plessis, and S. R. Stock, "X-ray computed tomography," *Nature Reviews Methods Primers 2021 1:1*, vol. 1, pp. 1–21, 2 2021.

[269] J. Schindelin, I. Arganda-Carreras, E. Frise, V. Kaynig, M. Longair, T. Pietzsch, S. Preibisch, C. Rueden, S. Saalfeld, B. Schmid, J. Y. Tinevez, D. J. White, V. Hartenstein, K. Eliceiri, P. Tomancak, and A. Cardona, "Fiji: an open-source platform for biological-image analysis," *Nature Methods 2012 9:7*, vol. 9, pp. 676–682, 6 2012.

[270] S. J. Cooper, A. Bertei, P. R. Shearing, J. Kilner, and N. P. Brandon, "Taufactor: An open-source application for calculating tortuosity factors from tomographic data," *SoftwareX*, vol. 5, pp. 203–210, 2016.

[271] C. Steger, "An unbiased detector of curvilinear structures," *IEEE Transactions on pattern analysis and machine intelligence*, vol. 20, no. 2, pp. 113–125, 1998.

[272] D. Legland, I. Arganda-Carreras, and P. Andrey, "Morpholibj: integrated library and plugins for mathematical morphology with imagej," *Bioinformatics*, vol. 32, no. 22, pp. 3532–3534, 2016.

[273] T. M. Higgins, S. Finn, M. Matthiesen, S. Grieger, K. Synnatschke, M. Brohmann, M. Rother, C. Backes, J. Zaumseil, T. M. Higgins, M. Matthiesen, S. Grieger, K. Synnatschke, M. Brohmann, M. Rother, C. Backes, J. Zaumseil, and S. Finn, "Electrolyte-gated n-type transistors produced from aqueous inks of $W_2$ nanosheets," *Advanced Functional Materials*, vol. 29, p. 1804387, 1 2019.

[274] C. J. J. Zhang, S. H. Park, S. E. O'Brien, A. Seral-Ascaso, M. Liang, D. Hanlon, D. Krishnan, A. Crossley, N. McEvoy, J. N. Coleman, and V. Nicolosi, "Liquid exfoliation of interlayer spacing-tunable 2D vanadium oxide nanosheets: High capacity and rate handling li-ion battery cathodes," *Nano Energy*, vol. 39, pp. 151–161, 9 2017.

[275] L. A. Segura and P. G. Toledo, "Pore-level modeling of isothermal drying of pore networks: Effects of gravity and pore shape and size distributions on saturation and transport parameters," *Chemical Engineering Journal*, vol. 111, no. 2-3, pp. 237–252, 2005.

[276] M. Naito, T. Yokoyama, K. Hosokawa, and K. Nogi, *Nanoparticle technology handbook*. Elsevier, 2018.

[277] Z. Yu, R. Carter, and J. Zhang, "Measurements of pore size distribution, porosity, effective oxygen diffusivity, and tortuosity of pem fuel cell electrodes," *Fuel Cells*, vol. 12, no. 4, pp. 557–565, 2012.

[278] C. J. Martinez, B. Hockey, C. B. Montgomery, and S. Semancik, "Porous tin oxide nanostructured microspheres for sensor applications," *Langmuir*, vol. 21, no. 17, pp. 7937–7944, 2005.

[279] P. Sun, R. Ma, and T. Sasaki, "Recent progress on exploring exceptionally high and anisotropic $H^+/OH^-$ ion conduction in two-dimensional materials," *Chemical science*, vol. 9, no. 1, pp. 33–43, 2018.

[280] R. Tian, M. Breshears, D. V. Horvath, and J. N. Coleman, "The rate performance of two-dimensional material-based battery electrodes may not be as good as commonly believed," *ACS nano*, vol. 14, no. 3, pp. 3129–3140, 2020.

[281] X. Xiao, P. Liu, J. S. Wang, M. Verbrugge, and M. P. Balogh, "Vertically aligned graphene electrode for lithium ion battery with high rate capability," *Electrochemistry Communications*, vol. 13, no. 2, pp. 209–212, 2011.

[282] P. P. Acharjya and D. Ghoshal, "Watershed segmentation based on distance transform and edge detection techniques," *International Journal of Computer Applications*, vol. 52, no. 13, pp. 6–10, 2012.

[283] A. Kaniyoor, T. S. Gspann, J. E. Mizen, and J. A. Elliott, "Quantifying alignment in carbon nanotube yarns and similar two-dimensional anisotropic systems," *Journal of Applied Polymer Science*, vol. 138, no. 37, p. 50939, 2021.

[284] Z. Li, R. J. Young, N. R. Wilson, I. A. Kinloch, C. Vallés, and Z. Li, "Effect of the orientation of graphene-based nanoplatelets upon the young's modulus of nanocomposites," *Composites Science and Technology*, vol. 123, pp. 125–133, 2016.

[285] J. R. Nimmo, "Porosity and pore size distribution," *Encyclopedia of Soils in the Environment*, vol. 3, no. 1, pp. 295–303, 2004.

[286] S. Zhang, M. Zheng, Z. Lin, N. Li, Y. Liu, B. Zhao, H. Pang, J. Cao, P. He, and Y. Shi, "Activated carbon with ultrahigh specific surface area synthesized from natural plant material for lithium–sulfur batteries," *Journal of Materials Chemistry A*, vol. 2, no. 38, pp. 15889–15896, 2014.

[287] G.-J. Li, X.-H. Zhang, and S. Kawi, "Relationships between sensitivity, catalytic activity, and surface areas of $SnO_2$ gas sensors," *Sensors and Actuators B: Chemical*, vol. 60, no. 1, pp. 64–70, 1999.

[288] L. Yin, J. Lv, and J. Wang, "Structural innovations in printed, flexible, and stretchable electronics," *Advanced Materials Technologies*, vol. 5, no. 11, p. 2000694, 2020.

[289] D. A. G. Bruggeman, "Berechnung verschiedener physikalischer konstanten von heterogenen substanzen. i. dielektrizitätskonstanten und leitfähigkeiten der mischkörper aus isotropen substanzen," *Annalen der physik*, vol. 416, no. 7, pp. 636–664, 1935.

[290] B. Tjaden, S. J. Cooper, D. J. Brett, D. Kramer, and P. R. Shearing, "On the origin and application of the bruggeman correlation for analysing transport phenomena in electrochemical systems," *Current opinion in chemical engineering*, vol. 12, pp. 44–51, 2016.

[291] B. Tjaden, D. J. Brett, and P. R. Shearing, "Tortuosity in electrochemical devices: a review of calculation approaches," *International Materials Reviews*, vol. 63, no. 2, pp. 47–67, 2018.

[292] K. K. Patel, J. M. Paulsen, and J. Desilvestro, "Numerical simulation of porous networks in relation to battery electrodes and separators," *Journal of power sources*, vol. 122, no. 2, pp. 144–152, 2003.

[293] X. Lin, X. Shen, Q. Zheng, N. Yousefi, L. Ye, Y.-W. Mai, and J.-K. Kim, "Fabrication of highly-aligned, conductive, and strong graphene papers using ultralarge graphene oxide sheets," *ACS nano*, vol. 6, no. 12, pp. 10708–10719, 2012.

[294] D. O'Suilleabhain, V. Vega-Mayoral, A. G. Kelly, A. Harvey, and J. N. Coleman, "Percolation effects in electrolytically gated $WS_2$/graphene nano: nano composites," *ACS applied materials & interfaces*, vol. 11, no. 8, pp. 8545–8555, 2019.

[295] C. Gabbett, A. G. Kelly, E. Coleman, L. Doolan, T. Carey, K. Synnatschke, S. Liu, A. Dawson, D. O'Suilleabhain, J. Munuera, E. Caffrey, J. B. Boland, Z. Sofer, G. Ghosh, S. Kinge, L. D. Siebbeles, N. Yadav, J. K. Vij, M. A. Aslam, A. Matkovic, and J. N. Coleman, "Understanding how junction resistances impact the conduction mechanism in nano-networks," *Nature Communications 2024 15:1*, vol. 15, pp. 1–13, 5 2024.

[296] C. Gabbett, L. Doolan, K. Synnatschke, L. Gambini, E. Coleman, A. G. Kelly, S. Liu, E. Caffrey, J. Munuera, C. Murphy, *et al.*, "Quantitative analysis of printed nanostructured networks using high-resolution 3d FIB-SEM nanotomography," *Nature Communications*, vol. 15, no. 1, p. 278, 2024.

[297] S. Liu, T. Carey, J. Munuera, K. Synnatschke, H. Kaur, E. Coleman, L. Doolan, and J. N. Coleman, "Solution-processed heterojunction photodiodes based on $WSe_2$ nanosheet networks," *Small*, p. 2304735, 2023.

[298] A. G. Kelly, D. Finn, A. Harvey, T. Hallam, and J. N. Coleman, "All-printed capacitors from graphene-bn-graphene nanosheet heterostructures," *Applied Physics Letters*, vol. 109, no. 2, 2016.

[299] D. O'Suilleabhain, A. G. Kelly, R. Tian, C. Gabbett, D. Horvath, and J. N. Coleman, "Effect of the gate volume on the performance of printed nanosheet network-based transistors," *ACS Applied Electronic Materials*, vol. 2, no. 7, pp. 2164–2170, 2020.

[300] J. G. Berryman, "Random close packing of hard spheres and disks," *Physical Review A*, vol. 27, no. 2, p. 1053, 1983.

[301] W. Xu, K. Zhang, Y. Zhang, and J. Jiang, "Packing fraction, tortuosity, and permeability of granular-porous media with densely packed spheroidal particles: monodisperse and polydisperse systems," *Water Resources Research*, vol. 58, no. 2, p. e2021WR031433, 2022.

[302] P. K. Dubey, D. Marian, and G. Fiori, "Multiscale simulations of 2-D material ink-based printed network devices," *IEEE Transactions on Electron Devices*, vol. 70, pp. 689–694, 2 2023.

[303] C. Forró, L. Demkó, S. Weydert, J. Vörös, and K. Tybrandt, "Predictive model for the electrical transport within nanowire networks," *ACS Nano*, vol. 12, pp. 11080–11087, 11 2018.

[304] S. P. Ogilvie, M. J. Large, H. J. Wood, A. A. Graf, F. Lee, J. P. Salvage, A. A. King, and A. B. Dalton, "Size selection and thin-film assembly of $MoS_2$ elucidates thousandfold conductivity enhancement in few-layer nanosheet networks," *Nanoscale*, vol. 14, pp. 320–324, 1 2022.

[305] P. He and B. Derby, "Inkjet printing ultra-large graphene oxide flakes," *2D Materials*, vol. 4, no. 2, p. 021021, 2017.

[306] C. A. Klein and W. D. Straub, "Carrier densities and mobilities in pyrolytic graphite," *Physical Review*, vol. 123, no. 5, p. 1581, 1961.

[307] M. V. Bracamonte, G. I. Lacconi, S. E. Urreta, and L. E. F. Foa Torres, "On the nature of defects in liquid-phase exfoliated graphene," *The Journal of Physical Chemistry C*, vol. 118, no. 28, pp. 15455–15459, 2014.

[308] A. K. Geim and K. S. Novoselov, "The rise of graphene," *Nature materials*, vol. 6, no. 3, pp. 183–191, 2007.

[309] F. Giubileo and A. Di Bartolomeo, "The role of contact resistance in graphene field-effect devices," *Progress in Surface Science*, vol. 92, no. 3, pp. 143–175, 2017.

[310] E. Caffrey, J. M. Munuera, T. Carey, and J. N. Coleman, "Quantifying the effect of nanosheet dimensions on the piezoresistive response of printed graphene nanosheet networks," *Nanoscale Horizons*, 2024.

[311] D. E. O. Cortes, *Lateral size dependence of piezoresistivity and photoconductivity in TMD networks*. PhD thesis, Universidad de los Andes, 2024.

[312] Z. Püspöki, M. Storath, D. Sage, and M. Unser, "Transforms and operators for directional bioimage analysis: a survey," *Focus on bio-image informatics*, pp. 69–93, 2016.

[313] S. Wang, W. Li, J. Xue, J. Ge, J. He, J. Hou, Y. Xie, Y. Li, H. Zhang, Z. Sofer, and Z. Lin, "A library of 2D electronic material inks synthesized by liquid-metal-assisted intercalation of crystal powders," *Nature Communications 2024 15:1*, vol. 15, pp. 1–11, 7 2024.

[314] H. Li, Q. Zhang, C. C. R. Yap, B. K. Tay, T. H. T. Edwin, A. Olivier, and D. Baillargeat, "From bulk to monolayer $MoS_2$: evolution of raman scattering," *Advanced Functional Materials*, vol. 22, no. 7, pp. 1385–1390, 2012.

[315] G.-H. Nam, Q. He, X. Wang, Y. Yu, J. Chen, K. Zhang, Z. Yang, D. Hu, Z. Lai, B. Li, *et al.*, "In-plane anisotropic properties of 1T'-$MoS_2$ layers," *Advanced Materials*, vol. 31, no. 21, p. 1807764, 2019.

[316] N. Van Velson, H. Zobeiri, and X. Wang, "Thickness-dependent raman scattering from thin-film systems," *The Journal of Physical Chemistry C*, vol. 127, no. 6, pp. 2995–3004, 2023.

[317] A. K. Dash, H. Swaminathan, E. Berger, M. Mondal, T. Lehenkari, P. R. Prasad, K. Watanabe, T. Taniguchi, H.-P. Komsa, and A. Singh, "Evidence of defect formation in monolayer $MoS_2$ at ultralow accelerating voltage electron irradiation," *2D Materials*, vol. 10, no. 3, p. 035002, 2023.

[318] Y. Zhuo, I. A. Kinloch, and M. A. Bissett, "Simultaneous electrochemical exfoliation and functionalization of 2H-$MoS_2$ for supercapacitor electrodes," *ACS Applied Nano Materials*, vol. 6, no. 19, pp. 18062–18070, 2023.

[319] D. Song, A. Mahajan, E. B. Secor, M. C. Hersam, L. F. Francis, and C. D. Frisbie, "High-resolution transfer printing of graphene lines for fully printed, flexible electronics," *ACS nano*, vol. 11, no. 7, pp. 7431–7439, 2017.

[320] W. J. Hyun, E. B. Secor, M. C. Hersam, C. D. Frisbie, and L. F. Francis, "High-resolution patterning of graphene by screen printing with a silicon stencil for highly flexible printed electronics," *Advanced Materials*, vol. 27, no. 1, pp. 109–115, 2015.

[321] S. Biccai, C. S. Boland, D. P. O'Driscoll, A. Harvey, C. Gabbett, D. R. O'Suilleabhain, A. J. Griffin, Z. Li, R. J. Young, and J. N. Coleman, "Negative gauge factor piezoresistive composites based on polymers filled with $MoS_2$ nanosheets," *Acs Nano*, vol. 13, no. 6, pp. 6845–6855, 2019.

[322] D. J. Finn, M. Lotya, G. Cunningham, R. J. Smith, D. McCloskey, J. F. Donegan, and J. N. Coleman, "Inkjet deposition of liquid-exfoliated graphene and $MoS_2$ nanosheets for printed device applications," *Journal of Materials Chemistry C*, vol. 2, no. 5, pp. 925–932, 2014.

[323] G. Cunningham, D. Hanlon, N. McEvoy, G. S. Duesberg, and J. N. Coleman, "Large variations in both dark-and photoconductivity in nanosheet networks as nanomaterial is varied from $MoS_2$ to $WTe_2$," *Nanoscale*, vol. 7, no. 1, pp. 198–208, 2015.

[324] G. Cunningham, M. Lotya, N. McEvoy, G. S. Duesberg, P. van der Schoot, and J. N. Coleman, "Percolation scaling in composites of exfoliated $MoS_2$ filled with nanotubes and graphene," *Nanoscale*, vol. 4, no. 20, pp. 6260–6264, 2012.

[325] A. Behnam and A. Ural, "Computational study of geometry-dependent resistivity scaling in single-walled carbon nanotube films," *Physical Review B - Condensed Matter and Materials Physics*, vol. 75, p. 125432, 3 2007.

[326] S. Monaghan, F. Gity, R. Duffy, G. Mirabelli, M. McCarthy, K. Cherkaoui, I. M. Povey, R. E. Nagle, P. K. Hurley, J. R. Lindemuth, and E. Napolitani, "Hall-effect mobility for a selection of natural and synthetic 2D semiconductor crystals," *Joint International EUROSOI Workshop and International Conference on Ultimate Integration on Silicon-ULIS, EUROSOI-ULIS 2017 - Proceedings*, pp. 27–30, 6 2017.

[327] R. Dagan, Y. Vaknin, A. Henning, J. Y. Shang, L. J. Lauhon, and Y. Rosenwaks, "Two-dimensional charge carrier distribution in $MoS_2$ monolayer and multilayers," *Applied Physics Letters*, vol. 114, p. 101602, 3 2019.

[328] M. Chen, D. Cui, N. Wang, S. Weng, Z. Zhao, F. Tian, X. Gao, K. He, C.-T. Chiang, S. Albawardi, *et al.*, "Inkjet-printed $MoS_2$ nanoplates on flexible substrates for high-performance field effect transistors and gas sensing applications," *ACS Applied Nano Materials*, vol. 6, no. 5, pp. 3236–3244, 2023.

[329] B. A. Boukamp, "Distribution (function) of relaxation times, successor to complex nonlinear least squares analysis of electrochemical impedance spectroscopy?," *Journal of Physics: Energy*, vol. 2, no. 4, p. 042001, 2020.

[330] C. D. English, G. Shine, V. E. Dorgan, K. C. Saraswat, and E. Pop, "Improved contacts to $MoS_2$ transistors by ultra-high vacuum metal deposition," *Nano Letters*, vol. 16, pp. 3824–3830, 6 2016.

[331] X.-K. Li, R.-X. Sun, H.-W. Guo, B.-W. Su, D.-K. Li, X.-Q. Yan, Z.-B. Liu, and J.-G. Tian, "Controllable doping of transition-metal dichalcogenides by organic solvents," *Advanced Electronic Materials*, vol. 6, no. 3, p. 1901230, 2020.

[332] I. Shlimak, *Is hopping a science?: selected topics of hopping conductivity*. World Scientific, 2015.

[333] J. Xue, S. Huang, J.-Y. Wang, and H. Xu, "Mott variable-range hopping transport in a $MoS_2$ nanoflake," *RSC advances*, vol. 9, no. 31, pp. 17885–17890, 2019.

[334] H. Qiu, T. Xu, Z. Wang, W. Ren, H. Nan, Z. Ni, Q. Chen, S. Yuan, F. Miao, F. Song, *et al.*, "Hopping transport through defect-induced localized states in molybdenum disulphide," *Nature communications*, vol. 4, no. 1, p. 2642, 2013.

[335] J. S. Kim, J. Kim, J. Zhao, S. Kim, J. H. Lee, Y. Jin, H. Choi, B. H. Moon, J. J. Bae, Y. H. Lee, *et al.*, "Electrical transport properties of polymorphic $MoS_2$," *ACS nano*, vol. 10, no. 8, pp. 7500–7506, 2016.

[336] N. Huo, Y. Yang, Y.-N. Wu, X.-G. Zhang, S. T. Pantelides, and G. Konstantatos, "High carrier mobility in monolayer CVD-grown $MoS_2$ through phonon suppression," *Nanoscale*, vol. 10, no. 31, pp. 15071–15077, 2018.

[337] I. Vladimirov, C. Chow, A.-J. Strudwick, W. Kowalsky, M. G. Schwab, D. Kälblein, and R. T. Weitz, "Bulk transport and contact limitation of $MoS_2$ multilayer flake transistors untangled via temperature-dependent transport measurements," *physica status solidi (a)*, vol. 212, no. 9, pp. 2059–2067, 2015.

[338] X. Cui, G.-H. Lee, Y. D. Kim, G. Arefe, P. Y. Huang, C.-H. Lee, D. A. Chenet, X. Zhang, L. Wang, F. Ye, *et al.*, "Multi-terminal transport measurements of $MoS_2$ using a van der Waals heterostructure device platform," *Nature nanotechnology*, vol. 10, no. 6, pp. 534–540, 2015.

[339] F. Xia, V. Perebeinos, Y.-m. Lin, Y. Wu, and P. Avouris, "The origins and limits of metal–graphene junction resistance," *Nature nanotechnology*, vol. 6, no. 3, pp. 179–184, 2011.

[340] B.-K. Kim, T.-H. Kim, D.-H. Choi, H. Kim, K. Watanabe, T. Taniguchi, H. Rho, J.-J. Kim, Y.-H. Kim, and M.-H. Bae, "Origins of genuine ohmic van der Waals contact between indium and $MoS_2$," *npj 2D Materials and Applications*, vol. 5, no. 1, p. 9, 2021.

[341] W. Choi, D. Yin, S. Choo, S.-H. Jeong, H.-J. Kwon, Y. Yoon, and S. Kim, "Low-temperature behaviors of multilayer $MoS_2$ transistors with ohmic and schottky contacts," *Applied Physics Letters*, vol. 115, no. 3, 2019.

[342] E. Caffrey, T. Carey, L. Doolan, A. Dawson, E. Coleman, Z. Sofer, O. Cassidy, C. Gabbett, and J. N. Coleman, "Using electrical impedance spectroscopy to separately quantify the effect of strain on nanosheet and junction resistance in printed nanosheet networks," *Small*, vol. 21, no. 5, p. 2406864, 2025.

[343] A. Sinnott, *Mechanical Characterisation of Printed Nanosheet Network Thin Films*. PhD thesis, Trinity College Dublin, 2024.

[344] J. Xue, S. Huang, J.-Y. Wang, and H. Xu, "Mott variable-range hopping transport in a $MoS_2$ nanoflake," *RSC advances*, vol. 9, no. 31, pp. 17885–17890, 2019.

[345] Z. Li, L. Peng, J. Zhang, J. Li, Y. Zeng, Y. Luo, Z. Zhan, L. Meng, M. Zhou, and W. Wu, "Transition between efros–shklovskii and mott variable-range hopping conduction in polycrystalline germanium thin films," *Semiconductor Science and Technology*, vol. 32, no. 3, p. 035010, 2017.

[346] J. Cheng, S. Poehler, M. Laskar, L. Ma, S. Kannappan, S. Rajan, Y. Wu, and W. Lu, "Temperature dependent carrier transport in few-layered $MoS_2$: from hopping to band transport," *Journal of Physics D: Applied Physics*, vol. 55, no. 19, p. 195109, 2022.